Effects of Impurities on the Performance and Cost of V-Fe-Cr-Ti-based Solid Solution Alloys

zur Erlangung des akademischen Grades eines

DOKTORS DER INGENIEURWISSENSCHAFTEN (Dr.-Ing.)

der Fakultät für Chemieingenieurwesen und Verfahrenstechnik des

Karlsruher Instituts für Technologie (KIT)

genehmigte

DISSERTATION

von

Dipl. Ing. Ulrich Ulmer

aus Gelnhausen

Referent: Prof. Dr.-Ing. Roland Dittmeyer

Korreferent: Prof. Dr.rer.nat. Maximilian Fichtner

Tag der mündlichen Prüfung: 21. März 2016

Parts of this work have already been published in

Ulrich Ulmer, Kohta Asano, Andreas Patyk, Hirotoshi Enoki, Yumiko Nakamura, Alexander Pohl, Roland Dittmeyer and Maximilian Fichtner: "Cost reduction possibilities of vanadium-based solid solutions - microstructural, thermodynamic, cyclic and environmental effects of ferrovanadium substitution", *J. of Alloys and Compounds*, 648, (2015), 1024 - 1030

Ulrich Ulmer, Kohta Asano, Thomas Bergfeldt, Venkata Sai Kiran Chakravadhanula, Roland Dittmeyer, Hirotoshi Enoki, Christian Kübel, Yumiko Nakamura, Alexander Pohl and Maximilian Fichtner: „Effect of oxygen on the microstructure and hydrogen storage properties of V–Ti–Cr–Fe quaternary solid solutions", *Int. J. of Hydrogen Energy*, 39, (2014), 20000-20008.

Danksagung

An dieser Stelle bedanke ich mich bei allen, die zum Gelingen dieser Arbeit beigetragen haben. Namentlich erwähnen möchte ich hier:

Prof. Dr. Roland Dittmeyer, der es ermöglicht hat, diese Arbeit zu erstellen.

Prof. Dr. Maximilian Fichtner danke ich für die Aufgabenstellung, die Betreuung und für den Freiraum, eigene Ideen entwickeln und verfolgen zu können.

Dr. Yumiko Nakamura, Dr. Kohta Asano und Dr. Hirotoshi Enoki danke ich für die Aufnahme und Betreuung am AIST.

Dr. Alexander Pohl danke ich für die Unterstützung bei den XRD-Auswertungen und die vielen interessanten Gespräche während der gemeinsamen Mittagessen. Dr. Jianjiang Hu hat mich in die Kunst der Wasserstoffspeicherung eingeführt, wofür ihm mein Dank gebührt.

Dr. Venkata Sai Kiran Chakravadhanula und Dr. Christian Kübel danke ich für die Unterstützung während der TEM-Messungen und Auswertungen. Dr. Thomas Diemant hat XPS-Messungen durchgeführt und war während der Auswertung stets mit wertvollen Tips zur Stelle. Hierfür danke ich ihm.

Weiterhin möchte ich mich beim Konsortium des H2FC-Projektes für die hervorragende Zusammenarbeit bedanken. Hier gilt mein Dank insbesondere Dr. Magnus Sorby für die Einladungen zu den Synchrotron-Messungen am ESRF in Grenoble sowie Dr. Marek Bielewski und Dr. Pietro Moretto für die Zusammenarbeit während der Planung und Ausführung des Round Robin Tests und der Zyklierungen.

Weiterhin bedanke ich mich bei Frau Mila Dieterich für die Zyklierungsversuche am DLR.

„Last but not least“ möchte ich mich bei meiner Familie und meinen Freunden bedanken, die mich während meiner Zeit als Doktorand seelisch und moralisch unterstützt haben und mir stets Verständnis entgegengebracht haben.

Eidesstattliche Erklärung

Hiermit erkläre ich an Eides statt, dass ich die vorliegende Dissertation selbstständig angefertigt habe und nur die angegebenen Hilfsmittel verwendet habe. Von mir wurde noch kein Promotionsversuch unternommen.

Karlsruhe, den

____

Ulrich Ulmer

Abstract

In the present thesis, the effects of impurities are investigated on the performance and cost of AB-, AB_2- and AB_5-type intermetallic hydrides and vanadium (V) - iron (Fe) - chromium (Cr) - titanium (Ti) solid solution alloys for solid state hydrogen storage. These materials are chosen for the investigations due to their thermodynamic and kinetic properties suitable for the Liquid Organic Reaction Cycle (LORC), which is currently under development for the storage of thermal energy.

The first part of the thesis deals with the development of low-cost V-Fe-Ti-Cr-based hydrogen storage materials. High-purity, expensive raw metals V and Ti contained in the alloys are substituted with cheaper, low-purity alternatives, such as V containing a high level of residual oxygen, ferrovanadium (FeV) and Ti sponge. The effects of the substitutions are investigated. Alloys containing high and low residual oxygen concentrations are synthesized and characterized by X-ray diffraction (XRD), scanning/transmission electron microscopy (SEM and TEM) and volumetric measurements. Two different FeV raw metals (FeV 1 or FeV 2) are used in substitution for V and Fe, and the microstructure and hydrogen storage properties of the resulting alloys are characterized by XRD, SEM and volumetry. High-purity Ti is substituted with Ti sponge. The structural and thermodynamic effects of the substitution are investigated. V, Fe and Ti are finally replaced by FeV and Ti sponge to obtain low-cost hydrogen storage materials.

Both the microstructure and hydrogen storage properties are negatively affected when FeV 1 or 2 are used for the synthesis of the alloys in substitution for V and Fe. The C14 Laves secondary phase is formed as the level of substitution increases. An alteration of hydrogen storage properties is observed, which manifests itself in a steady increase in equilibrium hydrogen pressure and a decrease in reversible hydrogen capacity with the level of substitution. This originates in the introduction of impurities contained in FeV, such as O, Al and Si. The materials prepared with FeV 2 exhibit more favorable properties for hydrogen storage than those prepared with FeV 1, which is due to the lower impurity concentration of FeV 2 as compared to FeV 1. The substitution of high-purity Ti with cheaper Ti sponge is found to have negligible effects on the microstructure and hydrogen storage properties of the resulting alloys. A correlation is established between arc melting current, concentration of impurities and hydrogen storage properties of the resulting alloys prepared with FeV 2 and Ti sponge through variation of the synthesis conditions. The raw material price to store an equal amount of hydrogen is reduced by 88 % when the storage material is synthesized using FeV 2 and Ti sponge.

In the second part of the thesis, the reactions of gaseous or liquid impurities at or with the surface of the storage materials are investigated. XRD, thermogravimetry coupled with differential scanning calorimetry and mass spectrometry (TG-DSC-MS), gas chromatography (GC), X-ray photoelectron spectroscopy (XPS) and volumetry are used to study the passivation behaviour of $TiFeH_x$, $Ti_{0.95}Zr_{0.05}Mn_{1.49}V_{0.45}Fe_{0.06}H_x$, $LaNi_5H_x$ and $V_{40}Fe_8Ti_{26}Cr_{26}H_x$ upon dispersion in liquid acetone or toluene. The cyclic stability of V-Fe-Cr-Ti-based solid solution alloys is investigated in H_2 blended with impurities by means of volumetric measurements. XPS measurements are used to study the passivation mechanism of these materials in O_2-contaminated H_2. Two strategies to engineer V-Fe-Cr-Ti-based storage materials with surface structures exhibiting superior cyclic durability in O_2-contaminated H_2 are presented.

Hydrogen is confined in $Ti_{0.95}Zr_{0.05}Mn_{1.49}V_{0.45}Fe_{0.06}H_x$, TiFeH and $V_{40}Fe_8Ti_{26}Cr_{26}H_x$ after contact with acetone. Liquid toluene passivates $V_{40}Fe_8Ti_{26}Cr_{26}H_x$, while TiFeH and $Ti_{0.95}Zr_{0.05}Mn_{1.49}V_{0.45}Fe_{0.06}H_x$ are either mildly deactivated (TiFeH), or a complete hydrogen desorption occurs ($Ti_{0.95}Zr_{0.05}Mn_{1.49}V_{0.45}Fe_{0.06}H_x$) also in the presence of toluene. Both organic liquids are found to be inert towards $LaNi_5H_x$. CO, propane and propene are formed during the desorption of H_2 from $V_{40}Fe_8Ti_{26}Cr_{26}H_x$ in liquid acetone, methylcyclohexane is formed in the case of liquid toluene. These

reactions are not observed when dehydrogenated $V_{40}Fe_8Ti_{26}Cr_{26}$ is dispersed in the organic liquids, indicating an increased reactivity during hydrogen desorption of the metal hydride. Significant amounts of carbon-containing species are detected at the surface and subsurface of acetone- or toluene-treated $V_{40}Fe_8Ti_{26}Cr_{26}$. The modification of the surface and subsurface chemistry and the resulting blocking of catalytic sites is believed to be responsible for the containment of hydrogen in the bulk.

Manifold interactions between storage material and impurity are observed during the absorption of H_2 by V-Fe-Ti-Cr-type solid solution alloys when trace amounts of gaseous impurities are blended with H_2. These interactions vary with the nature of the impurity and range from no observable effect in the case of toluene and N_2 to deactivation in the case of CO_2 and O_2. The introduction of a small amount of rare earth elements (in the form of Mischmetal (Mm), a mixture of La and Ce) into the alloy provides hydrogen-transparent diffusion pathways into the bulk of the material when the remaining oxidized surface is already intransparent for hydrogen. This affects an improved cyclic stability of the resulting alloy in O_2-containing hydrogen as compared to the same alloy without addition of Mm. The obtained surface-modified storage material absorbs hydrogen after 20 cycles in a hydrogen-oxygen mixture, in which the unmodified material is deactivated after four hydrogenation cycles.

Zusammenfassung

In der vorliegenden Arbeit werden die Auswirkungen von Verunreinigungen auf die Leistungsfähigkeit und Kosten von AB-, AB_2- und AB_5-artigen Legierungen sowie von Vanadium (V) – Eisen (Fe) – Chrom (Cr) – Titan (Ti)-basierten kubisch raumzentrierten Mischkristallen für die Wasserstoffspeicherung in Feststoffen untersucht. Diese Materialien werden aufgrund ihrer geeigneten thermodynamischen und kinetischen Eigenschaften für den „Liquid Organic Reaction Cycle“ (LORC), der für die Speicherung von thermischer Energie entwickelt wird, für die Untersuchungen ausgewählt.

Im ersten Teil der Arbeit werden V-Fe-Cr-Ti-basierte Wasserstoffspeichermaterialien mit reduzierten Rohmaterialkosten entwickelt. Die hochreinen und teuren Rohmetalle V und Ti, die in den Legierungen enthalten sind, werden durch die günstigeren und unreineren Alternativen V mit hohem Sauerstoffgehalt, Ferrovanadium (FeV) sowie Titanschwamm ersetzt. Die Auswirkungen der Ersetzung werden untersucht. Legierungen, die eine niedrige bzw. hohe Sauerstoffkonzentration aufweisen, werden hergestellt und mittels Röntgendiffraktometrie (XRD), Elektronenmikroskopie (SEM und TEM) und Volumetrie charakterisiert. V und Fe werden durch zwei unterschiedliche FeV Ausgangslegierungen (FeV 1 oder FeV 2) ersetzt, und die Mikrostruktur und Wasserstoffspeichereigenschaften der erhaltenen Legierungen werden mittels XRD, SEM und Volumetrie untersucht. Hochreines Ti wird durch Titanschwamm ersetzt. Die Auswirkungen der Ersetzung werden auf die strukturellen und thermodynamischen Eigenschaften der Legierung untersucht. Anschließend werden sowohl V als auch Ti durch FeV und Titanschwamm ersetzt, um kostengünstige Wasserstoffspeichermaterialien zu erhalten.

Sowohl die Mikrostruktur als auch die Wasserstoffspeichereigenschaften werden negativ beeinflusst wenn FeV 1 oder FeV 2 in Substitution für V und Fe für die Synthese der Legierungen verwendet werden. Die C14 Lavesphase wird bei hohen Substitutionsgraden als Sekundärphase gebildet. Eine Änderung der Wasserstoffspeichereigenschaften in Form einer Erhöhung des Gleichgewichtdruckes der Wasserstoffsorption sowie einer verminderten reversiblen Wasserstoffkapazität wird mit steigendem Substitutionsgrad beobachtet. Dies wird durch die Einführung von im FeV enthaltenen Verunreinigungen, wie beispielsweise O, Al und Si, hervorgerufen. Die mit FeV 2 hergestellten Materialien weisen bessere Wasserstoffspeichereigenschaften als die mit FeV 1 hergestellten Materialien auf. Dies liegt im niedrigeren Verunreinigungsgehalt von FeV 2 im Vergleich zu FeV 1 begründet. Die Auswirkungen der Substitution von hochreinem Ti mit Titanschwamm auf die Mikrostruktur und Wasserstoffspeichereigenschaften der erhaltenen Legierung sind vernachlässigbar. Durch Variation der Synthesebedingungen wird eine Korrelation zwischen der während des Schmelzens der Legierung angewendeten Stromstärke mit den Konzentrationen an Verunreinigungen und den Wasserstoffspeichereigenschaften der erhaltenen Legierungen hergestellt. Der Rohmaterialpreis, um eine gleiche Menge Wasserstoff zu speichern, fällt im Fall des FeV 2- und titanschwammsubstitutierten Materials um 88 % geringer aus als im Fall des mit hochreinen Ausgangsstoffen hergestellten Materials.

Im zweiten Teil der Arbeit werden die Reaktionen von gasförmigen oder flüssigen Verunreinigungen an oder mit der Oberfläche von Wasserstoffspeichermaterialien untersucht. XRD, Thermogravimetrie gekoppelt mit Differenzialrasterkalorimetrie und Massenspektrometrie (TG-DSC-MS), Gaschromatographie (GC), Röntgenphotoelektronenspektroskopie (XPS) und Volumetrie werden verwendet, um das Passivierungsverhalten von $TiFeH_x$, $Ti_{0.95}Zr_{0.05}Mn_{1.49}V_{0.45}Fe_{0.06}H_x$, $LaNi_5H_x$ und $V_{40}Fe_8Ti_{26}Cr_{26}H_x$ während der Dispersion in flüssigem Aceton oder Toluol zu untersuchen. Die Zyklenstabilität von V-Fe-Cr-Ti-basierten Mischkristallen in einem Gemisch aus H_2 mit verschiedenen Verunreinigungen wird mittels Volumetrie untersucht. XPS-Messungen werden angewendet, um den Passivierungsmechanismus dieser Materialien in O_2-verunreinigtem H_2 zu untersuchen. Zwei

Strategien zur Entwicklung von Materialien mit Oberflächenstrukturen, die eine verbesserte Zyklenstabilität in O_2-kontaminiertem H_2 aufweisen, werden vorgeschlagen.

Nach Kontakt mit flüssigem Aceton wird Wasserstoff in $Ti_{0.95}Zr_{0.05}Mn_{1.49}V_{0.45}Fe_{0.06}H_x$, TiFeH und $V_{40}Fe_8Ti_{26}Cr_{26}H_x$ eingeschlossen. Flüssiges Toluol wirkt passivierend auf $V_{40}Fe_8Ti_{26}Cr_{26}H_x$, während TiFeH und $Ti_{0.95}Zr_{0.05}Mn_{1.49}V_{0.45}Fe_{0.06}H_x$ entweder sanft passiviert werden (TiFeH), oder es findet eine vollständige Wasserstoffdesorption auch in Anwesenheit von Toluol statt ($Ti_{0.95}Zr_{0.05}Mn_{1.49}V_{0.45}Fe_{0.06}H_x$). Beide organischen Substanzen verhalten sich gegenüber $LaNi_5H_x$ inert. CO, Propan und Propen werden während der H-Desorption von $V_{40}Fe_8Ti_{26}Cr_{26}H_x$ in flüssigem Aceton gebildet. Methylcyclohexan entsteht im Fall von flüssigem Toluol. Wird desorbiertes $V_{40}Fe_8Ti_{26}Cr_{26}$ verwendet, so werden diese Reaktionen nicht beobachtet, was auf eine erhöhte Oberflächenaktivität des Metallhydrids während der Wasserstoffdesorption hinweist. Signifikante Mengen kohlenstoffhaltiger Verbindungen werden in den oberflächennahen Bereichen von aceton- oder toluolbehandeltem $V_{40}Fe_8Ti_{26}Cr_{26}$ beobachtet. Diese Änderung der chemischen Zusammensetzung der Oberfläche und die daraus resultierende Blockierung der katalytisch aktiven Plätze ist wahrscheinlich verantwortlich für den Einschluss des Wasserstoffs im Kern des Materials.

Vielfältige Wechselwirkungen werden während der Wasserstoffabsorption von V-Fe-Cr-Ti-artigen Mischkristallen in Gemischen von H_2 und Spuren von Verunreinigungen beobachtet. Diese Wechselwirkungen variieren je nach Art der Verunreinigung zwischen keiner Minderung der Wasserstoffabsorptionsfähigkeit, wie im Fall von Toluol oder N_2 beobachtet, und Deaktivierung, die in den Fällen von O_2 und CO_2 auftritt. Durch die Einführung einer kleinen Menge seltener Erden in Form von Mischmetall (ein Gemisch aus La und Ce) in die Legierung lassen sich “wasserstofftransparente” Diffusionspfade in den Kern des Materials erzeugen, wenn die übrige Oberfläche bereits “wasserstoffintransparent” geworden ist. Dies resultiert in einer verbesserten Zyklenstabilität des Mm-modifizierten Materials in O_2-kontaminiertem H_2 im Vergleich mit einem ähnlichen Material ohne Zugabe von Mm. Das erhaltene oberflächenmodifizierte Material absorbiert nach 20 Zyklen noch Wasserstoff in einem Wasserstoff-Sauerstoff-Gemisch, in dem das nicht modifizierte Material bereits nach vier Zyklen deaktiviert ist.

Table of Contents

Abbreviations

TES	Thermal Energy Storage
J	Joule
m	Mass (kg)
g	Gram
c_p	Specific heat capacity (J/kg*K)
T	Temperature (K)
PCM	Phase change material
h	Enthalpy (J/kg)
A	Reactant A of a chemical reaction
B	Reactant B of a chemical reaction
Mg	Magnesium
O	Oxygen
H	Hydrogen
Ca	Calcium
eV	Electron volt (1.6×10^{-19} J)
Wh	Watt hour
th	Thermal
MCH	Methylcyclohexane
MB	Methylbenzene (Toluene)
LORC	Liquid organic reaction cycle
Pt	Platinum
Al	Aluminum
DoE	U.S. Department of Energy
CSP	Concentrated solar thermal power
M	Metal
c	Concentration (mol/m^3)
F	Number of degrees of freedom
C	Number of components, alt.: Carbon
P	Number of phases
a	Activity (mol/m^3)
ΔH_0	Standard enthalpy of reaction (J/mol)
ΔS_0	Standard entropy of reaction (J/molK)
t	Time (s, min, or h)
i	Incubation
Pa	Pascal (Pa, kg/ms^2)
La	Lanthanum
Ni	Nickel
Ti	Titanium
Fe	Iron
V	Vanadium
Mn	Manganese
Na	Sodium
Li	Lithium
Å	Ångström [10^{-10} m]
bcc	body-centered cubic
bct	body-centered tetragonal
fcc	face-centered cubic
Nb	Niobium
Zr	Zirconium

Cr	Chromium
Mn	Manganese
Cu	Copper
Pd	Palladium
N	Nitrogen
R_A	Radius of the central point of a polyhedron (m)
R_x	Radius of the building block of a polyhedron (m)
FeV	Ferrovanadium
Ar	Argon
A	Ampere
p	Pressure (Pa)
v	Volume (m^3)
n	Amount of gas (mol)
R	Gas constant (J/mol K)
PCI	Pressure-composition isotherm
Mm	Mischmetal

1 Introduction

Availability of energy has become a central issue in modern societies for a number of reasons, the most important of which involve the provision of work, heat and electricity to "fuel" our economies and to make life comfortable.

Fossil fuels represent the major sources of energy in our current energy mix. While the exploitation of unconventional shale oil and gas is expected to delay the inevitable end of the petroleum age, the era of *cheap* oil appears to be coming to an end. Estimates on the depletion of coal, the most abundant fossil fuel, vary between 100 and 250 years [1], [2]. Environmental concerns associated with the extraction and combustion of fossil fuels intensify the growing unease over our current energy production system.

The quest for alternative sources of energy has gained momentum and is supported by governments and industries around the world. Abundant and so-called "renewable" energy is, in principle, available from the sun to run the earth in a sustainable way. Solar energy can be harnessed directly by agricultural, photovoltaic or solar thermal means, or indirectly for example in the form of wind or water power. However, an important problem with the effective use of renewable energy is that the schedule of energy use is often not synchronous with its acquisition. Thus, buffer, or storage systems are necessary in order to compensate for the mismatch between energy generation and energy use.

In this context, the storage of thermal energy (Thermal Energy Storage or TES) is of great importance. Excess thermal energy generated in peak times can be stored in a TES system, where it is available for later use when energy demand exceeds energy supply. This could be hours, days or months later. Heat released from the storage system can either be used directly to heat buildings, districts or towns, or it could be transformed into electrical energy, which is fed into the electricity grid, using a steam turbine. TES therefore increases the availability and the dispatchability of a broad range of "renewable" energy technologies, such as (concentrated) solar thermal power, the co-generation of heat and power, or heat pumps.

Thermal energy can be stored by three methods:

1. *Sensible thermal energy storage* through utilizing heat capacity and temperature difference between a storage material and its ambience: $Q\sim m\left(c_p \cdot \Delta T\right)$; energy density: 100 – 170 kJ kg^{-1}.
2. *Latent thermal energy storage* through a phase change of a storage material and the resulting consumption/release of heat: $Q\sim m\left(\Delta h_{phase\ change}\right)$; energy density: 200 – 300 kJ kg^{-1}.
3. *Thermochemical storage* through endothermal and exothermal reactions: $Q\sim m(\Delta h_{reaction})$; energy density: 1500 – 4000 kJ kg^{-1} [3].

From the three storage methods, *thermochemical storage* offers the highest storage density as well as the longest storage time with negligible thermal losses, if the products of the endothermal reaction are stored separately from each other. The choice of a suitable storage method is also influenced by the temperature level at which the heat is available.

One possibility for thermochemical storage is represented by the liquid organic reaction cycle (LORC), which is currently under development at the Karlsruhe Institute of Technology. A schematic process diagram is depicted in Figure 1-1.

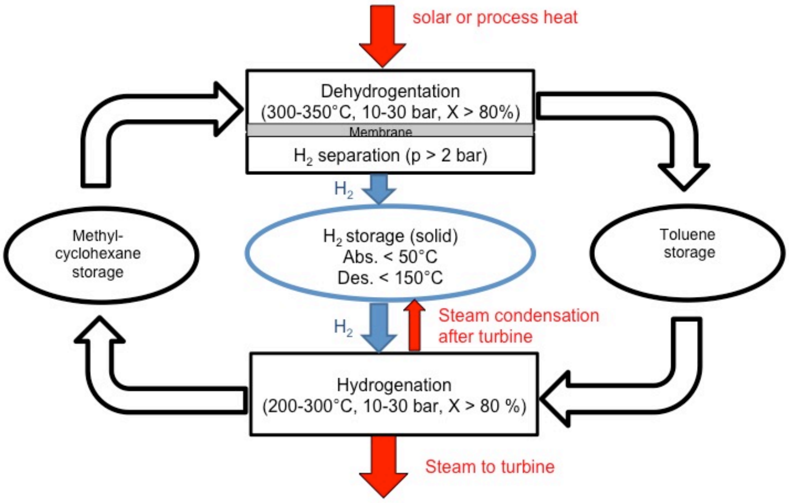

Figure 1-1: Schematic of the methylcyclohexane – toluene – hydrogen system for thermal energy storage [4]**.**

Thermal energy is stored during the endothermal, catalytic dehydrogenation of organic liquids such as methylcyclohexane. Reaction products toluene and hydrogen (H_2) are formed and stored separately. Heat release is accomplished through the exothermal reverse reaction of toluene and hydrogen. Thus, methylcyclohexane is formed, and the reaction cycle is closed.

Toluene and methylcyclohexane are considered unproblematic for storage, as they exist in liquid state at ambient temperature and pressure conditions and can be stored in simple containers in a compact and safe manner if the regulations of storing highly flammable and mildly toxic liquid organic substances are followed. Hydrogen shall be stored at ambient temperature at a pressure of 2-3 bar. Under these conditions, hydrogen exists in a gaseous state and, due to its low density, occupies a large volume. In order to reach high compactness of the process, hydrogen compression by physical or chemical means is desirable. At the same time, energy demand for compression should be as low as possible and safety aspects of the storage method should also be considered.

Hydrogen can be compressed and stored by different methods. Well-established hydrogen storage technologies such as pressurized tanks or storage as a cryogenic liquid are associated with high energy input, thereby rendering them unattractive for the LORC process described above. In solid state hydrogen storage systems, hydrogen is intercalated or bound covalently to solid materials. High volumetric hydrogen densities are achieved in these systems under moderate temperature and pressure conditions, and, depending on the storage material, the gravimetric hydrogen density can also be high [5], [6].

Intermetallic hydrides based on transition or rare earth metals have the unique ability to reversibly intercalate hydrogen atoms in their metal matrix structure. The interatomic distance between hydrogen atoms is decreased during this intercalation process [7], resulting in very high volumetric hydrogen densities. Intermetallics exhibit lower gravimetric hydrogen densities than high-pressure gaseous or liquified hydrogen tanks, however, for stationary applications, such as the thermal energy storage process described above, this is not as crucial as for mobile applications. Candidate hydrides must nevertheless satisfy a number of criteria for successful utilization, such as high H-storage capacity (for compactness of the storage system), low cost (both materials and processing), fast kinetics, durability during pressure/temperature swing cycles, safety and low toxicity, resistance to contamination and common impurities and minimal demands for hydride sorbent bed activation [8].

AB-, AB_2- or AB_5-type hydrides are formed by combining stoichiometric amounts of a strong hydride forming element A and a weak hydride forming element B. Storage capacities of well-known intermetallic hydrides, such as TiFe-, $TiMn_2$- or $LaNi_5$-related compounds, are in the range between 1 – 1.8 mass%, hydriding kinetics are fast, cyclic stability is high, the activation is easy, and hydrogen can be absorbed and desorbed at moderate temperature and pressure conditions. Reversible capacities > 2 mass% at ambient conditions can only be achieved with non-stoichiometric V-Ti-based solid solutions [9], [10].

A major factor that limits the practical applicability of intermetallic hydrides and V-Ti-based solid solutions is the high cost of the hydriding alloys. This reduces the economic competitiveness of hydrides as compared to pressurized hydrogen storage tanks despite energetic advantages of the solid state hydrogen storage method. Thus, advanced, high-performance hydrogen storage materials are necessary that operate at mild conditions and cost only a fraction of the currently available alloys. V-Ti-based solid solutions offer higher hydrogen densities per unit volume and unit mass than AB_x-type alloys. This is beneficial for many hydrogen storage applications. However, they are also considerably more expensive than AB_x-type hydrogen storage materials. For example, storing 100 kg of H_2 in a typical V-Ti-Fe-Cr solid solution with the composition $V_{40}Fe_8Ti_{26}Cr_{26}$ requires an investment of approximately 640,000 USD for the storage alloy alone if high-purity raw metals are used. For comparison, $LaNi_5$ (AB_5), $TiMn_2$ ("Hydralloy C", AB_2) or TiFe (AB)-type cost about 431,430, 323,600 or 72,220 USD to store the same amount of H_2, respectively.

The differences in storage material prices mainly originate in the different costs of the metals that constitute the respective hydrogen storage alloys. For example, the price of one kg vanadium V, lanthanum La or titanium Ti is 390, 90, or 25 USD, respectively. High-purity V is an expensive element, however, there exists a high potential to reduce its cost by substituting high-purity V with cheaper, low-purity V or ferrovanadium (FeV; contains about 80 % V, 10 – 18 % Fe and impurities) [11–15].

In the case of low-purity V, the last purification steps of the production process are omitted. Depending on the purity that is necessary, a cost reduction of about 10 – 20 % is possible. From both a scientific as well as an economic point of view, it is relevant to investigate the effects of impurities contained within the raw materials on the microstructure and hydrogen storage properties of the resulting solid solution alloys. Oxygen has been identified as a particularly harmful impurity on V-Ti-related hydrogen storage materials, as it negatively affects both the microstructure and the hydrogen storage properties through the promotion of secondary phase formation, destabilization of the hydride and reduced hydrogen capacity [16–18]. The effects of oxygen on the microstructure and hydrogen storage properties of V-Ti-type solid solution alloys with a composition similar to the materials investigated in this work have not been reported yet and are investigated in chapter 4.2.3.1.

The FeV production path differs strongly from the V production path and requires less energy input and fewer intermediate steps. Consequently, FeV is available for 30 USD/kg, which is less than 1/10 the price of high-purity V. Pursuing an analogous strategy of using cheaper intermediates instead of high-purity metals, the cost of Ti may also be reduced from 25 to around 10 USD/kg if titanium sponge is used. Ti sponge represents an intermediate product in the production process of high-purity Ti. FeV and Ti sponge contain many impurities, such as O, C, N, Al or Mg, that may influence the composition, microstructure and hydrogen storage properties of the resulting solid solution alloys. Depending on the FeV production process, the concentrations of these impurities in FeV may differ. Therefore, two types of FeV raw materials (denoted as FeV 1 and FeV 2) are used in this work for the synthesis of the storage alloys. The microstructural, thermodynamic and cyclic effects of substituting high-purity V and Fe with FeV 1 or FeV 2 are investigated in chapter 4.2.3.2. In chapter 4.2.3.3, high-purity Ti is replaced by Ti sponge and the resulting structural and thermodynamic effects are studied. Finally, high-purity V, Fe and Ti are substituted by FeV and Ti sponge in chapter 4.2.3.4. The influence of the synthesis conditions (arc melting current) on the content of impurities (O, C and N) and the hydrogen storage properties are tested, and the long-term cyclic stability of the resulting optimized material is investigated and compared to the material obtained with high-purity raw materials.

In addition to high raw material costs, most metal hydrides show the unfortunate tendency to passivate during cycling in impure hydrogen gas. Impurity effects result from the interaction of gaseous impurities with the hydriding alloy surfaces. Because the absorption and desorption of hydrogen are highly dependent on surface structure, surface “poisoning” can have dramatic effects on hydriding kinetics and capacity. Although in the LORC system described above, hydrogen is separated from toluene *in situ* in the dehydrogenation reactor, contact between metal hydride and toluene cannot be ruled out. While hydrocarbons such as methane or ethane are known to be innocuous to intermetallic AB- and AB_5-type compounds [19], hydrogen absorption by pure metallic Ti is inhibited by propane [20], [21], and other organic substances such as acetone are known to passivate the surface of V-Ti-based solid solutions alloys [16], [22]. The acetone passivation mechanism has not been explained yet, and it is not known whether other transition metal hydrides are also passivated after acetone contact. Additionally, the effects of liquid or gaseous toluene on intermetallic hydrides have not been systematically studied before. Therefore, in chapter 4.3.1 the effects of acetone and toluene on the AB-, AB_2- and AB_5-type intermetallic hydrides TiFe, $Ti_{0.95}Zr_{0.05}Mn_{1.49}V_{0.45}Fe_{0.06}$ and $LaNi_5$ and a V-Fe-Cr-Ti-type solid solution are investigated. The passivation behaviour after contact of the organic liquids with already absorbed metal hydrides is studied. Reaction mechanisms of acetone/toluene on the surface of the solid solution alloy $V_{40}Fe_8Ti_{26}Cr_{26}$ are investigated in more detail.

In addition to toluene, other gaseous impurities that may interact with the hydrogen storage alloy to be used in the LORC process are O_2, N_2, CO_2 or H_2O. They may enter the system either through leakages or as a consequence of a deactivation of the dehydrogenation catalyst through the deposition of coke. In order to reactivate the catalyst, the deposited coke has to be burned, and thus impurity gases originating from the reactivation may be present in the system. The cyclic behavior of V-Ti-based solid solutions with hydrogen containing various impurities, such as toluene, O_2, CO_2 or H_2O is investigated in chapter 4.3.2.1.

Two approaches aimed at engineering V-Ti-based storage materials with surface structures which exhibit improved durability upon cycling in impure hydrogen are described and tested in chapter 4.3.2.2. These approaches are based on the observation that AB_5-based hydrogen storage materials such as $LaNi_5$ exhibit the highest tolerance against gas-phase impurities. Either the A element (La) or the B element (Ni) are introduced in a V-Fe-Cr-Ti-based solid solution alloy. In the case of La, it is investigated whether the formed agglomerates provide hydrogen diffusion pathways into the bulk of the material also when cycled in hydrogen containing impurities such as O. For Ni, it is tested whether the enrichment of this element at the surface through selective leaching of the remaining other elements (V, Fe, Cr, Ti) improves the catalytic activity of the surface for H_2 dissociation and bulk penetration also in presence of O_2.

2 Fundamentals

2.1 Thermal Energy Storage – Definitions and Classifications

It is useful to begin this chapter by defining a few of the terms that will be frequently used. In *thermal energy storage systems* heat is supplied to or withdrawn from a storage system (so-called heat or "cold" storage). A *storage cycle* involves three steps: charge, storage and discharge [3]. Thermal energy storage is classified into short-term and long-term storage according to different storage durations. *Storage time* in a short term thermal energy storage varies from several hours to a few days. In long-term storage systems, storage time ranges between weeks and months. Seasonal thermal energy storage can be realized in long-term storage systems, e.g., by collecting and storing solar thermal energy during the summer months and releasing the stored energy in winter [23].

With respect to electricity generation in thermodynamic machines, thermal energy is rated based on its temperature. It is classified into low-grade (T < 100 °C), medium-grade (100 °C < T < 350 °C) and high-grade (T > 350 °C) heat [3], [24].

In thermodynamics, *heat* is defined as the *thermal energy transferred across a boundary of one region of matter to another*. As a process variable, heat is a characteristic of a process, not a property of a system. It is not contained within the boundary of the system. On the other hand, *thermal energy is a property of a system*, and exists on both sides of a boundary [25].

2.2 Thermal energy storage methods: sensible, latent and thermochemical/sorption storage

There are three types of heat storage systems: *sensible heat storage*, *latent heat storage*, and *thermochemical heat storage*.

In a *sensible heat storage* system, thermal energy is stored by increasing or decreasing the temperature of a storage material. The amount of thermal energy stored is calculated according to equation (1):

$$Q = m \cdot \int_{T_0}^{T_1} c_p \, dT \cong m \cdot c_p \cdot \Delta T, \tag{1}$$

when neglecting the temperature dependence of c_p, where Q is the amount of thermal energy stored in the material (J), m is the mass of storage material (kg), c_p is the specific heat of the storage material at constant pressure ($J/kg \cdot K$), and ΔT is the temperature change. The storage material can be a liquid (e.g. water [26], a molten salt [27], [28]) or a solid (e.g. rock [29] or concrete [30]). Each material has its own advantages and disadvantages, but usually the material is selected according to its heat capacity and the available space for storage [31]. Other important properties for the selection of a suitable material are density, thermal conductivity, vapor pressure, compatibility with container materials, and chemical stability [32].

In *latent heat storage*, heat is released or absorbed during the phase transition of a material. Heat release or storage occurs during a constant-temperature process, usually the melting or solidification of a phase change material (PCM). Other phase transitions such as solid-gas, solid-solid or liquid-gas have also been investigated [33]. The amount of stored heat is calculated with the following equation (2):

$$Q = m \cdot \Delta h_{phase\ change}, \tag{2}$$

where Q is the amount of stored heat in the material (J), m is the mass of storage material (kg), and Δh is the enthalpy of the phase change of the storage material (J/kg). The best known and most widely used phase change material is water [33], [34], which has been used for cold storage in the form of ice since ancient times. Potential PCM's include inorganic materials (e.g. water [33] or hydrated salts [35], [36]), eutectic mixtures of inorganic materials [37], [38], and organic materials (e.g. paraffins [33] or fatty acids [33], [36], [39]). Many materials have been studied as PCM, but only a few of them have been commercialized [40–42], mainly due to problems such as phase separation, subcooling, corrosion, long-term stability, and low heat conductivity. Usually PCM's are selected based on the appropriate melting enthalpy, availability and cost [3].

Thermochemical heat is stored during chemical reactions or sorption processes, according to equation (3):

$$AB + \Delta h_{reaction} \rightleftharpoons A + B. \tag{3}$$

During thermal charge of the storage system, the equilibrium is shifted to the right side of reaction equation (3). This initiates an endothermic chemical reaction of educt AB, and products A and B are formed. Shifting of the equilibrium is usually achieved through a temperature increase. Heat in form of the enthalpy of reaction, $\Delta h_{reaction}$, is consumed and stored in the form of "chemical potential". For thermal discharge, the equilibrium in reaction equation (3) is shifted again to the left side. During the reverse reaction, heat is retrieved and can be used, for example, for power generation, heating, or other purposes.

A thermal energy storage utilizing the involved reaction enthalpy presupposes the reversibility of the intended reaction as well as sufficient reaction rates. Furthermore, the absence of side reactions is desired. By suppressing the exothermic reverse reaction $A + B \rightarrow AB$, the duration of storage can in principle be infinite with negligible thermal losses. Depending on the reaction system, this can either be reached by kinetic limitations (e.g. absence of catalyst and/or low temperature) or by thermodynamic limitations (e.g. physical absence of the reaction partners) [3], [43].

Thermochemical energy storage is subdivided into chemical reaction and sorption systems [24]. Research in chemical reaction systems has been mainly focused on the hydration or carbonatation of metal oxides. Examples for these reactions are the hydration reaction of MgO and H_2O to $Mg(OH)_2$, and the carbonatation reaction of CaO and CO_2 to $CaCO_3$ [44].

Sorption systems are further subdivided into adsorption and absorption systems [3].

Thermal energy storage by means of adsorption utilizes the heat, which is liberated or consumed when a gaseous or liquid adsorbate is bound to the surface of a porous adsorbent material or when it is desorbed therefrom, respectively. If the adsorbate-adsorbent interaction is weak, the adsorbate is physisorbed at the surface of the adsorbent by Van-der-Waals forces. Chemisorption occurs if the interaction between adsorbate and adsorbent is strong, and new electronic bonds between these two species are formed. The energetic threshold separating the binding energy of "physisorption" from that of "chemisorption" is conventionally accepted to be about 0.5 eV per adsorbed species (i.e. 48 kJ/mol) [45]. Well-studied adsorbate-adsorbent combinations are water-zeolite and water-silica gel systems [46].

In an absorption system, an absorbate (usually a gas or a liquid) is incorporated in the bulk of another absorbent material, typically a solid or a liquid, or is released therefrom, respectively. During desorption, the absorbate is released from the absorbent endothermically, and the system is hereby thermally charged. Incorporation of the absorbate in the absorbent (absorption) is a heat-releasing, exothermal process, in which the thermal energy storage system is discharged. Solid-gas or solid-liquid absorption processes studied for thermal energy storage are those between metal salts and water [47], [48], ammonia [49], [50], or methanol [51] as well as metals and metal alloys with hydrogen [52–57].

Usual selection criteria for materials used in thermochemical storage systems are [58], [59]:

- high affinity by the sorbate for the sorbent
- high storage density
- high thermal conductivity and high heat transfer from sorbate to heat exchanger
- regeneration (thermal charging) temperature as low as possible: this results in higher efficiency
- environmentally safe, non-toxic
- non-corrosiveness of materials
- good thermal and chemical stability under operating conditions
- low material cost.

2.3 Comparison of the thermal energy storage methods

The U.S. Department of Energy (DOE) released specific technical targets for thermal energy storage on a system level (including, tanks, heat exchangers etc.) in concentrated solar thermal power plants (CSP), reported here:

- TES operating temperatures higher than 600 °C to assure high efficiencies of the power plant,
- TES exergetic efficiency higher than 95 %,
- TES specific cost lower than 15 $\$/kWh_{th}$,
- TES volumetric energy density higher than 25 kWh_{th}/m^3 [60].

The thermal energy storage methods described in sections 2.1.1 and 2.1.2 vary in their respective storage densities, times, temperatures and specific cost per kWh_{th}. Energy densities with respect to the storage material and storage temperatures of sensible, latent and thermochemical storage methods are compared in Figure 2.3-1.

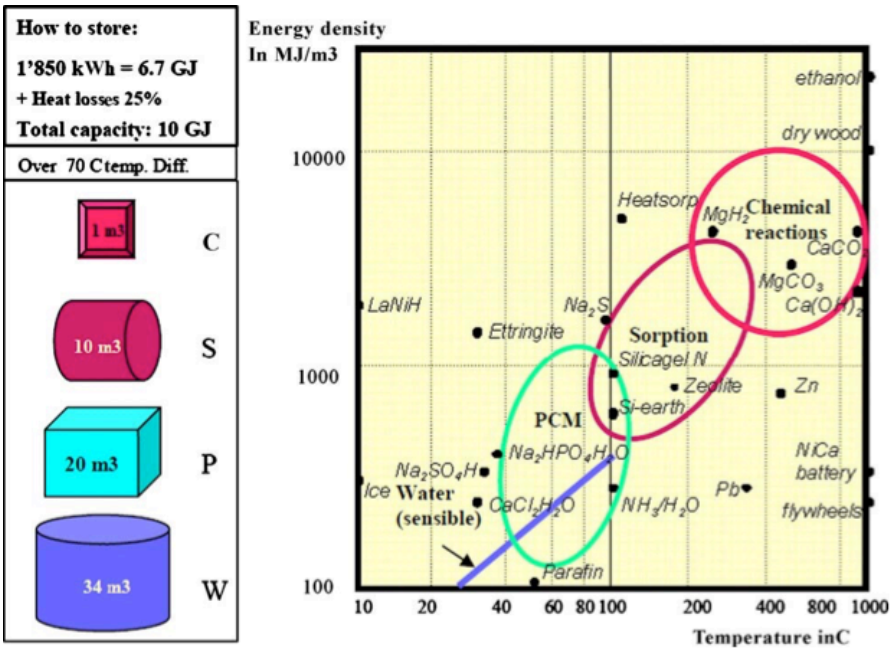

Figure 2.3-1: Right figure: energy density and storage temperature of different TES materials. Left figure: Storage volumes for 10 GJ thermal energy (W – water; P – phase change; S – sorption; C – chemical reaction) [89].

Thermochemical storage materials show the highest energy density per unit volume. Additionally, a broad range of storage temperatures from < 0 °C to 1000 °C can be realized by selecting an appropriate material.

Metal hydride-based thermal energy storage systems, which are extensively researched, show the potential to exceed the DOE targest mentioned above [57], [61]. Due to the lower temperature range of the hydrogenation reaction, the LORC process is not able to meet the DOE targets. However, it may be possible to exceed the targets if the working fluid is exchanged to a fluid, which can be hydrogenated at higher temperatures.

It is important to note that the storage density on a system level is considerably reduced as compared to the storage material due to additional volume and weight generated by the heat exchangers, storage vessels, pumps, compressors, piping etc.

2.4 The methylcyclohexane - toluene - hydrogen system (LORC process)

One possibility for thermochemical heat storage is represented by the methylcyclohexane – toluene – hydrogen – system (Figure 1-1), which is currently under development at the Karlsruhe Institute of Technology.

Thermal charge occurs during the endothermic, catalytic dehydrogenation of methylcyclohexane (MCH) in a microstructured membrane reactor using a Pt/Al_2O_3 catalyst [4]. A microstructured reactor is used because of the low heat transfer resistance and the large membrane area per catalyst volume. Reaction products toluene and hydrogen (H_2) are formed. Heat in the form of the enthalpy of reaction ($\Delta_R H_{298\,K} = 204.8\ kJ\ mol^{-1}$) is stored thermochemically according to reaction equation (4):

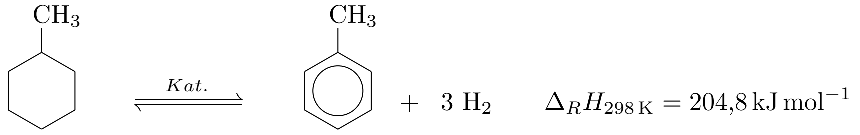

$$\Delta_R H_{298\,\mathrm{K}} = 204{,}8\,\mathrm{kJ\,mol^{-1}}$$

(4)

Hydrogen is separated *in situ* through a palladium membrane, thereby shifting the thermodynamic equilibrium to the product side according to Le Chatelier's principle [62]. Additionally, the membrane enables separation of the reaction products toluene and H_2, which are to be stored separately. Toluene is a liquid at ambient temperature and pressure conditions and can be stored efficiently after condensation. The formed hydrogen exists in the gaseous state at ambient conditions and occupied a volume about 500 times as large as the volume of toluene if it was stored without compression. The volumetric storage density of the system would then be low, and therefore hydrogen needs to be compressed in order to increase storage density. Compact hydrogen storage can, in principle, be achieved by mechanical compression and storage in state-of-the-art pressurized tanks. However, high volumetric hydrogen densities are achieved only at high overpressures, which is associated with considerable energy input and thus a reduced efficiency of the heat storage process. Intercalated hydrogen in solids, such as metal hydrides, shows a high volumetric hydrogen density at moderate temperature and pressure conditions. Additionally, hydrogen storage in a metal hydride benefits the overall efficiency of the heat storage process. Hydrogen pressure at the permeate side of the membrane reactor is > 2 bar, and the rehydrogenation pressure for the heat release reaction is > 10 bar (Figure 1-1). Through a proper selection of the metal hydride, hydrogen absorption and desorption can be achieved at conditions matching the optimum process requirements and thereby eliminates the necessity for mechanical compression before the hydrogenation reactor.

For heat release, toluene and H_2 are recombined in another microstructured reactor and the reverse, strongly exothermic reaction is initiated. Here a microstructured reactor is used due to the excellent heat transfer properties of these reactors.

Heat storage and release reactions take place between 250 and 350 °C, depending on the process conditions. The methylcyclohexane – toluene – hydrogen – system is therefore suitable for storage of medium grade thermal energy, which typically incurs in industrial processes [63], [64], geothermal [65] or biomass [66], [67] driven power plants, or solar collectors [64], [68], [69]. It is used for example to generate electricity using organic Rankine cycles with efficiencies of 8 – 20 %.

The different hydrogen storage methods are briefly reviewed in the following chapter. An emphasis is put on the energetic inputs that are required for hydrogen compression, as this is an important aspect for the optimization of thermodynamic systems such as the LORC process.

2.5 Hydrogen Storage Methods

Hydrogen can be stored with the following methods:

- as compressed gas in high pressure tanks,
- as cryogenic liquid at 20 K,
- adsorbed on the surface of porous solids,
- bound chemically in organic substances,
- absorbed in solids, such as metal hydrides,
- hybrid combinations of the above mentioned methods.

Gaseous hydrogen compression from 1 bar to 300 or 700 bar increases the volumetric hydrogen density from 0.08 kg/m^3 at 1 bar to 20 or 36 kg/m^3 at 300 or 700 bar, respectively [6]. High-pressure tanks are necessary for this, and appropriate safety measures must be applied to prevent potentially catastrophic tank failures, leakages or hydrogen embrittlement. Hydrogen exhibits real gas behaviour at pressures > 100 bar, and thus considerable energy input is necessary to compress the gas to higher pressures [70].

Liquefaction is another possibility to increase hydrogen density. Liquified hydrogen exhibits a density of 71 kg/m^3 and thus occupies a smaller volume than the pressurized gas. However, the liquefaction process is energy-intensive and costly relative to the energy density that can be achieved. Hydrogen condenses at 20 K (1 bar), and great technical effort has to be provided to reach such a low temperature. Gaseous hydrogen first has to be pre-cooled below its inversion temperature of 190 K, before it can be further cooled down and liquefied by the Linde- or Claude-process [71]. At least 30 % of the specific energy content of hydrogen are required for the liquefaction process. The critical temperature of hydrogen is 32 K (above this temperature hydrogen is gaseous), and liquid hydrogen containers are constructed as open systems to prevent strong overpressures. Heat transfer through the container affects the loss („boil-off“) of approximately 5 % hydrogen per day [5], [70].

In a physisorption system, molecular hydrogen is adsorbed on the surface of porous, high surface area materials (adsorbent) by weak Van-der-Waals forces. The interaction energy of hydrogen and the adsorbent ranges between 1 and 10 kJ/mol H_2. As a consequence of the low interaction energy, physisorption is a reversible process with fast charging and discharging kinetics, however, high capacities of > 4 mass% can only be achieved at low temperatures (approximately 77 K) and elevated pressures. Several compounds have been investigated as adsorbents, such as metal organic frameworks (MOF) [72], nanostructured carbon [73] or zeolites [74].

Hydrogen bound to solid or liquid materials at atmospheric temperature and pressure conditions presupposes a binding enthalpy of at least $\Delta H_B \geq 30$ kJ/mol H_2. The binding enthalpy in chemical hydrogen storage systems, such as organic substances or metal hydrides, lies in the range of 20 to 100 kJ/mol H_2. Thus, the chemical interactions between hydrogen and the storage material are strong enough to enable room temperature hydrogen storage.

Liquid organic hydrides such as carbazoles [75], [76], methylcyclohexane [4], [77] or decalin [78] have been investigated as hydrogen storage materials. Hydrogen uptake or release takes place in catalytic reactions at elevated temperatures. Challenges that need to be overcome for practical use are the sluggish reaction kinetics at low temperatures, unwanted by-product formation [79] or catalyst deactivation [4].

Solid state hydrogen storage offers potential advantages as compared to the above mentioned storage methods with respect to volumetric and/or gravimetric hydrogen density, temperature and pressure conditions that need to be applied to store and release hydrogen, as well as safety aspects.

Due to its unique electronic configuration with one electron in the 1 s orbital, hydrogen forms chemical bonds with many elements of the periodic table [80]. Among the plethora of possible binding partners, however, only few are suitable for practical storage applications.

The „perfect“ hydrogen storage material would absorb a large quantity of hydrogen under moderate overpressure and desorb it after a mild increase of temperature or decrease of pressure. Cyclic stability would be high, there were no safety-related concerns, and the material would be composed of cheap and earth-abundant elements. To date, no existing hydrogen storage material fulfils all these requirements. AB-, AB_2- or AB_5-type intermetallic hydrides such as $LaNi_5$, $TiMn_2$ or TiFe or V-Ti-based solid solutions show high volumetric hydrogen densities, excellent reversibility over thousands of cycles and ab- or desorb hydrogen under moderate temperature and pressure conditions. However, their reversible gravimetric hydrogen density does not exceed 2.5 mass% H and raw material cost is high. Cheaper complex hydrides or Mg-based materials with higher gravimetric storage density either do not store hydrogen reversibly or require high temperature and pressure conditions in order to initiate ab/desorption due to kinetic limitations. This renders them unattractive with regard to the LORC process.

For hydrogen storage it is generally undesired to work with a storage material which releases and consumes high amounts of heat to initiate the ab/desorption reactions and operates at high temperature. This is different for thermal energy storage materials, where high temperatures and reaction enthalpies are preferred.

2.6 Hydrogen-metal-systems

Hydrogen (H) reacts with many metals and metal alloys (M) and forms metal hydrides (MH), either by electrochemical water splitting (as used in metal hydride batteries), or by dissociative chemisorption, according to reaction equation (5):

$$M + \frac{x}{2} H_2 \rightleftharpoons M_x. \tag{5}$$

Interatomic distance between hydrogen atoms absorbed in solid materials is reduced as compared to gaseous or liquid hydrogen, and, as a result, the volumetric hydrogen density is increased [81].

Metal-hydrogen systems are classified into metal hydrides and complex hydrides [82]. In most classical metal hydrides, molecular hydrogen occupies interstitial sites of a host metal or alloy. In complex hydrides hydrogen is covalently bound to a metal or non-metal atom to form a complex anion. The charge of the anion is balanced by a cation, which is usually an alkali or alkaline earth ion.

Within this work, only interstitial hydrides were investigated. Therefore, this review emphasizes the fundamentals and properties particularly of these materials.

2.6.1 Thermodynamics of hydrogen-metal systems

Hydrogen sorption is a chemical process and proceeds in several steps. Hydrogen absorption of a metallic host is depicted schematically in Figure 2.6.1-1.

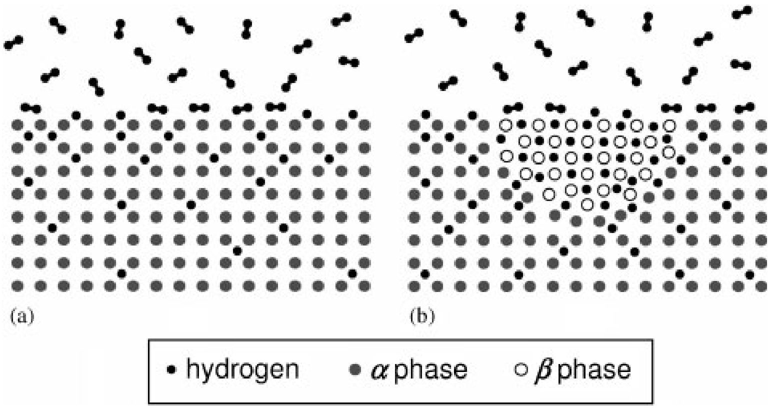

Figure 2.6.1-1: Simplified representation of the formation of a metal-hydrogen solid solution, referred to as the α-phase, (a), and the nucleation of the β-phase of the hydride host (b) [83].

Firstly, hydrogen molecules are physisorbed on the surface of the metal, followed by dissociative chemisorption of individual H atoms. A solid solution of hydrogen atoms in the interstitial sites of the metal is formed, which is referred to as the α-phase. As hydrogen concentration in the α-phase increases, hydrogen-hydrogen interactions become important and a more stable phase nucleates (β-phase). This phase transition is usually characterized by a crystalline structure change, volume expansion, and a nucleation energy barrier associated with volume expansion and interface energy between the phases.

Thermodynamics of hydride formation and dissociation are typically represented in pressure-composition isotherms, shown schematically in Figure 2.6.2-2 (a).

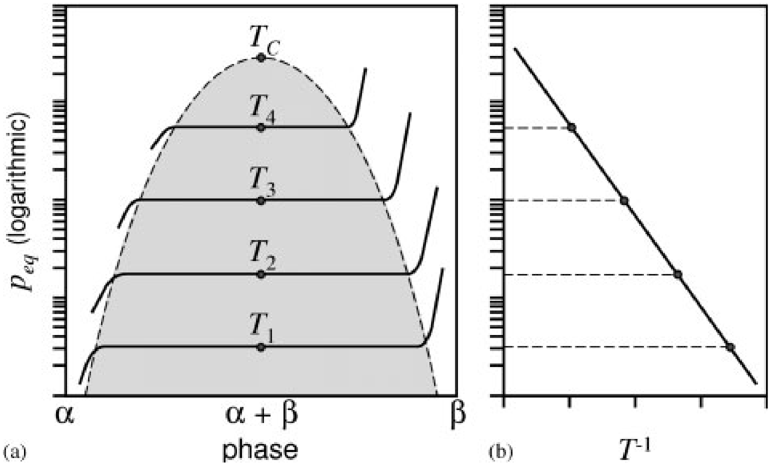

Figure 2.6.2-2: Schematic representation of pressure-composition isotherms (a), and the corresponding Van't Hoff plot (b) [83].

The α-phase is formed at low hydrogen concentrations. Solubility of gases such as H in metals is best described in form of an equilibrium reaction with equilibrium constant K_H. Hydrogen concentration c_H increases in proportion with the square root of the hydrogen partial pressure, p_{H_2}, according to Sieverts's law [84]:

$$c_H = K_H \cdot p_{H_2}^{1/2}. \tag{6}$$

If the concentration of hydrogen in the metal exceeds a threshold concentration, the β-phase nucleates (two-phase region of Figure 2.6.2-2 (a)). Three phases (α- and β-phase, gaseous H_2) and two components (hydrogen and metal) coexist. According to Gibb's phase rule

$$F = C - P + 2, \tag{7}$$

where F is the number of degrees of freedom, C is the number of components and P is the number of phases in thermodynamic equilibrium with each other, the system has one degree of freedom. Thus, at a given temperature T and a variable hydrogen concentration c_H, the equilibrium pressure of the phase transition from α- to β-phase is constant. If the phase transition α ➔ β is complete (only β-phase and gaseous hydrogen coexist), Sieverts law is effective again and hydrogen concentration c_H increases proportial to the square root of the partial pressure p.

At a fixed temperature and pressure, the main driving force for the hydride reaction is the Gibb's free energy ΔG . A negative ΔG through a chemical reaction indicates that the process is thermodynamically favourable. Taking into account the non-ideality of the compounds by replacing pressure p with activity a, ΔG of the reaction M + H_2 ➔ MH_2 can be approximated by

$$\Delta G = \Delta G_0 + RT \ln \left(\frac{a_{MH_2}}{a_M \cdot p_{H_2}}\right), \text{ where } \Delta G_0 = \Delta H_0 - T\Delta S_0. \tag{8}$$

For an ideal solid with no impurities, the activity is approximately unity. The Gibb's free energy at standard conditions ΔG_0 is composed by the enthalpy of reaction ΔH_0 (heat of reaction) and the energetic contribution due to entropy change $(-T\Delta S_0)$. Values of the standard enthalpy (ΔH_0) and entropy (ΔS_0) of reaction are obtained experimentally from a Van't Hoff plot (Figure 2.6.2-2 (b)). It is constructed by plotting the logarithm of the equilibrium pressures measured at different temperatures against the inverse temperature T^{-1}. Since equilibrium corresponds to $\Delta G = 0$, ΔH_0 and ΔS_0 can be obtained, respectively, from the slope and intercept of the Van't Hoff plot

$$\ln \left(p_{H_2}^{eq}\right) = \frac{\Delta H_0}{RT} - \frac{\Delta S_0}{R}. \tag{9}$$

Neglecting surface reconstruction and entropy change in the lattice, the main contribution to ΔS_0 stems from the entropy reduction of gaseous to chemisorbed, solid hydrogen, which is in the order of $-130\, Jmol^{-1}K^{-1}$ for most metal-hydrogen systems [5], [83]. For an application of a metal hydride in the LORC process described in section 2.1.2, an equilibrium pressure between 0.1 and 1 MPa at 25 or 100 °C, respectively, gives an enthalpy value in the range of 30 – 40 kJ/mol H_2.

For classical intermetallic hydrides, empirical correlations between ΔH and physical parameters such as unit cell volume [85], [86], interstitial site size [87], [88], elastic moduli [89], [90] and electronic specific heat [89], [91], [92] were established. These empirical correlations are useful for the optimization of metal-hydrogen systems for specific technical applications. In addition, semi-empirical models were developed to predict ΔH for large classes of metal hydrides. A frequently applied model is Miedema's *rule of inversed stability* [93–95]. It relates the heat of formation of the hydride of an intermetallic compound to the heat of formation of the intermetallic compound itself and of the binary hydrides of the metals constituting the compound.

The maximum achievable hydrogen concentration in an interstitial metal or alloy hydride is often significantly below the concentration that would be theoretically possible if all interstices were occupied by hydrogen. On an atomistic level, site occupation and maximum achievable hydrogen concentrations of metal-hydrogen systems can be described by the *„geometrical model"* [96], which takes into account geometric and electrostatic factors. Geometric factors are constituted by the observation that the geometric shape of interstices determines whether the site is occupied or not. Correlations between hydrogen equilibrium pressure and interstitial hole size (hole size is defined as the largest sphere, which can be inserted into the hole) suggest that hydrogen prefers to occupy large interstices [88]. Based on the geometry of the unit cells and the shape and radii of the metal atoms, hole sizes of the interstices can be estimated [87], and only holes which can be filled with spheres with a radius of ≥ 0.4 Å are found to be occupied by H [96]. The second factor of the „geometrical model" takes into account electrostatic repulsion between hydrogen atoms. H is believed to show anion-like behaviour in binary and ternary metal hydrides [94]. Electrostatic repulsion between the atoms leads to a minimum hydrogen atom separation of about 2.1 Å [96], [97]. Thus, according to this model (the so-called Westlake criterion), the maximum hydrogen content of a particular metal structure corresponds to the maximum number of spheres which can be packed into the interstitial space without violating the conditions of minimum sphere size (0.4 Å) and sphere separation (2.1 Å).

The PCI curve depicted in Fig. 2.3.1-2 (a) represents the ideal behavior of hydrogen ab- or desorption. However, in real hydrogen-metal systems a pressure hysteresis between absorption and desorption pressure (absorption pressure is larger than desorption pressure) and a plateau slope is observed, as shown in Figure 2.6.1-3:

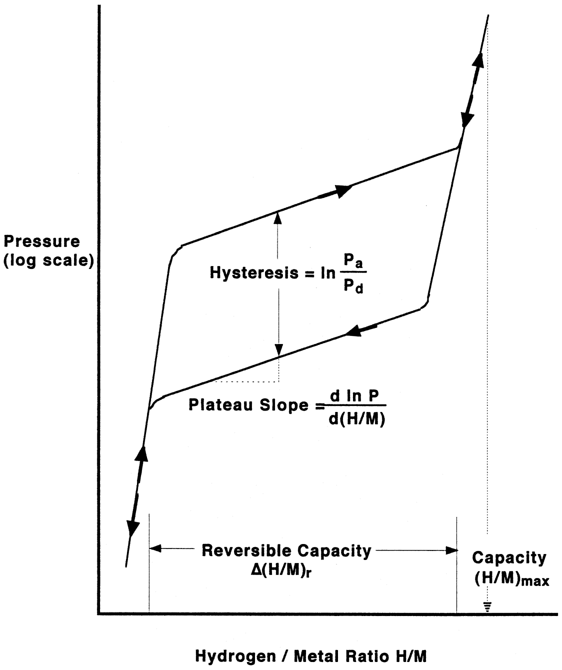

Figure 2.6.1-3: Schematic isothermal pressure-composition hysteresis loop [98].

Pressure hysteresis is observed in most hydrogen-metal systems, but its extent varies depending on the storage material, its composition and microstructure. In intermetallic hydrides such as $LaNi_5$ [99] or V-Ti-based solid solutions [100] pressure hysteresis is most pronounced during the initial activation cycles and decreases with the number of cycles. Hysteresis in the Pd-H system increases with the number of cycles, while it was found to decrease with cycling for the Pd-Ni-H system [101].

The hysteresis effect reduces storage material efficiency and has to be taken into account for in practical applications, because it affects the operating pressure of a solid state hydrogen storage tank [102].

The origins of pressure hysteresis in hydrogen-metal systems are still debated among the scientific community. Various models have been developed by successfully fitting the experimental data under different assumptions, e.g. a plastic deformation model [103–105], dislocations formed during both the hydriding and dehydriding processes [99], [102], [106–108], a metastable phase from oversaturating the α-phase [109], and hydrogen-metal and hydrogen-hydrogen interaction kinetics

[110]. Comprehensive reviews on various types of theoretical models were presented by Qian [111], Flanagan [112] and their coworkers.

Sloping pressure plateaux are generally present in hydrogen-metal systems and suggest that fractions of the storage material absorb hydrogen at different equilibrium pressures. Several origins of sloping plateaux were suggested, such as compositional heterogeneity in alloys or intermetallic compounds, which cause differences in the local environments of the absorbed hydrogen atoms [113–115], or the establishment of local equilibrium at the interface but not in the bulk [116]. Sloping plateaux are relevant for practical applications and have to be considered during design of solid state hydrogen storage tanks.

2.6.2 Activation and decrepitation

Activation is the procedure needed to initiate the first hydrogen absorption and to bring the storage material up to maximum H-capacity and hydriding/dehydriding kinetics. The metal surface is usually covered by a metal oxide layer and several other adsorbents (e.g. CO_2, hydrocarbons, water), which either block the catalytically active metal sites important for hydrogen dissociation, or act as a diffusion barrier for hydrogen atoms, or both. The first penetration of hydrogen into the metal is facilitated by removing some of the adsorbed species by evacuating at elevated temperature and subsequent hydrogenation at high pressure. A second stage of activation involves internal cracking of metal particles leading to an increase in reactive surface area.

Decrepitation means the self-pulverization of large metal particles into fine powder due to the buildup of large strain during hydrogenation and dehydrogenation. It is a common phenomenon that results from a combination of hydriding volume change and the brittle nature of hydriding alloys. This effect is most pronounced during the initial hydrogen sorption processes and declines with the number of cycles [98].

2.6.3 Kinetics of solid-state reactions

Hydrogen sorption can be described as a heterogeneous reaction between hydrogen and metal (or alloy). The hydriding reaction intrinsic to the material (see Figure 2.6.1-1 for a schematic representation) consists of the following sequence of five processes (additional aspects such as mass transfer of H_2 to/from the surface of the metal hydride may become important in beds of metal hydride powder):

I. physisorption of hydrogen molecules,
II. dissociation of hydrogen molecules into atoms (chemisorption),
III. diffusion of hydrogen atoms from the surface to the bulk through a surface layer,
IV. nucleation of the hydride phase,
V. diffusion of hydrogen atoms through the hydride layer (shrinking core model; applicable to intermetallic hydrides),
VI. hydride formation at the hydride interface [117].

If one of the processes in this sequence (I.-VI.) is considerably slower than the other ones, the slowest process governs the overall reaction kinetics, and is referred to as the rate-limiting step. The reaction rate of a hydrogen-metal system depends on the properties of the storage material, experimental conditions (e.g. temperature or pressure), and the respective reaction step. (De-)hydrogenation reaction rates generally follow a sigmoidal curve progression, as shown schematically in Figure 2.6.3-1.

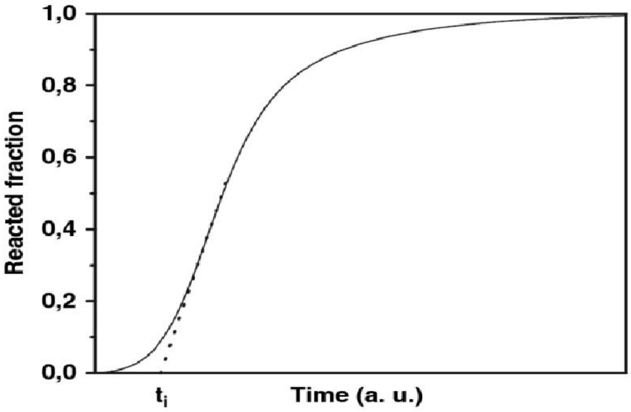

Figure 2.6.3-1: Reacted fraction as a function of time [118].

The sigmoidal fraction f diagram results from the nonlinear kinetic equation $\frac{dc}{dt} = a \cdot c - b \cdot c^2$ (a and b are constant coefficients referring to formation and decay (or dissociation) simultaneously; c is the concentration of the species). Two distinct reaction phases, nucleation $(t \leq t_i)$ and growth $(t > t_i)$, are observed. The hydriding reaction commences slowly by forming nuclei at the beginning of the process $(t \leq t_i)$, and then proceeds at a higher rate with the end of the incubation time and the beginning of the growth phase $(t > t_i)$.

Kinetic studies are performed to identify optimal operating conditions of a metal hydride system. Absorption or desorption rates are determined under varying temperature and pressure conditions, and these studies also provide insights into the underlying reaction mechanisms of (de)hydrogentation as well as the rate-limiting steps.

Storage materials show maximum reaction rates if the metal surfaces are clean and free of adsorbed or chemisorbed impurities, such as CO, CO_2, hydrocarbons, ammonia, water, or oxygen. Catalytic sites promoting the chemisorption and dissociation of hydrogen molecules are easily accessible for hydrogen on a clean metal surface. Coverage of the surface by impurities may impede access to the catalytic sites by two mechanisms. The first mechanism represents impediment by geometric factors in the form of a diffusion barrier of adsorbed/chemisorbed species, which has to be penetrated by hydrogen molecules in order to reach the metal surface. The second mechanism is a complete blocking of the catalytic sites at the surface through the formation of new chemical species, such as metal oxides, suboxides, or chemisorbed CO [119]. Oxygen, e.g., has a strong tendency to form surface metal oxides, and the oxygen atoms generally bind to the same sites that catalytically promote hydrogen chemisorption and dissociation. This leads to slower sorption kinetics as well as to decreased capacity, as shown in Figure 2.6.3-2 for $LaNi_5$ cycled in hydrogen containing 300 ppm NH_3.

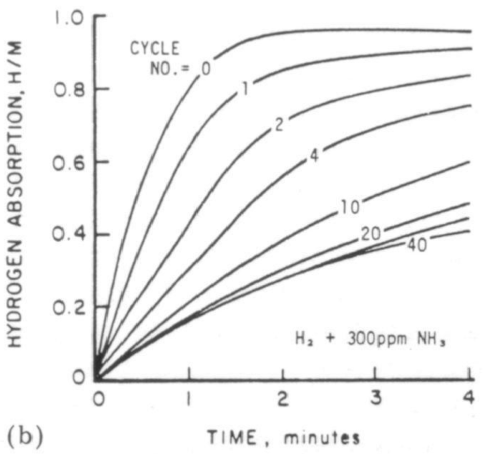

Figure 2.6.3-2: Hydrogen absorption kinetics of $LaNi_5$ in hydrogen containing 300 ppm NH_3 [19].

2.7 *Metal hydrides for the LORC process*

The hydrogen storage material to be utilized in the LORC process should absorb hydrogen at approximately 0.2 MPa at ambient temperature and desorb at a pressure of about 1 MPa at 100 °C. The temperature and pressure window suitable for the LORC process along with equilibrium Van't Hoff lines of selected hydrides of elements and compounds is depicted in Figure 2.7-1.

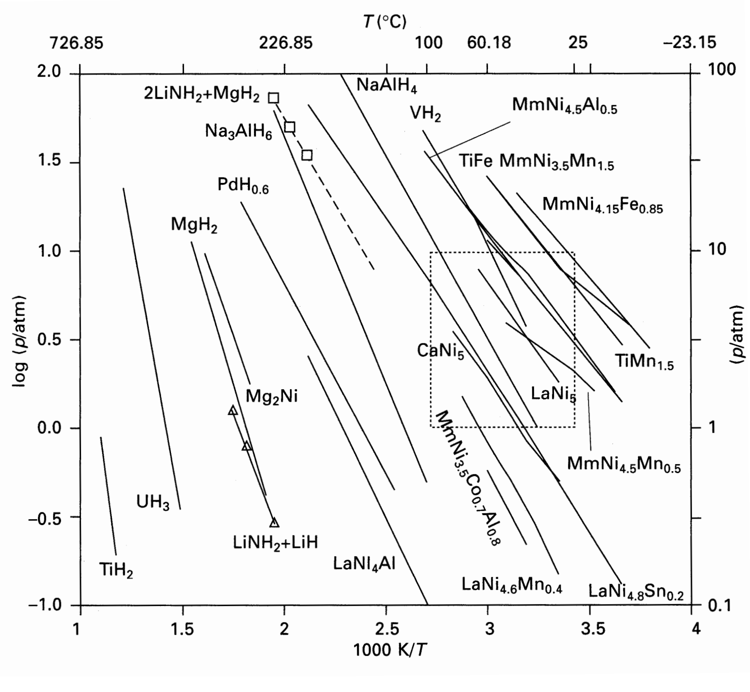

Figure 2.7-1: Van't Hoff plots of elementary and compound hydrides [120].

Most of the 91 natural elements below hydrogen will hydride under appropriate conditions. Unfortunately, the thermodynamic properties are not convenient relative to the 0.1-1 MPa, 25-100 °C range of utility chosen for application in the LORC process and most other practical applications (small box on the right of the diagram).

In order to capitalize on practical applications of reversible hydrides, strong hydride forming elements denoted by A have been combined with weak hydride forming elements denoted by B to form alloys that have the desired intermediate thermodynamic affinities for hydrogen. A classic and well-known example is the combination of La (forming LaH_2 with $p_d \approx 10^{-30}$ MPa at 25°C and $\Delta H_f = -208\ kJ\ mol^{-1}\ H_2$) with Ni (NiH, $p_d = 340\ MPa$ at 25 °C, $\Delta H_f = -8.8\ kJ\ mol^{-1}\ H_2$) to form the intermetallic compound $LaNi_5$ ($LaNi_5H_6$, $p_d = 0.16\ MPa$ at 25 °C and $\Delta H_f = -30.9\ kJ\ mol^{-1}\ H_2$, Van't Hoff line in the desired range in Figure 2.7-1). This extraordinary ability to „interpolate“ between the extremes of elemental hydriding behaviour has led to the modern world of reversible hydrides. Metal hydrides suitable for hydrogen storage in the desired temperature and pressure range (0.2-1 MPa, 25-100 °C) are intermetallic AB-type (e.g. TiFe), AB_2-type (e.g. $TiMn_2$) or AB_5-type materials (e.g. $LaNi_5$) [98]. Their thermodynamic properties can be adjusted easily to match a certain application. Additionally, elemental V is in the desired range. V forms solid solutions with many elements that are close to V in the periodic table, e.g. Ti, Fe, Cr or Mn. The resulting mixtures remain in a single homogeneous phase and the crystal structure of the solvent (V) remains unchanged after addition of the solute (the other metals).

Extended research has been dedicated recently to complex hydrides such as alanates [121–123], boronates [124–126], amides [127–129], magnesium-based materials [52], [130], or reactive hydride composites [131], [132] aimed at engineering novel hydrogen storage materials with appropriate thermodynamic properties in the desired range, sufficient reaction kinetics and reversibility. Until now, $NaAlH_4$ appears to be the only complex hydride where it seems feasible to achieve these goals. However, in the desired temperature and pressure range the reaction kinetics are extremely sluggish [133], and hence it will not be considered further in this work.

In the following chapters four different classes of hydrogen storage materials with suitable thermodynamic and kinetic properties for the LORC process will be reviewed: AB_5-, AB_2- and AB-type materials and V-Ti-based solid solution alloys. V-Ti-based solid solution alloys will be reviewed in more detail, since the majority of experimental results was attained with these materials.

2.7.1 *AB_5 ($LaNi_5$)*

Van Vucht *et al*. first reported the reversible uptake and release of six hydrogen atoms per $LaNi_5$ formula unit at room temperature and a pressure of 2.5 bar H_2 [134]. This corresponds to a volumetric and gravimetric hydrogen density of 6.2 mol L^{-1} and 1.4 mass%, respectively. $LaNi_5$ is one of the most well-studied hydrogen storage materials and shows favorable thermodynamic and kinetic properties, which makes it an attractive candidate storage material for stationary hydrogen storage applications [135], heat pumps [136] or hydrogen compressors [137]. Pressure hysteresis and plateau slope are less pronounced [138], activation is easy as the material spontaneously reacts with hydrogen at moderate overpressure of approximately 2 MPa at room temperature [99], decrepitation is complete after 2-3 cycles [139], and tolerance against gaseous impurities, such as O, CO or H_2O, is high as compared to most other storage materials [19].

$LaNi_5$ crystallizes in a hexagonal $CaCu_5$-type structure (P6/mmm space group) with lattice parameters of a = 5.02 Å and c = 3.99 Å. A solid solution of hydrogen atoms in the metal matrix is formed until the composition is $LaNi_5H_{0.02}$. Upon further increase of the hydrogen content, the hydride phase precipitates, which shows a $P6_3mc$ space group with a lattice volume increased by 24 % as compared to the dehydrogenated alloy. The hydride phase fraction increases with hydrogen content, and the fraction of the dehydrogenated phase decreases simultaneously. The phase transformation is complete when the composition reaches $LaNi_5H_6$ [99], [140], [141].

Thermodynamic properties of $LaNi_5$ can be modified and adjusted to match the requirement of a specific application by substituting the B element (Ni). As a result of the substitution, the unit cell volume is modified. This has consequences on the heat of hydride formation, and consequently the formation and dissociation pressures are altered. Systematic investigations on the effect of partial replacement of La or Ni were performed: $LaNi_4M$ (M ≡ Pd, Co, Fe, Cr, Ag, Cu) and $La_{0.8}R_{0.2}Ni_5$ (R ≡ Nd, Gd, Y, Er, Th, Zr) [95], $LaNi_{5-x}M_x$ with M ≡ Al [86], [138], [142], [143], Cu [144] or Gd, In and Sn [145] have been studied. Substitution of Ni by these elements expands the unit cell volume, e.g. from 86.9 $Å^3$ for $LaNi_5$ to 89.6 $Å^3$ when M ≡ Al and x = 1 ($LaNi_4Al$) [146]. Level of substitution and unit cell volume generally correlate well with thermodynamic properties and parameters, such as formation/dissociation pressure or heat of formation. Partial substitution in $LaNi_5$ may also result in a smaller hydrogen content of the related hydrides. The hydrogen capacity of $LaNi_4Al$ is reduced by 22 % as compared to $LaNi_5$, but small substitution levels of $x \leq 0.4$ have negligible effects on the capacity [138].

Several Ni-substituted $LaNi_5$ derivates meet the thermodynamic properties of the LORC process. Al and Sn were selected as substituting elements due to favorable thermodynamic and kinetic properties of the substituted compounds in the desired temperature and pressure range, with good characterization in the literature, and good tolerance against impurities.

$LaNi_5$ has been cycled in hydrogen containing O_2, N_2, CO_x, C_xH_y, H_2O, NH_3 or CH_3SH, and different mechanisms of metal hydride-impurity interactions were observed [19], [147]. N_2 and C_xH_y act innocuously, NH_3 retards the sorption kinetics, and O_2, CO_x, H_2O and CH_3SH poison the surface and lead to complete blocking of the sorption reactions after prolonged cycling at high impurity concentrations. However, the category and degree of damage can change markedly with temperature, number of cycles and impurity concentration.

A critical disadvantage of $LaNi_5$ and its related compounds is their high raw material price and the low availability of rare earth metals, particularly lanthanum, which constitute a significant fraction of the storage materials.

2.7.2 AB_2 (Hydralloy C, $TiMn_2$ derivates)

H storage properties of AB_2-type alloys were first reported in the works of Beck and Reilly [148], [149]. Typically, Ti or Zr or combinations thereof represent the A element, and the B elements are mainly different combinations of 3d elements, e.g. V, Mn, Cr or Fe. These phases show a C14 or C36 hexagonal or C15 cubic Laves phase structure. Laves phases are intermetallic phases that have the composition AB_2 and are classified based on the geometry of the constitutent atoms. The ratio of the atomic diameters, d_A/d_b is about 1.2 to 1.3. AB_2 compounds show gravimetric hydrogen storage densities in the range of 1.5 to 1.9 mass%, which is higher than the capacity of the AB_5 compounds. Lower raw material cost is an additional advantage, however, their tolerance against gas phase impurities is generally weaker as compared to AB_5 alloys, [150], and few reports are available on the effects of O_2, N_2 [151], CO or CH_4 [152]. The reason for the lower tolerance against impurities as compared the AB_5 alloys is not known.

AB_2-type alloys of Ti and Mn are the most common in this family. They have been optimized with respect to their hydrogen storage properties and are commercially available in the form of „Hydralloy" materials with different equilibrium properties. Activation is easy, they exhibit excellent cyclic stability and extremely rapid sorption kinetics [153]. Within this work, the material "Hydralloy C5" with the the composition $Ti_{0.95}Zr_{0.05}Mn_{1.49}V_{0.45}Fe_{0.06}$ has been used.

"Hydralloys" have hexagonal (C14) structure, and the lattice expands isotropically after hydrogenation [154].

Thermodynamic properties of $TiMn_2$-related storage materials can be easily tuned by alloying elements of larger or smaller atomic radius in the material.

2.7.3 AB (TiFe)

Reversible hydrogen sorption of TiFe was reported in 1974 by Reilly and Wiswall [155]. This alloy absorbs a maximum of 1.9 mass% H and is composed of cheaper elements as compared to AB_5 or AB_2 materials.

Several distinct phase transitions accompanied by crystal structure changes are observed in the TiFe-H system. TiFe crystallizes in an ordered cubic CsCl-type crystal structure with Pm-3m space group. The α-phase (solid solution of H in TiFe) with CsCl structure exists up to a composition of $TiFeH_{0.1}$ [156], [157]. At an equilibrium pressure of 0.5 MPa at 300 K, the α-phase transforms into the β-phase. Precipitation of the β-phase is accompanied by lattice expansion and distortion, resulting in a crystal structure change from cubic to orthorhombic structure [158]. The first phase transformation $\alpha \rightarrow \beta$ is complete when the composition of the resulting solid material corresponds to TiFeH. The equilibrium pressure then increases sharply, until a second, more sloping pressure plateau is observed at approximately 1 MPa. It corresponds to the $\beta \rightarrow \gamma$-transition, which is complete when the composition reaches $TiFeH_{1.9}$. The incorporation of more hydrogen atoms causes further lattice distortion, and the orthorhombic cell transforms back into a cubic cell with an expanded lattice parameter of 6.61 Å for the γ-phase as compared to 2.98 Å for the alpha phase [155].

For most practical applications where flat pressure plateaux are desired, only the formation and dissociation of TiFeH is useful. This limits the practical capacity to 1 mass%.

Activation is much more of a concern for TiFe than for other AB_5- or AB_2-type hydrides, because it requires a rather involved process at high temperatures and elevated pressures. Several cycles of hydrogenation at elevated temperature and pressure and subsequent desorption under vacuum are necessary to bring the material up to maximum capacity and kinetics [159]. Activation is facilitated by substituting small amounts of Fe or Ti by other elements, such as Zr and/or Nb [160], [161], Mm [162], Cr or Mn [163], Ni [164], O [165], or O in combination with Cu or Nb [166], which causes precipitation of secondary phases acting as promoters for hydrogen uptake. Plastic deformation techniques, such as high-pressure torsion [167] or groove-rolling [168] represent additional successful strategies that facilitate the activation procedure.

Thermodynamic properties of TiFe can be easily adjusted by addition of ternary elements with smaller or larger atomic radius, which results in an expansion or contraction of the unit cell.

Tolerance against gas phase impurities of TiFe is generally poorer than of the AB_2 and AB_5 type alloys [19]. Fewer cycles are necessary to deactivate TiFe as compared to $LaNi_5$, and the reactivation procedure requires evacuation at high temperature and numerous cycles in pure hydrogen [19], [147].

2.7.4 *V-Ti-based solid solutions*

Systematic studies on the formation of vanadium hydride were first reported by Reilly and Wiswall [169] and Maeland [170]. Elementary V shows a body-centered cubic (bcc) crystal structure. Two hydrides, the β- and γ-phases, are formed at different equilibrium conditions. The solid solution α-phase extends to $VH_{0.05}$ and is accompanied by an expansion of the V lattice from 3.03 Å to 3.04 Å. At $VH_{0.05}$ the body-centered tetragonal (bct) β-phase (monohydride) appears with a decrease in the a axis 3.0 Å and an expansion in the c direction to 3.30 Å. A two-phase region at an equilibrium pressure of approximately 10^{-1} Pa at 298 K extends to the composition $VH_{0.46}$, at which the α-phase disappears. A linear expansion of the a- and the c-axes is observed as the hydrogen content in the β-phase further increases. When the composition reaches $VH_{0.9}$, the face-centered cubic (fcc) γ-phase preciptitates. A second phase transformation β ➔ γ phase occurs at an equilibrium pressure of 0.28 MPa at 298 K. The pure γ phase (dihydride) with a lattice parameter of 4.2 Å is formed at VH_2 [169–171].

A body-centered cubic unit cell has six octahedral (O) voids located at the center of each face of the unit cell and 18 tetrahedral (T) voids, as shown in Figure 2.7.4-1.

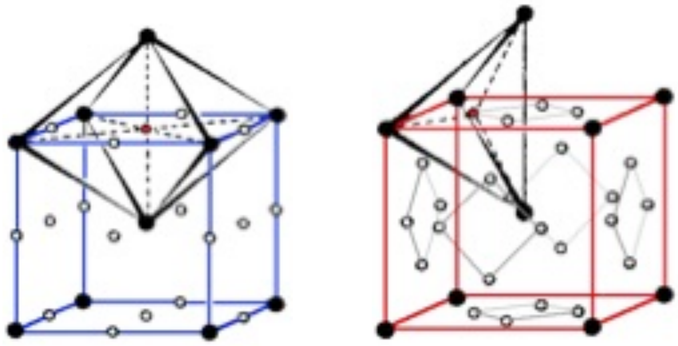

Figure 2.7.4-1: Body-centered cubic unit cell with octahedral (left) and tetrahedral (right) interstitial voids [172].

Assuming that the building blocks forming the polyhedra (in the case of BCC crystals the polyhedra are of octahedral and tetrahedral shape) have a spherical shape and that a spherical interstice is located at the center of each polyhedron, a ratio R_A/R_x between the radius of the building blocks forming the polyhedra and of the spherical interstitial site can be approximated, where R_A and R_x stand for the radius of the spherical interstitial void and the radius of the spherical building block, respectively. For octahedral sites, this ratio is approximately 0.41 and for tetrahedral sites it is 0.23 [173]. Consequently, octahedral sites are larger than tetrahedral sites. This has implications on the site occupation of hydrogen and other interstitial atoms, such as O, C or N. Interstitial atoms tend to occupy large voids first, however, in the case of V-Ti-based solid solutions the site occupation has been shown to depend strongly on the alloy composition [174], [175]. The site occupation of the monohydride phase shifts from O sites for pure metallic V to T sites if metal atoms with larger atomic radius are introduced in the alloys [176].

V hydride shows high volumetric and gravimetric hydrogen densities of 160 kg H_2 / m^3 and 3.8 mass%, respectively, but only the formation and dissociation of the dihydride (second pressure plateau at 0.28 MPa and 298 K) is useful for hydrogen storage at ambient temperature. The total amount of hydrogen dissolved in V-Ti-based solid solutions (equivalent to full hydrogenation of mono- and dihydride) will be denoted from here on as „total capacity“. Hydrogen storage capacity at ambient conditions is limited to a maximum of about 2.5 mass% (formation and dissociation of the dihydride), which will be denoted as „reversible capacity“.

Activation of elemental V and other bcc metals is notoriously difficult, which has been attributed to the presence of oxide layers on the surface. These layers do not enable dissociation of hydrogen molecules and act as blocking layers for hydrogen diffusion into the bulk [177–179]. Even in the absence of an oxide layer, it has been shown that there still appears to be an intrinsic barrier for hydrogen absorption of pure vanadium [180–182]. Alloying with metals whose metallic radii are smaller than those of the host metal has been shown to facilitate activation considerably, and the hydrides are formed readily at room temperature and moderate overpressure [182]. Furthermore, the equilibrium pressure can be modified by the addition of elements of smaller or larger metallic radii. This allows to tailor the thermodynamics of hydride formation/dissociation to match the specific requirement of an application [85], [183]. Titanium has a larger metallic radius (1.45 Å) than V (1.31 Å). Hence, the addition of Ti stabilizes the hydride. The metallic radii of Cr, Fe and Ni are smaller than V (Cr and Fe: 1.24 Å, Ni: 1.25 Å), and consequently they are added in order to destabilize V-based hydrides. The formation of secondary phases is partly observed in V-Ti-based solid solution alloys. Secondary phases that may be formed during the synthesis of the alloys are the C14 Laves phase (see chapter 2.6.5) or Ti-Ni phases when a large amount of Ni is added to the alloy. Furthermore, impurities contained in the raw metals, such as O, may promote the formation of impurity-rich phases [9], [16], [184].

Knowledge about the cyclic behavior of V-Ti-based solid solutions in impure hydrogen is scarce, and effects of small amounts of O_2, CO_x, CH_4 and H_2S impurities have only recently been studied by Shen *et al*. [185] and Suwarno *et al*. [186]. The results indicate that V-Ti-based solid solutions show a tendency to passivate even at low impurity concentrations < 10 ppm after prolonged cycling.

With a raw material price of 390 US $/kg V is an expensive element. Hence, considerable past and present research interest has been dedicated to the development of V-based hydrogen storage materials with reduced raw material cost. One way to achieve this is to dissolve cheaper elements in the host vanadium solvent, such as Cr (15 US $/kg), Fe (1 US $/kg), Ti (25 US $/kg) or Mn (4 US $/kg). Disordered solid solutions are formed that contain 40 to 65 % less expensive V while retaining high total and reversible hydrogen capacities. Several researchers have reported V-based solid solutions with tunable thermodynamics and favorable kinetic and cyclic properties with reversible capacities ranging between 1.7 and 2.4 mass% [9], [10], [183], [187–189]. These hydrogen storage alloys show reduced raw material costs as compared to pure V. However, even these solid solution alloys with high levels of V substitution are still too expensive for many applications. Hence, researchers have started to explore further strategies to reduce the raw material costs.

Commercial ferrovanadium (FeV) master alloys containing about 80 % V, 10 – 17 % Fe and other impurities cost around 30 US $/kg, less than 1/10 the price of high-purity V. Several researchers have investigated the effect of commercial FeV on the microstructure and hydrogen storage properties of V-Ti-based solid solutions [190–196]. Yan *et al.* reported a BCC alloy prepared with FeV, which desorbs 2.35 mass% at 298 K [193]. However, no cyclic properties of this alloy were reported. Wu *et al*. investigated the surface properties of a material using commercial FeV, which showed a reversible capacity of 1.8 mass% after 25 cycles [190]. Yan *et al*. and Wu *et al*. added rare earth elements before arc melting the raw materials, which acted as impurity getters. However, the addition of rare earths is generally undesired for the same reasons as already discussed in Chapter 1. Dou *et al*. investigated the effect of FeV substitution in a V-Ti-Mn alloy without addition of rare earths, but no cyclic properties were reported also here [197].

V of lower purity is 10 – 20 % cheaper than high-purity V. The last purification steps are omitted, resulting in a reduced energy demand and a lower price as compared to high-purity V. The effects of impurities such as Si [198], Al [199], O [16], [17], transition metals [200], C [201] or B [202] have been investigated by several groups. The results may be important with respect to reduced costs of the storage materials by using low-purity raw metals or FeV. Ferrovanadium contains impurities such as Al, Si, C, O and N that are introduced in the alloy. Oxygen has been identified as a particularly harmful impurity, as it negatively affects both the microstructure and the hydrogen storage properties through the promotion of secondary phase formation, destabilization of the hydride and reduced hydrogen capacity [16–18]. Deoxidization by the addition of a small amount of rare earth metal to circumvent the negative effects of oxygen has been reported by Mi *et al.* [18].

V and Ti are the most expensive elements contained in V-Ti-based solid solution alloys. In the following chapter, the different production paths for these elements are highlighted with an emphasis on the origins of the price variations of the obtained raw metals.

2.8 Vanadium, ferrovanadium and titanium production processes

V is present in the earth's crust at a mean concentration of 150 g/t, and is therefore one of the more common metals. It is more abundant than Cu and Ni and of similar abundance as Zn. It is a common structural material with a broad range of applications in ferrous steels, non-ferrous alloys and as industrial catalysts. About 80 % of the vanadium used for industrial purposes is used in the form of FeV, the remaining 20 % are used as pure V, V_2O_5 or other V-containing compounds. Different production paths are used to produce pure V or FeV. They are specified in the following two paragraphs. Comprehensive reviews on the different V and FeV production paths have been published by Bauer *et al.* [13] and Moskalyk [11], for example.

Vanadium: Pure V is difficult to produce because raw V is contaminated by many other elements. The feedstock contains V_2O_5, which after separation is reduced by using Ca or Al. The obtained vanadium is then further purified by means of electron beam melting.

Ferrovanadium: The majority of vanadium pentoxide recovered is converted to FeV for use in producing steel alloys. After melting scrap iron in an electric arc furnace, a mixture of Al, V_2O_5, and a flux consisting of either calcium fluoride or calcium oxide is added to the melt. The aluminothermic process reduces the vanadium oxide to metal, which dissolves in the molten Fe to create FeV.

The main difference between the two paths is the addition of scrap Fe and the omission of electron beam melting (EBM) in the case of the FeV path. EBM is an energy consuming process, and performing or omitting these rather involved purification steps is ultimately reflected in the price difference between pure V (390 US $/kg) and FeV (30 US $/kg) although the V content of FeV is about 80 % [15].

Titanium is relatively widely distributed and abundant. With an estimated concentration in the earth's crust of 0.6 %, it is the ninth in order of abundance. Almost all naturally occuring Ti is found in the form of its dioxide, TiO_2. The large heat of formation of TiO_2 (945.4 kJ/mol) combined with the high solubility of O in Ti at high temperatures has so far made it impossible to develop an economic process for the direct reduction of TiO_2 to Ti metal. The standard industrial processes for the production of Ti metal are therefore based on Ti halides.

The most common Ti production process is the *Kroll process.* In a typical production, rutile (a mineral primarily composed of TiO_2) is reacted with chlorine gas to form $TiCl_4$. After purification, $TiCl_4$ is reduced with Mg as reducing agent, with Ti sponge and $MgCl_2$ as products. The Ti sponge typically contains C, N, O, H, Fe, Mg and Cl impurities and is further purified by means of arc melting, electron beam or plasma melting, or other metallurgical processes [14].

Similar to the vanadium/ferrovanadium paths, the price differences between Ti (25 US $/kg) and Ti sponge (10 US $/kg) mainly originate in omission of energy intensive purification steps necessary to obtain pure titanium metal [15].

2.9 System Aspects and Challenges in Material Design

Table 2.9-1 summarizes thermodynamic properties and material cost of TiFe, Hydralloy C ($TiMn_2$-related material), $LaNi_5$ and $V_{40}Fe_8Ti_{26}Cr_{26}$. These materials were selected as candidate hydrides for the LORC process mainly due to their suitable and easily tunable thermodynamic properties.

Alloy	H_2 capacity [mass%]	Hydrogen equilibrium pressure @ 25 °C [MPa]	Plateau slope [d(p_f)/d(mass%	Hysteresis [p_a/p_d]	Minimum mass required to store 100 kg H_2 [kg]	Raw material cost to store 100 kg H_2 [USD]
$TiFe_{0.7}Mn_{0.3}$ (AB)	1.8	0.15	0.1	2.9	5563	81300
Hydralloy C (AB_2)	1.8	0.5	0.4	4	5195	323600
$LaNi_{4.9}Al_{0.1}$ (AB_5)	1.4	0.1	0	1.02	6687	431430
$V_{40}Fe_8Ti_{26}Cr_{26}$ (solid solution)	2.5	0.2	0.1	2	3990	639930

Table 2.9-1: Properties of selected metal hydrides.

Thermodynamic properties of the intermetallic AB-, AB_2- and AB_5-type alloys and V-Ti-based solid solution can be easily adjusted by varying the stoichiometry of elements with large or small atomic radii. Hydriding kinetics are extremely fast for all materials. If the metal surfaces are clean, heat transfer has been identified as the rate-limiting step during hydrogen sorption [203]. Additionally, solid state storage tanks filled with AB-, AB_2- and AB_5-type alloys are *off-the-shelf* products that are commercially available from several companies [204], [205].

V-Ti-based solid solutions have not yet been tested in tank applications, however, their higher gravimetric and volumetric hydrogen density as compared to AB-, AB_2- and AB_5-type alloys can make them attractive due to the decreased volume and weight of the hydrogen storage tank in the LORC process. Even though they are the most expensive storage material on the list, they offer high potential for cost reductions by substituting high-purity V and Ti by FeV and Ti sponge. It should be noted that TiFe and Hydralloy C also contain Ti, and Hydralloy C additionally contains V. Hence, these materials also exhibit cost reduction potential. Hydralloy C contains 10 – 15 at% V, and hence the cost reduction potential is lower as compared to V-Ti-based solid solutions containing at least 35 at% V.

$LaNi_5$ and TiFe have been extensively studied with respect to their behavior upon cycling in impure hydrogen. Similar reports on Hydralloy C or V-Ti-based solid solutions are scarce. None of the materials has been cycled in hydrogen containing toluene or methylcyclohexane, but knowledge on the reactions taking place upon contact between toluene/methylcyclohexane and the metal hydrides is essential for the right choice of hydride for the LORC process.

Methods for protecting metal hydrides from passivation by gaseous impurities have been developed. These include the fluorination of the surface of rare earth metal containing hydrides [206–208] or the deposition of Pd, Pt, Cu or combinations of these elements on the surface of H absorbing alloys [165], [181], [186], [209], [210]. The common idea of these methods is that the alloy surface is chemically modified or coated with elements exhibiting a reduced reactivity with the gaseous impurities. The ability to dissociate hydrogen molecules is retained and diffusion pathways for the hydrogen atoms to the core of the hydrogen absorbing alloy are provided.

A disadvantage of these surface treatments is that additional steps during the preparation of the hydrogen storage alloys are necessary with associated higher costs. Fluorination treatment is only effective in the case of rare earth containing alloys, and the deposition of Pd or Pt noble metals significantly increases the cost of the storage material due to high cost and low availability of these metals. Alternative, smart, low-cost surface treatment methods are therefore necessary.

2.10 Aim of Thesis

The overall aim of this PhD thesis is the design and testing of novel low-cost V-Ti-based solid solutions with improved tolerance against hydrogen containing impurities.

Chapter 3 introduces the scientific methods that were used to perform the experiments.

In chapter 4 the experimental results are presented.

Chapter 4.1 deals with $LaNi_5$-derived hydrogen storage materials. They were tested as reference materials to gain experimental experience and to validate the experimental methods.

The research presented in chapter 4.2 is aimed at designing advanced, low-cost V-Ti-based solid solution alloys.

First, in chapter 4.2.1 a V-Fe-Cr-Ti-based hydrogen storage solid solution is designed through systematic variation of the stoichiometry in order to obtain a material with thermodynamic and cyclic properties matching the requirements of the LORC process.

Second, with an optimized stoichiometry, the effect of substituting high-purity V with V containing a high fraction of residual oxygen (high-oxygen V) is investigated in chapter 4.2.2.1. High-oxygen V is about 15 % cheaper than low-oxygen V. Additionally, oxygen is a major impurity of FeV, and the effect of oxygen on V-Fe-Ti-Cr solid solution alloys has not been reported yet.

Third, high-purity V and iron (Fe) are substituted by two types of FeV with different compositions. This is presented in chapter 4.2.2. The effects of substituting high-purity V and Fe with FeV on the phase composition, and the structural, thermodynamic and cyclic properties of the obtained solid solution alloys are investigated. Based on the observations, recommendations for a proper selection of FeV are worked out.

Fourth, high-purity titanium (Ti) is substituted by cheaper Ti sponge of lower purity aimed at investigating whether Ti sponge affects the microstructure and hydrogen storage properties of the obtained solid solution alloys.

Fifth, alloys containing cheap, low-purity FeV and Ti sponge are synthesized and characterized. Strategies to reduce the concentrations of harmful impurities during the preparation of the solid solution alloys are developed. With optimized composition and synthesis conditions, long-term cycling experiments are performed in order to compare the cyclic stability of expensive, high purity solid solution alloys synthesized with pure V and Ti with the durability of low-cost alloys prepared with FeV and Ti sponge.

In chapter 4.3 of the thesis, the focus shifts from impurities contained within the materials themselves to gaseous or liquid impurities reacting at or with the surface of the storage alloys.

First, in chapter 4.3.1 the emphasis is put on the surface reactions of organic substances such as toluene and acetone with TiFe, $LaNi_5$, Hydralloy C and $V_{40}Fe_8Ti_{26}Cr_{26}$. Literature reports are scarce and detailed knowledge about possible reactions between organic substances and metal hydrides is highly relevant with respect to the LORC process. The aim is to gain insights into the mechanisms responsible for deactivation of metal hydrides during contact with the organic substances.

Second, two approaches are presented, which are targeted at improving the durability upon cycling V-Fe-Cr-Ti-type solid solution alloys in hydrogen containing oxygen. Upon cycling in a hydrogen/oxygen mixture the metal hydride surface is known to be oxidized, which causes a deterioration of the storage kinetics and capacity. In both approaches, the surface structure of $LaNi_5$, the hydrogen storage alloy showing the best cyclic stability, is partly imitated through the addition of the A-element (La) or the B-element (Ni) of $LaNi_5$.

In the first approach, a small amount of nickel (Ni), one constituent of $LaNi_5$, is introduced into V-Fe-Cr-Ti-based solid solution. Selective leaching of V, Fe, Cr and Ti is applied to enrich Ni at the alloy surface. It is investigated whether surface Ni improves the catalytic properties of the hydride surface to absorb and desorb hydrogen in the presence of oxygen impurities.

The second approach involves the introduction of a small amount of rare earth metal in the form of „mischmetal“ Mm, a mixture of lanthanum and cerium, in the solid solution. Rare earth metals do not dissolve in the V-Ti-Fe-Cr solid solution and are present in the form of agglomerates distributed within the alloy. It is investigated whether the rare earth elements (and/or their oxides) provide diffusion pathways into the alloy when the surface of the V-Fe-Cr-Ti solid solution is passivated by oxide formation. The rare earth oxides would then act as pathways for hydrogen to enter the alloy, and thus the tolerance against oxygen may be improved.

Finally, the experimental results are embedded in a broader context with respect to practical applications of the investigated materials, such as the LORC process.

3 Experimental section

A part of the experimental work was carried out in the Energy Technology Research Institute at the National Institute for Advanced Industrial Science and Technology (AIST) in Tsukuba, Japan. The same synthesis and characterization methods were applied in Karlsruhe and Tsukuba, but different equipments were used. Experimental results obtained in Tsukuba are marked.

3.1 Synthesis of the materials

3.1.1 Arc melting

All alloys used within this thesis were synthesized by melting stoichiometric amounts of the pure metals in an electric arc furnace. A schematic representation of such a furnace is shown in Figure 3.1.1-1 and its working principles are briefly explained.

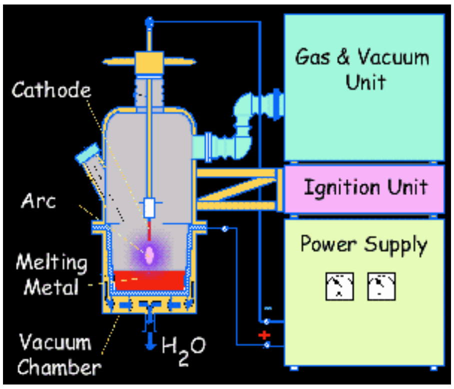

Figure 3.1.1-1: Schematic representation of an electric arc furnace [211]**.**

An electric arc is created through a flow of an electric current between a tungsten anode and a water-cooled copper crucible (cathode). Current passing through normally nonconductive media, such as air or Ar, effects an electric breakdown of the gas. This results in a plasma discharge. The pure metals are placed in cavities distributed on the Cu crucible. They are directly exposed to the electric arc, which builds up between anode and cathode. High temperatures exceeding 3000 °C are generated within the arc, and the metals are molten and can dissolve to form an alloy.

Arc furnaces vary in size, with capacities of a few dozen grams used in research laboratories and by dentists, to several hundred tons industrial units used for steelmaking.

Of considerable practical significance for the treatment of the melt are the evaporation reactions of harmful metallic and nonmetallic impurities having high vapor pressure. The solubility of gases like O, N and H is governed by the Sieverts's law, according to equation (6).

The solubility is proportional to the square root of the partial pressure of the gas. When the temperature of the melt changes, the equilibrium constant K will also change. Because solubility of gases usually decreases with increasing temperature, the partial pressure of the gas above the melt at a given gas concentration in solution must increase. Concentrations of gases in the melt and the resulting alloys can therefore be reduced by decreasing the pressure above the melt or increasing the temperature of the melt.

Additionally, concentrations of non-gaseous impurities with detrimental effects on the properties of the alloys can be reduced through chemical reactions. This is exemplified at the reaction of carbon (C_{melt}) and oxygen (O_{melt}) dissolved in the melt and forming gaseous carbon monoxide (CO_{gas}), according to equation (10):

$$C_{melt} + O_{melt} \rightarrow CO_{gas}. \tag{10}$$

The mass action law for reaction equation (10) can be written as

$$c_C \cdot c_O = \mathrm{K(T)} \cdot p_{CO}, \tag{11}$$

where c_C and c_O represent the concentrations of carbon and oxygen, respectively, $K(T)$ is the temperature-dependent equilibrium constant and p_{CO} is the CO partial pressure. It can be seen that there is a dependence of the pressure above the melt and the temperature of the melt. High temperatures and low pressures accelerate the CO reaction with the result that the content of dissolved carbon and oxygen can be reduced [212].

In the current work, high-purity alloys were prepared by using elements with purities of > 99.9 %. The effect of low and high residual oxygen concentration in vanadium raw metals was investigated using two V materials of differing oxygen concentrations (low-oxygen: < 300 mass ppm O; high-oxygen: < 10000 mass ppm O). The oxygen content was quantified by O/N analysis, which is explained in the appendix of the thesis. Deoxidization by the addition of 1 at% rare earth metal to circumvent the negative effects of oxygen was investigated, which has also been reported for other materials before by Mi *et al.* [18].

FeV, low-purity V and Ti sponge contain high concentrations of impurities, e.g. O, N or C, that have detrimental effects on the microstructure and H storage properties of the solid solution alloys. Hence, it is relevant to investigate the effect of the synthesis conditions on the impurity concentrations.

In a typical synthesis, about 25 g of raw metals were placed in the cavities of the copper crucible. After repeated evacuation and flushing cycles using purified Ar, the reaction chamber was evacuated using a turbo-molecular pump. 500 mbar Ar were introduced into the chamber, and the alloys were melted, turned around and remelted four times to improve homogeneity. The current of the electric arc was increased from 300 A during the first step to 400 - 450 A in the subsequent remelting steps. With an optimized FeV and Ti sponge composition, the current of the electric arc was varied between 400 A and 500 A in steps of 50 A. 500 A was determined as the maximum possible current that could be applied with the used arc melting device. If the current was further increased, the melt began to splash and it was difficult to retain it in the cavity. The obtained alloys were then tested upon their composition by ICP-OES and the concentrations of O and N were detected by O/N analysis and C by C/S analysis. These methods are explained in the appendix of the thesis.

The compositions of the two FeV materials and of Ti sponge were also tested by ICP-OES and O, N and C analysis. The results are listed in Table 3.1.1-1 and Table 3.1.1-2.

Material	V	Fe	Al	Si	O	N	C
FeV 1 (Taiyo Koko Co.)	80 at%	10 at%	8 at%	2 at%	2100 mass ppm	1200 mass ppm	1220 mass ppm
FeV 2 (GfE)	78 at%	17 at%	2 at%	< 1 at%	7400 mass ppm	1200 mass ppm	1800 mass ppm

Table 3.1.1-1: Elemental compositions of the two FeV materials used in this thesis.

Ti	Mg	Fe
95 at%	4 at%	< 1at%

Table 3.1.1-2: Composition of Ti sponge.

In Tsukuba an arc melter by Diavac was used and in Karlsruhe, the arc melter AM by Edmund Bühler was used. Both arc melters were of similar capacity and the same currents were applied.

The V-Ti-based solid solution alloys synthesized and tested in Tsukuba were annealed at 1200 °C for two hours under Ar atmosphere in order to improve homogeneity. Annealing ovens were tested also in Karlsruhe and several unsuccessful attempts were undertaken to modify them according to the need. Hence, the samples were used in their as-casted state. The results presented in chapter 4.1 and in the first part of chapter 4.2 were collected in Tsukuba. It is marked in the results section when the remaining results were collected in Karlsruhe.

3.1.2 *Surface modification procedures*

Selective leaching has been used as the first approach to modify the surface composition of V-Fe-Cr-Ti-based solid solution alloys. During leaching, metals are extracted from a solid and dissolve in a typically water-based, liquid electrolyte. Electrochemical reactions occur, which are driven by a difference of potential between the solid and the electrolyte. The reaction proceeds according to reaction equation (12):

$$\mathrm{M} \Leftrightarrow M^{z+} + ze^{-}, \tag{12}$$

where M stands for metal, e^- stands for electron and z stands for the number of electrons. The solubility of a specific metal in an electrolyte depends on the chemical nature of the metal, the type, pH value and temperature of the electrolyte as well as the amount and chemical nature of already dissolved metals.

In Table 3.1.2-1 the solubility of various elements contained in V-Fe-Ti-Cr-based solid solution alloys in acidic or alkaline electrolytes are compared.

Common oxidation numbers	Element/ compound	Solubility in water	Solubility in acid	Solubility in base	Reference(s)
2, 3, 4, 5	V	Insoluble	Soluble	Soluble	[213–217]
	V_2O_5	Soluble	Soluble	Soluble	[218], [219]
	V_2O_4	Soluble	Soluble	Soluble	[218]
	$VOSO_4 \bullet 3H_2O$	Soluble	Soluble	Soluble	[218]
	$(VO_2)_2SO_4$	Soluble	Soluble	Soluble	[218]
2,3	Ni	Insoluble	Soluble	Insoluble	[213–216], [219]
	NiO	Insoluble	Insoluble	Insoluble	[218]
	$Ni(OH)_2$	Insoluble	Soluble	Insoluble	[218]
	$NiSO_4$	Soluble	Soluble	Insoluble	[218]
2,3	Fe	Soluble	Soluble	Soluble	[213–216]
	Fe_2O_3	Insoluble	Soluble	Insoluble	[218]
	$FeSO_4 \bullet 7H_2O$	Soluble	Soluble	Insoluble	[218]
2, 3, 4	Ti	Insoluble	Soluble		[213], [214]
2, 3, 6	Cr	Soluble	Soluble		[213], [214]

Table 3.1.2-1: Solubility of various metals and compounds.

A material with the composition $V_{40}Fe_8Ti_{32}Cr_{16}Ni_4$ was used for the leaching experiments. This composition was chosen because the resulting hydride is partly stable at ambient temperature and pressure conditions. Reactivation after the leaching procedure could be achieved when a hydrogenated alloy was leached and a subsequent thermal desorption. It was leached using a 9 mol/L NaOH solution at 40 °C. The detailed experimental procedures of the leaching experiments are presented in section H in the appendix.

In order to quantify the number of leached atoms from the solid surface, the filtrate was analysed by ICP-OES. The number of dissolved atoms in the filtrate was calculated based on the ICP-OES results, and an enrichment factor α_i was calculated for each element according to equation (13):

$$\alpha_i = \frac{a_{diss,i}}{a_{S,i}}, \tag{13}$$

where $a_{diss,i}$ stands for the molar fraction of element i in solution and $a_{S,i}$ stands for the molar fraction of element i in the solid. If $\alpha_i > 1$, the element was enriched in the electrolyte, if $\alpha_i = 1$, the element was dissolved in the same molar fraction as present in the solid, and if $\alpha_i < 1$ the element was enriched in the solid. 0.15 g of sample were also dissolved completely and measured as a reference by ICP-OES.

A larger amount of material (4.5 g) was leached with 9 M NaOH solution at 40 °C for 30 min and used to investigate the hydrogen storage properties of the resulting material.

3.2 Analytical methods

3.2.1 X-ray diffraction (XRD)

Powder X-ray diffraction (XRD) is a tool used for identifying the atomic and molecular structures, phase compositions, crystallite sizes and microstrains of crystalline materials.

Electromagnetic radiation of wavelengths between 1 pm and 10 nm (x-rays) is subjected to the same diffraction laws as electromagnetic radiation of longer wavelengths, such as visible light. Interatomic distances in crystals are in a similar size range as the wavelength of X-ray radiation. Hence, for x-ray radiation the lattice structure of a crystalline material acts as a 3D diffraction lattice.

If X-rays are irradiated on a crystal at an incident angle θ, these X-rays are diffracted and constructively or destructively interfere with each other. Constructive interference occurs if the path difference between the X-rays diffracted at several lattice planes with a distance d from each other hold a whole-numbered multiple of the wavelength λ of the incident x-ray radiation. This is expressed by the Bragg equation:

$$\mathrm{n} \cdot \lambda = 2 \cdot \mathrm{d} \cdot \sin(\theta). \tag{14}$$

The measured diffraction patterns can be compared to patterns of known reference materials, and conclusions about the composition of crystalline materials can be drawn.

X-ray diffractometers using Cu-K-α-radiation (wavelength 1.54 Å) were used for characterization. In Tsukuba, powder XRD data were obtained using a Rigaku RINT-2500 V X-ray diffractometer equipped with a rotating anode X-ray source. In Karlsruhe, a Bruker „D8 advance“ diffractometer was used.

The characteristic wavelength of X-ray radiation depends on the anode material used as X-ray source. Fluorescence of an investigated material may occur if the atomic number of one or more elements contained in the sample is slightly lower than of the element used as X-ray source. A large fraction of the incident X-ray radiation is absorbed in such a case, which results in unfavorable signal-to-noise ratios [220]. The V-Ti-based solid solution, TiFe and Hydralloy C studied in this work contain Fe, which may fluoresce if irradiated by Cu radiation. In order to investigate that and to test the reproducibility of the XRD data obtained in Japan, $V_{40}Fe_8Ti_{26}Cr_{26}$ was measured on three different instruments in Tsukuba (Cu radiation) and Karlsruhe (Cu and Mo radiation). The relevant parameters (phase composition, lattice parameter and microstrain) were found to be identical within the experimental error at all instruments, and thus all samples were measured using Cu radiation. All measurements were performed in Bragg-Brentano geometry (Figure 3.2.1-1). Both the X-ray source and the detector are circularly moved around the sample by – Θ and Θ, respectively. The divergent and diffracted beams are focused at a fixed radius from the sample position. High peak intensities and good resolution are achieved in this reflection geometry.

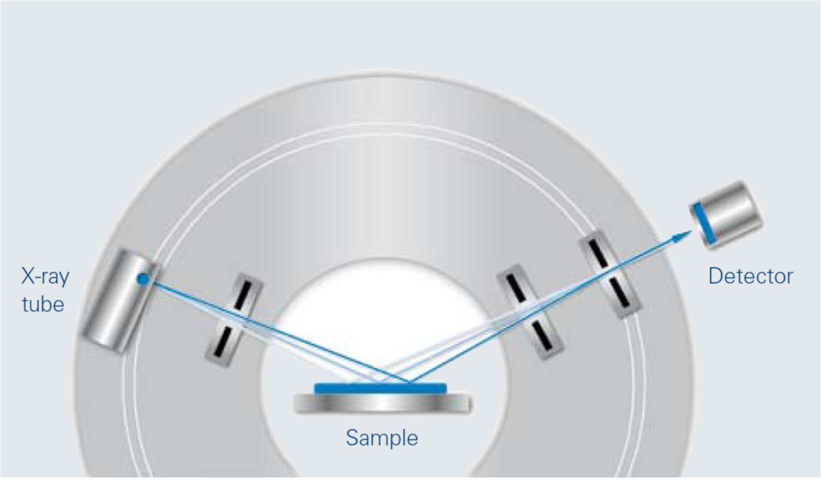

Figure 3.2.1-1: Schematic representation of the Bragg-Brentano geometry [221].

Air-sensitive samples were loaded on gas-tight sample holders inside the glove box under Ar atmosphere.

Rietveld refinement

Rietveld refinement of powder diffraction patterns is a tool used to quantify phase fractions and microstructural parameters such as lattice constants, microstrains and crystallite sizes. The method uses a least squares approach to refine a calculated line profile $y_{n,c}$ until it matches the observed profile $y_{n,o}$ of the diffracted intensities.

$$S = \sum_{hkl} w_n \left|y_{n,o} - y_{n,c}\right|^2 \rightarrow minimum. \tag{15}$$

The factor w refers to the weights given to the various observations so that errors in more accurately data „count“ more than do those in other data [222]. The calculated line profile F_c is determined using the following equation (16):

$$y_{n,c} = s \sum_{k} H_k \cdot L_k \cdot P_k \cdot A \cdot S_r \cdot E_x \cdot |F_k|^2 \cdot \phi \cdot (2\theta_n - 2\theta_k) + y_{n,b}, \tag{16}$$

with s representing the scaling factor, H_k an area frequency factor, P_k a texture factor, A an absorption factor, S_r a surface roughness factor, E_x an extinction factor, F_k a structure factor, ϕ the reflex profile function, θ_n and θ_k the difference between observed and calculated Bragg-peak position, and F_u observed background intensity [223].

The quality of a Rietveld refinement may be inferred by the calculation of an „R-factor“, such as the *weighted profile R-factor* R_{wp}:

$$R_{wp} = \sqrt{\frac{\sum w_n \left(y_{n,o} - y_{n,c}\right)^2}{\sum w_n \left(y_{n,o}\right)^2}}, \tag{17}$$

The quantity minimized is the sum of the squares of the weighted differences between the measured ($y_{n,o}$) and calculated ($y_{n,c}$) values for each measured point on the powder diagram that is used for least-squares refinement. It measures how well the structural model fits the diffraction intensities and how well the background and the diffraction positions and peak shapes have been fitted [224].

Peak shapes in powder X-ray diffraction

There is no sharp boundary between substances which are crystals having a long range order in three dimensions and those, which are amorphous solids with no long range order. XRD peaks of a perfect, crystalline sample measured in a perfect diffractometer would be extremely sharp. In reality, such perfection is not realised, and powder diffraction patterns exhibit peak broadening and asymmetry. Two sources of broadening and asymmetry have been identified, (1) an instrumental contribution and (2) contribution from the sample. The instrumental contribution can be determined by measuring a well-crystalline standard. Sample contributions are caused by deviations from ideal crystal symmetry and may arise through several factors, such as

- disorder in site occupancy, positional or orientational disorder,
- structural „mistakes“ such as stacking faults or twin faults,
- concentration gradients in non-stoichiometric compounds,
- crystal lattice distortion (microstrain) due to dislocations and concentration gradients, and
- small crystallite size [225].

3.2.2 Electron microscopy

Electron microscopy is an imaging method used to investigate surface structures of materials. A beam of accelerated electrons serves as the source of illumination. The wavelength of an electron is up to 100 000 times shorter than that of visible light photons. Thus, an electron microscope has a higher resolving power than a light microscope and can reveal the structure of smaller objects. Two types of electron miscroscopes are in use, the *scanning electron microscope* (SEM) and the *transmission electron microscope* (TEM).

An SEM generates images by scanning the surface of a specimen with a focused electron beam. The beam interacts with the specimen surface. This causes the emission of secondary and backscattered electrons or X-rays, all of which provide information about the properties of the surface of the specimen. The emitted electrons are detected to generate images of high resolution and depth of focus.

A TEM is built up similarly to an optical microscope, except that a high voltage electron beam instead of visible light transmits the specimen and electromagnetic or electrostatic lenses are used instead of optical lenses. A thin specimen with a thickness < 100 nm is used in a TEM. When electrons are transmitted through the specimen, they interact with the atoms of the specimen and are partly scattered. The scattering intensity depends on the atomic number as well as the number of passed atoms. The emerging beam carries information about the structure of the specimen.

High resolution transmission electron microscopy (HRTEM) capitalizes on interference of the electron beam with the crystal structure. Atomic resolution is possible.

In an STEM (*scanning transmission electron microscope*), an electron beam scans across the thinned specimen in a similar fashion as with a SEM, but better resolution and image quality is achieved as compared to an SEM. So-called „bright-field“ images use transmitted electrons to form an image, „dark-field“ images are generated by using scattered electrons. Incoherently scattered electrons at high angles can be used to create images highly sensitive to variations in the atomic number of the atoms contained in the specimen. This method is known as *high-angle annular dark-field imaging* (HAADF).

The atoms of the specimen act as a diffraction grating to the transmitting electrons, which are diffracted. *Selected area electron diffraction* (SAED) is the corresponding crystallographic technique that is performed inside the TEM in order to obtain information about the local crystal structure and phase composition.

X-ray radiation is emitted when an electron beam such as the one used in an SEM or TEM interacts with the specimen. The wavelength of the X-rays is characteristic for the respective elements contained in the specimen. A quantitative analysis of the elemental composition is possible through analyzing the X-rays by a detector. This method is known as EDX, which is short for *energy dispersive X-ray spectroscopy*. *Electron energy loss spectroscopy* (EELS) is generally regarded as the complementary method to EDX, as it is suitable to quantitatively determine compositions of light elements, whereas EDX is more suitable for heavier elements. In EELS, the energy loss of inelastically scattered electrons can be measured via an electron spectrometer and interpreted in terms of what caused the energy loss.

For more detailed descriptions about the working principles of electron microscopes, the reader is referred e.g. to references [226] (SEM) and [227] (TEM).

In this work the samples were measured either using a S3400-N Hitachi SEM equipped with a Genesis 2000H EDX spectrometer (Tsukuba) or with a LEO 1530 Gemini Zeiss SEM equipped with an X-Max^N EDX detector (Karlsruhe). According to the manufacturers, the accuracy of the compositions as determined by EDX is ± 0.5 at%. Samples before hydrogenation were prepared by cutting a slice of approximately 1 mm thickness from the alloy and embedding it in a polymer. The surface was polished and the sample was connected to the sample holder by conductive silver to enable electron transfer. Average compositions were determined at three different spots of the ingots: at the edge (x_1=r), at the centre (x_2=0•r) and at a third spot between those two points (x_3=1/2•r). They were determined by collecting EDX spectra of an area of approximately 100 x 100 mm^2 and are referred to in the text as average composition. In addition, the compositions of individual points within the different phases were also determined by collecting EDX point spectra. These are referred to as relative concentrations. After hydrogenation, the powdery samples were spread on sticky carbon tapes.

3.2.3 X-ray photoelectron spectroscopy (XPS)

X-ray photoelectron spectroscopy (XPS) is a non-destructive surface chemical analysis technique that can be used to analyse the chemical composition of a surface at information depths of 1 – 3 nm. An XP spectrum is collected by irradiating a specimen with a beam of X-rays, which results in the excitation and emission of electrons from the core shells of near surface atoms. The atom is ionized during that process. In a subsequent relaxation step the electron hole is filled by an outer shell electron of higher energy level. Some of the emitted photoelectrons leave the specimen and can be detected.

From the law of conservation of energy

$$E_{photon} = E_{binding} + E_{kinetic} + \phi, \tag{18}$$

where E_{photon} is the known energy of the incident monochromatic X-ray photon with a particular wavelength, $E_{kinetic}$ is the kinetic energy of the emitted electron, which is measured by a detector, and ϕ is a work function taking into account the energy loss of photoelectrons absorbed by the detector, the binding energy $E_{binding}$ of the electron can be calculated.

The binding energy is characteristic for the element as well as the respective atom orbital from which the photoelectron is emitted. If the atom is chemically bonded to another chemical species, the binding energy of the electron may shift to a lower or higher value. This is known as „chemical shift“ of the signal position, which allows to draw conclusions about the oxidation state of an element and chemical bonds between the detected elements.

XPS can be used for quantitative analysis of elemental compositions of the near surface. The cross-section for the emission of a photoelectron is not dependent upon the chemical environment of the atom. Hence, the number of photoelectrons of a certain binding energy emitted from the specimen (i.e., the intensity of a spectrum) is proportional to the concentration of the element. Elemental compositions of the near surface can be calculated by using element-specific, empirically derived relative sensitivity factors, which are used to scale the measured peak areas so that variations in the peak areas are representative of the amount of material in the sample surface [228].

If knowledge about the chemical composition and environment of the atoms below the surface is desired, the outer surface layers can be removed by means of ion sputtering. Concentration profiles as a function of depth can thus be determined.

XP spectra shown in this work were measured at the Institute for Surface Chemistry and Catalysis, Ulm University, Germany, by Dr. Thomas Diemant. A Physical Electronics XPS apparatus (PH 5800 MultiTechnique ESCA System) using monochromatic Al-K-α radiation (1486.6 eV) was used. A surface of 0.8 x 0.8 mm^2 was analyzed at a detection angle of 45 °. Ion sputtering was performed using Ar^+ ions ($I_{sp} \approx 1$ µA, $U_{sp} = 5$ kV). The applied sputtering rate corresponds to a removal of approximately 1 nm sample per minute.

3.2.4 Volumetry

Hydrogen sorption properties were determined by volumetric apparatuses, also known as Sieverts's apparatuses. A schematic representation of such an apparatus is shown in Figure 3.2.4-1.

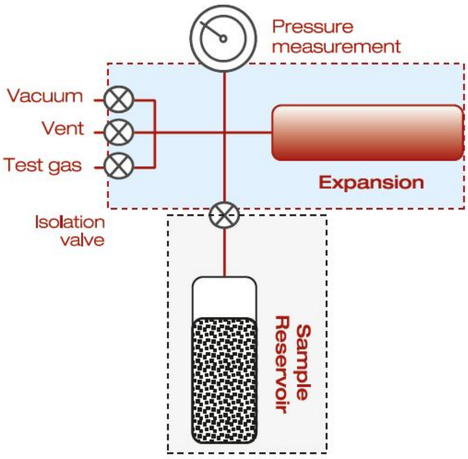

Figure 3.2.4-1: Schematic representation of a volumetric apparatus used for characterization of H storage properties [229].

Based on the law of ideal gases

$$p \cdot v = n \cdot R \cdot T, \tag{19}$$

and taking into account real gas behavior at elevated pressures at > 100 bar, the amount of gas n in a defined volume v can be calculated by measuring pressure p and temperature T. R is the universal gas constant.

During a typical hydrogen absorption measurement, a sample of known mass is inserted into a sample reservoir (lower grey part in Figure 3.2.4-1). This is connected to the rest of the apparatus (upper blue part in Figure 3.2.4-1). After flushing and evacuation, the valve connecting the sample reservoir with the expansion volume is closed and hydrogen gas is introduced into the upper part of the apparatus. The gas is allowed to equilibrate for a few minutes, and then the valve between expansion volume and sample reservoir is opened. Hydrogen flows in and the sample absorbs hydrogen until reaching an equilibrium state, which is characterized by constant pressure and sample temperature. The amount of hydrogen absorbed by the sample corresponds to the difference between the amount of gaseous hydrogen in the apparatus before opening the valve and after reaching equilibrium state, monitored by the pressure difference. Hydrogen desorption is performed in the reverse order, starting with an absorbed sample and then desorbing into the lowered pressure of the expansion volume.

Pressure-composition isotherms (PCI, Fig. 2.3.1-2 and 2.3.1-3) are measured through a stepwise increase/decrease of the hydrogen pressure and allowing the sample to reach equilibrium at each measurement point. Kinetic measurements of initial hydrogen absorption are performed by applying high hydrogen pressure between 5 and 8 MPa and absorbing the whole sample in one step.

The effects of gaseous impurities on the hydrogen absorption properties of V-Ti-based solid solution alloys were studied by means of pressure measurements. The samples were activated during 15 absorption-desorption cycles in order to ensure a complete decrepitation of the particles. This was necessary to expose the full surface area and hereby reduce possible side effects of pristine metal surface exposed during cycling in impure H_2. After activation, hydrogen gas containing the impurities 1000 ppm CO_2 or N_2, 200 ppm H_2O or toluene, or 250 ppm O_2 was used. The gases were supplied by BASI Gase & Technik GmbH. A testing certificate, in which the real impurity concentrations were listed, was also provided. All impurity concentrations deviated a maximum of ± 5 ppm from the specified concentrations.

Kinetic curves are generally plotted in the form of reacted fraction as a function of reaction time. The procedure and assumptions that were made are described in the following paragraph.

A Swagelok reactor made of stainless steel was used for the experiments. An empty reactor without sample was measured as a reference at the same pressure and temperature conditions that were applied for the measurements of the samples. The whole system was evacuated and the valve between the reactor and the rest of the apparatus was closed. 1 MPa of H_2 was then introduced into the rest of the apparatus. When the valve between reactor and the rest of the apparatus was opened, the pressure decreased as a result of hydrogen gas flowing into the reactor. In the case of the empty reactor without sample, a pressure drop by about 0.06 MPa was recorded. When the reactor was filled with an absorbing sample, the final pressure that was reached was lower than in the case of the empty reactor. The pressure difference between the measurements with and without sample corresponds to the absorption capacity of the respective sample. After the initial activation cycles, the capacity was assumed as 100 %, and the pressure difference was used to normalize the reacted fraction to 100 % (full capacity; reacted fraction = 1). If during a subsequent experiment in impure hydrogen gas the final pressure was higher than during the initial absorption, it was assumed that less hydrogen was absorbed, which corresponded to a reduction of the reacted fraction. Depending on the surface properties of the respective sample, a slower pressure decrease also corresponded to slower absorption kinetics. The reactor was dipped into a thermal oil bath. The temperature during the absorption in pure H_2 was measured at the outside of the reactor during the first experiments. Due to the small amount of sample (approx. 0.3 g), no temperature variation was noted.

In the left image of Figure 3.2.4-2 the pressure vs. time curves of the empty reactor without sample, during the measurement with 0.3 g sample in pure H_2 and in H_2 blended with 250 ppm O_2 are shown. The right image shows the corresponding kinetic curves as shown in this work.

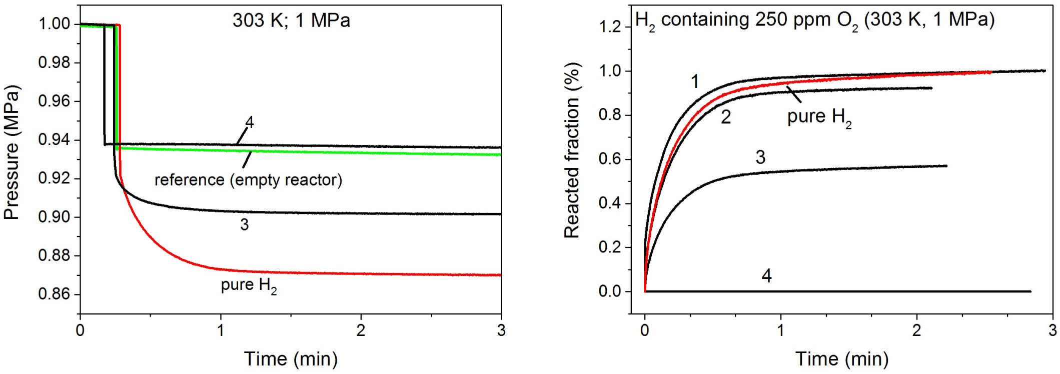

Figure 3.2.4-2: Pressure measurements as a function of time of the empty reactor (green), absorption in pure H_2 (red) and after various cycles in H_2 containing 250 ppm O_2 (left image). The right image shows the resulting kinetic curves displaying the reacted fraction as a function of time.

In Tsukuba and in Karlsruhe home-built Sieverts apparatuses were used. In Karlsruhe, the expansion volume was determined by means of expansion measurements using He gas and calibrated by measuring a $LaNi_5$ standard material.

3.2.5 Thermogravimetry combined with differential scanning calorimetry and mass spectrometry (TG-DSC-MS)

TG-DSC-MS is an analytic tool used to investigate the processes occuring during thermal treatment of a material. In essence, it combines three separate analytical methods, thermogravimetry (TG), differential scanning calorimetry (DSC) and mass spectrometry (MS).

Thermogravimetric analysis measures mass changes of a sample as a function of temperature by means of a microbalance. Assuming there are no other volatile species the result of such a measurement gives the hydrogen capacity of a sample.

A DSC measures the difference in the amount of heat required to increase or decrease the temperature of a sample and a reference. Both the sample and the reference are maintained at nearly the same temperature thoughout the experiment. Thermal effects occurring during endo- or exothermal events, such as chemical reactions or phase transformations, result in different heat fluxes to the sample as compared to the reference and can be investigated [230].

Mass spectrometry is an analytical technique in which atoms or molecules from a sample are ionized, separated in a quadrupole mass filter according to their mass-to-charge-ratio (m/z), and then recorded. Thus, information is obtained about the chemical composition of the gases evolved during thermal treatment of a sample.

For the measurement, a few Milligrams of the sample material are filled into a crucible, which is placed on one arm of a microbalance. An empty reference crucible is placed on the other arm. Both crucibles are inserted into a furnace and an appropriate atmosphere for the measurement is provided. Sample and reference temperatures are controlled in a pre-programmed temperature/time profile. During the whole time of the experiment, the evolved gases are analyzed by MS. Upon heating, the sample may undergo endo- or exothermal chemical reactions and/or phase transitions. If such events occur, the weight loss/gain can be measured by TG and the associated thermal effects can be investigated by DSC. Evolved gases can be analyzed by MS.

The TGA-DSC-MS measurements were conducted with a Setaram thermal analyzer SENSYS evo TGA-DSC equipped with a Pfeiffer OmniStar mass spectrometer for the analysis of the evolved gases. Measurements were performed in 0.1 MPa He atmosphere at a heating rate of 5 °C/min under 20 mL/min He flow.

3.2.6 Gas chromatography (GC)

Gas chromatography (GC) is a chemical analysis method used to separate chemical compounds in a mixture of gases or liquids. The separating component is a narrow tube or capillary filled with a specific packing material, the so-called *column*. A gaseous sample of known volume is injected at the entrance of the column, and a carrier gas stream (typically an inert gas, called *mobile phase*) sweeps the sample molecules through the column. The column is tightly filled with the packing material (the *stationary phase*, typically a microscopic layer of liquid or polymer on an inert solid support), with which the sample molecules interact while being swept through the column. Depending on the strength of the interactions, different components of the sample are held back differently and eventually elute at the end of the column at a different time, the so-called *retention time*. By calibrating the GC with known substances, the different retention times can be assigned to specific compounds. The compounds escaping from the column are detected, with the most common detectors being flame ionization or thermal conductivity detectors. Alternatively, the GC can be connected to a mass spectrometer which acts as the detector [231].

Within this work, the reactions of acetone and toluene on the surface of the solid solution alloy $V_{40}Fe_8Ti_{26}Cr_{26}$ were investigated by GC measurements. The detailed measurement procedures are described in Section D of the Appendix. For the toluene reaction the gaseous reaction products were analyzed using an Agilent 7890A gas chromatograph. The GC was equipped with a DB-624 capillary column (l = 30 m, d = 0.45 mm, s = 2.55 µm) and a molsieve Plot5A (l = 15 m, d = 0.53 mm, s = 50 µm), to provide full information on organic components and permanent gases. Acetone reaction products were analyzed using a 7890A GC by Agilent equipped with a Porapak Q column (l = 2 m, d = 2 mm, 80/100 mesh) and a molsieve 5a (l = 2 m, d = 2 mm, 80/100 mesh). Both GC's were equipped with a flame ionization and a thermal conductivity detector.

4 Results

4.1 LaNi$_5$: a reference system

LaNi$_5$-derived materials have been proven in a broad range of stationary applications such as hydrogen or thermal energy storage and hydrogen separation and were therefore chosen as reference systems for comparison with the more complex and advanced V-Ti-based solid solution systems studied later in this thesis. Additionally, they were utilized as well-suited model systems in order to gain experience and validate the experimental methods.

For intermetallic hydrides studied in this thesis, sorption kinetics are in general fast. In many cases, the heat transfer to/from the sample is the rate-limiting step. Hence, the structural (e.g. phase composition, crystallographic parameters) and thermodynamic properties (equilibrium pressure, hydrogen capacity) were considered to be the most relevant properties.

In Figure 4.1-1 the pressure-composition isotherms (PCI) are presented of LaNi$_{4.9}$Al$_{0.1}$ at various temperatures with the corresponding Van't Hoff plot.

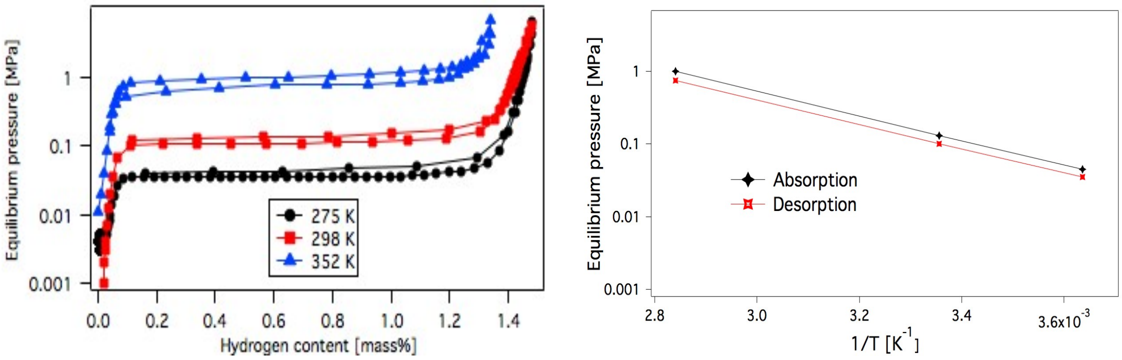

Figure 4.1-1: Pressure-composition isotherms of LaNi$_{4.9}$Al$_{0.1}$ after 50 cycles at 275 K, 298 K and 352 K (left) and the corresponding Van't Hoff plot (right).

The measured PCI curves correspond well with previous literature reports on Al-substituted LaNi$_5$ [86], [138], [232]. Enthalpies and entropies of hydride formation and dissociation were calculated as $\Delta H = -32.5\, kJ \cdot mol^{-1}\, H_2$ and $\Delta S = -111.3\, J \cdot mol^{-1} K^{-1}$ for hydride formation and $\Delta H = 32.1\, kJ \cdot mol^{-1}\, H_2$ and $\Delta S = 107.9\, J \cdot mol^{-1} K^{-1}$ for hydride dissociation. This is in good agreement with Diaz *et al.*, who reported $\Delta H = -32.6\, kJ \cdot mol^{-1}\, H_2$ and $\Delta S = 110.5\, J \cdot mol^{-1} K^{-1}$ for hydride dissociation [138].

The volumetric method for PCI measurements was validated using LaNi$_{4.9}$Sn$_{0.1}$, a material exhibiting similar properties as LaNi$_{4.9}$Al$_{0.1}$, and the results obtained in Tsukuba were compared to those obtained at KIT in Karlsruhe. Absorption PCI curves are shown in Figure 4.1-2.

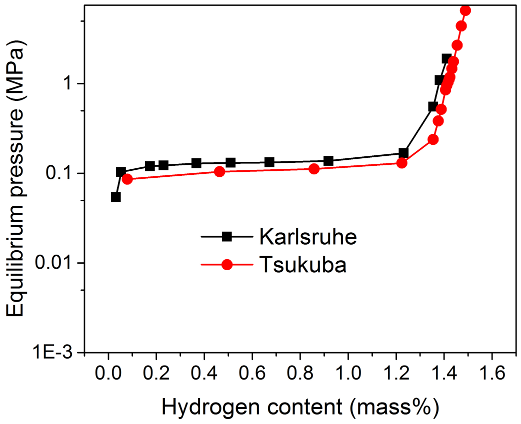

Figure 4.1-2: Absorption PCI of $LaNi_{4.9}Sn_{0.1}$ measured at 298 K in Tsukuba and in Karlsruhe.

An equilibrium pressure of 0.1 MPa was measured in both apparatuses, and a reproducible storage capacity of approximately 1.4 mass% H was calculated at 1 MPa. It was concluded that the sorption properties could be measured with sufficient reproducibility in both laboratories.

With $LaNi_5$-derivatives as reference materials, the focus was now shifted to the more advanced V-Ti-based solid solutions.

4.2 V-Ti-based solid solution alloys

4.2.1 Alloy design

Based on a previous literature report by Yan *et al.* [183], an appropriate stoichiometry of $V_{40}Fe_8Ti_xCr_y$ was selected: V content should be as low as possible in order to minimize the content of this expensive material. Fe was added so that the composition of (V+Fe) resembled that of the cheaper FeV master alloy. Cr was chosen as an additional element due to the lower hysteresis as compared to other frequent substitutional elements such as Mn [16], [85].

As a first step, the thermodynamics of hydrogen sorption was adjusted so that a resulting material would be suitable for the LORC process. This was achieved through variation of the Ti/Cr ratio. XRD patterns of $V_{40}Fe_8Ti_xCr_y$ are presented in Figure 4.2.1-1.

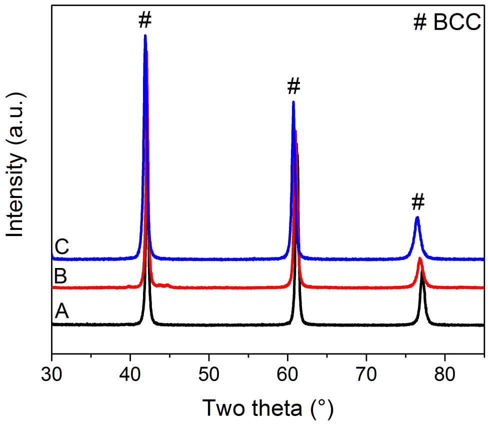

Figure 4.2.1-1: XRD patterns of $V_{40}Fe_8Ti_xCr_y$ with x = 26 (A), 30 (B) and 32 (C), and y = 26 (A), 22 (B), and 20 (C) in the annealed state.

The samples show a body-centered cubic crystal structure. Small amounts of C14 Laves secondary phases are observed in some of the samples. Peak shift towards lower diffraction angles is observed at higher Ti and lower Cr contents. This effect originates in the larger atomic radius of Ti (147 pm) as compared to V (134 pm). The addition of Ti expands the unit cell, and according to Bragg's equation (12) a peak shift is observed. SEM images are presented in Fig. E-1 in the appendix.

In Figure 4.2.1-2 PCI curves of $V_{40}Fe_8Ti_xCr_y$ at various Ti/Cr ratios are shown.

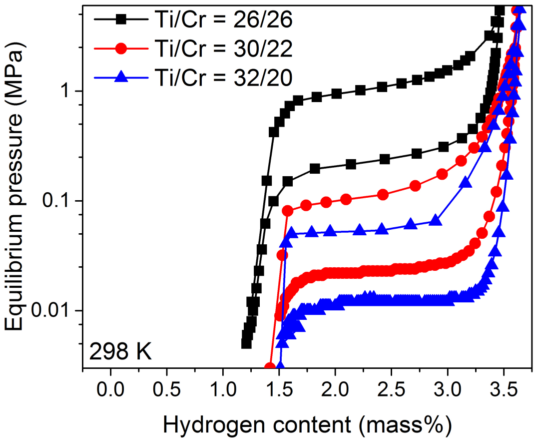

Figure 4.2.1-2: Pressure-composition isotherms of $V_{40}Fe_8Ti_xCr_y$ at 298 K.

For all materials tested in the present work, the equilibrium pressure of monohydride formation was below the detection limit of the apparatus of 0.001 MPa. The pressure transducer recorded a pressure value of 0 MPa. These points are not shown on the logarithmic scale. A relationship between the Ti/Cr ratio and the equilibrium formation and dissociation pressures is observed. This is represented in Figure 4.2.1-3.

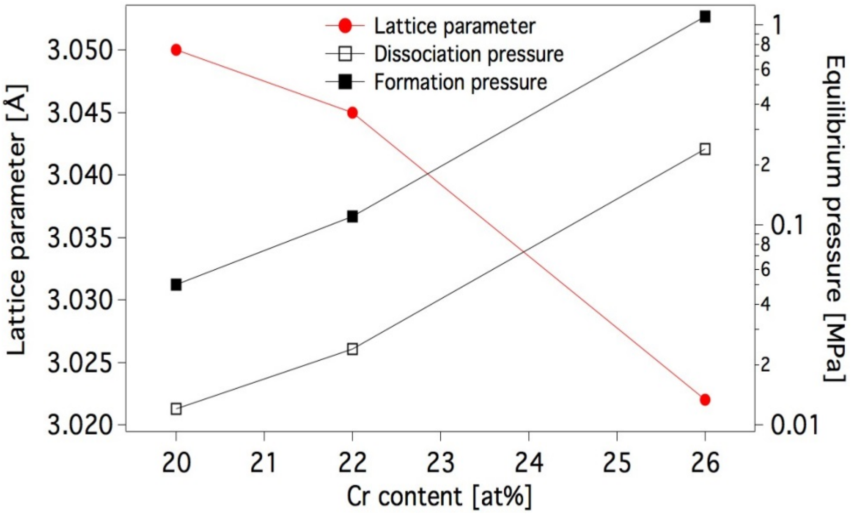

Figure 4.2.1-3: Equilibrium pressure of dihydride formation and dissociation and lattice parameter as a function of Cr content.

The lattice parameter, as determined by XRD, can be modified through variation of the Ti/Cr ratio. As a result, the equilibrium pressures of dihydride formation and dissociation can be modified. For a Cr content of 20 at%, the formation equilibrium pressure amounts to 0.5 MPa, and 1.1 MPa are measured at 26 at% Cr.

Variation of the Ti/Cr ratio is hence well-suited to tailor the thermodynamic properties of the storage material. The results are in good agreement with previous reports e.g. by Nomura *et al.* [194], Yan *et al.* [183] and Wu *et al.* [189], who observed similar relationships between Ti/Cr content, lattice parameters and equilibrium pressures.

In order to investigate the cyclic stability and the equilibrium properties after cycling, $V_{40}Fe_8Ti_{26}Cr_{26}$ was cycled 50 times and a PCI curve was measured subsequently. This is presented in Figure 4.2.1-.

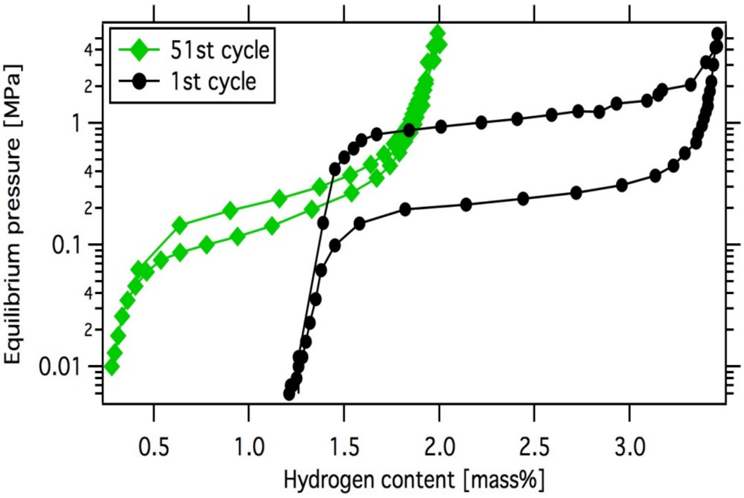

Figure 4.2.1-4: Pressure-composition isotherms of $V_{40}Fe_8Ti_{26}Cr_{26}$ during the first and 51st cycle at 298 K.

Upon cycling, H is stored and released only during the formation and dissociation of the dihydride between 6 MPa and 0.01 MPa. The sample shows a reversible capacity of 2.2 mass% in the first cycle. 1.7 mass% H are stored after 50 cycles, corresponding to a degradation of the reversible capacity by 23 %. For an application in which the material is cycled in a narrow pressure window (e.g., between 0.1 and 1 MPa), the reversible capacity corresponds to approximately 1.3 mass%. The formation and dissociation pressures decreases from 1.1 MPa to 0.2 MPa and from 0.24 MPa to 0.1 MPa upon cycling, respectively, the pressure plataux become increasingly sloping. These results are comparable to previous reports by Cho *et al.* [188], Itoh *et al.* [233] and Lin *et al.* [234]. PCI curves were also measured at various temperatures for the first cycle, and a Van't Hoff plot was constructed. These curves are shown in Figures F-1 and F-2 in the Appendix. Enthalpy and entropy of hydride formation and dissociation were calculated as $\Delta H = -30.2 \pm 0.2\, kJ \cdot mol^{-1}\, H_2$ and $\Delta S = -120.6 \pm 0.6\, J \cdot mol^{-1} K^{-1}$ for hydride formation and $\Delta H = 32.6 \pm 0.2\, kJ \cdot mol^{-1}\, H_2$ and $\Delta S = 120.4 \pm 0.5\, J \cdot mol^{-1} K^{-1}$ for hydride dissociation (the equilibrium pressures at the middle of the pressure plateaux were used for the calculations). These values are in the expected range, also compared to similar materials reported in the literature [16]. The difference between enthalpy of hydride formation and enthalpy of hydride dissociation originates in the hysteresis between formation and dissociation pressure, which is more pronounced for $V_{40}Fe_8Ti_{26}Cr_{26}$ and related materials during the initial cycles than in the case of $LaNi_5$-derived systems. Upon cycling, the hysteresis factor decreases.

Based on these results, $V_{40}Fe_8Ti_{26}Cr_{26}$ was chosen as an appropriate composition for further investigations due to favorable thermodynamic properties that can be adjusted easily with respect to the LORC process and high total and reversible hydrogen capacities at a relatively low content of expensive vanadium.

4.2.2 Cost reduction possibilities in V-Ti-based solid solutions

Experimental results of the approaches to reduce the raw material cost of V-Ti-based solid solutions are presented in the following chapters.

4.2.2.1 Effect of oxygen

In a first step, the effect of oxygen on the microstructure and hydrogen storage properties of V-Fe-Cr-Ti solid solutions was analyzed. This study had two purposes. On the one hand, oxygen is contained as a major impurity in FeV, and hence it is important to investigate its effect on the storage material. On the other hand, low-purity vanadium of high oxygen content is cheaper than high-purity vanadium of low oxygen content. The effect of oxygen on V-Fe-Ti-Cr-type solid solutions has not been reported before.

In Figure 4.2.2.1-1 SEM images of three $V_{40}Fe_8Ti_{26}Cr_{26}$ alloys prepared with high-oxygen V, low-oxygen V and high-oxygen V and 1 at% La for deoxidization (denoted below as „high-oxygen sample“, „low-oxygen sample“ and „deoxidized sample“) are presented. The images were obtained from polished cross sections of the alloys in annealed state. The compositions of the phases determined by EDX are listed in Table E-1 in the appendix.

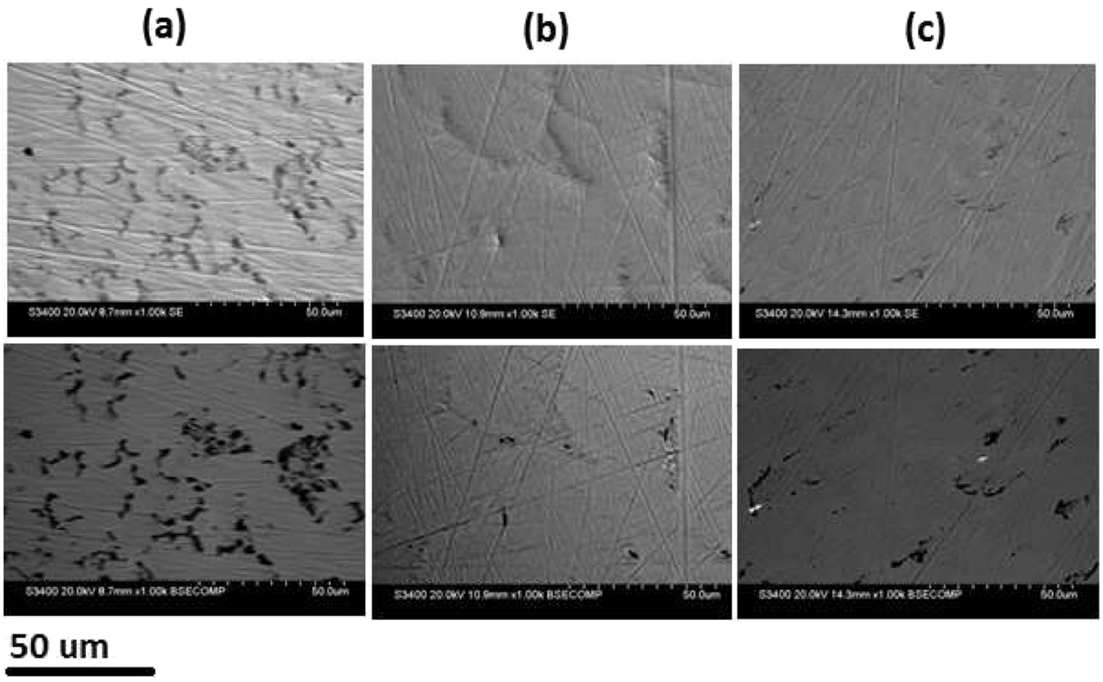

Figure 4.2.2.1-1: SEM images of $V_{40}Fe_8Ti_{26}Cr_{26}$ with (a) high oxygen concentration, (b) low oxygen concentration and (c) deoxidized using 1 at% La. SE: secondary electron images (top); BSE: back-scattered electron images (bottom).

The high-oxygen sample contains a large fraction of Ti-rich secondary phase. The secondary phase is clearly visible in the form of dark areas in the secondary electron or back-scattered electron images, respectively. This phase consists of 78.3 - 95.9 at% Ti. Consequently, the fraction of Ti in the main phase is reduced to an average of 22.3 at% as compared to 23.2 at% and 23.0 at% for the low-oxygen and deoxidized samples, respectively. EDX spectra of the secondary phase also show considerable oxygen content (not shown). This observation suggests a reaction between oxygen and titanium proceeds during the preparation of the alloy.

Both the low-oxygen and the deoxidized sample only show a small fraction of secondary phase. For the low-oxygen sample, the secondary phase consists of 34.0 - 38.2 at% Ti and for the deoxidized sample, the fraction of Ti is found to be 35.5 - 46.1 at%. The secondary phase is most likely a Laves phase or a related one. For the deoxidized sample, small inclusions of La oxide are visible as white spots distributed within the alloy. The solubility of La or La oxides in V, which is the main constituent of the alloy, is below 0.1% [235].

Figure 4.2.2.1-2 shows the XRD patterns of the low-oxygen, high-oxygen and deoxidized samples.

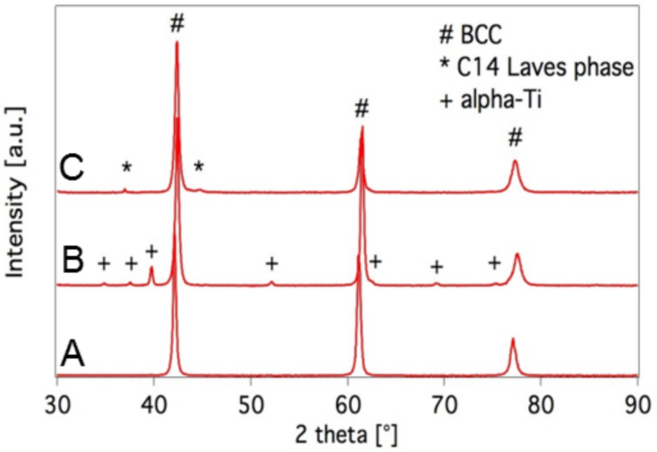

Figure 4.2.2.1-2: XRD patterns of $V_{40}Fe_8Ti_{26}Cr_{26}$ (A) prepared with low-oxygen V, (B) prepared with high-oxygen V and (C) prepared with high-oxygen V and 1 at% La.

The low-oxygen sample shows a BCC structure with a lattice parameter of 3.0308 (2) Å. No additional phases are detected by XRD.

The diffraction pattern of the high-oxygen sample exhibits peaks of two distinct phases, the BCC main phase and a secondary phase isostructural with α-Ti. The refined lattice parameter of the BCC main phase is 3.0141 (3) Å, corresponding to a reduction of 0.016 Å (0.53 %) compared to the low-oxygen sample. The lattice parameters of the α-Ti-like secondary phase are $a = 2.9707(73)$ Å and $c = 4.7843(61)$ Å. Pure α-Ti has a hexagonal close-packed structure with lattice parameters of $a = 2.951$ Å and $c = 4.686$ Å [236]. Thus, the unit cell of the α-Ti-like phase is found to be expanded by ~ 0.01 Å in a-direction and ~ 0.1 Å in c-direction. It has been reported that the lattice parameter of α-Ti depends on the oxygen content [237–239]. With an increased O-content, the lattice of α-Ti will be expanded. Based on these reports the average oxygen content of the secondary, α-Ti-like phase is estimated as 25 ± 5 at% O. Obviously, Ti with its strong affinity to O functions as a deoxidizer and forms the Ti-O phase. Rietveld refinement of the high-oxygen pattern reveals the fraction of α-Ti-like phase to amount to 3 % and BCC main phase to 97 %.

For the deoxidized sample, the BCC main phase and minor peaks corresponding to the C 14 Laves phase are detected. Thus, the addition of 1 at% lanthanum inhibits the formation of α-Ti-like phase that occurs during the preparation of the alloys using high-oxygen V. The lattice parameter of the La-deoxidized sample is 3.0297(3) Å, close to the value of the low-oxygen sample. The free energy of rare earth oxide formation is the largest of all known metals [240]. Therefore, these metals show the highest affinity towards oxygen and act as oxygen getters.

The oxygen content of the low-oxygen, high-oxygen and deoxidized samples was also measured by oxygen analysis. They amount to 0.045 mass% O, 0.515 mass% O and 0.069 mass% O, respectively. The oxygen content of the deoxidized sample is in a similar range as compared to the low-oxygen sample.

The α-Ti-like phase of the high-oxygen sample was further investigated by TEM. The purpose of the study was 1) to confirm the α-Ti-like structure of the secondary phase, 2) to determine its composition, and 3) to clarify whether oxygen is found in the BCC main phase.

Figure 4.2.2.1-3 shows a STEM-HAADF image of the α-Ti-like and BCC main phase, EEL spectra of the indicated areas and SAED pattern of the α-Ti-like phase.

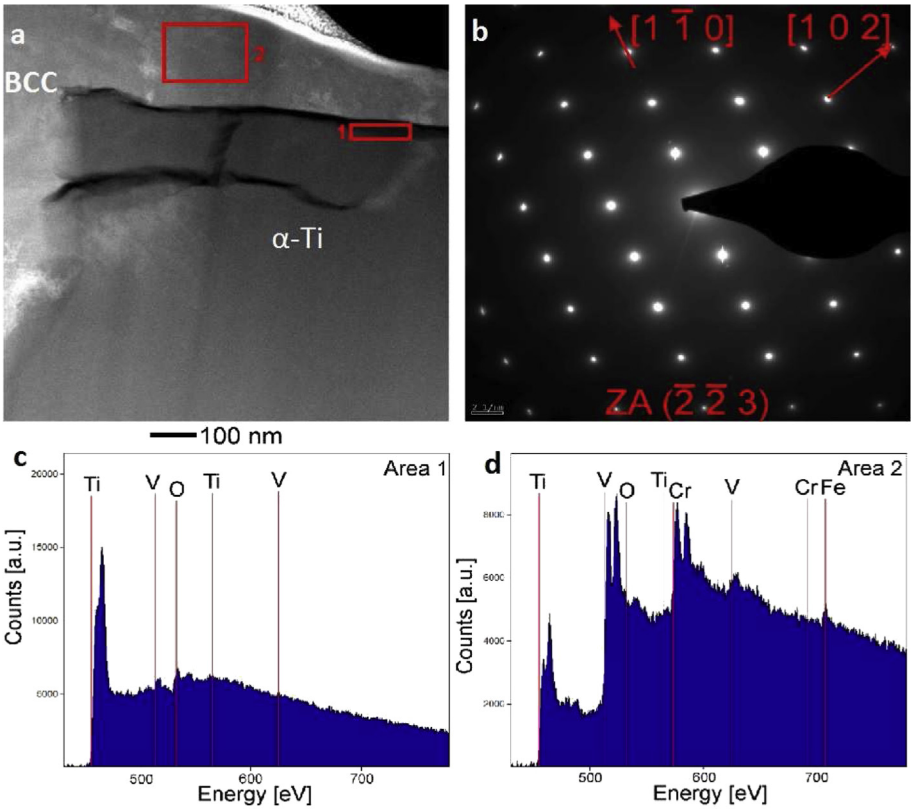

Figure 4.2.2.1-3: (A) STEM-HAADF image of the α-Ti-like and BCC main phase of the high-oxygen sample, (b) SAED pattern on the α-Ti-like phase in the $\langle\bar{2}\bar{2}3\rangle$ zone axis with the corresponding d values of $2.57(1\bar{1}0)_{\alpha\text{-Ti}}$, $1.77(102)_{\alpha\text{-Ti}}$, (c) & (d) EEL spectra of the areas 1 & 2 indicated in (a).

The α-Ti and the BCC main phase are separated from each other by a well-defined phase boundary. The EEL spectrum of the BCC main phase shows characteristic energy loss signals corresponding to V, Ti, Cr and Fe. No oxygen is detected by EELS, indicating an oxygen concentration below the detection limit of around 1 at% in the BCC main phase. The EEL spectrum of the α-Ti-like phase only shows Ti, O and V edges. EEL spectra were collected at various positions and oxygen was found to be distributed homogeneously within the secondary phase. The presence of V in the secondary phase is not noticed by SEM or XRD analysis, but is in good agreement with the Ti-V and Ti-O phase diagrams showing a solubility of V and O in α-Ti at room temperature [239], [241].

The SAED pattern of the α-Ti-like phase is in agreement with the $\langle\bar{2}\bar{2}3\rangle$ zone axis of a hexagonal close-packed structure (α-Ti).

Pressure-composition isotherms of the low-oxygen, high-oxygen and deoxidized sample are presented in Figure 4.2.2.1-4.

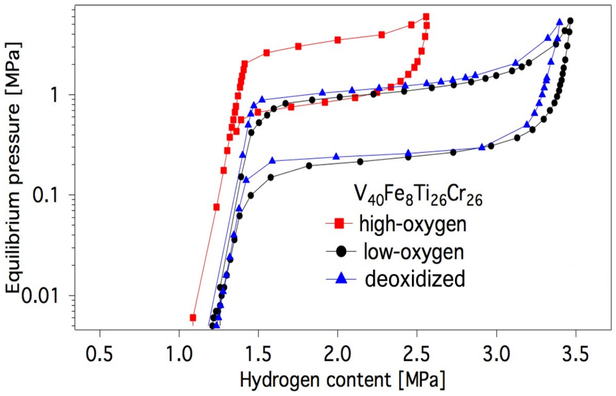

Figure 4.2.2.1-4: Pressure-composition isotherms of $V_{40}Fe_8Ti_{26}Cr_{26}$ at 298 K prepared with high-oxygen V, low-oxygen V and deoxidized using 1 at% La.

The low-oxygen sample shows a pressure of dihydride formation (p_f) and dissociation (p_d) of 1.15 MPa and 0.24 MPa at 298 K, respectively. For the high-oxygen sample, the equilibrium formation and dissociation pressures are raised to 3.5 MPa and 0.8 MPa. Compared to the high-oxygen sample without addition of La, the addition of 1 at% La effectively reduces the equilibrium pressure to 1.18 MPa for hydride formation and 0.26 MPa for hydride dissociation. Thermodynamic properties of the deoxidized sample are similar to those of the low-oxygen sample. This is in good agreement with XRD results of the alloys, as the low-oxygen and deoxidized sample exhibit similar lattice parameters. Thermodynamic properties are known to depend strongly on the alloy composition and lattice parameter [85].

The low-oxygen sample shows a total capacity of 3.5 mass% H, the deoxidized sample shows a capacity of 3.4 mass% H. This slightly reduced capacity is possibly due to the inclusions of La oxide found within the alloy, which act as inert material. The high-oxygen sample exhibits a total capacity of 2.5 mass% H.

Tsukahara *et al.* reported the hydrogen content of a $V_3TiNi_{0.56}Co_{0.14}Nb_{0.047}Ta_{0.047}$ to depend strongly on the oxygen concentration. Below 5000 ppm O concentration, the capacity was largely unaffected. For oxygen concentrations >5000 ppm, the capacity was reduced [17]. In contrast, the total hydrogen capacity of the low- and high-oxygen V-Ti-Mn alloys studied by Nakamura *et al.* was not affected by oxygen. Oxygen is known to reduce the hydrogen capacity of pure V [242]. The alloy studied by Tsukahara *et al.* contained a high vanadium fraction of 63 at%. In the present work, the V content was 40 at%, and the material studied by Nakamura *et al.* contained 36.7 at% V. It is interesting to note that for the alloy studied in the present work, the overall hydrogen capacity is reduced, while for the V-Ti-Mn alloy investigated by Nakamura *et al.*, the overall capacity was not affected by oxygen, despite the fact that the vanadium content of our alloy was only 3.7 at% higher.

Finally, it should be noted that deoxidization of the high-oxygen alloys can also be achieved by using other rare earth elements such as yttrium or cerium.

In summary, these results confirm that oxygen has negative effects on the microstructure and hydrogen storage properties of V-Fe-Ti-Cr-based solid solution alloys. This study represents the first reported investigation on the effect of oxygen on an alloy of such stoichiometry. Furthermore, the structure of the phase isostructural with α-Ti formed during the preparation of the high-oxygen-containing alloy has been investigated with unprecedented detail. Deoxidization of cheaper, low-purity raw metals of high oxygen content is necessary to obtain storage materials of homogeneous microstructure and excellent sorption properties.

4.2.2.2. Microstructural, thermodynamic and cyclic effects of vanadium substitution

The first ferrovanadium (FeV) that was tested as a substitute of pure V was FeV 1 provided by Taiyo Koko Co (detailed composition in section 3.1). In order to gain experience on the effects of substituting V and Fe by FeV, V and Fe concentrations of the alloy $V_{(40-40\bullet x)}Fe_{(8-8\bullet x)}Ti_{26}Cr_{26}(FeV)_{(48\bullet x)}$ were gradually reduced in steps of x = 0, 0.15, 0.3, 0.45, 0.6, 0.75 and 0.9 while simultaneously increasing the amount of FeV added in substitution for V and Fe.

The tested FeV contains 2100 ppm O, which was considerably less than the high-oxygen V that was tested in section 4.2.2.1. Hence, this investigation was performed without addition of rare earth metals.

In FigureFigure 4.2.2.2-1 SEM pictures of $V_{(40-40\bullet x)}Fe_{(8-8\bullet x)}Ti_{26}Cr_{26}(FeV)_{(48\bullet x)}$ with x = 0, 0.3, 0.6 and 0.9 are presented. The compositions of the phases determined by EDX are listed in Table E-2 in the appendix.

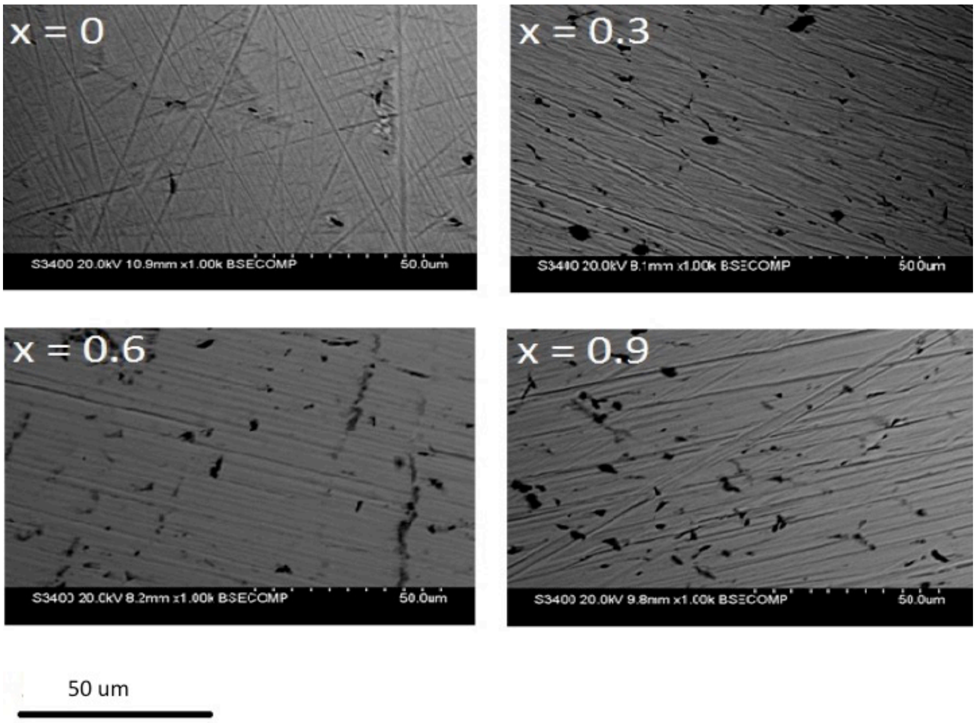

Figure 4.2.2.2-1: Back-scattered electron SEM micrographs of $V_{(40-40\bullet x)}Fe_{(8-8\bullet x)}Ti_{26}Cr_{26}(FeV)_{(48\bullet x)}$ with x = 0, 0.3, 0.6 and 0.9.

An increase in FeV content leads to the formation of secondary and ternary phases, which are clearly visible in the form of dark areas in the back-scattered SEM images. Besides the BCC main phase, two phases of differing Ti contents are observed. The prevalent secondary phase contains between 30 and 45 at% Ti and was identified by XRD as a C14 Laves phase. This is in agreement with previous reports [191], [192], [195]. A ternary phase, which is not detected by XRD, with up to 94 at% Ti is likely to be isostructural with α-Ti. The substitution of V and Fe by FeV affects the average composition of the FeV-containing alloys as compared to the alloys prepared from pure elements. While the concentrations of Ti and Cr remains unchanged or only mildly affected as in the case of V, the content of Fe gradually decreases from an average of 8.1 % at x = 0 to an average of 5.6 % at x = 0.9. This originates in the lower fraction of Fe in the FeV alloy compared to the starting material (FeV: Fe/V = 1/8; starting alloy: Fe/V = 1/5). The concentration of iron was not adjusted, because Fe is known to increase the hydrogen equilibrium pressure in a similar way as Al [199]. Concentrations of Al and Si increase from near 0 at x = 0 to 4.1 % Al or 1.3 % Si at x = 0.9 due to significant concentrations of these elements in FeV, as a consequence of the production process of FeV [235]. The observed increasing Al and Si content is in agreement with what would be expected from the introduction of the impure FeV in the alloy. However, it should be noted that the measured values are small and only slightly above the experimental error.

XRD patterns of $V_{(40-40\bullet x)}Fe_{(8-8\bullet x)}Ti_{26}Cr_{26}(FeV)_{(48\bullet x)}$ with x = 0, 0.15, 0.3, 0.45, 0.6, 0.75 and 0.9 are shown in Figure 4.2.2.2-2. In Table G-1 in the appendix the crystallographic data of the alloys is summarized.

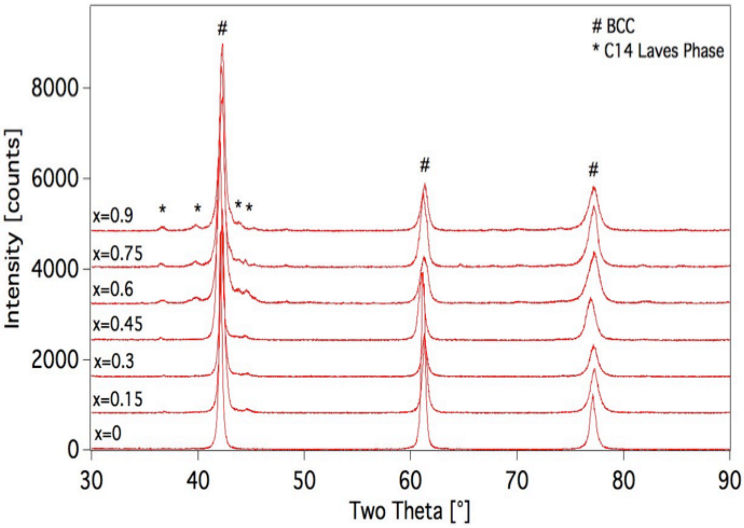

Figure 4.2.2.2-2: XRD patterns of $V_{(40-40\bullet x)}Fe_{(8-8\bullet x)}Ti_{26}Cr_{26}(FeV)_{(48\bullet x)}$ with x = 0, 0.15, 0.3, 0.45, 0.6, 0.75 and 0.9.

Without (V + Fe) substitution (x = 0) the material has a single phase BCC structure. At increasing fractions of FeV, the C14 Laves phase is introduced into the alloy, with a maximum fraction of 3 % at x = 0.6, 0.75 or 0.9. No relationship between FeV content and lattice parameter is observed. While the lattice gradually shrinks between x = 0 and x = 0.45 from a = 3.0308(3) Å to a = 3.0214(2) Å, an expansion is observed between x = 0.6 to x = 0.9 from 3.0297(3) Å to 3.0305(2) Å, respectively. For refinement of the patterns, the body-centred cubic vanadium phase (Im-3m) was taken. However, for samples with x = 0.15 and x = 0.3 a satisfying fit could only be achieved if an additional body-centred cubic Fe phase was included in the fit. No pure iron agglomerates are observed by SEM, suggesting these BCC Fe clusters to be too small to be detected as separate entities by SEM.

In Figure 4.2.2.2-3 pressure-composition isotherms after substitution of different (V + Fe) fractions by FeV are presented. Table F-1 in the appendix summarizes a list of selected material properties.

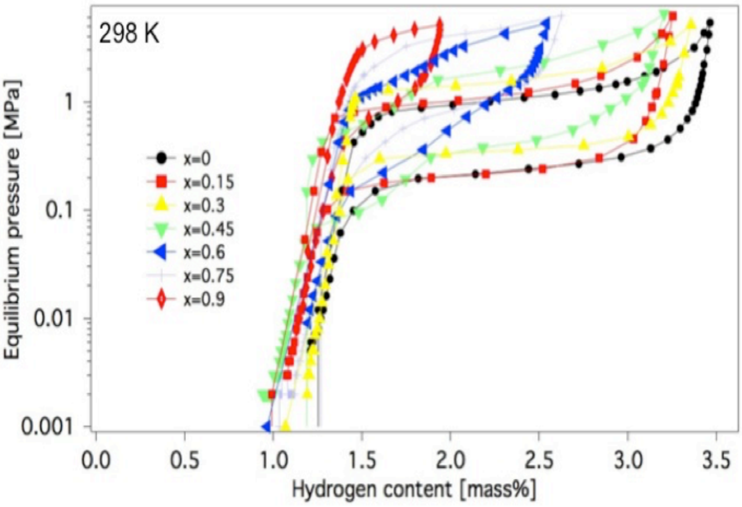

Figure 4.2.2.2-3: Pressure-composition isotherms of $V_{(40-40\bullet x)}Fe_{(8-8\bullet x)}Ti_{26}Cr_{26}(FeV)_{(48\bullet x)}$ with x = 0, 0.15, 0.3, 0.45, 0.6, 0.75 and 0.9 at 298 K.

The substitution of V and Fe by FeV raises the equilibrium plateau pressure of dihydride formation/dissociation from p_f = 1.2 MPa to 5.0 MPa at x = 0 and 0.9, respectively. The dissociation pressure is also raised from p_d = 0.2 MPa to 1.0 MPa. Both formation and dissociation pressure are raised in equal portions, resulting in approximately constant hysteresis factors irrespective of the FeV content.

The capacities of monohydride formation are largely unaffected by the addition of FeV. For all systems studied in this work, the phase transformations from solid solution to monohydride are complete between 1.0 and 1.2 mass% H. No correlation is observed between FeV and hydrogen content of the phase boundary of the solid solution/monohydride two-phase region. Several impurities such as Al, Si or O are introduced into the alloy by the substitution of V by FeV. It has been reported that these impurities can destabilize the hydride and thus raise the plateau pressure [16], [198], [199]: the observation that the capacity of the monohydride is less affected by impurities than the capacity of dihydride suggests that the impurity effect is more pronounced for those interstitial sites filled by hydrogen atoms during the formation of the dihydride. Site occupation of hydrogen atoms in the monohydride phase of BCC solid solutions has been shown to depend strongly on alloy composition, and shifts from occupation of octahedral O_z sites to occupation of tetrahedral T sites after substituting V with elements such as Cr or Al [174], [176]. Both elements are also present in the alloys studied in this work. Due to the small amount of impurity atoms in relation to the available sites, the capacity is unaffected. In contrast, the capacity of dihydride formation gradually decreases with FeV content at the given temperature, indicating a stronger impurity effect on the sites occupied by H atoms during dihydride formation. The addition of FeV to the system raises the plateau pressure of dihydride formation (p_f) and dissociation (p_d) from p_f = 1.15 MPa and p_d = 0.24 MPa to p_f = 6.0 MPa and p_d = 1 MPa from x = 0 and x = 0.9, respectively, at 298 K. The pressure plateaux become increasingly sloping at higher FeV contents, with sloping factors increasing from S = 0.6 to S = 5.2 when the FeV content is raised from x = 0 to x = 0.9. Sloping pressure plateau~~x~~ have been attributed to inhomogeneity in an alloy or intermetallic compound [114]. The interstitial sites occupied by H are neighbours to a variation of atomic species, resulting in a broader distribution of occupation energies of the hydrogen atoms in the interstitial sites within the material.

In order to investigate the effect of (V + Fe) substitution by FeV on the cyclic stability, the materials with x = 0.3, 0.6 and 0.9 were subjected to 50 pressure-swing cycles. Pressure-composition isotherms of the 52nd cycle are presented in Figure 4.2.2.2-4.

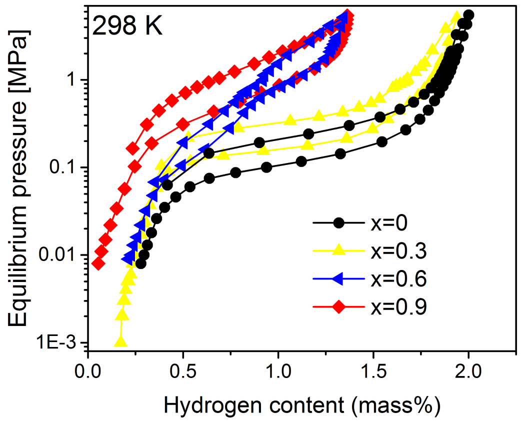

Figure 4.2.2.2-4: Pressure-composition isotherms of $V_{(40-40\cdot x)}Fe_{(8-8\cdot x)}Ti_{26}Cr_{26}(FeV)_{(48\cdot x)}$ with x = 0, 0.3, 0.6 and 0.9 at 298 K after 50 pressure-swing cycles during the 52nd cycle.

At x = 0.3 the capacity decays from 2.1 mass% during the first to 1.6 mass% after 50 cycles, corresponding to a similar degradation of 23 % as compared to the high-purity sample (x = 0). A decrease of pressure hysteresis is observed for all samples. Thermodynamic properties with the highest degree of (V + Fe) substitution (x = 0.9) were investigated in more detail. This is shown in Figure 4.2.2.2-5.

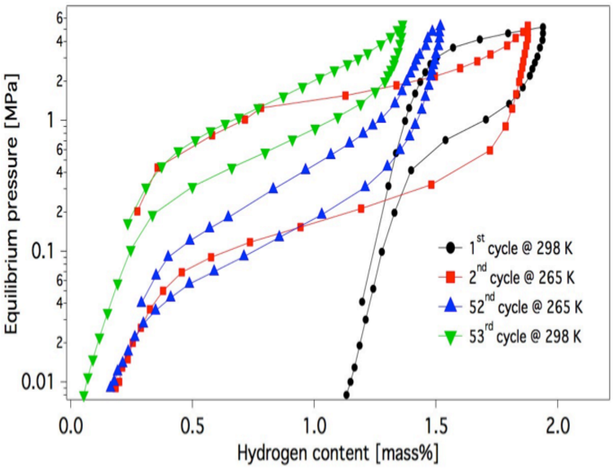

Figure 4.2.2.2-5: Thermodynamic properties of $V_{(40-40\cdot x)}Fe_{(8-8\cdot x)}Ti_{26}Cr_{26}(FeV)_{(48\cdot x)}$ with x = 0.9.

During the second cycle at 265 K the reversible capacity amounts to 1.6 mass%, as compared to 0.7 mass% during the first cycle. This suggests that the material was not hydrogenated completely during the first absorption at 298 K and 6 MPa. Upon prolonged cycling, the capacity is reduced from 1.6 to 1.3 mass% at 265 K or 1.2 mass% at 298 K, corresponding to a degradation of 19%. Plateau slope increases from 4.4 to 5.3 after 50 cycles and the hysteresis factor is reduced from 5 to 2. Therefore, even with a FeV content of x = 0.9, material properties change in a similar manner as with lower FeV contents (0 or 0.3). The lower overall and reversible hydrogen content of the systems containing higher fractions of FeV are most likely caused by the introduction of impurities such as Al, Si, N or O into the alloy.

Microstructural changes occurring upon cycling were also investigated. XRD patterns of the materials containing varying levels of FeV were recorded after 50 cycles and are shown in Figure 4.2.2.2-6.

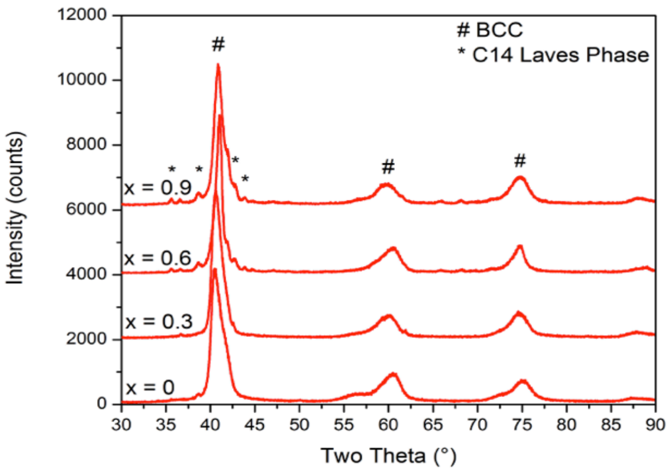

Figure 4.2.2.2-6: XRD patterns of $V_{(40-40x)}Fe_{(8-8x)}Ti_{26}Cr_{26}(FeV)_{48x}$ with x = 0, 0.3, 0.6, 0.9 after 50 pressure-swing cycles. Patterns were collected after dehydrogenation to < 0.01 MPa at 298 K.

The samples show a BCC crystal structure in the monohydrided state after 50 cycles. This suggests that H atoms occupy the T sites in that state [176]. The cubic lattice is distorted considerably after 50 cycles. XRD peaks become asymmetric, with the (110) peak broadening towards higher angles, and the broadening of the 200 and 211 peaks being more pronounced in the reverse direction. A similar phenomenon was observed by Itoh *et al*. and was ascribed to the formation of a secondary phase [233]. It is believed that this secondary phase forms during extended cycling and does not absorb hydrogen anymore. According to the authors, the formation of this phase contributes to the capacity decay [233].

In order to quantitatively describe the broadening of the XRD peaks, the Full Width at Half Maximum (FWHM) of the (110) peak before and after cycling were determined. Results are presented in Table 4.2.2.2-1.

X-value	FWHM annealed [°]	FWHM 50 cycles [°]
0	0.315	1.579
0.15	0.463	-
0.3	0.463	1.321
0.45	0.508	-
0.6	0.522	1.190
0.75	0.565	-
0.9	0.574	1.137

Table 4.2.2.2-1: Crystallographic data of annealed and cycled $V_{(40-40\bullet x)}Fe_{(8-8\bullet x)}Ti_{26}Cr_{26}(FeV)_{(48\bullet x)}$ with x = 0, 0.15, 0.3, 0.45, 0.6, 0.75 and 0.9.

Before cycling, the FWHM increases with FeV content. This is in agreement with the results obtained by Dou *et al.* [197], and may be caused by either of the reasons for peak broadening mentioned above. As can be expected and is also determined by SEM-EDX, the fraction of impurities (Al, Si, O, N, C) increases with the level of FeV substitution x. The increase of the FWHM value correlates well with x, which would indicate a relationship between the two parameters. However, it is also possible that the FWHM is also caused by a reduction of the crystallite size. Since no satisfying Rietveld refinements or Williamson-Hall-plots could be achieved with the patterns, it is impossible to clearly identify the cause of the peak broadening.

The cycling results include one more point which has not yet been highlighted before. After 50 cycles, the FWHM of the material with x = 0 increases from 0.315 ° to 1.579 °. At x = 0.9 the increase is less pronounced, from 0.574 ° to 1.137 °, resulting in a lower FWHM value for the material with a high level of (V + Fe) substitution than the material obtained using high purity V. This effect may originate from the following explanation: the materials with a high degree of (V + Fe) substitution show a reduced reversible capacity as compared to the materials synthesized with high-purity V. During cycling of the high-purity V material, a higher fraction of interstitial sites are subjected to hydrogen atoms cyclically diffusing in and out, resulting in the accumulation of dislocations, strain, and microstress. As for the (V + Fe)-substituted material, a smaller fraction of interstitial sites are subjected to H atoms diffusing in and out, and are thus largely unaffected by the hydrogen-induced effects, which would otherwise result in a broadening of the diffraction peaks. Consequently, the FWHM values for the FeV-substituted materials do not increase as sharply as compared to those with no or a lower level of substitution.

In summary, the substitution of (V + Fe) with FeV 1 has the effect of increasing the plateau pressure and plateau slope and reducing the reversible capacity of the dihydride. Based on these results, FeV 2 provided by Gesellschaft für Elektrometallurgie mbH, which has a different composition, was tested. It contains a lower fraction of Al (2 at%) and Si (< 1 at%), however, the concentration of O is higher compared to FeV 1 (around 7400 mass ppm). The concentrations of the remaining impurities are comparable for both FeV materials.

In Figure 4.2.2.2-7 the SEM micrograph of $V_{40}Fe_8Ti_{26}Cr_{26}$ synthesized with full substitution of (V + Fe) by FeV 2 is presented. In a first attempt, the materials were synthesized without deoxidizing agent.

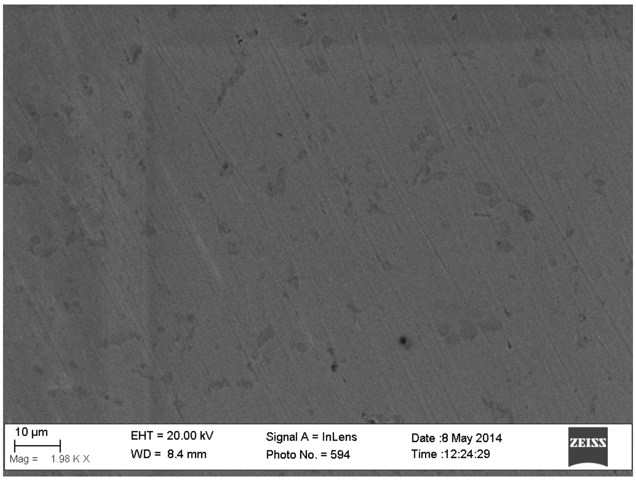

Figure 4.2.2.2-7: SEM micrograph of $V_{40}Fe_8Ti_{26}Cr_{26}$ synthesized with 100 % FeV.

Similar to the material substituted with FeV 1, three phases of differing compositions are observed. The V BCC phase close to the target composition is the prevalent one. The compositions of the secondary phases (C14 Laves phase, α-Ti) are similar to the compositions of the secondary phases observed in the materials prepared with FeV 1. The detailed compositions are listed in Table E-3 in the appendix.

In Figure 4.2.2.2-8 the XRD pattern of $V_{40}Fe_8Ti_{26}Cr_{26}$ after substitution of high-purity V and Fe with FeV 2 is presented.

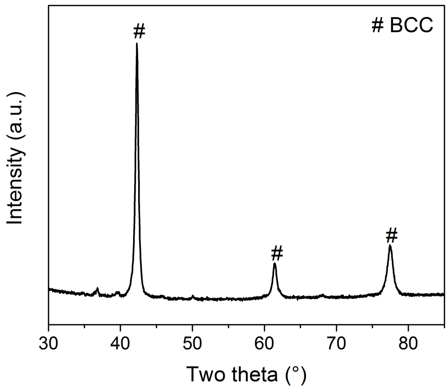

Figure 4.2.2.2-8: XRD pattern of $V_{40}Fe_8Ti_{26}Cr_{26}$ after substitution of (V + Fe) with FeV 2 in the as-cast state.

The sample shows a BCC structure with minor amounts of secondary phases. The non-BCC peaks can be assigned to the C14 Laves phase and ceramic impurities from the mortar that was used to crush the sample into a powder. A lattice parameter of 3.0108(4) Å is measured, which is slightly reduced by 0.02 Å as compared to the material with highest content of FeV 1 (x = 0.9). A sample prepared with high-purity V and Fe was also measured. The lattice parameter is 3.0224(1) Å, which is in good agreement with the lattice parameter of the same material prepared before the annealing treatment (lattice parameter of 3.0223(2) Å).

In Figure 4.2.2.2-9 pressure-composition isotherms of $V_{40}Fe_8Ti_{26}Cr_{26}$ prepared with high-purity V and Fe or with FeV 2 are presented.

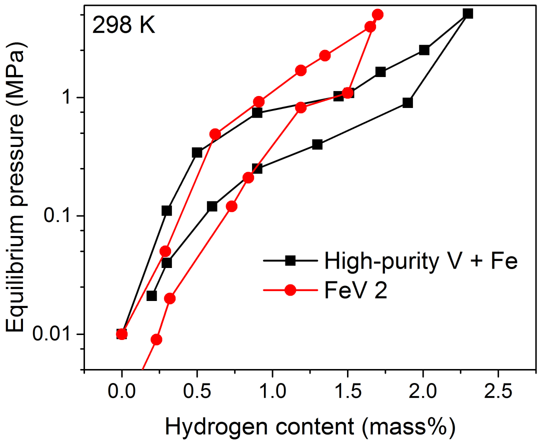

Figure 4.2.2.2-9: Pressure-composition isotherms of $V_{40}Fe_8Ti_{26}Cr_{26}$ at 298 K after 10 activation cycles prepared with high-purity V and Fe and after substitution of V and Fe with FeV 2.

Substitution of V and Fe with FeV 2 leads to an increase of hydride formation and dissociation equilibrium pressures from 0.8 MPa to 1.3 MPa for hydride formation and from 0.4 MPa to 0.8 MPa for hydride dissociation, respectively. The reversible capacity decreases from 2.3 mass% for the high-purity material to 1.7 mass% for the material prepared with FeV 2. The material shows a total capacity of 2.3 mass%, and the initial absorption is shown in Fig. F-3 in the appendix.

By cross-linking the SEM, XRD and PCI results of V and Fe substitution with FeV 2 and comparing them to the results obtained for FeV 1, the substitutional effects of the two ferrovanadium compositions can be concluded. Substitutional effects of FeV 2 are less pronounced than in the case of FeV 1. The microstructure is less affected when FeV 2 is used as compared to FeV 1. A lower fraction of secondary phases is formed. Significant fractions of secondary phases are found in the FeV 1-substituted samples at substitution levels of $x \geq 0.6$. The fully FeV 2-substituted material shows a much lower fraction of secondary phases. Additionally, hydrogen capacity and equilibrium pressures of hydride formation and dissociation are less affected when V and Fe are substituted by FeV 2 as compared to FeV 1. Therefore, FeV 2 is used for further investigations of low-cost V-Ti-based solid solution alloys based on FeV. This will be continued in chapter 4.2.2.4.

4.2.2.3 Substitution of titanium with Ti sponge

Ti was also identified as an expensive element in V-Ti-based solid solutions. On the search for cheaper alternatives, Ti sponge was identified as a possible low-purity raw material.

The fully Ti-substituted hydrogen storage material shows similar microstructural and thermodynamic properties as the storage material synthesized with high-purity Ti. In Figure 4.2.2.3-1 the SEM micrograph of $V_{40}Fe_8Ti_{26}Cr_{26}$ after substituting high-purity V with Ti sponge is presented.

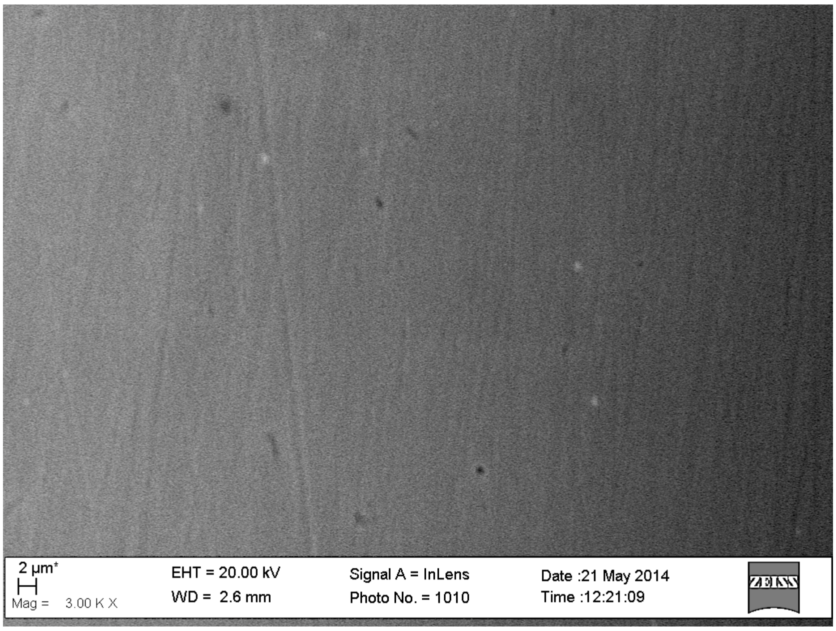

Figure 4.2.2.3-1: SEM micrograph of $V_{40}Fe_8Ti_{26}Cr_{26}$ synthsized with Ti sponge.

Two distinct phases are observed in the alloy synthesized using Ti sponge. The prevalent phase is the BCC main phase with a composition close to the target composition. A secondary phase is visible in the form of dark areas distributed within the main phase, which has a similar composition as the C14 Laves phase identified in other alloys by XRD. The fraction of this phase is in a similar range as in the case of the materials synthesized with high-purity Ti. The detailed compositions are listed in Table E-4 in the appendix.

Figure 4.2.2.3-2 shows the XRD pattern of $V_{40}Fe_8Ti_{26}Cr_{26}$ after substitution of Ti with Ti sponge.

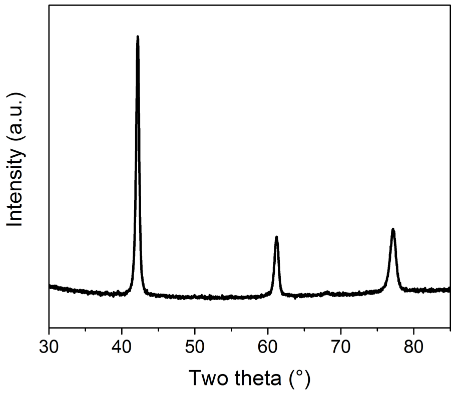

Figure 4.2.2.3-2: XRD pattern of $V_{40}Fe_8Ti_{26}Cr_{26}$ with substitution of Ti with Ti sponge.

The pattern shows a single BCC phase with a lattice parameter of 3.0268(1) Å. This is in the range of the sample prepared with high-purity Ti. A lattice parameter of 3.0224(1) Å is measured in that case.

Pressure-composition isotherms of the material prepared with Ti sponge are presented in Figure 4.2.2.3-3. PCI curves of the high-purity sample are also included as a reference.

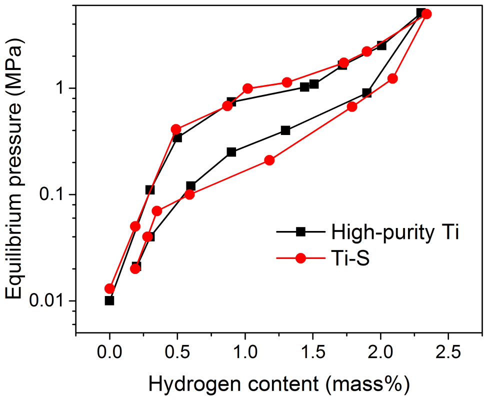

Figure 4.2.2.3-3: Pressure-composition isotherms of $V_{40}Fe_8Ti_{26}Cr_{26}$ prepared with high-purity Ti and after substitution with Ti sponge.

Both samples exhibit a reversible capacity of 2.3 mass% and comparable thermodynamic properties. The initial absorption is also shown in Fig. F-3 in the appendix. A total capacity of 3.5 mass% H is measured for both samples.

In conclusion, the replacement of high-purity Ti with cheaper Ti sponge is reported in this chapter for the first time. The experimental results gathered here indicate that replacing high-purity Ti with Ti sponge has negligible effects on the microstructure and sorption properties of the obtained storage material. Hence, Ti sponge appears to be a viable alternative for the more costly, highly purified Ti.

4.2.2.4 Substitution of V and Ti with FeV and Ti-sponge

With the combined results from sections 4.2.2.2 and 4.2.2.3, high-purity V, Fe and Ti were substituted with FeV 2 and Ti sponge. One at% mischmetal (Mm) was added for deoxidization. Three samples were synthesized at varying arc melting currents in order to investigate the effect of the preparation conditions on the microstructure and sorption properties of the resulting alloys. One sample was melted at the same conditions that were applied for the synthesis of the materials investigated in the previous chapters (450 A). Arc melting currents of 400 A and 500 A were tested in order to investigate if the current has an effect on the structural, compositional and hydrogen sorption characteristics.

In Figure 4.2.2.4-1 the SEM micrographs are presented of $V_{40}Fe_8Ti_{26}Cr_{26}$ prepared with FeV 2, Ti sponge and 1 at% Mm at arc melting currents of 400 A and 500 A. The detailed compositions as determined by SEM-EDX and ICP-OES are listed in Table E-5 and Table E-6 in the appendix.

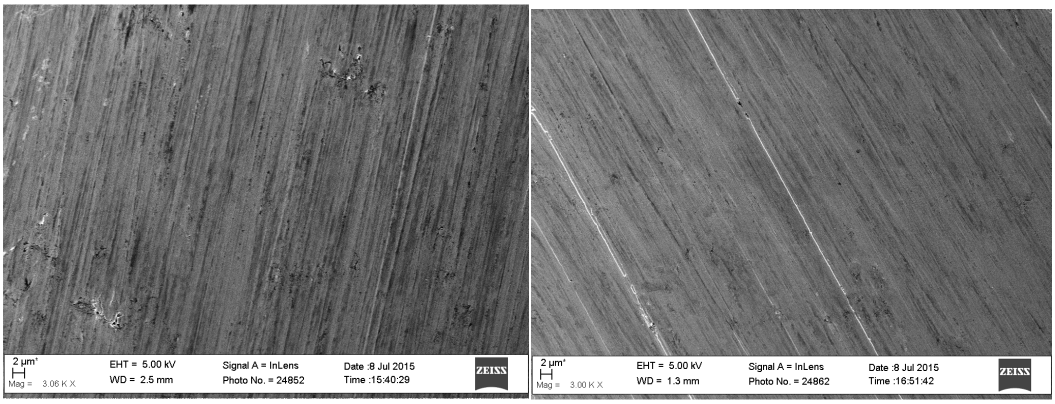

Figure 4.2.2.4-1: SEM micrographs of $V_{40}Fe_8Ti_{26}Cr_{26}$ prepared with FeV 2, Ti sponge and 1 at% Mm melted at arc melting currents of 400 A (left) and 500 A (right).

The BCC phase is the predominant phase. Small amounts of secondary phases with a similar composition to the C14 Laves phase are visible. The average composition of all three alloys is close to the target values of $V_{40}Fe_8Ti_{26}Cr_{26}$ when omitting impurities such as Al, Si or O, which are present in minor amounts.

In Figure 4.2.2.4-2 XRD patterns of $V_{40}Fe_8Ti_{26}Cr_{26}$ prepared with FeV 2, Ti sponge and 1 at% Mm at arc melting currents of 400 A, 450 A and 500 A are presented.

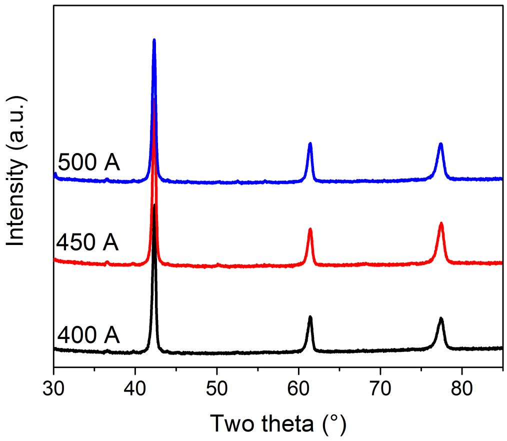

Figure 4.2.2.4-2: XRD patterns of $V_{40}Fe_8Ti_{26}Cr_{26}$ prepared with FeV 2, Ti sponge and 1 at% Mm melted at arc melting currents of 400 A, 450 A and 500 A.

All samples show a single phase BCC structure. Minor impurity peaks are detected, which are assigned to SiO_2 that was introduced in minor amount during the pulverization of the as-casted alloys. In Table 4.2.2.4-1 the crystallographic data of the alloys is summarized.

Arc melter current	400 A	450 A	500 A
Lattice parameter	3.0229(1) Å	3.0225(1) Å	3.0237(1) Å
R_{wp}	3.829 %	3.358 %	3.337 %

Table 4.2.2.4-1: Crystallographic data of $V_{40}Fe_8Ti_{26}Cr_{26}$ prepared with FeV 2, Ti sponge and 1 at% Mm prepared at arc melting currents of 400 A, 450 A and 500 A.

All lattice parameters are in a similar range and close to the value that is measured in the case of the sample prepared with high-purity V, Fe and Ti (3.0224(1) Å). No relationship between arc melting current and lattice parameter is observed. This is in line with SEM observations, where a small amount of secondary phase is observed.

The initial hydrogen absorption of the samples prepared at varying arc melting currents is shown in Figure 4.2.2.4-3.

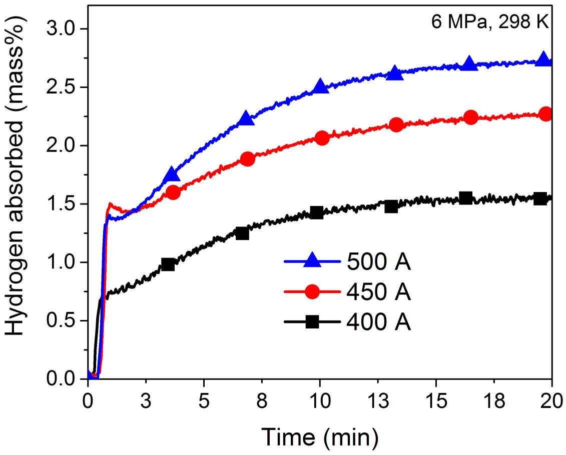

Figure 4.2.2.4-3: Initial hydrogen absorption of $V_{40}Fe_8Ti_{26}Cr_{26}$ prepared with FeV 2, Ti sponge and 1 at% Mm prepared at arc melting currents of 400 A, 450 A and 500 A.

All three samples readily react with hydrogen after flushing with Ar and a short evacuation at 298 K. The total hydrogen capacities differ among the samples, and 1.6 mass%, 2.3 mass% and 2.8 mass% H are absorbed after melting the alloys at currents of 400 A, 450 A, and 500 A, respectively. A relationship exists between arc melting current and total capacity, and a higher current is beneficial to achieve a higher capacity.

The materials were subjected to 15 pressure-swing cycles at room temperature. Subsequently, the pressure-composition isotherms were measured. Results are presented in Figure 4.2.2.4-4

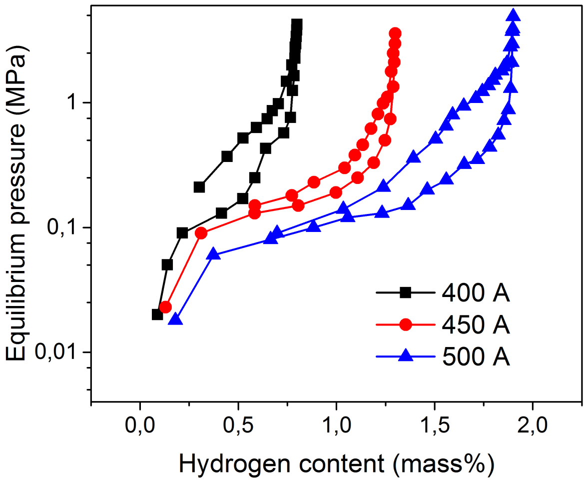

Figure 4.2.2.4-4: Pressure-composition isotherms of $V_{40}Fe_8Ti_{26}Cr_{26}$ prepared with FeV 2, Ti sponge and 1 at% Mm prepared at arc melting currents of 400 A, 450 A and 500 A after 15 cycles at 303 K.

The reversible capacity, which is useful during the formation and dissociation of the dihydride, increases with higher arc melting current. The highest capacity of 1.6 mass% is observed for the material melted at 500 A, the lowest capacity of approximately 0.6 mass% is measured in the case of the material melted at 400 A. The flatness of the pressure plateaux improves at higher arc melting currents. With a sloping factor of 1.3 the plateau of hydride formation is most sloping at a melting current of 400 A. Hydride dissociation occurs in two distinct desorption steps, with a first plateau at around 7 MPa and a second one around 1.5 MPa. A mean sloping factor of 1.3 is determined for the complete hydride dissociation process between 0.7 MPa and 0.1 MPa. At arc melting currents of 450 A (0.1) and 500 A (0.09), both hydride formation and dissociation plateaux are flatter as compared to the material melted at 400 A. The sloping factors for hydride dissociation decreases to 0.1 or 0.9 after melting at 450 A or 500 A, respectively.

In order to elucidate the reasons for this relationship, the as-casted alloys are tested upon their content of O, C and N impurities. The results are presented in the following Figure 4.2.2.4-5.

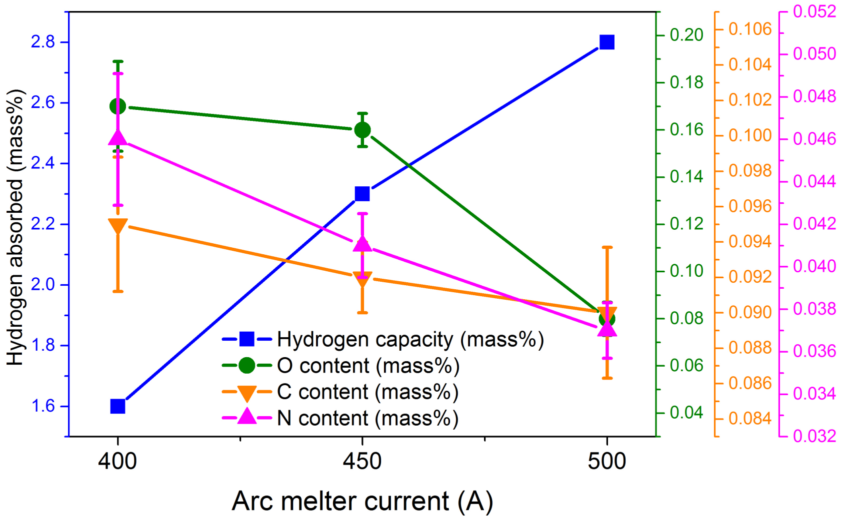

Figure 4.2.2.4-5: Total hydrogen capacity and O, C and N content of $V_{40}Fe_8Ti_{26}Cr_{26}$ synthesized with FeV2, Ti sponge and 1 at% Mm as a function of arc melting current.

After melting at higher current, the content of the impurities O, C and N decreases. An oxygen content of 0.17 mass% is measured after melting at a current of 400 A. This value is below the oxygen concentration of the high-oxygen sample (0.515 mass% O) investigated in chapter 4.2.2.1, but higher than the value of the low-oxygen (0.045 mass% O) or deoxidized (0.069 mass% O) samples. Hence, a partial deoxidization is achieved through the addition of Mm at the applied current. The oxygen content decreases to 0.08 mass% O if a current of 500 A is applied, which is in the range of the low-oxygen and deoxidized alloys investigated in chapter 4.2.2.1. No formation of α-Ti is observed for any of the samples, which indicates that a higher oxygen concentration is necessary for this phase to form.

The concentrations of C and N also decrease from 0.095 mass% C to 0.090 mass% C and from 0.046 mass% N to 0.036 mass% N at melting currents of 400 A or 500 A, respectively. It is likely that light impurity atoms such as O, C and N evaporate during the melting process. A higher arc melting current leads to a higher temperature of the melt, which causes the evaporation of light-weighted elements or of elements which exhibit high vapor pressures at lower temperatures. The concentrations of V, Fe, Ti and Cr are not affected by the variation of arc melting currents (Table E-5 and Table E-6). Therefore, it is exclusively the light-weighted impurities that evaporate during melting. Variation of the arc melting current is therefore a viable and easy strategy to reduce the level of impurities. Similar reports on the removal of metallic or non-metallic impurities have been reported before for other metals [243–245]. However, this study represents the first systematic investigation of the influence of the arc melting conditions on the content of impurities in the resulting alloys. A relationship between the impurity content and the hydrogenation properties of the storage materials is also observed, and the results indicate that repeated melting at elevated current is beneficial for the hydrogen storage properties (i.e., hydrogen capacity and thermodynamic properties of the metal hydrides).

The total hydrogen capacity of the materials prepared in this work are slightly below the capacities of other FeV-based H storage materials reported e.g. by Yan *et al.* [193] or Wu *et al.* [190], who measured total capacities of 3.6 mass% H. However, these authors did not report detailed melting procedures.

It is possible that a higher capacity of the FeV-based materials can be achieved through repeated arc melting steps at high melting current and at low pressures above the melt. However, if such procedures are applied, the energetic (and resulting economic) advantages of FeV as compared to pure V and Fe are less pronounced. Another strategy to further reduce the content of impurities in the storage alloys would be to melt the raw metals in an atmosphere composed of Ar blended with H_2 gas instead of pure Ar. This has been shown to further reduce the content of non-metallic impurities [243], but also has a negative effect on the synthesis cost.

The long-term cyclic stability over 1000 hydrogenation cycles of the materials prepared with high-purity and with low-purity raw metals was also investigated, in that case in cooperation with the German Aerospace Institute (DLR) in Stuttgart. Although the evaluation of the experiments could not be completed before the submission of this thesis, a decrease of the hydrogen storage capacity could be observed for the first 100 cycles. After that, the capacity decay was less pronounced.

In the next chapter, the relationships between the type of raw material, the price of the resulting storage alloy and the economic and environmental effects of the respective raw materials are discussed in more detail.

4.2.2.5 Economic impact of (V+Fe) and Ti substitution by FeV and Ti sponge

In order to assess the cost reduction achieved by substituting V+Fe by FeV and high-purity Ti by sponge, the cost of storing 100 kg of hydrogen in the material prepared with high-purity V and Fe is compared to the material prepared with x = 0.9 FeV 1. The raw materials and respective cost used in the alloy are V 390 US $/kg, FeV 30 US $/kg, Fe 2 US $/kg, Ti 25 US $/kg and Cr 15 US $/kg [15]. For the calculation, the reversible capacity after 50 cycles is taken (1.7 and 1.2 mass% for x = 0 or x = 0.9). Storing 100 kg of H in the unsubstituted material requires 5882 kg of metal hydride. The necessary metal hydride would cost approximately 978130 US $. At x = 0.9, the raw material cost for storing 100 kg H would be reduced to 325000 US $/kg. Therefore, after taking into account the reduced capacity of the FeV 1-substituted material, the overall raw material cost can be reduced to approximately 1/3 of the high-purity reference material.

Under the assumption that the cost of FeV 2 is equal to the cost of FeV 1, the same calculation can be performed for the material prepared with FeV 2, Ti sponge (10 US $/kg) and Mm (12 US $/kg). The reversible capacity after 20 cycles is taken for the cost analysis (1.6 mass%). Storing 100 kg of hydrogen requires 6163 kg of storage alloy. The respective storage material costs 116477 US $, which is around 1/3 of the price of the material substituted with FeV 1 (x = 0.9). This difference originates in the higher storage capacity of the material substituted by FeV 2, the complete level of substitution (10 % pure V and Fe are still contained in the FeV 1-substituted material), and the substitution of pure Ti with Ti sponge. Mm accounts to 2 % of the storage alloy cost (2219 US $ for 185 kg).

The FeV 2- and Ti sponge-substituted material is therefore considerably cheaper than the AB_2- and AB_5-based hydrogen storage alloys $LaNi_5$ (431430 US $/100 kg H_2) and Hydralloy C (323600 US $/100 kg H_2) and in the range of the TiFe-based storage material $TiFe_{0.7}Mn_{0.3}$ (81300 US $/100 kg H_2).

4.3 *Gas-phase impurity effects*

In the following chapter the focus shifts from impurities contained in the bulk of the materials to impurities reacting on or with the surface of the storage materials. These investigations are relevant with respect to practical applications of hydrogen storage alloys, because "technical" hydrogen is usually not of highest purity, but may contain impurities, which interact with the storage material.

4.3.1 *Reactions of organic liquids on metal hydride surfaces*

First, the reactions of the organic liquids acetone and toluene on the surface of AB-, AB_2- and AB_5-type metal hydrides TiFe, $Ti_{0.95}Zr_{0.05}Mn_{1.49}V_{0.45}Fe_{0.06}$ ("Hydralloy C5") and $LaNi_5$ and $V_{40}Fe_8Ti_{26}Cr_{26}$ were investigated. These materials were chosen because of their practical and commercial relevance and favorable thermodynamic and kinetic properties with respect to the LORC process. Toluene and acetone were chosen as model organic substances, because toluene is inherently present as an impurity in the LORC process, and acetone is known to passivate the surface of V-Ti-based solid solution alloys. Hence, it is important to understand the interactions and reaction mechanisms of these two organics on the surfaces of intermetallic hydrides.

Throughout this chapter, the samples are named according to the type of hydrogen storage material and the pretreatment of the respective sample before the experiments. $LaNi_5$, $Ti_{0.95}Zr_{0.05}Mn_{1.49}V_{0.45}Fe_{0.06}$ and TiFe are respectively abbreviated as "AB_5", "AB_2" and "AB". $V_{40}Fe_8Ti_{26}Cr_{26}$ is referred to as "BCC". In order to clarify the pretreatment, "-H" is added to refer to a hydrogenated sample. To indicate which of the organic liquids has been used during the pretreatment, "ace" is added for acetone or "tol" for toluene. A thermal desorption is abbreviated as "des". For example, toluene-treated and subsequently thermally desorbed $V_{40}Fe_8Ti_{26}Cr_{26}$ is abbreviated as "BCC-H-tol-des".

A storage material utilized in the LORC process desribed above is likely to come into contact with small levels of gaseous impurities, particularly toluene. Additionally, gases such as O_2, N_2 or CO_2 may enter the H storage system through leakages or as a result of the reactivation of the dehydrogenation catalyst. Hence, it is important to know about the effects of these impurities on the kinetics and capacity of the metal hydrides.

In order to investigate whether hydrogen is confined in the storage materials after dispersion of the hydrogenated samples in the organic liquids, XRD investigations were performed. Several authors have reported that hydrogenation of AB_5, AB and BCC causes structural changes in the respective materials [16], [140], [141], [157], [158], [189], [246]. In the case of AB_2-type hydrogen storage materials ($Ti_{0.95}Zr_{0.05}Mn_{1.49}V_{0.45}Fe_{0.06}$ falls in that class) lattice expansion is observed upon insertion of H atoms without further structural changes [154]. This results in a significant peak shift of the hydride XRD pattern as compared to the dehydrogenated material. Hence, if the hydrides are maintained at ambient conditions or after acetone/toluene treatment either distinct reflections of the hydride phase or a peak shift should be observed in the XRD patterns of our samples. In the other case, the absence of such modifications would indicate that hydrogen has desorbed from the samples.

In Figure 4.3.1-1, XRD patterns of the acetone- or toluene-treated samples are presented. Reference patterns of samples, which were hydrogenated and subsequently desorbed at ambient temperature and pressure conditions, are also included. The crystallographic parameters are summarized and discussed in Table G-2 in the appendix.

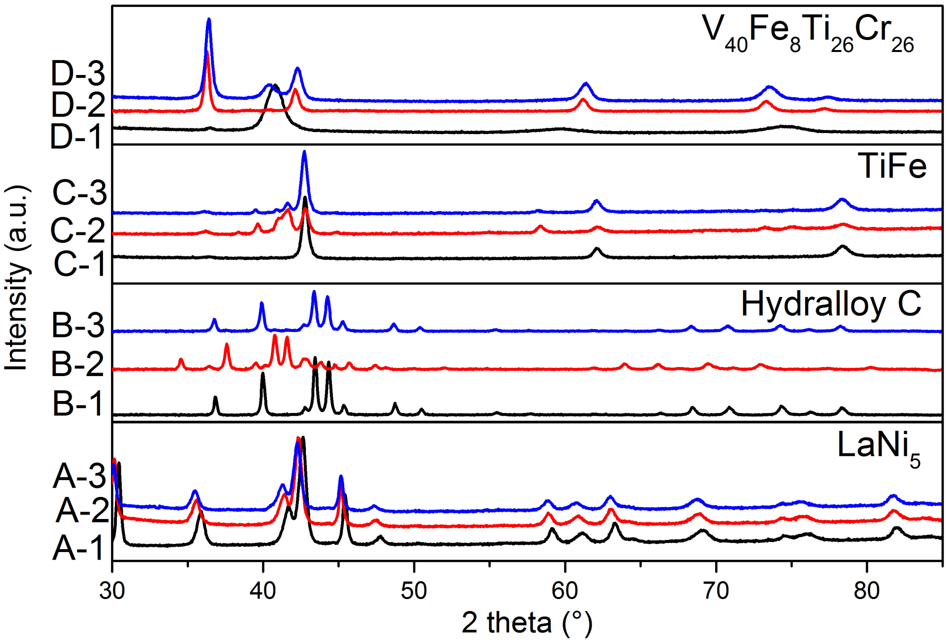

Figure 4.3.1-1: XRD patterns of AB_5-H (A), AB_2-H (B), AB-H (C) and BCC-H (D) after desorption at ambient temperature and 1 bar (-1), or acetone treatment (-2) or toluene treatment (-3).

In agreement with equilibrium properties of AB_5-H (p_d = 0.2 MPa), no hydride phase peaks are observed after desorption at ambient temperature and pressure. Also after acetone/toluene treatment, no peaks of the hydride phase are evident. The patterns of the acetone- or toluene-treated samples exhibit a small peak shift towards lower angles, which suggests that minor amounts of hydrogen are still dissolved.

The diffraction patterns of AB_2-H desorbed at ambient conditions and AB_2-H-tol are identical. This indicates that equal amounts of hydrogen are desorbed from both materials either after desorption in Ar atmosphere or when immersed in toluene. After treatment with acetone (AB_2-H-ace), a considerable peak shift by 3° towards lower angle is observed. Two phases (77 ± 2 % hydride phase, 23 ± 2 % dehydrogenated phase, see Table G-2) are evident in the pattern. AB_2 shows an orthorhombic structure (space group $P6_3/mmc$) irrespective of the pretreatment. The considerable peak shift observed after hydrogenation is in agreement with a previous report by Chao *et al.*, who observe a 3 ° shift (Cu-kα radiation) of a hydrogenated Zr-based multiphase AB_2-type alloy towards lower angles [154]. XRD of the Hydralloy C5 hydride has, to the best of our knowledge, not been reported yet. Isotropic lattice expansion by 6 % in both a- and c-direction is observed.

The body-centered cubic structure is observed in the patterns of both AB and AB-H desorbed at ambient conditions. Distinct peaks, which can be attributed to the orthorhombic hydride phase [157], [158], are visible for both AB-H-ace and AB-H-tol. 69 ± 2 % and 20 ± 2 % TiFeH are quantified by Rietveld analysis in these samples, respectively (Table G-2).

BCC shows a body-centered cubic structure in the as-cast state and a distorted body-centered cubic structure for BCC-H desorbed at ambient conditions. A small peak, which is ascribed to the face-centered cubic (FCC) dihydride phase, is also observed in the case of BCC-H. Acetone treatment is effective in confining hydrogen inside the material, and 100 % FCC dihydride phase is found in the case of BCC-H-ace. The crystal structure of the dihydride phase is in agreement with previous reports on similar materials [16], [85], [189]. 82 ± 2 % FCC dihydride and 18 ± 2 % monohydride phase are quantified in BCC-H-tol (Table G-2).

In order to study the long-term passivation behavior of BCC-H, XRD patterns of BCC-H-ace and BCC-H-tol were collected after different times after the deactivation treatment and storage in a glove box. Results are shown in Figures G-2 and G-3 in the Appendix. The hydrides are stable for several weeks, which indicates that the passivation treatment is effective in containing the atomic hydrogen within the samples for extended time periods.

Combined TG-DSC-MS measurements were performed to 1) identify the products of the passivation reactions, which were adsorbed at the surface of the metal hydride alloys after acetone or toluene treatment, and 2) investigate the desorption behavior during thermal treatment of the deactivated samples. Figure 4.3.1-2 shows the TG-DSC-MS curves of AB-H-ace and AB_2-H-ace.

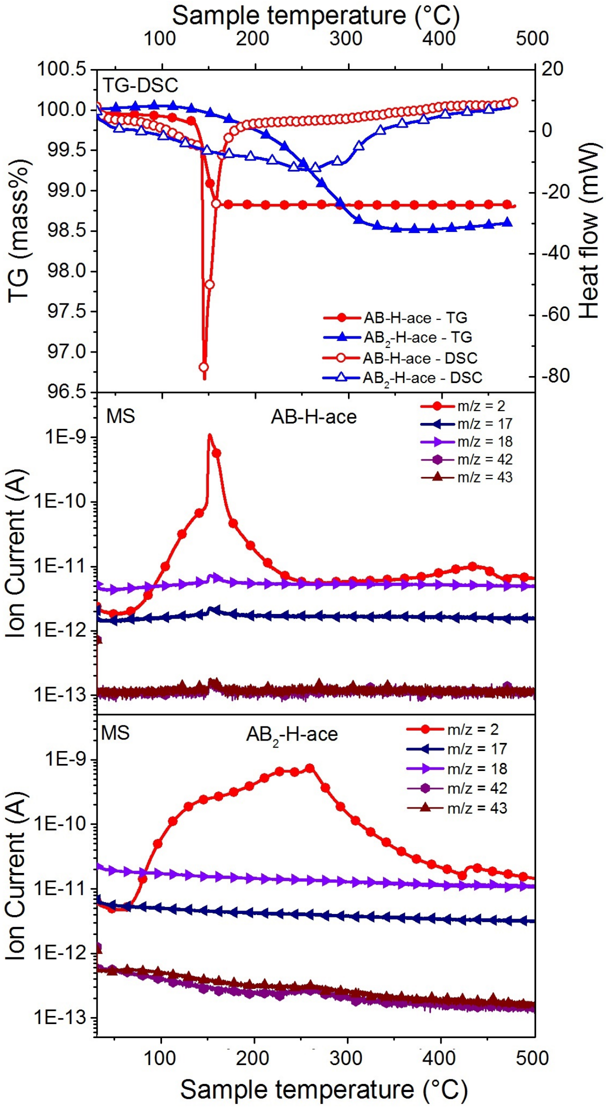

Figure 4.3.1-2. TG-DSC-MS curves of thermal desorption of AB-H-ace and AB_2-H-ace.

Weight loss of AB-H-ace starts at a temperature of about 80 °C. The main contribution stems from hydrogen (m/z = 2), which is clearly detected by MS. Intense weight loss is observed at 145 °C and a strong endothermal DSC peak is recorded simultaneously. This event is accompanied by the detection of hydrogen, a small amount of water (m/z = 17, 18) and a trace amount of acetone (m/z = 42, 43). No further significant mass loss or thermal events are observed in the TG-DSC curves when the temperature reaches 160 °C. 1.2 mass% are released from the sample.

The desorption behavior of AB_2-H-ace differs from that of AB-H-ace. Mass loss occurs over a broader temperature range from about 100 °C to 330 °C and hydrogen is detected starting at a temperature of about 70 °C. The mass loss curve is more flat, and the associated endothermal DSC signal is much broader than in the case of AB-H-ace. No water and acetone are detected.

In Figure 4.3.1-3 the TG-DSC-MS curves of BCC-H-ace and the TG curve of AB_5-H-ace are presented.

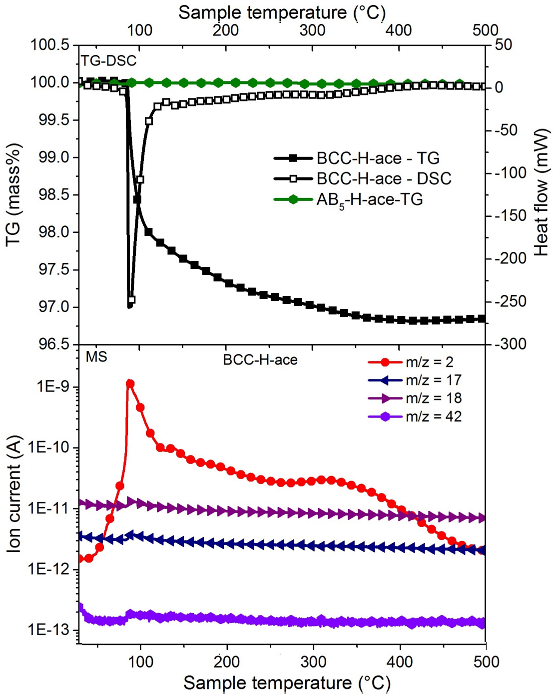

Figure 4.3.1-3. TG curves of AB_5-H-ace and BCC-H-ace.

No weight loss is detected upon heating of AB_5-H-ace, which is in agreement with XRD results. No hydride phase is observed (Fig. 4.3.1-1). BCC-H-ace releases hydrogen at about 50 °C, and a more significant release takes place between 90 and 100 °C. A strong endothermal DSC signal is recorded simultaneously. Water and traces of acetone are also detected during this event. Hydrogen is released over a broad temperature range and a weight loss of 3.4 mass% is recorded, corresponding to the accumulated hydrogen content of the two hydrides of V-Ti-based solid solution alloys [247]. Small amounts of hydrocarbon ion fragments corresponding to methane, ethane and propane are also detected during the thermal desorption of the acetone-treated samples. CO and CO_2 ion fragments are observed as well. It was difficult to reproduce the respective concentrations even between different batches of the same material. However, the chemical species are reproducibly detectable.

Figure 4.3.1-4 shows the TG curves of AB-H-tol, AB_2-H-tol and AB_5-H-tol and the TG-DSC-MS curves of BCC-H-tol.

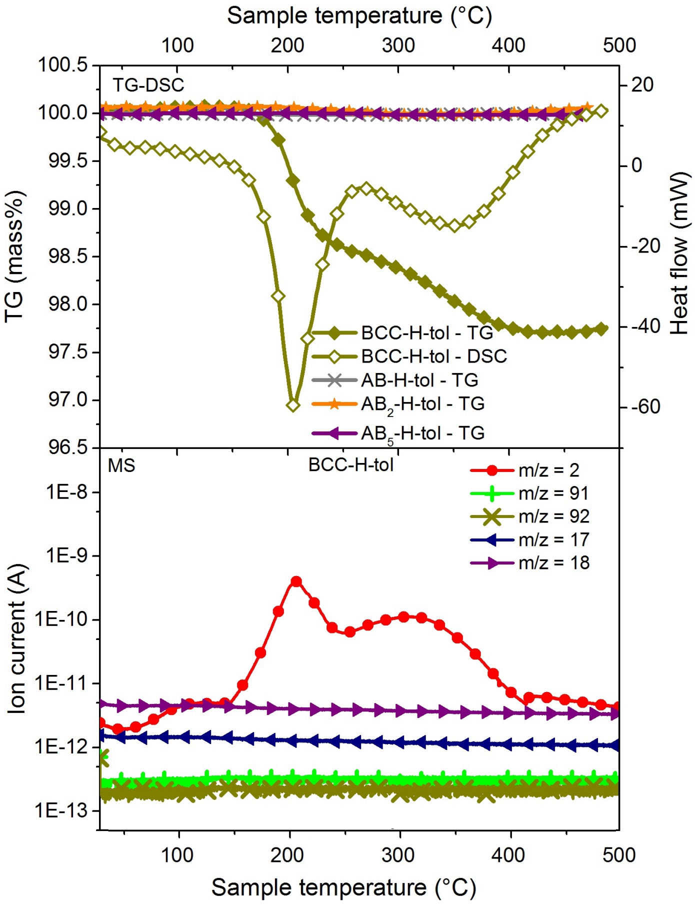

Figure 4.3.1-4. TG-DSC curves of AB-H-tol, AB_2-H-tol and AB_5-H-tol and TG-DSC-MS curves of BCC-H-tol.

No weight loss is detected from AB-H-tol, AB_2-H-tol and AB_5-H-tol. For AB_2-H-tol and AB_5-H-tol, this is in agreement with XRD observations. No hydride phases are observed (Fig. 4.3.1-1). 20 % of the hydride is evident in the XRD pattern of AB-H-tol. This indicates that the hydride decomposes into AB and H_2 either during evacuation of the TGA reaction chamber or before. Consequently, toluene treatment of AB-H causes the formation of a weak passivation layer, which has a mild effect on the desorption kinetics. BCC-H-tol desorbs small amounts of hydrogen at 50 °C, however, measurable weight loss is observed only at ca. 150 °C, and another pronounced hydrogen release event takes place at ca. 200 °C. The concentrations of water and toluene are below the detection limit of the mass spectrometer. A total of about 2.3 mass% H is desorbed, which is in agreement with XRD observations (Fig. 4.3.1-1, sample D-3). 18±2 % monohydride phase is found in the sample. Consequently, the accumulated hydrogen content of the mono- and dihydride is reduced as compared to BCC-H-ace, where 100 % dihydride is evident.

In order to further clarify the reactions on the surfaces of hydrogen absorbing alloys, BCC was chosen for further investigation due to its stronger deactivation behavior as compared to the other materials.

The volatile products formed during the reaction of acetone/toluene with BCC-H were determined by GC measurements. The detected substances are listed in Table 4.3.1-1.

	Reaction products			
Organic substance	Methylcyclohexane	CO	Propane	Propene
Toluene	0.2 vol.-%	-	-	-
Acetone	-	0.3 vol.-%	0.3 vol.-%	0.3 vol.-%

Table 4.3.1-1. Reaction products of the reactions of acetone/toluene on the surface of BCC-H. The remaining gases that were detected were H_2 and toluene or acetone, respectively.

The reaction of toluene on BCC-H yields 0.2 vol% methylcyclohexane. This indicates that toluene is hydrogenated at the surface of BCC-H. In the case of acetone, the reaction products are 0.3 vol.-% CO, 0.3 vol.-% propane and 0.3 vol.-% propene. No methane or ethane are detected.

Measurements were also performed with dehydrogenated BCC in hydrogen atmosphere, and no methylcyclohexane is observed in the case of toluene and no CO, propene and propane are observed in the case of acetone.

In order to further elucidate the surface properties of BCC-H after contact with acetone or toluene, XPS measurements were performed of the pristine surface and after various sputter times. Figure 4.3.1-5 shows the C 1s and O 1s spectra of BCC after three hydrogen sorption cycles in the desorbed state.

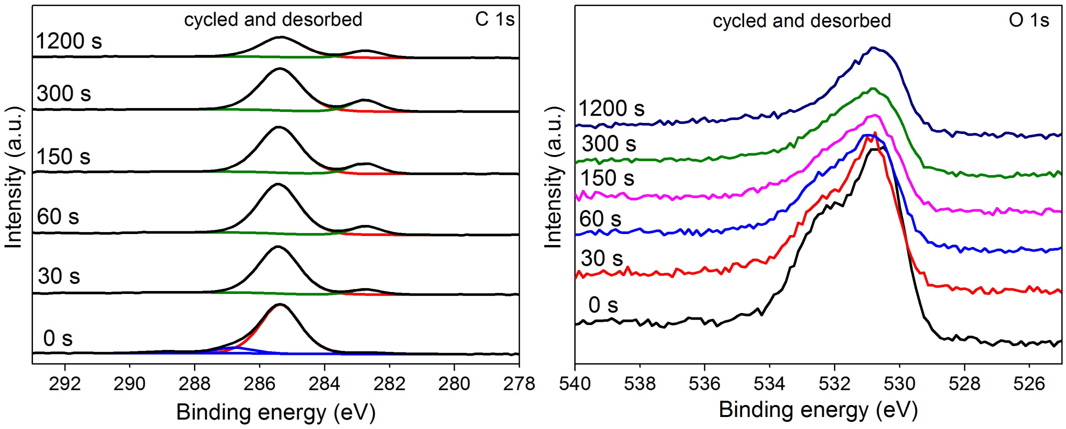

Figure 4.3.1-5. C 1s (left) and O 1s XP spectra (right) of BCC-H after various sputter times between 0 s (no sputtering) and 1200 s after three cycles in pure H and subsequent desorption.

The C 1s XP spectrum (Fig. 4.3.2-5, left) of the initial surface of the cycled sample before sputtering (0 s) shows a peak of high intensity at 285.3 eV, which can be attributed to aliphatic carbon species. Additionally, much smaller peaks are observed at 282.6 eV (carbide), 286.8 eV (C-O species) and 288.9 eV (C=O species) [248]. After 30 s sputtering (corresponding to approximately 0.5 nm of removed surface), the peaks related to the C-O bond disappear and the carbide-related peak gains in intensity. With increasing sputtering time, the carbide peak gains more and more in intensity while the intensity of the main peak (at 283.5 eV) stays initially almost constant and decreases only after the last sputter step to half of the initial value. The position of the carbide-related peak implies that most of the carbon atoms are bound to vanadium or titanium [151], [249]. These observations are in agreement with the O 1s region (Fig. 4.3.1-5, right), where two elementary peaks at 530.8 eV and 532.5 eV are observed. The peak at 530.8 eV corresponds to a metal oxide and its intensity decreases successively with sputtering depth. The 532.5 eV peak is attributed to hydroxyl groups (and C-O species) and is visible mainly in the spectrum of the pristine surface and remains only as a shoulder to the first peak after sputtering [250], [251].

C 1s and O 1s XP spectra of BCC-H-ace are presented in Figure 4.3.1-6.

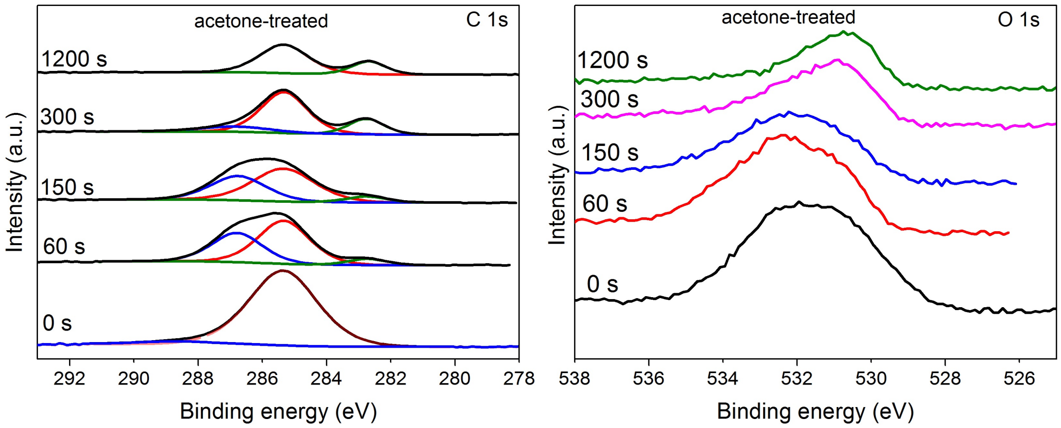

Figure 4.3.1-6. C 1s and O 1s XP spectra of BCC-H-ace after various sputter times between 0 s (no sputtering) and 1200 s.

The surface and subsurface chemistry of the acetone-treated sample differ significantly from the surface of the cycled sample. The surface before sputtering is mainly covered by hydrocarbons (285.3 eV). The C=O carbonyl peak of adsorbed acetone is reported in literature at 287.6 eV after adsorption at cryogenic temperatures [252]. No such peak is observed on our samples. This is not surprising, when taking into account that intact acetone should decompose or desorb from the sample surface under the working conditions of the present measurements (ultrahigh vacuum, RT). A weak peak is observed at 288.7 eV, which is also observed on the cycled sample without acetone contact. After 60 s sputtering, the carbide-related peak (282.7 eV) is observed, and a third peak is detected at 286.8 eV, which is attributed to C-O-related species, such as alkoxy- or ether-related compounds, again. The 286.8 eV peak is still present with the same intensity after sputtering for 150 s. After 300 s sputtering, the peak has a very low intensity, and it completely disappears after 1200 s. With longer sputtering times, the hydrocarbon- and carbide-related peaks predominate.

The O 1s spectrum at the surface before sputtering shows a broad and large peak. More detailed information on the chemical state of oxygen can not be retrieved here. After sputtering for 60 s, the spectrum shows, similar to the first sample, two distinct peaks at 532.5 eV and at 530.8 eV, which are attributed correspondingly again to O-H and C-O groups and metal oxide, respectively. In agreement to the results of the C 1s spectra, the peak at 532.6 eV, which is attributed (amongst others) to C-O species, remains clearly visible after 150 s and loses intensity after that. The metal oxide peak is predominant after longer sputtering times.

In Figure 4.3.1-7 the C 1s and O 1s XP spectra of BCC-H-ace after thermal desorption is shown.

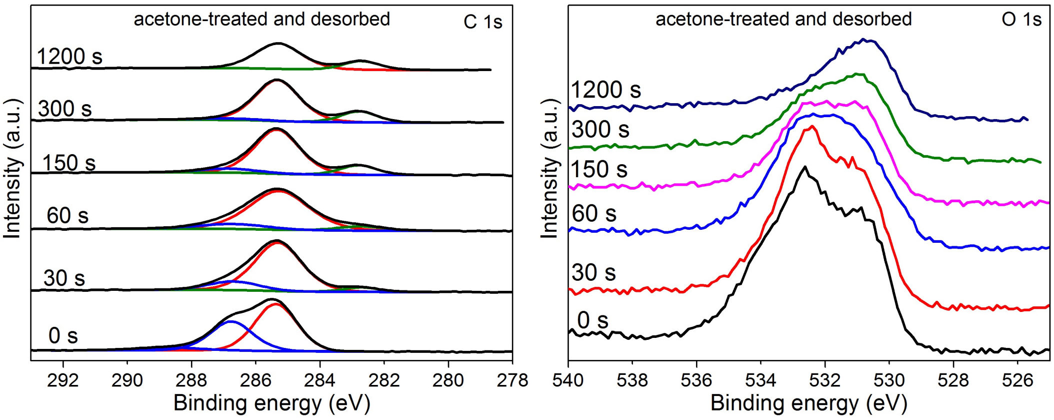

Figure 4.3.1-7. C 1s and O 1s XP spectra of BCC-H-ace-des at various sputter times between 0 s (no sputtering) and 1200 s.

The initial surface is covered by hydrocarbons (285.3 eV) and C-O-related species, such as alkoxy- and ether-related compounds (286.8 eV) and further traces of carbonyl (C=O) compounds (288.8 eV). After 30 s sputtering the carbonyl carbon peak is not observed anymore, and a carbide peak at 282.7 eV becomes evident. With prolonged sputtering time, the intensity of the 286.8 eV peak further decreases, and it disappears after 1200 s (approximately 20 nm of removed surface) of sputtering, while the carbide-related peak gains in intensity. The O 1s spectrum of the initial surface shows two peaks at 530.8 eV and 532.5 eV, corresponding to metal oxide, hydroxyl and C-O groups, respectively. Before sputtering and after the first step (30 s), the peak assigned to C-O species (and hydroxyl) is predominant, and its intensity decreases after 60 s sputtering. After prolonged sputtering (1200 s), the metal oxide peak is predominant. This behavior fits again to the continuous decline of the C-O-related peak in the C 1s spectra.

These observations further support the earlier assumptions that acetone reacts at the surface of the metal hydride. Much stronger peaks related to C-O species (C 1s: 286.8 eV, O 1s: 532.5 eV) are observed at the subsurface of BCC-H-ace than in case of BCC-H (the sample cycled in pure H_2 without acetone contact). This indicates that acetone decomposes during the contact with the metal hydride surface. The decomposition of acetone has been studied by XPS by Armstrong *et al.* on Si(100) under UHV conditions [252]. Their observations differ significantly from our findings, and the reasons will be discussed below. They observe three distinct peaks at 285.4 eV, 284.5 eV and 282.6 eV in their deconvolution of the monolayer XP spectra. The authors assign the 285.4 eV peak to carbonyl carbon that is reduced in bond order (from C=O to C-O) and has gained electron density from Si, and the 284.5 eV and 282.6 eV peaks are assigned to aliphatic and carbidic carbon, respectively. Two types of mechanisms for the interaction of acetone with the Si surface are proposed. In one part of the acetone molecules, the C=O carbonyl bonds are completely broken, resulting in Si-O bonds and bonding between Si and the aliphatic rest. For the remaining part of the acetone molecules, the carbonyl C=O bond is suggested to break partly, and a C-O single bond is maintained. Bonds between the central carbon atom and Si and between oxygen and Si are suggested. In our case, the surface and subsurface chemistry of the three samples differs significantly as compared to the literature report [252]. We attribute the peak at 285.3 eV to aliphatic carbon, the same peak is observed also on samples which did not come into contact with acetone and is also observed after prolonged sputtering times. During acquisition of the detail C 1s spectra, that same peak gains in intensity through re-adsorption of removed carbon from the remaining gas in the XPS chamber, which further supports this assumption. Alkoxy- or ether-related peaks are observed at the subsurface of the acetone-treated sample. These species diffuse into the subsurface region of the material. The corresponding peaks in the XPS spectra of BCC-H-ace are observed after 300 s of sputtering. With a removal of approximately 1 nm of surface per minute of sputtering, it can be estimated that these species diffuse 5 nm into the subsurface region of the material.

In Figure 4.3.1-8 the C 1s XP spectra of BCC-H-tol and BCC-H-tol-des are presented.

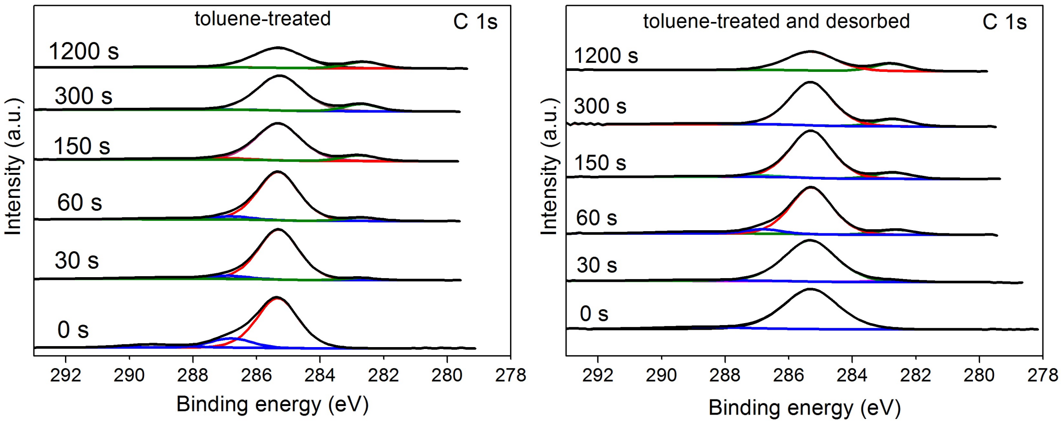

Figure 4.3.1-8. C 1s XP spectra of BCC-H-tol (left) and BCC-H-tol-des (right).

The toluene-treated surface is covered by hydrocarbons (285.3 eV), C-O-related species, such as alkoxy- and ether-related compounds (286.8 eV) and further traces of oxygen-containing carbon species at 289.3 eV. After 30 s and 60 s sputtering the 289.3 eV peak disappears and the intensity of the peak at 286.8 eV decreases significantly. Additionally, the carbide peak at 282.7 eV becomes evident, whose intensity increases with longer sputtering times. After 300 s of sputtering, only the carbide- and hydrocarbon-related peaks at 282.7 eV and 285.3 eV are evident.

After thermal desorption of the toluene-treated sample, the surface is still covered mainly by hydrocarbons and a small amount of C-O-containing species at 288.9 eV. Similar to the deactivated state, the carbide-related peak at 282.7 eV appears after 30 s and gradually gains in intensity with longer sputtering times. A C-O-related peak at 286.8 eV is observed after sputtering for 60 s. With longer sputtering times, the C-O-related peak disappears. The hydrocarbon-related peak at 285.3 eV gradually loses intensity with sputtering, and the carbide-related peak gains in intensity. This behavior fits again to the development of the O 1s spectra, which are shown for the toluene-treated (and subsequently desorbed) samples in Figure I-1 in the appendix.

Concentration depth profiles of cycled BCC, BCC-H-ace or -tol and BCC-H-ace-des or –tol-des are presented in Fig. I-2 – I-6 in the appendix.

In brief, the profiles show for all samples a continuous decrease of the oxygen content from 30 – 35 at% before sputtering to 10 – 15 at% after 1200 s sputtering. Prolonged sputter time do not lead to further significant changes. The C concentration on the other hand stay more or less constant for all samples until 300 s sputtering. After that a clear decrease is observed. Furthermore, the initial C amount reflects the sample treatment. The lowest content is observed for cycled BCC (37 at%). Significantly higher concentrations are detected for the acetone- and toluene-treated samples with or without desorption step (> 50 at%). Similarly, the remaining C content after 7200 s sputtering is much higher for these samples. While the C concentration decreases below 10 at% for the cycled sample, the acetone-treated samples (with or without desorption) show ~20 at%, and the toluene-treated samples ~33 at%. This indicates that a significant amount of carbon diffuses to the subsurface of the latter samples after contact with acetone or toluene.

The hydrogen absorption properties of BCC were tested after immersing the activated, dehydrogenated powder in dried acetone or toluene. As reference, a sample without acetone or toluene contact was desorbed at ambient temperature and pressure in a glove box. The absorption kinetic curves are presented in Figure 4.3.1-9.

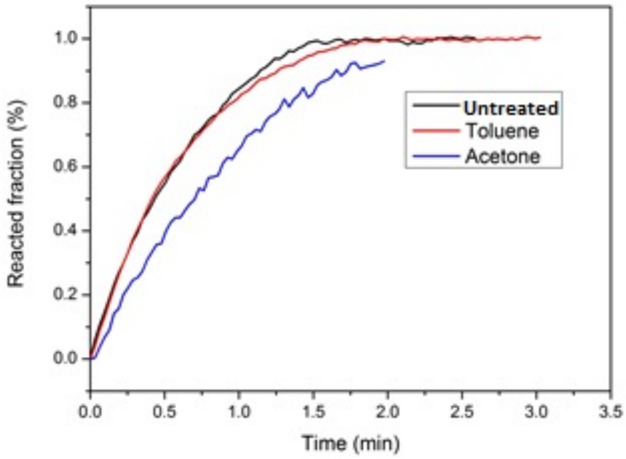

Figure 4.3.1-9. Hydrogen absorption kinetic curves of BCC after immersing the activated, dehydrogenated powders in dried acetone, toluene. The glove box sample was left before the experiment at ambient temperature and pressure in the glove box as reference. The absorption experiments were performed at 5 MPa and 298 K.

All the samples absorb hydrogen with similar kinetics. More than 90 % hydrogen is absorbed after 1.5 min. This indicates that the surface of BCC readily dissociate hydrogen molecules and the atoms are not hindered from bulk penetration after contact with these substances.

Cross-linking the observations acquired in this chapter, the effects of acetone and toluene on hydrogen absorbing alloys AB, AB_2, AB_5 and BCC can be concluded as follows.

AB_5-H is the most tolerant of the investigated materials. No hydride phase is observed after the immersion of AB_5-H in either acetone or toluene, and no hydrogen is released from AB_5-H-ace or -tol in the TGA. This indicates that the presence of neither acetone nor toluene prevents already absorbed hydrogen from desorption. It is possible that the desorption kinetics are influenced by the presence of the organic liquids.

AB-H, AB_2-H and BCC-H are deactivated by acetone treatment. Hydride phases are observed in AB_2-H-ace, AB-H-ace and BCC-H-ace by XRD at desorption conditions, and elevated temperatures are necessary to induce hydrogen desorption in the TGA. A passivation layer is formed at the surface of these metal hydrides that inhibits absorbed hydrogen atoms from desorption.

Toluene mildly deactivates AB-H-tol and has a more pronounced deactivating effect on BCC-H-tol, as evident by XRD and TGA-DSC analysis. AB_2-H-tol is inert towards liquid toluene.

In the following, a mechanism for the reactions of acetone/toluene on transition metal hydrides is postulated.

For both acetone and toluene, the respective reaction products propene, propane and CO (acetone reaction) or methylcyclohexane (toluene reaction) are detected by GC only after immersion of already absorbed samples in the organic liquids. Only acetone/toluene and H_2 is detected if desorbed samples are used. Furthermore, negligible effects are observed on the absorption kinetics or capacity after the immersion of desorbed samples in any of the organic liquids. In conclusion, the supply of absorbed hydrogen atoms from the bulk of the material significantly enhances the reactivity of the metal hydride surface with respect to the conversion of organic molecules. Evidently, hydrogen desorption is effective for the activation of the metal surface and thereby increases the surface reactivity.

In the case of acetone, our findings indicate that acetone reacts at the hydride surface during the desorption of BCC-H in liquid acetone. The gaseous reaction products are detected by GC after the reaction, or they remain adsorbed at the hydride surface and are detected by XPS of BCC-H-ace or MS during the thermal desorption treatment of BCC-H-ace. Aside from acetone and hydrogen, the detected species are propene, propane and CO (GC), and short-chained hydrocarbons (methane, ethane and propane), CO, CO_2 and H_2O (MS). These observations would indicate two types of reactions occurring simultaneously during the immersion of H-loaded metal hydrides in liquid acetone: 1) the reduction of the acetone molecules without rupture of the C-C bonds to the products propane, propene and water, metal oxides or hydroxides, and 2) the decomposition of acetone, forming CO_x and short-chained hydrocarbons, such as methane. Both reactions are shown schematically in Figure 4.3.1-10.

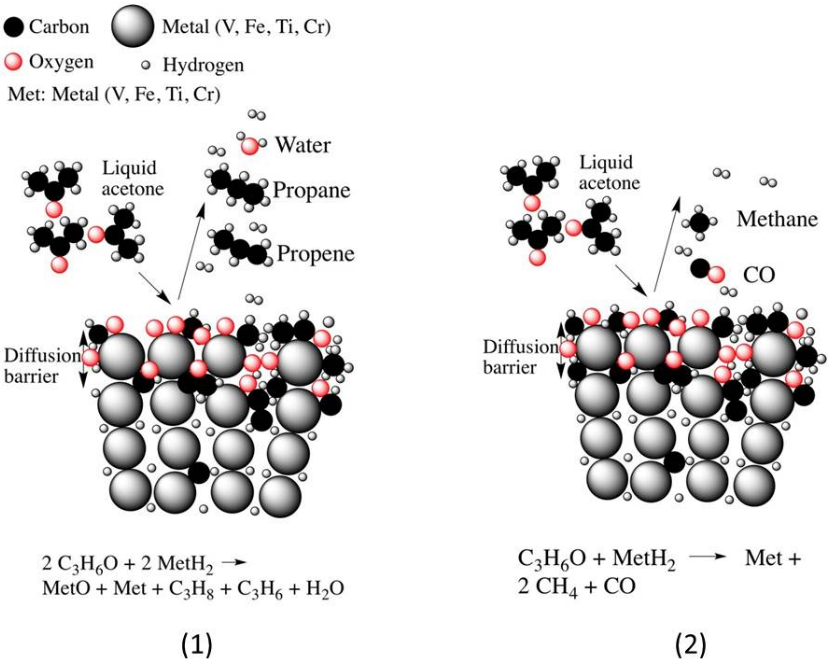

Figure 4.3.1-10. Schematic representation of the reactions of acetone on the metal hydride surface.

The first reaction path (1) depicted on the left side of Figure 4.3.1-10 is evident by the detection of propene, propane and water by GC and MS. It is suggested that acetone is first reduced on the metal hydride surface to propene. It is postulated that propane is formed at the hydride surface as a result of the hydrogen desorption reaction. One fraction of the propene molecules is driven away from the reactive surface during hydrogen desorption. The other fraction is completely hydrogenated at the reactive hydride surface, which converts them into propane. Hydrogenation reactions on metal hydride surfaces have been reported for ethene or CO_2, which are known to be converted to ethane or methane on the surface of $LaNi_5H_6$ [253] or $MgNi_2D_4$ [254] by absorbed hydrogen or deuterium, respectively. The remaining oxygen of the acetone molecule is either reduced to water, which is adsorbed at the metal hydride surface or dissolved in the liquid acetone, or reacts with the metals to form metal oxides (V-, Fe-, Ti- and Cr oxides were also detected by XPS at the surface and subsurface) or hydroxides. Hydroxyl groups are also detected by XPS at the subsurface region of the sample, which also supports this conclusion.

The reaction depicted on the right side of Figure 4.3.1-10 (reaction (2)) is not as evident as the first one, however, it is proposed based on the following observations. CO was detected after the immersion of BCC-H in liquid acetone. No CO was detected if a dehydrogenated sample was immersed in acetone, or if pure acetone without previous contact to metal or metal hydride was measured by GC. This would suggest that CO had formed as a result of the decomposition of acetone, as depicted schematically in Figure 4.3.1-10 and the proposed reaction equation 2) included in the same figure. However, based on stoichiometry (acetone contains three C atoms), methane should also be formed during such a reaction. It is expected that the remaining two alkyl (CH_3) groups of acetone are hydrogenated at the surface of the desorbing BCC-H. In a CO/CH_4 mixture, one should expect that CO would show a stronger tendency to adsorb at the surface of the metal, and hence it is surprising that no methane was detected by GC if both CO and CH_4 were formed. Methane (and ethane) were detected only during thermal treatment of BCC-H-ace. Additionally, the surface of BCC-H-ace was covered mainly by aliphatic carbon, as evident by XPS. Possibly, the remaining CH_3 groups of the acetone molecules reacted with the metal atoms (metal carbides were also observed at the subsurface of BCC-H-ace by XPS), or the formed CH_4 remained adsorbed at the surface. Pronounced hydroxyl- and C-O-related signals were detected at the subsurface after sputtering. These species were not detected on the (sub)surface of the cycled sample without acetone contact, providing evidence that the the C- and O-containing species further diffused into the subsurface region and were partly reduced by H. In particular the formed CO would show a strong passivating effect on the surface of the material. The surface and subsurface is hence modified as a result of acetone treatment.

An additional possible reaction would be the formation of volatile metal carbonyles such as vanadium or titanium carbonyle, which could be formed during the reaction of CO with these metals.

The chemical species that are formed in the first and second reaction paths partly adsorb at the surface and diffuse to the subsurface region of the material, as evident by the concentration depth profiles measured by XPS. Increased carbon concentrations are measured in the (sub)surface regions of the acetone-treated or acetone-treated and desorbed samples as compared to the cycled sample without acetone contact.

The C- and O-containing chemical species found in the (sub)surface region of the material represent a kinetic barrier for absorbed hydrogen to recombine at the surface and escape to the gas phase. As the reaction progresses, more and more C- and O-containing species diffuse into the subsurface region of the material. This results in a continuously growing kinetic barrier for hydrogen desorption until the desorption reaction finally stops. It is believed that the catalytically active surface sites important for the association of absorbed hydrogen atoms are blocked by the adsorbed species. Similar passivation and poisoning mechanisms have been reported in the literature for gaseous impurities, such as O_2, H_2O, hydrocarbons, CO or CO_2, which form blocking layers on transition metal hydride surfaces and hereby inhibit the hydrogen sorption reactions [19], [147], [186], [255]. The acetone-treated hydrides are stabilized through this kinetic barrier for extended time periods up to several weeks, as evident by XRD.

If a sufficient amount of thermal energy is provided to overcome the kinetic barrier formed by the adsorbed species, the hydrogen desorption reaction is initiated. This event is accompanied by the release of water, hydrocarbons, CO and CO_2, as observed by MS. The intensity of the XPS peaks corresponding to the hydroxyl groups and C-O-related species also decreases markedly after thermal desorption, which further supports these assumptions. Water is detected during thermal desorption of BCC-H-ace and AB-H-ace. No water is detected during desorption of AB_2-H-ace. However, the dehydrogenation process occurs over a much broader temperature range than in the case of both

BCC-H-ace and AB-H-ace. Here, the detected amount of water is very low. It is likely that water is also formed during desorption of AB_2-H-ace but its concentration was not sufficient to be detected by the instrument. Desorption from BCC-H-ace and AB-H-ace, instead, occurs in a much narrower temperature range.

For the toluene reaction, the products are H_2, toluene and methylcyclohexane. This indicates that toluene is hydrogenated at the surface of the metal hydride during the hydrogen desorption reaction. The proposed reaction mechanism is depiced in Figure 4.3.1-11.

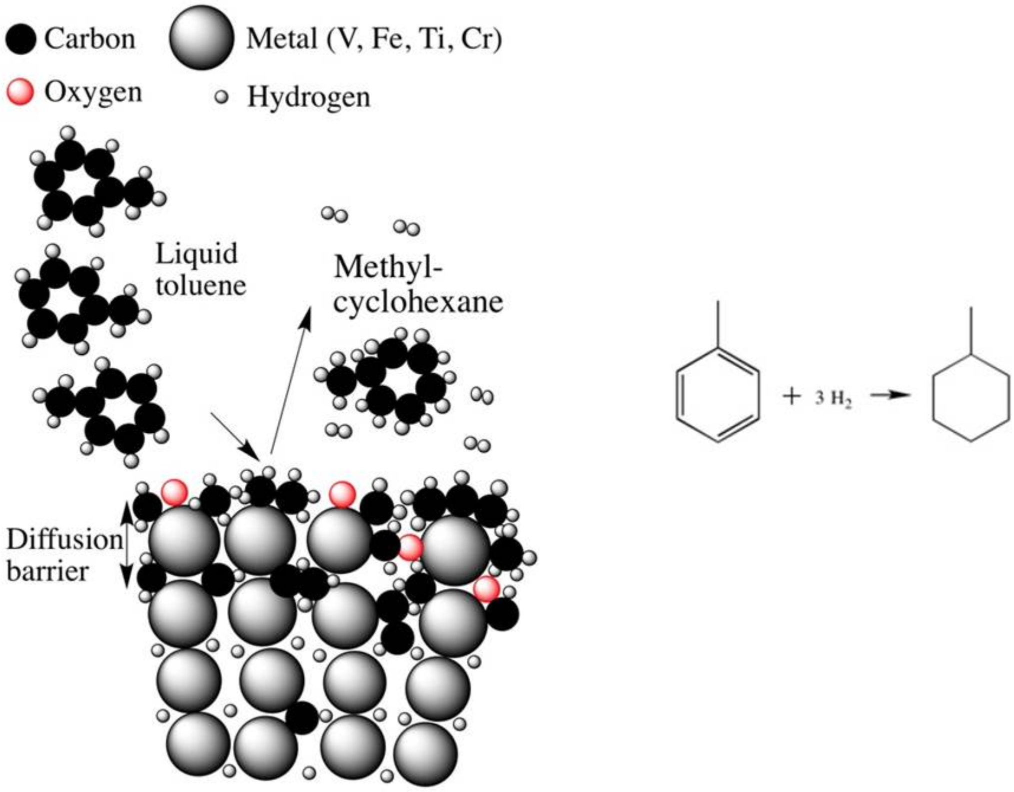

Figure 4.3.1-11: Schematic representation of the toluene reaction on the metal hydride surface.

Analog to the acetone reaction, it is postulated that the surface is passivated by the deposition of carbon as the reaction progresses, and after a certain time, the reaction stops due to a kinetic barrier formed by adsorbed species in the (sub)surface region. This is also reflected in the concentration depth profiles of the toluene-treated sample BCC-H-tol, where significant carbon concentrations are evident either after contact with toluene or after thermal desorption (BCC-H-tol-des) . The surfaces of vanadium and titanium are known to be sensitive even towards low concentrations of impurities. Hydrogen absorption of titanium is known to be inhibited through carbon deposition and the formation of titanium carbide even after cycling in hydrogen containing minor amounts of hydrocarbons [21]. The formation of Ti carbohydride was observed, which is believed to be responsible for the deterioration of the hydrogen uptake kinetics [21].

These findings indicate that the metal hydride surface has a stronger passivation tendency during the hydrogen desorption reaction. This effect may either originate from a higher activity of the surface catalytic sites, through the supply of atomic hydrogen molecules from the bulk, or a combination of both factors. A measurable conversion is observed of toluene to methylcyclohexane at room temperature, which is remarkable if one considers that toluene hydrogenation typically requires temperatures of at least 100 °C due to kinetic limitations of the reaction [256–259].

Recommendations for a proper selection of metal hydrides for the targeted applications in thermal energy and hydrogen storage can be provided. $LaNi_5$ shows the strongest tolerance towards the organic liquids, followed by $Ti_{0.95}Zr_{0.05}Mn_{1.49}V_{0.45}Fe_{0.06}$ and TiFe. $V_{40}Fe_8Ti_{26}Cr_{26}$ is deactivated by both organic liquids. Precautions should be taken if materials with strong passivation behavior are used for the targeted applications, e.g. a thorough separation of hydrogen from the organic substance through a membrane.

A thermal energy or hydrogen storage process should be designed in such a way that contact between liquid organics and hydrogen storage alloys is avoided during hydrogen desorption of the respective metal hydride. On the one hand, the metal hydrides show the tendency to passivate as a result of the contact with the organic liquids, which is more or less pronounced depending on the metal hydride.

On the other hand, for a thermal energy storage system such as the one proposed by Kreuder *et al.* [4], parasitic hydrogenation of toluene in the metal hydride storage material is undesired, since the amount of recoverable thermal energy is directly proportional to the amount of toluene and H_2 reacting exothermally in the reactor to methylcyclohexane. Already reacted toluene and H_2 would therefore reduce the overall efficiency of the process. If organic molecules exhibiting similar reaction patterns as acetone would be used in a thermal energy or hydrogen storage application, in which combinations of solid and liquid hydrogen carriers are used, the dissociation of the organics would be undesired. In addition to the need to separate the dissociation products from the system, such dissociation would create a continouus need for “fresh” organic liquid. Such reactions would have to be taken into account for during the design of thermal energy or hydrogen storage applications.

4.3.2 Effects of gas-phase impurities on the cyclic stabilty

4.3.2.1 Kinetic and surface properties during cycling in pure and impure H_2

De/hydrogenation kinetics are strongly dependent on surface properties of the respective storage material. The formation of passivation layers at the surface of the hydriding alloys may influence the hydrogen sorption kinetics as well as the reversible capacity. Upon hydrogenation, the alloy particles decrepitate into a fine powder. This phenomenon mainly occurs during the initial cycles. As a result, fresh surfaces are exposed as the particle size decreases. For the investigation of hydrogenation kinetics, it is essential to ensure a constant particle size distribution (i.e., the length of diffusion pathways within the particles) and surface area (i.e., the number of available catalytic surface sites), since both factors may influence the kinetics. Furthermore, if the particles would further decrepitate during cycling in impure hydrogen, fresh surfaces without previous contact to gaseous impurities would be exposed. An influence on kinetics and cyclic stability is possible, and thus it is desirable to minimize this effect. An additional aspect that has to be considered is that the chemical treatments, which are aimed at improving the tolerance against gaseous impurities, show a maximum effect if the whole surface area is treated (chapter 4.3.2.2).

In order to investigate the decrepitation behavior of V-Fe-Cr-Ti solid solution alloys, the particle size distribution of $V_{40}Fe_8Ti_{28}Cr_{24}$ was determined after various hydrogen sorption cycles by SEM. This is presented in Figure 4.3.2.1-1 along with the corresponding SEM micrograph after 14 cycles.

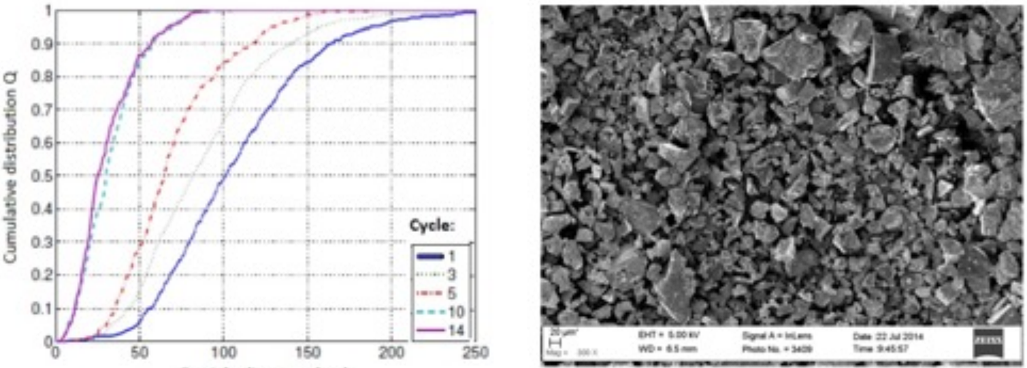

(a) (b)

Figure 4.3.2.1-1: (A) cumulative distribution Q of $V_{40}Fe_8Ti_{28}Cr_{24}$ as a function of the particle diameter during the first 14 hydrogenation cycles, and (b) the SEM micrograph of the powder after 14 cycles.

As expected, the mean particle diameter decreases with the number of hydrogenation cycles. For example, the Q_{50} value (defined as the particle diameter d_{50}, at which 50 % of the particles exhibit a smaller diameter $d < d_{50}$ and 50 % of the particles exhibit a larger diameter $d > d_{50}$) decreases from 100 ± 15 µm after the first cycle to approximately 30 ± 10 µm after ten cycles. A decrease in particle size goes along with an increase in total surface area. If sperical particles are assumed, the observed decrepitation between cycles one and 14 corresponds to an increase in surface area by a factor of 3. The decrepitation is most pronounced during the first ten hydrogenation cycles. No significant change in particle size is observed between cycles 10 and 14.

These results are in agreement with a previous report by Miraglia *et al.*, who investigated the particle size distribution of a $TiV_{0.8}V_{1.2}$ + 4 wt% Zr_7Ni_{10} composite alloy powder. The particle size distribution is reported to be centered (i.e., the d_{50} value) around 50 – 60 µm after three cycles [260]. No further results on the particle size evolution after more than three cycles are reported, and our investigations strongly suggest that the particles further decrepitate during the consecutive cycles.

Based on these results, all materials investigated in the following chapters were cycled 15 times before performing the kinetic studies in pure/impure hydrogen gas and the surface treatments.

In Figure 4.3.2.1-2 the hydrogen absorption kinetic curves of $V_{40}Fe_8Ti_{28}Cr_{24}$ are presented. The absorption pressure was 1 MPa, desorptions were performed in dynamic vacuum, and the temperature was 303 K.

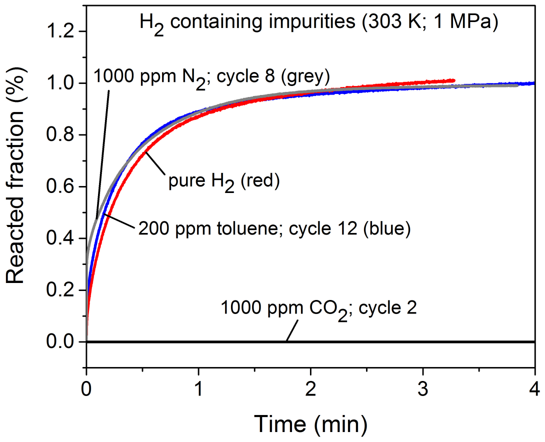

Figure 4.3.2.1-2: Hydrogen absorption kinetic curves of $V_{40}Fe_8Ti_{28}Cr_{24}$ at 1MPa pure H_2, H_2 blended with 1000 ppm N_2, H_2 blended with 200 ppm toluene, or H_2 blended with 1000 ppm CO_2 at 1 MPa and 303 K.

The absorption reaction in pure hydrogen exhibits fast reaction kinetics. More than 90 % of the final absorption capacity is reached in less than 1 min. The observed reaction kinetics are considerably faster than reported previously. Miraglia *et al.* reported an absorption reaction time of 16 min for a $TiV_{0.8}V_{1.2}$ + 4 wt% Zr_7Ni_{10} composite alloy at 293 K and 1 MPa [260]. Three initial activation cycles were performed in their work and the particle size distribution is also reported. In the present work, 15 activation cycles were performed based on the analysis of the particle size distributions. The slower hydrogenation kinetics reported by Miraglia *et al.* may originate from this larger particle size or from the addition of the secondary alloy phase, which is found at the particle surfaces and may inhibit the hydrogenation kinetics. Another possible explanation for the slower kinetics may be insufficient removal of the heat of absorption, which may cause strong heating of the sample. No detailed information on the type of reactor or the amount of used sample were provided by Miraglia *et al.* [260].

The absorption kinetics of hydrogen containing 200 ppm toluene or 1000 ppm N_2 are comparable to the absorption kinetics of the material reacting with pure H_2, at least within the number of cycles investigated within this work (8 for N_2 and 12 for toluene). Long-term cycling experiments are currently in progress in collaboration with the Joint Research Center of the European Commission (JRC) in Petten, Netherlands. The cyclic stability in H_2 blended with toluene is investigated. CO_2 strongly inhibits the absorption reaction, and the sample does not absorb any hydrogen after the second cycle.

Shown from our previous experiments and in previous literature reports, oxygen contained in the H_2 gas represents a critical impurity with a strong tendency to passivate the surface of the storage alloy. The passivation and reactivation behaviour of a V-Ti-based solid solution alloy was investigated during cycling in H_2 containing 250 ppm O_2. Figure 4.3.2.1-2 shows the hydrogen absorption kinetic curves of $V_{40}Fe_8Ti_{32}Cr_{16}$ in pure hydrogen, hydrogen containing 250 ppm O_2 and the reactivation in pure H_2. The content of Ti was increased by 4 at% as compared to the material tested above in order to facilitate the reactivation of the NaOH-treated samples, which will be discussed in more detail in chapter 4.3.2.2. The absorption pressure was 1 MPa, desorptions were performed in dynamic vacuum, and the temperature was 303 K.

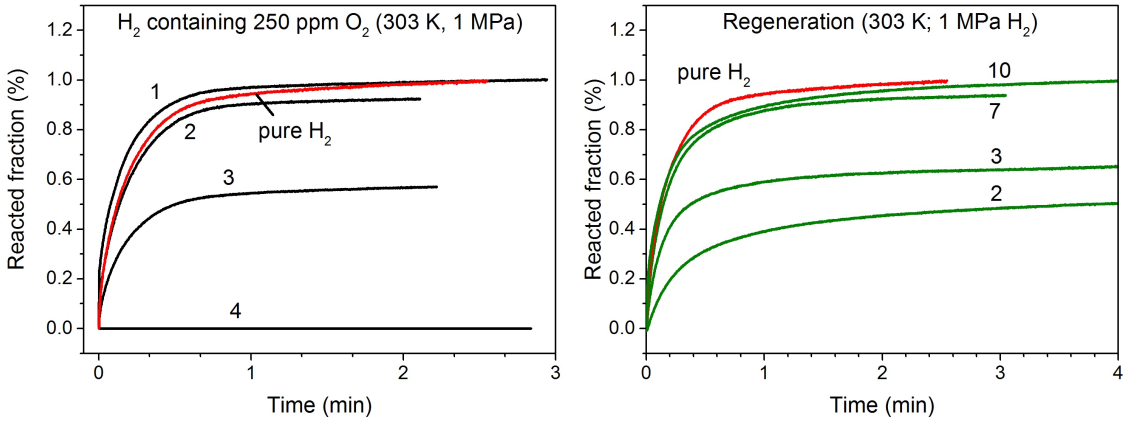

Figure 4.3.2.1-2: Hydrogen absorption kinetic curves of $V_{40}Fe_8Ti_{32}Cr_{20}$ at 1MPa H_2, H_2 containing 250 ppm O_2 and during reactivation in pure H_2 after four cycles in O_2-contaminated H_2 at 1 MPa and 303 K.

The absorption behavior during the first cycle in H_2 blended with 250 ppm O_2 is similar to the behavior observed in pure H_2. A slight reduction in final capacity is observed during the second cycle. A more pronounced reduction of capacity is recorded during the third cycle. Here, a reduction to around 50 % of the initial capacity is observed. No hydrogen is absorbed during the fourth cycle. These results indicate an oxygen-induced surface passivation, which becomes more pronounced with an increasing number of reaction cycles. It is likely that this passivation layer inhibits the dissociation and diffusion of the hydrogen atoms. A similar cyclic response in O_2-blended H_2 has been observed before for TiFe [147], $Zr_{0.9}Ti_{0.1}V_2$ [151] or $Ti_{25}V_{35}Cr_{40}$ [185].

The storage material can successfully be reactivated by heating the material to 150 °C under dynamic vacuum und subsequent cycling in pure H_2 at room temperature. About 90 % of the storage capacity is regained after six cycles. It should be noted that the initial heating step is necessary to reactivate the surface for hydrogen absorption. Such thermal reactivation treatment has been reported for $Ti_{1.13}Fe$ by Hirata *et al.* [261], and is also in line with our observation that acetone-deactivated materials (see the previous chapter) readily absorb hydrogen after the reactivation of the samples (i.e., thermal desorption of the confined hydrogen). Hirata *et al.* attribute their observations to the fact that hydrogen desorption is never complete, but some of the absorbed hydrogen always remains retained in each cycle. The formation and growth of surface oxides play an important role in the accumulation of hydrogen in each cycle. Thermal desorption initiates the partial reduction of surface metal oxides and thereby reactivates the surface sites [261], [262].

In order to elucidate on the passivation mechanism of oxygen-contaminated $V_{40}Fe_8Ti_{32}Cr_{20}$, XPS measurements of the surface and subsurface region were performed. As a reference, the Ti, V and O XP spectra of $V_{40}Fe_8Ti_{26}Cr_{26}$ cycled in pure H_2 are presented in Figure 4.3.2.1-3. The sample was transferred into the XPS chamber without air or moisture contact.

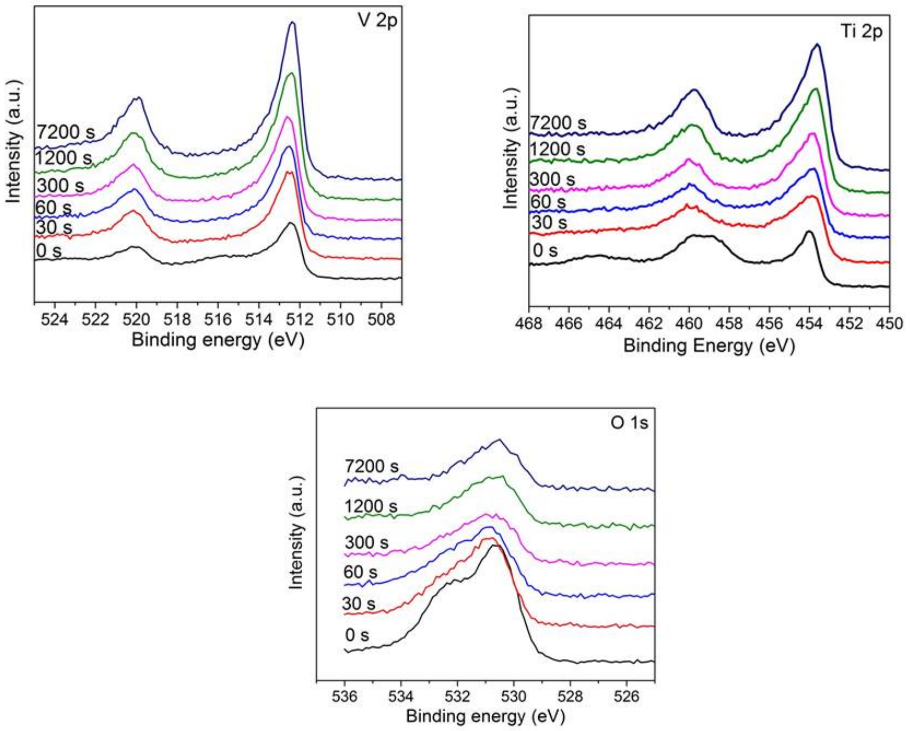

Figure 4.3.2.1-3: O 1s and V 2p spectra (left) and Ti 2p spectra of cycled $V_{40}Fe_8Ti_{26}Cr_{26}$ without oxygen, air or moisture contact.

The V 2p spectra of the surface before sputtering shows an intense peak at 512.4 eV corresponding to metallic V. An additional peak is observed at around 516 eV, which is attributed to a mixed-valence V oxide (V^{n+}) [151]. The intensity of the metallic V peak at 512.4 eV increases with sputtering time, while the peak corresponding to V oxide is of low intensity after the first sputtering step and is not observed after the subsequent sputtering steps. The Ti 2p XP spectra of the surface before sputtering show peaks corresponding to metallic Ti (454 eV) and TiO_2 (Ti $2p_{3/2}$ and Ti $2p_{1/2}$ at 459 eV and 464.4 eV, respectively) [263]. After sputtering, only the peak corresponding to metallic Ti is observed. The O 1s spectrum of the surface before sputtering exhibit two peaks at 530.9 eV and 532.5 eV, which are attributed to metallic oxide and hydroxyl groups, respectively. The intensity of the hydroxyl peak decreases markedly after the first sputtering step, and this peak is not observed after prolonged sputtering. The metallic oxide peak is observed in all spectra, however, its intensity gradually decreases with each sputtering step.

The XPS spectra of $V_{40}Fe_8Ti_{32}Cr_{20}$ cycled four times in hydrogen containing 250 ppm O_2 after various sputtering times are presented in Figure 4.3.2.1-4.

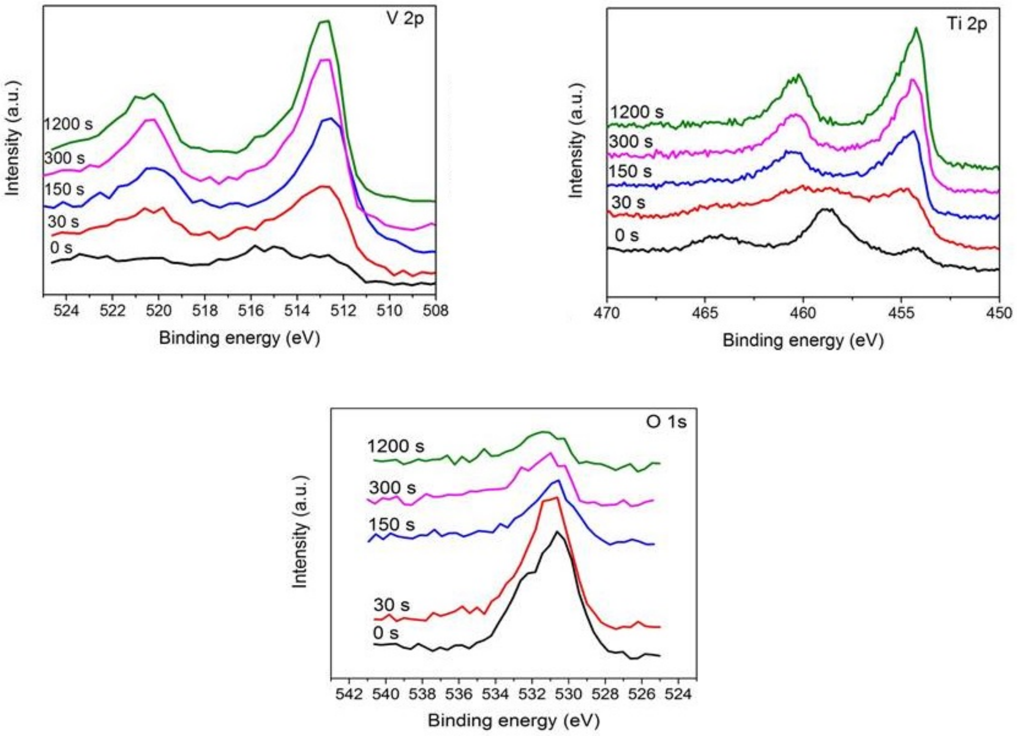

Figure 4.3.2.1-4: V 2p (top left), Ti 2p (top right) and O 1s (bottom) XP spectra of $V_{40}Fe_8Ti_{32}Cr_{20}$ after four hydrogenation cycles in H_2 containing 250 ppm O_2. Sputtering was performed between 0 s (no sputtering) and 1200 s.

The V 2p spectrum of the initial surface of the oxygen-poisoned sample shows two broad peaks, which can be attributed to metallic V (512.4 eV) and mixed valence V oxides (514.5 eV – 517.2 eV) [151]. After 30 s sputtering, the metallic V peak gains in intensity, and the peaks related to V oxides are visible in the form of a shoulder to the V metallic peak. With sputtering depth, the metallic V peak becomes more intense, while the V oxide peaks disappears after 150 s of sputtering. The Ti 2p XP spectrum of the initial surface exhibits distinct peaks at 454 eV, 459 eV and 464.4 eV, corresponding to metallic Ti (454 eV) and TiO_2 (Ti $2p_{3/2}$ and Ti $2p_{1/2}$ at 459 eV and 464.4 eV, respectively) [263]. The peak corresponding to metallic Ti gains in intensity after the first sputtering step, while the intensity of the TiO_2 peak decreases. After 150 s of sputtering, the $Ti_{metallic}$ peaks (Ti $2p_{3/2}$ at 454 eV and Ti $2p_{1/2}$ at 461 eV) are pronounced and become more intense with increasing sputtering depth. No Ti oxide peaks are observed in these spectra. The O 1s spectrum of the surface before sputtering (0 s) shows a pronounced peak at 530.9 eV, which corresponds to metallic oxide. A second peak is observed at 532.5 eV, which is attributed to hydroxyl groups [250], [251]. After sputtering for 30 s the hydroxyl peak becomes less intense, and it disappears after 150 s of sputtering. With longer sputtering time, the intensity of the metal oxide peak decreases.

These results indicate that metal oxides are formed at the surface during cycling in H_2 blended with O_2. This is also in good agreement with previous studies on the passivation behavior and surface structure of other intermetallic hydrogen storage materials [19], [20], [147], [179], [207], [255], [264]. These oxide layers cause the passivation of the hydride surface of $V_{40}Fe_8Ti_{32}Cr_{20}$ upon cycling in O_2-contaminated hydrogen.

4.3.2.2 Improved hydrogen storage properties in impure H_2 through surface modifications

In the following chapter, two approaches are presented aimed to improve the cyclic stability of V-Fe-Cr-Ti solid solution alloys in H_2 blended with O_2. They are based on the observation that $LaNi_5$ exhibits the highest stability during cycling in H_2-O_2 mixtures. In order to improve the tolerance of V-Fe-Cr-Ti solid solution alloys towards O_2, either La (A element in $LaNi_5$) or Ni (B element in $LaNi_5$) were added to the alloy.

The first approach of engineering suitable surface structures with improved catalytic properties for hydrogen dissociation is the introduction of the B element of $LaNi_5$, Ni.

It has been reported in the literature that a high fraction of Ni negatively influences the hydrogen storage properties of V-Ti-based solid solution alloys [184], [265–267]. Thus, the approach is the addition of a small amount of Ni and subsequent leaching of the remaining elements (primarily Ti and V) from the surface of the alloy. The aim of this procedure is to enrich Ni at the surface of the storage material while retaining the beneficial hydrogen storage properties of the bulk. Fe or Cr were selected as the substitution elements for Ni due to their similar atomic radii as compared to Ni and comparable effects on the thermodynamics of hydride formation and dissociation [267]. Several compositions of Cr- or Fe-substituted V-Ti-based solid solution alloys were tested upon their respective hydrogen storage properties. The total and reversible capacities and thermodynamic properties of the tested alloys are summarized in Table 4.3.2.2-1.

Alloy	Hydrogen capacity [mass%]	Reversible capacity [mass%]	Plateau pressure [MPa]
$V_{40}Fe_8Ti_{32}Cr_{20}$	3.4 ± 0.1	2.1	0.03 (303 K)
$V_{40}Fe_8Ti_{28}Cr_{20}Ni_4$	3.3 ± 0.1	2.0	0.09 (303 K)
$V_{40}Fe_8Ti_{28}Cr_{24}$	3.3 ± 0.1	1.2	0.07 (298 K)
$V_{40}Fe_8Ti_{28}Cr_{16}Ni_8$	1.8 ± 0.1	0.9	0.3 (298 K)
$V_{40}Ni_8Ti_{28}Cr_{24}$	1.7 ± 0.1	0.5	0.01 – 1.2 (298 K)

Table 4.3.2.2-1: Total and reversible capacities of the hydrogen storage alloys prepared with various Ni contents.

All alloys prepared with 8 at% Ni exhibit a reduced total hydrogen capacity as compared to the materials prepared without Ni. At 4 at% Ni, a large total and reversible capacity of 3.3 mass% and 2.0 mass% is measured, which was close to the material prepared without Ni.

In Figure 4.3.2.2-1 the XRD pattern of the alloys summarized in Table 4.3.2.2-1 are shown.

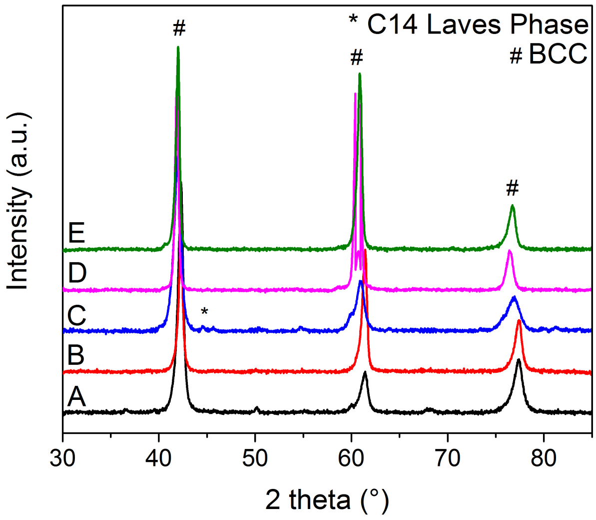

Figure 4.3.2.2-1: XRD patterns of (A) $V_{40}Fe_8Ti_{28}Cr_{24}$, (B) $V_{40}Fe_8Ti_{28}Cr_{26}Ni_8$, (C) $V_{40}Ni_8Ti_{28}Cr_{24}$, (D) $V_{40}Fe_8Ti_{32}Cr_{20}$, and (E) $V_{40}Fe_8Ti_{32}Cr_{26}Ni_4$ in the as-cast state.

The predominant phase in all samples is the body-centered cubic phase. A small fraction of the C14 Laves phase is observed in the case of $V_{40}Ni_8Ti_{28}Cr_{24}$. The lattice parameters of the samples are summarized in Table 4.3.2.2-2.

Alloy	Lattice paramter
$V_{40}Fe_8Ti_{28}Cr_{24}$	3.041 Å
$V_{40}Ni_8Ti_{28}Cr_{24}$	3.046 Å
$V_{40}Fe_8Ti_{28}Cr_{16}Ni_8$	3.018 Å
$V_{40}Fe_8Ti_{32}Cr_{20}$	3.056 Å
$V_{40}Fe_8Ti_{32}Cr_{16}Ni_4$	3.047 Å

Table 4.3.2.2-2: Lattice parameters of the materials with various Ti/Cr ratios and Ni contents.

In agreement with previous observations in chapter 4.2.1, the lattice parameter increases with a higher fraction of Ti. No clear correlation is observed between the substitution of Cr or Fe with Ni and the lattice parameter of the resulting alloys.

The surface treatment presented in the following paragraphs was performed by dispersing the activated storage alloys in aqueous solutions at various pH values. Trace amounts of gaseous water contained in H_2 are known to passivate the surface of activated hydrogen storage alloys [19], [147]. Therefore, suitable reactivation procedures had to be developed to enable hydrogen sorption after the dispersion of the storage alloys in aqueous solutions. Several attempts to reactivate the surface-treated alloys in their dehydrogenated state at elevated temperatures and pressures between vacuum and 10 MPa H_2 remained unsuccessful. However, reactivation of the surface-treated materials was succsessful if the (partly) absorbed hydrides were used instead of the desorbed materials. Thermal desorption of the contained hydrogen effectively reactivated the surface, and hydrogen could be ab- and desorbed after this procedure.

Based on the high capacities and low equilibrium pressure well below 0.1 MPa at ambient conditions, $V_{40}Fe_8Ti_{32}Cr_{20}$ and $V_{40}Fe_8Ti_{32}Cr_{16}Ni_4$ were chosen as suitable materials for the leaching experiments.

Several acids (H_2SO_4, HCl, HNO_3, HCl + HNO_3) and bases (NaOH, Na_2CO_3) were tested upon their ability to selectively dissolve V, Fe, Cr and Ti while retaining the Ni in its solid state. While the factor of enrichment is found to be unfavorable for acidic leaching ($\alpha_i \leq 1$ for V, Fe, Cr, Ti; $\alpha_i \geq 1$ for Ni), the desired dissolution of V and Ti can be achieved ($\alpha_i \geq 1$ for V, Ti; $\alpha_i \leq 1$ or 0 for Ni) by leaching under alkaline conditions at pH values < 7. NaOH was selected as an appropriate electrolyte, and several leaching parameters (concentration, temperature, leaching time and ratio between solid and electrolyte) were systematically varied to identify the optimum conditions. In Figure 4.3.2.2-2 the factors of enrichment are shown as a function of the NaOH concentration. Table H-1 in the appendix summarizes the varied parameters.

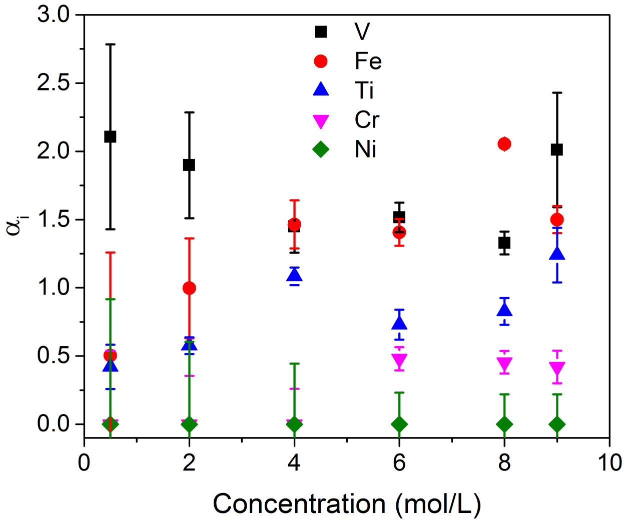

Figure 4.3.2.2-2: Factor of enrichment α_i of $V_{40}Fe_8Ti_{28}Cr_{16}Ni_8$ as a function of the NaOH concentration in the electrolyte. The experiments were performed at 60 °C, 30 min leaching time, 0.15 g powder in 3 mL electrolyte.

No Ni was detected by ICP-OES in the electrolyte, indicating that this element is not dissolved in the electrolyte. The factor of enrichment is $\alpha_{Ni} = 0$ for all tested concentrations of NaOH. For V, α_V is high at low NaOH concentrations (0.5 M and 2 M), decreases at intermediate concentrations, and increases again at $c_{NaOH} = 9$ mol/L. For Ti, the highest factors of enrichment are observed at NaOH concentrations of 8 and 9 mg/L. Ti and V are known to exhibit strong corrosion behavior upon contact with gaseous oxygen, and the formed surface metal oxides considerably inhibit hydrogen diffusion into the bulk [20], [21], [268–270]. Hence, the leaching procedure was optimized with respect to the selective removal primarily of these elements. In section H of the appendix, the variation of the leaching temperature is shown. All remaining parameters were kept constant. Based on these investigations, an appropriate leaching condition was selected as $c_{NaOH} = 9$ mol/L, T = 40 °C, S/L = 0.05 g/mL.

No pronounced changes in the microstructure of the NaOH-treated samples are observed by SEM. SEM micrographs and EDX elemental maps of the cycled and NaOH-treated samples are shown in section E in the appendix. In order to further elucidate the compositions of the leached materials, XPS measurements of the surface and subsurface region were performed. The XPS concentration depth profiles of the materials cycled in pure H_2 and of the NaOH-treated material are shown in Figure 4.3.2.2-3.

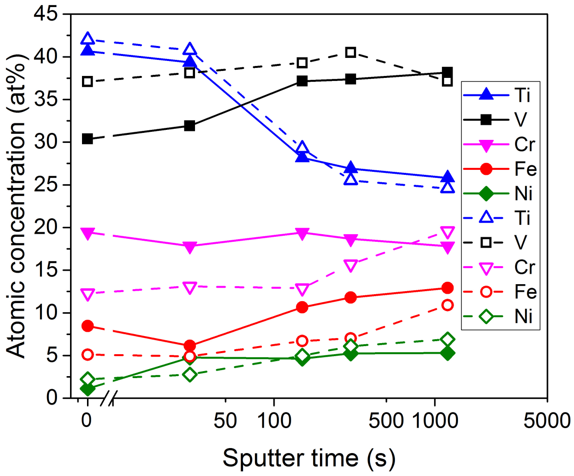

Figure 4.3.2.2-3: Atomic concentrations of the constitutent elements in $V_{40}Fe_8Ti_{32}Cr_{16}Ni_4$ as a function of the sputtering time. Open symbols and dashed lines are the cycled material without air or moisture contact, closed symbols are the leached material. C and O are not included and the concentrations were normalized to 100 %.

For both the cycled and the leached samples, the Ti concentration is higher at the surface and subsurface region of the sample (around 40 at%) as compared to the bulk and decreases with sputtering depth. After 150 s of sputtering, the Ti concentration in the cycled sample is largely constant at 25 – 27 at%. In the case of the leached sample, a further decrease to 20 at% after 1200 s of sputtering is observed. The concentration of V is higher in the surface and subsurface region of the cycled sample than in the case of the NaOH-treated sample. After the fourth sputtering step (1200 s), similar V concentrations are measured in both samples. As expected, the concentration depth profiles of Ni are similar for both samples. For Cr and Fe, the atomic concentrations are reduced as a result of the NaOH treatment.

These results indicate that the elements added to the alloy show different responses to the leaching treatment. In the case of V, the concentration in the surface and subsurface region can be reduced successfully through the leaching procedure. In contrast, the concentration of Ti is not reduced as compared to the cycled sample. This finding is not congruent with the ICP-OES analysis, since Ti ions are reproducibly detected in the electrolyte (9 M NaOH). This would indicate a dissolution of this element during the leaching process. It is likely that Ti atoms diffuse from the bulk of the material to the surface as the surface concentration of Ti is lowered as a result of the leaching procedure. It is known that Ti-Ti bonds and bonds between Ti and other metals can easily be broken. Furthermore, Ti exhibits a highly negative free energy of Ti oxide formation ($TiO_2: -850\ kJ \cdot mol^{-1}O_2$; $V_2O_5: -550\ kJ \cdot mol^{-1}O_2$; $Cr_2O_3: -700\ kJ \cdot mol^{-1}O_2$) [269]. Thus, it is likely that this combination of easily breakable Ti bonds and a strong affinity of Ti for oxygen is responsible for a surface segregation of Ti from the bulk of the particles to the surface. As surface Ti and other metals are dissolved, fresh metal atoms are exposed to the electrolyte. Dissolved oxygen and water molecules adsorb at the surface, and Ti, with its strong tendency to form Ti oxide passivation layers, shows a preferential tendency to diffuse to the surface and form bonds with these oxygen species.

The hydrogen storage properties of $V_{40}Fe_8Ti_{32}Cr_{20}$, $V_{40}Fe_8Ti_{32}Cr_{16}Ni_4$, and leached $V_{40}Fe_8Ti_{32}Cr_{16}Ni_4$ were also investigated. Figure 4.3.2.2-4 shows the pressure-composition isotherms of $V_{40}Fe_8Ti_{32}Cr_{20}$ and $V_{40}Fe_8Ti_{32}Cr_{16}Ni_4$ after 15 cycles and of leached $V_{40}Fe_8Ti_{32}Cr_{16}Ni_4$ after reactivation and three additional cycles in H_2.

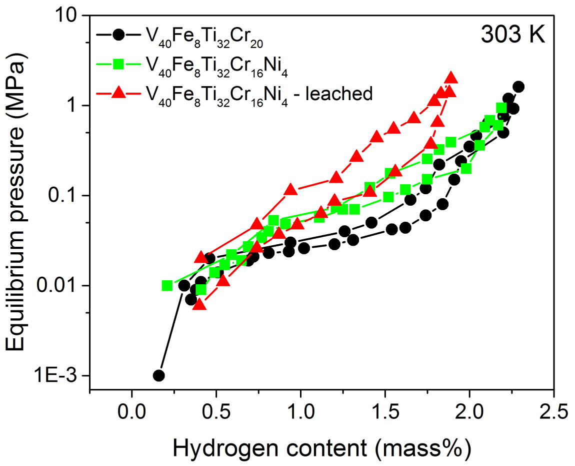

Figure 4.3.2.2-4: Pressure-composition isotherms of $V_{40}Fe_8Ti_{32}Cr_{20}$, $V_{40}Fe_8Ti_{32}Cr_{16}Ni_4$ and NaOH-leached $V_{40}Fe_8Ti_{32}Cr_{16}Ni_4$ at 303 K.

$V_{40}Fe_8Ti_{32}Cr_{20}$ shows a pressure plateau (defined at the midpoint of the plateau) of 0.03 MPa. When the hydrogen content reaches 1.5 mass%, the plateau becomes more sloping. The reversible capacity amounts to 2.1 mass%. The substitution of 4 at% Cr by Ni increases the equilibrium pressure to approximately 0.09 MPa at the midpoint of the plateau, and the entire plateau becomes more sloping. The reversible capacity amounts to approximately 2.0 mass%. The NaOH-leached material exhibits increased equilibrium pressures of hydride formation and dissociation of approximately 0.2 MPa and 0.06 MPa, respectively. Additionally, the plateau exhibits an increased sloping factor of 0.06 as compared to the unmodified material (S = 0.5). NaOH-leaching also effects an increase in hysteresis between the formation and dissociation pressures. For the unmodified material, the hysteresis factor is 1.5, and the hysteresis factor of the NaOH-leached material is 3.3.

The hydrogen absorption kinetic curves of $V_{40}Fe_8Ti_{32}Cr_{16}Ni_4$ and NaOH-leached $V_{40}Fe_8Ti_{32}Cr_{16}Ni_4$ are presented in Figure 4.3.2.2-5.

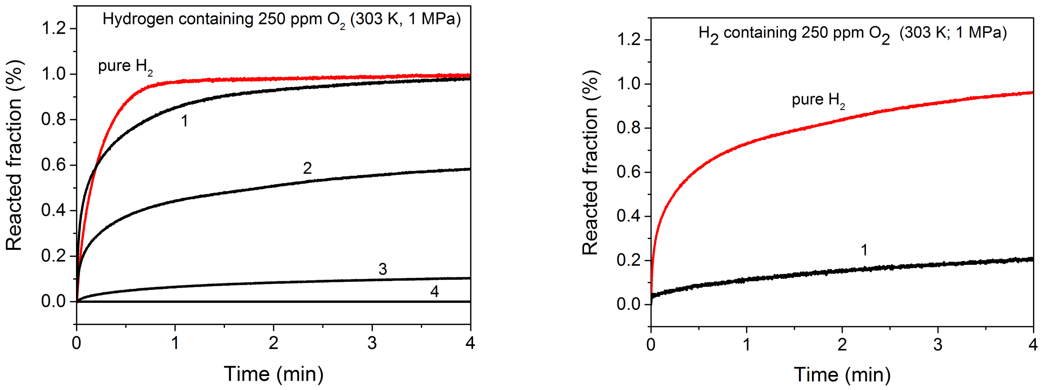

Figure 4.3.2.2-5: Hydrogen absorption kinetic curves of $V_{40}Fe_8Ti_{32}Cr_{16}Ni_4$ (left) and NaOH-leached $V_{40}Fe_8Ti_{32}Cr_{16}Ni_4$ in pure H_2 and in H_2 blended with 250 ppm O_2.

Under pure hydrogen atmosphere, the kinetics of hydrogen absorption are found to be slower than in the case of the sample, which was not NaOH-treated. Only a small amount of hydrogen absorption is detected during the first absorption in O_2-blended H_2. Hence, it is concluded that NaOH-leaching does not represent a viable strategy to improve the cyclic stability of V-Ti-type solid solution alloys.

The second approach that was pursued in order to improve the cyclic stability in oxygen-contaminated hydrogen was the addition of the A element of $LaNi_5$, La, in the form of “mischmetal”. Mischmetal is a mixture mainly of Ce, La and other rare earth metals. With solubilities in V below 0.1 %, rare-earth elements do not dissolve in the V-Ti BCC matrix [235]. Instead, these elements are mainly found at the surface and also in the form of small agglomerates distributed within the alloy with sizes of several µm (see chapter 4.2.2.1 and Ref. [18], [193]). It was investigated whether these rare-earth agglomerates provided diffusion pathways into the bulk of the material also when cycled in O_2-containing H_2. In chapters 4.2.2.1 and 4.2.2.4 three mass% of La/Mm were added to the alloys for deoxidization. In order to increase the number of Mm agglomerates in the alloy, six mass% were added in this part of the investigations.

In Figure 4.3.2.2-5 the SEM micrograph of $V_{40}Fe_8Ti_{26}Cr_{26}$ with addition of 6 mass% Mm is shown.

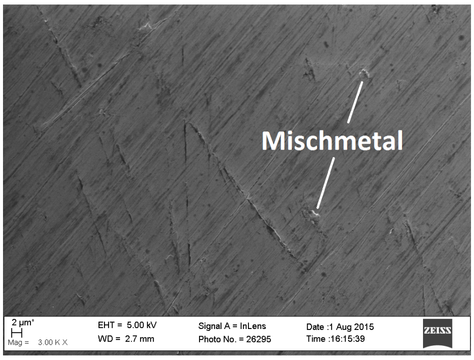

Figure 4.3.2.2-5: SEM micrograph of $V_{40}Fe_8Ti_{26}Cr_{26}$ with addition of 6 mass% Mm in the as-cast state.

Similar to the La agglomerates found in the deoxidized sample in chapter 4.2.2.1, Mm agglomerates with sizes of 1 -2 µm are clearly visible also in this alloy. They are distributed evenly within the alloy and are found at all positions from edge to center. The mischmetal composition is 43 % La, 56 % Ce and 1 % other rare earth metals (Pr, Nd). 59 % oxygen are also detected, which are not included in the calculation. The composition of the BCC main phase is close to the target composition, and a small amount of secondary phase with a composition similar to the C14 Laves phase is identified. The majority of Mm is found at the surface of the alloy ingot; no V, Fe, Cr or Ti are detected within the Mm agglomerates or surface Mm. In average, 0.4 at% Mm are detected within the alloy (surface Mm not included).

The XRD pattern of $V_{40}Fe_8Ti_{26}Cr_{26}$ with addition of 6 mass% Mm is presented in Figure 4.3.2.2-6.

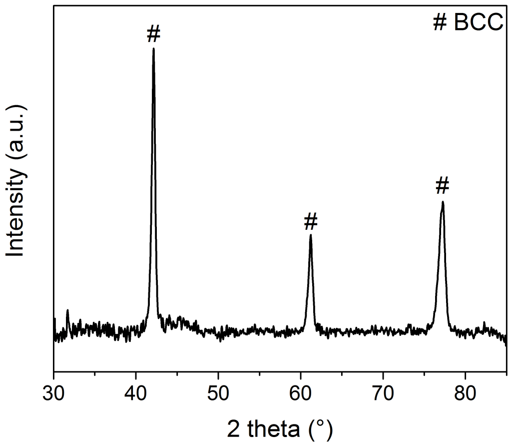

Figure 4.3.2.2-6: XRD pattern of $V_{40}Fe_8Ti_{26}Cr_{26}$ with addition of 6 mass% Mischmetal in the as-cast state.

The material shows a single phase BCC structure. No peaks attributed to Mm (La, Ce or their respective oxides) are identified.

Concentration depth profiles of $V_{40}Fe_8Ti_{26}Cr_{26}$ powder were determined by XPS after three hydrogenation cycles in pure hydrogen. The results are shown in Figure 4.3.2.2-7.

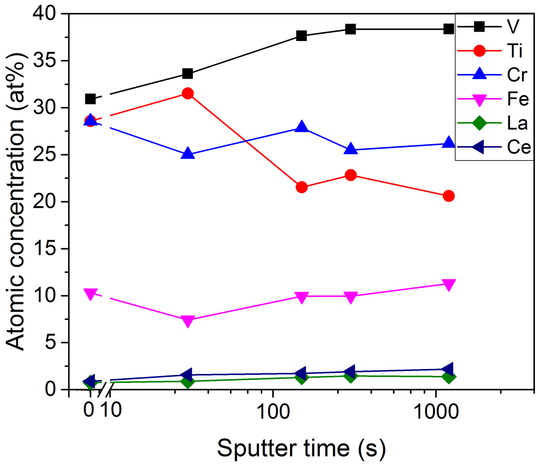

Figure 4.3.2.2-7: Concentration depth profiles of $V_{40}Fe_8Ti_{26}Cr_{26}$ with addition of 6 mass% Mischmetal after three hydrogenation cycles in pure H_2. O and C are not included.

The concentrations of La and Ce are largely constant between 1 and 1.5 at% for La and between 1 and 2 at% for Ce. The concentration profiles of the remaining elements exhibit similar progressions as observed for the samples without Mm addition (see Figure 4.3.2.2-3).

In Figure 4.3.2.2-8 the hydrogen absorption kinetic curves of $V_{40}Fe_8Ti_{26}Cr_{26}$ + 6 mass% Mm in pure H_2 and in H_2 containing 250 ppm O_2 are presented.

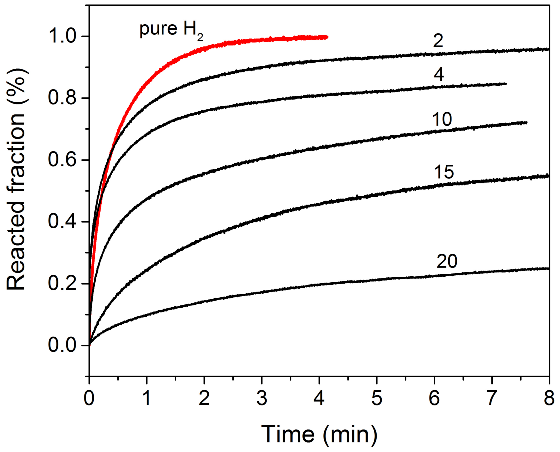

Figure 4.3.2.2-8: Hydrogen absorption kinetic curves of $V_{40}Fe_8Ti_{26}Cr_{26}$ with addition of 6 mass% Mm in pure hydrogen and hydrogen containing 250 ppm O_2 during the first 20 cycles.

The material reacts instantaneously with pure hydrogen, and more than 90 % of the reaction is complete after 90 s. The increased reaction time of this sample in pure H_2 as compared to the sample investigated in Figure 4.3.2.2-2 (90 % reacted in less than one min) most likely originates in the higher amount of Cr (26 at%) and lower fraction of Ti as compared to the sample in Figure 4.3.2.2-2, which contains 20 at% Cr and 32 at% Ti. A higher concentration of Cr, as applied in this material, results in a reduced lattice parameter, and consequently the equilibrium pressure is higher. The sample investigated here thus exhibits a lower driving force for hydrogen absorption, and the absorption kinetics are slower. After two cycles in H_2 containing 250 ppm O_2, the absorption kinetics are slightly reduced, and 90 % of the reaction is complete after 2.5 min. Absorption kinetics further deteriorate after four cycles, and a marked reduction of the storage capacity is observed. It should be noted that the sample without Mm addition does not absorb any hydrogen after four cycles (Fig. 4.3.2.2-2). With further cycling, both hydrogenation kinetics and final capacity decrease. After 20 reaction cycles, the sample still absorbs a detectable amount of hydrogen. This is remarkable when considering that the material without Mm addition does not absorb any hydrogen after four cycles in H_2 containing 250 ppm O_2. However, the reaction kinetics of the Mm-added material decrease considerably during cycling in O_2-blended H_2, and the sample reaches 40 % of the initial capacity after 30 min (Fig. F-4 in the appendix).

These results indicate that the cyclic stability in hydrogen containing oxygen can be considerably improved through the addition of Mm to the alloy. The proposed mechanism for the improvement of the cyclic stability in impure hydrogen is schematically represented in Figure 4.3.2.2-9.

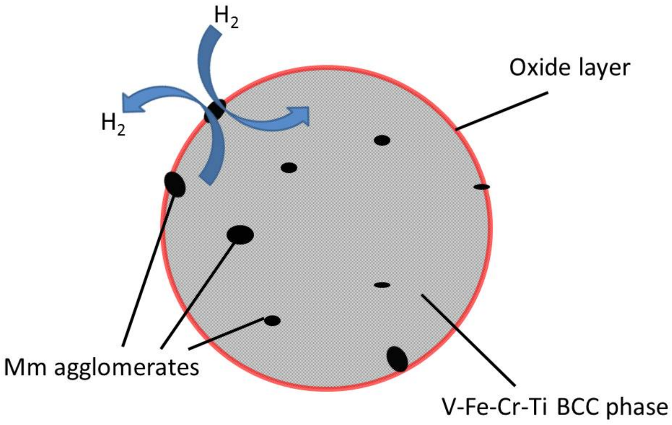

Figure 4.3.2.2-9: Schematic representation of the hydrogen sorption reaction mechanism of a V-Fe-Cr-Ti storage alloy particle with the addition of Mm in O_2-blended H_2.

Upon cycling in hydrogen containing oxygen, metal oxides are formed at the metal surface. The formation of V, Ti, Fe and Cr oxide strongly inhibits adsorption, chemisorption and bulk diffusion of H. This is reflected in the declining hydrogen absorption kinetics and capacity of the unmodified BCC alloy during cycling in hydrogen containing 250 ppm O_2 (Fig. 4.3.2.2-2 and discussion thereafter). When Mm is added to material, rare earth oxides are formed at the gas-solid interface of the Mm agglomerates. It is believed that they act as a "H-transparent window" through the "intransparent" BCC metal oxide layer and thus enable hydrogen diffusion into the bulk where a pure V-, Ti-, Cr- and Fe oxide layer would inhibit such diffusion. This is in agreement with the surface properties of $LaNi_5$, which was taken as a model system for the surface modification of the present work. Schlapbach *et al.* showed that surface segregation occurs on the $LaNi_5$ surface into a La-enriched surface layer mainly composed of La oxide and metallic Ni agglomerates. According to Schlapbach *et al.,* La oxide allows the penetration of molecular and atomic hydrogen, which then dissociate into atomic H at the surface of the Ni particles. This is followed by bulk diffusion of the H atoms. This protective overlayer is believed to be responsible for the high tolerance against gaseous impurities and the ease of initial activation of $LaNi_5$ as compared to other intermetallic hydrides [271]. In our case, we believe that the Mm inclusions provide diffusion pathways from the surface into the bulk of the alloy. It is likely that molecular hydrogen diffuses through the La and Ce oxide layer and dissociates at the interface of the Mm agglomerates and the BCC metal surface (the BCC metals exhibit a higher potential for hydrogen dissociation than La or Ce [272–274]). Atomic hydrogen then diffuses into the bulk and forms the metal hydride.

To further elucidate the surface properties of the Mm-added BCC samples after cycling in pure H_2 and in H_2 containing 250 ppm O_2, XPS measurements of the surface after various sputtering times were performed. In brief, the XP spectra of La and Ce were not useful to gain further information on the oxidation states of La and Ce (the constituents of Mm) before and after cycling in O_2-contaminated hydrogen. The intensity of the peaks was very weak, and hence no conclusions could be drawn.

Long-term cycling experiments of $V_{40}Fe_8Ti_{26}Cr_{26}$ with and without addition of Mm in O_2-contaminated hydrogen are currently performed at the JRC in Petten, Netherlands. These results shall be integrated in a later publication.

5 *Summary and Conclusion*

In this work, the effect of impurities on the performance and cost of AB-, AB_2- and AB_5-type intermetallic hydrides and V-Fe-Cr-Ti-based hydrogen storage materials has been investigated. V-Fe-Cr-Ti-based hydrogen storage materials show higher reversible hydrogen storage capacities than the optimized and commercially available AB-, AB_2- and AB_5-type hydrogen storage alloys. This property renders them attractive for stationary hydrogen storage applications, such as the liquid organic reaction cycle (LORC) process for the storage of thermal energy.

The first part of this work is focussed on cost reduction possibilities of V-Fe-Cr-Ti-based solid solution alloys.

First, several alloys with varying Ti/Cr ratios were synthesized. They exhibit high total and reversible gravimetric H storage capacities around 3.5 mass% H and 2.3 mass% H, respectively. The thermodynamic properties of hydride formation and dissociation can easily be tailored through the modification of the microstructure (i.e., the lattice parameter). Alloys with suitable thermodynamic properties to match the requirements of the LORC process are designed.

Second, the effects of high residual oxygen concentration in the V raw metal (10,000 ppm O for high-oxygen V; 300 ppm for low-oxygen V) on the microstructural and thermodynamic properties of the resulting V-Fe-Cr-Ti-based H storage material were investigated for the first time. A high oxygen concentration promotes the formation of a Ti-rich secondary phase isostructural with α-Ti, which is formed during the synthesis of the alloy by arc melting. The concentrations of O and Ti in the BCC main phase are reduced through the formation of the secondary phase. Thermodynamic properties of the sample prepared with high-oxygen V are altered: a high oxygen content leads to an increased equilibrium pressure of hydride formation and dissociation. Furthermore, the total hydrogen capacity of the high-oxygen sample is reduced. Deoxidization is achieved through the addition of 3 mass% (1 at%) rare earth metal (La, Ce or Y). This results in comparable thermodynamic properties and hydrogen capacity as the material prepared with low-oxygen V.

Third, the effects of two different commercial ferrovanadium raw materials (FeV 1 and FeV 2) were investigated with the aim of synthesizing low-cost hydrogen storage alloys. FeV 1 and FeV 2 contained varying amounts of impurities, such as O, C, N, Si or Al.

The work contains the first systematic study on the effects of substituting high-purity V and Fe with FeV (FeV 1) describing the microstructural, thermodynamic and cyclic effects of the substitution. An increased level of substitution promotes the formation of secondary phases with C14 Laves phase structure. A gradual increase in equilibrium pressures of hydride formation and dissociation, hysteresis and plateau slope is observed with a higher degree of substitution. Furthermore, the reversible capacity decreases from 2.2 mass% H to 1.6 mass% H as the level of substitution increases from 0 to 0.9. A degradation of reversible capacity by 23 % is observed after 50 cycles irrespective of the level of substitution. The alteration of thermodynamic properties correlates well with the increased concentrations of impurities in the alloy.

Improved microstructural and hydrogen storage properties are achieved when high-purity V and Fe are substituted by FeV 2 as compared to FeV 1. This raw material contains a lower fraction of impurities than FeV 1, and thus the effects related to the introduction of these impurities into the alloy are less pronounced. A lower fraction of C14 secondary Laves phase is found in the fully substituted material, and the total and reversible capacity is less affected than in the case of the material substituted with FeV 1. Therefore, FeV 2 is identified as more suitable for further investigations than FeV 1.

Fourth, pursuing a similar strategy of using cheaper, less pure intermediate products of the Ti production process, Ti sponge was identified as a low-cost alternative to high-purity Ti metal. The microstructural and thermodynamic effects of replacing high-purity Ti with Ti sponge were investigated in this work for the first time. No significant effects are observed, and hence Ti sponge represents a viable low-cost alternative to purified Ti.

Fifth, both high-purity V and Ti were substituted with FeV 2 and Ti sponge. 3 mass% Mischmetal (Mm) were added for deoxidization. The influence of the synthesis conditions on the hydrogen storage properties of the resulting alloys was studied in this work for the first time. Through variation of the arc melting current, a correlation between the preparation conditions and the content of the impurities C, N and O in the obtained hydrogen storage alloys was identified. It is believed that impurities with a high vapor pressure evaporate during the melting procedure. A higher melting current effects a lower concentration of impurities, and the hydrogen storage properties of the resulting metal hydrides improves as the concentrations of impurities decrease. Cost analysis of the hydrogen storage materials prepared with high-purity V and Ti and with FeV and Ti sponge yield a considerable cost reduction potential. The raw metal price to store an equal amount of hydrogen can be reduced by 88 % if FeV 2 and Ti sponge are used.

The second part of this work deals with the interactions of liquid or gaseous impurities with the surface of the metal hydrides and the resulting effects on the performance.

First, a systematic study of the passivation behavior of the AB-, AB_2- and AB_5-type transition metal hydrides TiFe, $Ti_{0.95}Zr_{0.05}Mn_{1.49}V_{0.45}Fe_{0.06}$ („Hydralloy C5“), $LaNi_5$ and the solid solution alloy $V_{40}Fe_8Ti_{26}Cr_{26}$ is presented upon dispersion of the hydrides in liquid toluene or acetone. $LaNi_5$ is the most tolerant of the studied materials, since it is affected neither by acetone nor by toluene treatment. Hydrogen is confined in the hydrides of TiFe, Hydralloy C5 and $V_{40}Fe_8Ti_{26}Cr_{26}$ after acetone treatment in spite of a thermodynamic driving force for hydrogen desorption. $V_{40}Fe_8Ti_{26}Cr_{26}$ hydride is also passivated by toluene treatment, while TiFeH is only mildly affected by toluene treatment, and Hydralloy C5 hydride is not affected at all. Hydrogen desorption of $V_{40}Fe_8Ti_{26}Cr_{26}$ hydride in liquid acetone yields CO, propene and propane. Methylcyclohexane is formed during hydrogen desorption in liquid toluene. These products are not detected if a dehydrogenated sample was used. This indicates a metal hydride surface reactivity that is considerably higher when the surface is populated by atomic hydrogen atoms during hydrogen desorption as compared to the dehydrogenated alloy surface. Investigation of the surface and subsurface regions of cycled and acetone- or toluene-treated $V_{40}Fe_8Ti_{26}Cr_{26}$ hydrides revealed increased concentrations of hydrocarbons and C-O-related species in these regions after contact with the organic liquids. It is shown that the surface deposition and diffusion of carbon-containing species to the subsurface is responsible for the inhibition of hydrogen desorption from the bulk. Hydrogen absorption of $V_{40}Fe_8Ti_{26}Cr_{26}$ after contact with acetone or toluene in the desorbed state proceeds at similar absorption rates as compared to the sample that is not brought into contact with these substances. This observation further supports the conclusion that the hydride surface reacts with the organics predominantly during hydrogen desorption.

Second, the effects of gaseous impurities blended with H_2 on the absorption kinetics of V-Fe-Ti-Cr-based solid solution alloys were studied in this work for the first time. The impurities toluene, O_2, N_2 and CO_2 are studied, since these gases could possibly come into contact with the hydrogen storage alloy in the LORC process. Trace amounts of gaseous toluene or N_2 are found to be innocuous towards the absorption kinetics and capacity of the storage material. Cycling in CO_2- or O_2-contaminated H_2 inhibits the hydrogen absorption reactions after a few reaction cycles. In the case of O_2-blended H_2, a reactivation procedure consisting of heating up the storage material to a higher temperature and subsequent cycling in pure H_2 is developed. The surface properties of V-Fe-Cr-Ti-type solid solution alloys are investigated before and after cycling in H_2 containing O_2. Surface metal oxides and hydroxides are observed after cycling in O_2-blended H_2. It is likely that these surface layers are responsible for the inhibition of the hydrogenation reaction.

Third, two novel approaches of engineering surface structures, which exhibit improved tolerance towards O_2, are presented. The approaches are based on the observation that $LaNi_5$ shows the highest tolerance towards O_2. It was investigated whether the introduction of the A- or B-element contained in $LaNi_5$ (La or Ni) improved the cyclic stability of V-Fe-Cr-Ti-based solid solution alloys.

In the first approach, it was tested whether a surface layer enriched with Ni would improve the hydrogen sorption properties of V-Fe-Ti-Cr solid solution alloys in O_2-contaminated H_2. Hence, a varying amount of Ni was introduced into the alloys and the resulting effects on the hydrogen sorption properties were investigated. It was found that a small amount of 4 at% Ni shows negligible effects on the structure and hydrogen sorption properties, while a larger amount of 8 at% affects the microstructure through the formation of a Ti-Ni phase and markedly reduces the hydrogen capacity. Ni enrichment at the surface was attempted by selectively removing the other constituting elements V, Fe, Ti and Cr from the surface of the alloy in a base leaching procedure. Optimum leaching conditions with respect to a removal primarily of V and Ti while retaining Ni in the solid were determined through a variation of several parameters. Electrolyte concentration, leaching time, leaching temperature and the ratio between solid and electrolyte were systematically varied in order to identify the optimum conditions. With an optimized leaching procedure (9 mol/L NaOH solution, 30 min leaching time at 40 °C), a sufficient amount of material was synthesized for an in-depth characterization of all relevant properties. It was shown by XPS analysis that V can be successfully removed from the surface, but the concentration depth profiles of Ti and Ni are identical to those of the reference samples. In the case of Ti, this observation contradicts the ICP-OES result, since Ti is reproducibly measured in the electrolytes. It is proposed that a segregation of Ti from the bulk of the material to the surface occurs when Ti atoms are dissolved in the electrolyte, and that this surface segregation is responsible for the similar Ti concentration profiles irrespective of the sample history. Due to the segregation of Ti, an enrichment of Ni at the surface cannot be achieved. The hydrogen storage properties of the NaOH-treated material were determined, and a reduction in reversible storage capacity from 2.0 mass% H without NaOH treatment to approximately 1.3 mass% H after NaOH treatment along with an increase in plateau slope and hysteresis is observed. Hydrogen absorption of H_2/O_2 mixtures show that the NaOH-treated sample exhibit inferior cyclic stability and kinetics than the pristine sample. On the basis of these results, it is concluded that the concept of enriching Ni at the surface does not represent a suitable strategy to improve the hydrogenation properties in O_2-contaminated H_2.

The second approach involved the introduction of the A element of $LaNi_5$ (La, used here in the form of Mm) into the V-Fe-Ti-Cr solid solution alloy. Microstructural analysis reveals the presence of Mm agglomerates with diameters of 1-2 µm. The cyclic stability of the obtained storage material in H_2 blended with 250 ppm O_2 is found to be considerably higher than of the material without added Mm. Four cycles are sufficient to deactivate the pristine sample. The Mm-added sample still absorbed a detectable amount of hydrogen after 20 cycles. These results suggest that small Mm agglomerates distributed within the alloy provide diffusion pathways into the bulk of the material when the remaining V-Fe-Ti-Cr surface is already intransparent for H_2 due to the formation of diffusion-inhibiting oxides.

6 Bibliography

[1] "BP Statistical Review of World Energy" 2013.

[2] "IEA World Energy Outlook," 2006.

[3] L. F. Cabeza, *Advances in Thermal Energy Storage Systems*. Woodhead Publishing, 2014.

[4] H. Kreuder, C. Müller, J. Meier, U. Gerhards, R. Dittmeyer, and P. Pfeifer, "Catalyst development for the dehydrogenation of MCH in a microstructured membrane reactor—For heat storage by a Liquid Organic Reaction Cycle," *Catalysis Today*, vol. 242, pp. 211–220, Mar. 2015.

[5] L. Schlapbach and A. Züttel, "Hydrogen-storage materials for mobile applications.," *Nature*, vol. 414, no. 6861, pp. 353–8, Nov. 2001.

[6] A. Züttel, "Hydrogen storage methods.," *Die Naturwissenschaften*, vol. 91, no. 4, pp. 157–72, Apr. 2004.

[7] M. Fichtner, "Nanotechnological Aspects in Materials for Hydrogen Storage," *Advanced Engineering Materials*, vol. 7, no. 6, pp. 443–455, Jun. 2005.

[8] P. R. Wilson, R. C. Bowman, J. L. Mora, and J. W. Reiter, "Operation of a PEM fuel cell with LaNi4.8Sn0.2 hydride beds," *Journal of Alloys and Compounds*, vol. 446–447, pp. 676–680, Oct. 2007.

[9] E. Akiba and H. Iba, "Hydrogen absorption by Laves phase related BCC solid solution," *Intermetallics*, vol. 6, no. 6, pp. 461–470, Jan. 1998.

[10] E. Akiba and M. Okada, "M etallic Hydrides III : Cubic Solid- Solution Alloys," *MRS Bulletin*, pp. 699–703, 2002.

[11] R. Moskalyk and A. Alfantazi, "Processing of vanadium: a review," *Minerals Engineering*, vol. 16, no. 9, pp. 793–805, Sep. 2003.

[12] S. Nakagawa, Personal communication, Taiyo Koko Ltd., 2013.

[13] G. Bauer, V. Güther, and H. Hess, "Vanadium and vanadium compounds," *Ullmann's Encyclopedia of Industrial Chemistry*, 1996.

[14] H. Sibum, V. Güther, and O. Roidl, "Titanium, titanium alloys, and titanium compounds," Journal *of Industrial Chemistry*, 2000.

[15] Metal pages [Online]. Available: http://www.metal-pages.com/, May 2016.

[16] Y. Nakamura, J. Nakamura, K. Sakaki, K. Asano, and E. Akiba, "Hydrogenation properties of Ti–V–Mn alloys with a BCC structure containing high and low oxygen concentrations," *Journal of Alloys and Compounds*, vol. 509, no. 5, pp. 1841–1847, Feb. 2011.

[17] M. Tsukahara, K. Takahashi, a Isomura, and T. Sakai, “Influence of oxygen on hydrogen storage and electrode properties for micro-designed V-based battery alloys,” *Journal of Alloys and Compounds*, vol. 265, no. 1–2, pp. 257–263, Jan. 1998.

[18] J. Mi, F. Lü, X. Liu, L. Jiang, Z. Li, and S. Wang, “Enhancement of cerium and hydrogen storage property of a low-cost Ti-V based BCC alloy prepared by commercial ferrovanadium,” *Journal of Rare Earths*, vol. 28, no. 5, pp. 781–784, Oct. 2010.

[19] G. D. Sandrock and P. D. Goodell, “Cyclic life of metal hydrides with impure hydrogen: Overview and engineering considerations,” *Journal of the Less Common Metals*, vol. 104, no. 1, pp. 159–173, Dec. 1984.

[20] I. N. Filimonov, V. V. Yuschenko, a. V. Smirnov, S. N. Nesterenko, I. V. Dobryakova, I. I. Ivanova, E. N. Lubnin, L. Galperin, and R. H. Jensen, “Deactivation of titanium during temperature-induced hydrogen absorption–desorption cycling,” *Journal of Alloys and Compounds*, vol. 390, no. 1–2, pp. 144–154, Mar. 2005.

[21] I. N. Filimonov, a. V. Smirnov, S. N. Nesterenko, I. I. Ivanova, L. B. Galperin, and R. H. Jensen, “Deactivation of titanium during temperature-induced hydrogen absorption–desorption cycling,” *Journal of Alloys and Compounds*, vol. 422, no. 1–2, pp. 258–263, Sep. 2006.

[22] T. Tamura, T. Kazumi, A. Kamegawa, H. Takamura, and M. Okada, “Protium absorption properties and protide formations of Ti–Cr–V alloys,” *Journal of Alloys and Compounds*, vol. 356–357, pp. 505–509, Aug. 2003.

[23] J. Xu, R. Z. Wang, and Y. Li, “A review of available technologies for seasonal thermal energy storage,” *Solar Energy*, vol. 103, pp. 610–638, May 2014.

[24] J. Cot-Gores, A. Castell, and L. F. Cabeza, “Thermochemical energy storage and conversion: A-state-of-the-art review of the experimental research under practical conditions,” *Renewable and Sustainable Energy Reviews*, vol. 16, no. 7, pp. 5207–5224, Sep. 2012.

[25] T. W. Leland and G. A. Mansoori, “Basic Principles of Classical and Statistical Thermodynamics,” 1986. Available: http://www.uic.edu/labs/trl/1.OnlineMaterials/BasicPrinciplesByTWLeland.pdf.

[26] Z. Lavan and J. Thompson, “Experimental study of thermally stratified hot water storage tanks,” *Solar Energy*, pp. 519–524, 1977.

[27] J. E. Pacheco, S. K. Showalter, and W. J. Kolb, “Development of a Molten-Salt Thermocline Thermal Storage System for Parabolic Trough Plants,” *Journal of Solar Energy Engineering*, vol. 124, no. 2, p. 153, 2002.

[28] U. Herrmann, B. Kelly, and H. Price, “Two-tank molten salt storage for parabolic trough solar power plants,” *Energy*, vol. 29, no. 5–6, pp. 883–893, Apr. 2004.

[29] A. Shitzer and M. Levy, “Transient Behavior of a Rock-Bed Thermal Storage System Subjected to Variable Inlet Air Temperatures: Analysis and Experimentation,” *Journal of Solar Energy Engineering*, vol. 105, no. 2, p. 200, 1983.

[30] D. Laing, W.-D. Steinmann, R. Tamme, and C. Richter, “Solid media thermal storage for parabolic trough power plants,” *Solar Energy*, vol. 80, no. 10, pp. 1283–1289, Oct. 2006.

[31] H. Mehling and L. F. Cabeza, *Heat and Cold Storage with PCM: An Up to Date Introduction into Basics and Applications*. Springer Berlin Heidelberg, 2008.

[32] A. I. Fernandez, M. Martínez, M. Segarra, I. Martorell, and L. F. Cabeza, “Selection of materials with potential in sensible thermal energy storage,” *Solar Energy Materials and Solar Cells*, vol. 94, no. 10, pp. 1723–1729, Oct. 2010.

[33] A. Abhat, “Low temperature latent heat thermal energy storage: heat storage materials,” *Solar energy*, vol. 30, pp. 313–332, 1983.

[34] L. Cabeza, H. Mehling, S. Hiebler, and F. Ziegler, “Heat transfer enhancement in water when used as PCM in thermal energy storage,” *Applied thermal engineering*, vol. 22, pp. 1141–1151, 2002.

[35] R. Naumann and H. Emons, “RESULTS OF THERMAL ANALYSIS FOR INVESTIGATION OF SALT HYDRATES AS LATENT HEAT-STORAGE MATERIALS,” *Journal of Thermal Analysis*, vol. 35, pp. 1009–1031, 1989.

[36] D. Hawes, D. Feldman, and D. Banu, “Latent heat storage in building materials,” *Energy and buildings*, vol. 20, pp. 77–86, 1993.

[37] N. Yoneda and S. Takanashi, “Eutectic mixtures for solar heat storage,” *Solar Energy*, vol. 21, no. 1, pp. 61–63, Jan. 1978.

[38] A.-M. a. El-Bassuoni, A. M. Tayeb, N. H. Helwa, and A. M. Fathy, “Modification of urea–sodium acetate trihydrate mixture for solar energy storage,” *Renewable Energy*, vol. 28, no. 10, pp. 1629–1643, Aug. 2003.

[39] G. A. Lane, “Low temperature heat storage with phase change materials,” *International Journal of Ambient Energy*, vol. 1, no. 3, pp. 155–168, Mar. 1980.

[40] “Climator,” Available: http://www.climator.com/en/home/, May 2015.

[41] “Rubitherm PCM,” Available: http://www.rubitherm.com/english/index.htm, May 2015.

[42] “Cristopia,”Available: http://www.cristopia.com, May 2015.

[43] A. Solé, I. Martorell, and L. F. Cabeza, “State of the art on gas–solid thermochemical energy storage systems and reactors for building applications,” *Renewable and Sustainable Energy Reviews*, vol. 47, pp. 386–398, Jul. 2015.

[44] G. Ervin, “Solar Heat Storage Using Chemical Reactions,” *Journal of solid state chemistry*, vol. 22, pp. 51–61, 1977.

[45] K. Oura, V. G. Lifshits, A. Saranin, A. V. Zotov, and M. Katayama, *Surface Science - An Introduction*. Springer Berlin Heidelberg, 2003.

[46] A. Hauer, “Evaluation of adsorbent materials for heat pump and thermal energy storage applications in open systems,” *Adsorption*, vol. 13, no. 3–4, pp. 399–405, Sep. 2007.

[47] D. Stitou, N. Mazet, and M. Bonnissel, “Performance of a high temperature hydrate solid/gas sorption heat pump used as topping cycle for cascaded sorption chillers,” *Energy*, vol. 29, no. 2, pp. 267–285, Feb. 2004.

[48] V. M. van Essen, H. a. Zondag, J. C. Gores, L. P. J. Bleijendaal, M. Bakker, R. Schuitema, W. G. J. van Helden, Z. He, and C. C. M. Rindt, “Characterization of MgSO[sub 4] Hydrate for Thermochemical Seasonal Heat Storage,” *Journal of Solar Energy Engineering*, vol. 131, no. 4, p. 041014, 2009.

[49] T. X. Li, R. Z. Wang, J. K. Kiplagat, L. W. Wang, and R. G. Oliveira, “Thermodynamic study of a combined double-way solid–gas thermochemical sorption refrigeration cycle,” *International Journal of Refrigeration*, vol. 32, no. 7, pp. 1570–1578, Nov. 2009.

[50] R. G. Oliveira, R. Z. Wang, J. K. Kiplagat, and C. Y. Wang, “Novel composite sorbent for resorption systems and for chemisorption air conditioners driven by low generation temperature,” *Renewable Energy*, vol. 34, no. 12, pp. 2757–2764, Dec. 2009.

[51] M. Pons and P. Grenier, “Experimental data on a solar-powered ice maker using activated carbon and methanol adsorption pair,” *Journal of solar energy …*, vol. 109, no. November 1987, pp. 303–310, 1987.

[52] B. Bogdanović, A. Reiser, and K. Schlichte, “Thermodynamics and dynamics of the Mg–Fe–H system and its potential for thermochemical thermal energy storage,” *Journal of Alloys and Compounds*, vol. 345, pp. 77–89, 2002.

[53] A. Reiser, B. Bogdanović, and K. Schlichte, “The application of Mg-based metal-hydrides as heat energy storage systems,” *International Journal of Hydrogen Energy*, vol. 25, 2000.

[54] M. Felderhoff and B. Bogdanović, “High temperature metal hydrides as heat storage materials for solar and related applications.,” *International journal of molecular sciences*, vol. 10, no. 1, pp. 325–44, Jan. 2009.

[55] M. Linder, R. Mertz, and E. Laurien, “Experimental results of a compact thermally driven cooling system based on metal hydrides,” *International Journal of Hydrogen Energy*, vol. 35, no. 14, pp. 7623–7632, Jul. 2010.

[56] H. Klein and M. Groll, “Development of a two-stage metal hydride system as topping cycle in cascading sorption systems for cold generation,” *Applied thermal engineering*, vol. 22, pp. 631–639, 2002.

[57] C. Corgnale, B. Hardy, T. Motyka, R. Zidan, J. Teprovich, and B. Peters, “Screening analysis of metal hydride based thermal energy storage systems for concentrating solar power plants,” *Renewable and Sustainable Energy Reviews*, vol. 38, pp. 821–833, Oct. 2014.

[58] K. E. N’Tsoukpoe, H. Liu, N. Le Pierrès, and L. Luo, “A review on long-term sorption solar energy storage,” *Renewable and Sustainable Energy Reviews*, vol. 13, no. 9, pp. 2385–2396, Dec. 2009.

[59] W. Wongsuwan and S. Kumar, “A review of chemical heat pump technology and applications,” *Applied Thermal Engineering*, vol. 21, pp. 1489–1519, 2001.

[60] "D.O.E. ARPA-E High Energy Advanced Thermal Storage. DOE-FOA-0000471, 2011,". Available: https://arpa-e-foa.energy.gov/FileContent.aspx?FileID=79a5 de09-8bfd-4590-9cb4-e42578248d90, July 2015.

[61] P. a. Ward, C. Corgnale, J. a. Teprovich, T. Motyka, B. Hardy, B. Peters, and R. Zidan, "High performance metal hydride based thermal energy storage systems for concentrating solar power applications," *Journal of Alloys and Compounds*, pp. 10–14, Jan. 2015.

[62] H. Le Chatelier and O. Boudouard, "On the flammable limits of gas mixtures," *Process Safety Progress*, vol. 24, no. 1, pp. 3–5, Mar. 2005.

[63] J. Larjola, "Electricity from industrial waste heat using high-speed organic Rankine cycle (ORC)," *International Journal of Production Economics*, vol. 41, no. 1–3, pp. 227–235, Oct. 1995.

[64] H. Chen, D. Y. Goswami, and E. K. Stefanakos, "A review of thermodynamic cycles and working fluids for the conversion of low-grade heat," *Renewable and Sustainable Energy Reviews*, vol. 14, no. 9, pp. 3059–3067, Dec. 2010.

[65] J. Lund, "Combined Heat and Power plant Neustadt-Glewe, Germany," *Geo-Heat Center Quarterly Bulletin*, pp. 31–34, 2005.

[66] I. Obernberger, "Decentralized biomass combustion: state of the art and future development11Paper to the keynote lecture of the session ``Processes for decentralized heat and power production based on cumbustion'' at the 9th European Bioenergy Conference, June 1996, Copen," *Biomass and Bioenergy*, vol. 14, no. 1, pp. 33–56, Mar. 1998.

[67] I. Obernberger, P. Thonhofer, and E. Reisenhofer, "Description and evaluation of the new 1 , 000 kW el Organic Rankine Cycle process integrated in the biomass CHP plant in Lienz , Austria 2 Introduction and technical description of the biomass-fired CHP plant in Lienz," *Euroheat & Power*, pp. 1–17, 2002.

[68] B. F. Tchanche, G. Papadakis, G. Lambrinos, and A. Frangoudakis, "Fluid selection for a low-temperature solar organic Rankine cycle," *Applied Thermal Engineering*, vol. 29, no. 11–12, pp. 2468–2476, Aug. 2009.

[69] A. Schuster, S. Karellas, E. Kakaras, and H. Spliethoff, "Energetic and economic investigation of Organic Rankine Cycle applications," *Applied Thermal Engineering*, vol. 29, no. 8–9, pp. 1809–1817, Jun. 2009.

[70] M. Ball and M. Wietschel, *The hydrogen economy - opportunities and challenges*. Cambridge University Press, 2009.

[71] R. Plank, F. Steimle, and K. Stephan, *Handbuch der Kältetechnik*. Springer Berlin Heidelberg, 1988.

[72] N. L. Rosi, J. Eckert, M. Eddaoudi, D. T. Vodak, J. Kim, M. O'Keeffe, and O. M. Yaghi, "Hydrogen storage in microporous metal-organic frameworks.," *Science (New York, N.Y.)*, vol. 300, no. 5622, pp. 1127–9, May 2003.

[73] Y. Ye, C. C. Ahn, C. Witham, B. Fultz, J. Liu, a. G. Rinzler, D. Colbert, K. a. Smith, and R. E. Smalley, “Hydrogen adsorption and cohesive energy of single-walled carbon nanotubes,” *Applied Physics Letters*, vol. 74, no. 16, p. 2307, 1999.

[74] Z. Yang, Y. Xia, and R. Mokaya, “Enhanced Hydrogen Storage Capacity of High Surface Area Zeolite-like Carbon Materials,” *Journal of the American Chemical Society*, vol. 129, no. 6, pp. 1673–1679, Feb. 2007.

[75] W. Peters, A. Seidel, S. Herzog, A. Bösmann, W. Schwieger, and P. Wasserscheid, “Macrokinetic effects in perhydro-N-ethylcarbazole dehydrogenation and H 2 productivity optimization by using egg-shell catalysts,” *Energy Environ. Sci.*, vol. 8, no. 10, pp. 3013–3021, 2015.

[76] V. N. Emel’yanenko, M. a. Varfolomeev, S. P. Verevkin, K. Stark, K. Müller, M. Müller, A. Bösmann, P. Wasserscheid, and W. Arlt, “Hydrogen Storage: Thermochemical Studies of N - Alkylcarbazoles and Their Derivatives as a Potential Liquid Organic Hydrogen Carriers,” *The Journal of Physical Chemistry C*, vol. 119, no. 47, pp. 26381–26389, Nov. 2015.

[77] R. Biniwale, S. Rayalu, S. Devotta, and M. Ichikawa, “Chemical hydrides: A solution to high capacity hydrogen storage and supply,” *International Journal of Hydrogen Energy*, vol. 33, no. 1, pp. 360–365, Jan. 2008.

[78] S. Hodoshima, S. Takaiwa, A. Shono, K. Satoh, and Y. Saito, “Hydrogen storage by decalin/naphthalene pair and hydrogen supply to fuel cells by use of superheated liquid-film-type catalysis,” *Applied Catalysis A: General*, vol. 283, no. 1–2, pp. 235–242, Apr. 2005.

[79] M. R. Usman, D. L. Cresswell, and a. a. Garforth, “By-Products Formation in the Dehydrogenation of Methylcyclohexane,” *Petroleum Science and Technology*, vol. 29, no. 21, pp. 2247–2257, Sep. 2011.

[80] M. V. C. Sastri, B. Viswanathan, and S. S. Murthy, *Metal hydrides: fundamentals and applications*. Narosa Publishing House [publisher], 1998.

[81] M. Fichtner, “Preface to the viewpoint set: Nanoscale materials for hydrogen storage,” *Scripta Materialia*, vol. 56, no. 10, pp. 801–802, May 2007.

[82] U. Eberle, M. Felderhoff, and F. Schüth, “Chemical and physical solutions for hydrogen storage.,” *Angewandte Chemie (International ed. in English)*, vol. 48, no. 36, pp. 6608–30, Jan. 2009.

[83] V. Bérubé, G. Radtke, M. Dresselhaus, and G. Chen, “Size effects on the hydrogen storage properties of nanostructured metal hydrides: A review,” *International Journal of Energy Research*, vol. 31, no. 6–7, pp. 637–663, May 2007.

[84] A. Sieverts, *Die aufnahme von gasen durch metalle*, Zeitschrift für Metallkunde, vol. 21. p. 37−46.

[85] Y. Nakamura and E. Akiba, “Hydriding properties and crystal structure of NaCl-type mono-hydrides formed from Ti–V–Mn BCC solid solutions,” *Journal of Alloys and Compounds*, vol. 345, no. 1–2, pp. 175–182, Oct. 2002.

[86] M. H. MENDELSOHN, D. M. GRUEN, and A. E. DWIGHT, “LaNi5-xAlx is a versatile alloy system for metal hydride applications,” *Nature*, vol. 269, no. 5623, pp. 45–47, Sep. 1977.

[87] C. B. Magee, J. Liu, and C. E. Lundin, “Relationships between intermetallic compound structure and hydride formation,” *Journal of the Less Common Metals*, vol. 78, no. 1, pp. 119–138, 1981.

[88] C. E. Lundin, F. E. Lynch, and C. B. Magee, “A correlation between the interstitial hole sizes in intermetallic compounds and the thermodynamic properties of the hydrides formed from those compounds,” *Journal of the Less Common Metals*, vol. 56, no. 1, pp. 19–37, 1977.

[89] T. Takeshita and K. G. Jr, “Low-temperature heat-capacity study of Haucke compounds CaNi5, YNi5, LaNi5, and ThNi5,” *Physical Review B*, vol. 21, no. 12, p. 5636, 1980.

[90] H. Lee, “Solubility of hydrogen and bulk modulus in transition metals,” *Journal of Materials Science*, vol. 13, pp. 1374–1380, 1978.

[91] Y. Wei-Ming and R. McLellan, “Thermodynamics of dilute platinum-hydrogen solid solutions,” *Journal of the Less Common Metals*, vol. 64, no. 2, pp. P11 – P16, 1979.

[92] “The Relation between the Electronic Structure and Hydrogen Storing Properties of Intermetallic Compounds,” *Zeitschrift für Physikalische Chemie*, vol. 117, p. 221, 1979.

[93] A. R. Miedema, K. H. J. Buschow, and H. H. Van Mal, “Which intermetallic compounds of transition metals form stable hydrides ?,” *Journal of the Less Common Metals*, vol. 49, no. 0, pp. 463–472, 1976.

[94] P. C. P. Bouten and A. R. Miedema, “On the heats of formation of the binary hydrides of transition metals,” *Journal of the Less Common Metals*, vol. 71, no. 1, pp. 147–160, 1980.

[95] H. H. Van Mal, K. H. J. Buschow, and A. R. Miedema, “Hydrogen absorption in LaNi5 and related compounds: Experimental observations and their explanation,” *Journal of the Less Common Metals*, vol. 35, no. 1, pp. 65–76, 1974.

[96] D. G. Westlake, “Hydrides of intermetallic compounds: A review of stabilities, stoichiometries and preferred hydrogen sites,” *Journal of the Less Common Metals*, vol. 91, no. 1, pp. 1–20, 1983.

[97] J.-J. Didisheim, K. Yvon, D. Shaltiel, P. Fischer, P. Bujard, and E. Walker, “The distribution of the deuterium atoms in the deuterated cubic laves-phase ZrV2D4·5,” *Solid State Communications*, vol. 32, no. 11, pp. 1087–1090, 1979.

[98] G. Sandrock, “A panoramic overview of hydrogen storage alloys from a gas reaction point of view,” *Journal of Alloys and Compounds*, vol. 293–295, pp. 877–888, Dec. 1999.

[99] E. H. Kisi, C. E. Buckley, and E. M. Gray, “The hydrogen activation of LaNi5,” *Journal of Alloys and Compounds*, vol. 185, no. 2, pp. 369–384, Jul. 1992.

[100] U. Ulmer, K. Asano, A. Patyk, H. Enoki, Y. Nakamura, A. Pohl, R. Dittmeyer, and M. Fichtner, “Cost reduction possibilities of vanadium-based solid solutions – Microstructural, thermodynamic, cyclic and environmental effects of ferrovanadium substitution,” *Journal of Alloys and Compounds*, vol. 648, pp. 1024–1030, Nov. 2015.

[101] H. Noh, T. B. Flanagan, Z. Gavra, J. R. Johnson, and J. J. Reilly, "The disappearance of hysteresis for the hydride phase transition in palladium-nickel alloys," *Scripta Metallurgica et Materialia*, vol. 25, no. 9, pp. 2177–2180, 1991.

[102] T. B. Flanagan and J. D. Clewley, "Hysteresis in metal hydrides," *Journal of the Less Common Metals*, vol. 83, no. 1, pp. 127–141, 1982.

[103] R. Balasubramaniam, "Accommodation effects during room temperature hydrogen transformations in the niobium-hydrogen system," *Acta Metallurgica et Materialia*, vol. 41, no. 12, pp. 3341–3349, 1993.

[104] B. J. Makenas and H. K. Birnbaum, "Phase changes in the niobium-hydrogen system I: Accommodation effects during hydride precipitation," *Acta Metallurgica*, vol. 28, no. 7, pp. 979–988, 1980.

[105] N. A. Scholtus and W. K. Hall, "Hysteresis in the Palladium—Hydrogen System," *The Journal of Chemical Physics*, vol. 39, no. 4, p. 868, 1963.

[106] T. B. Flanagan, B. S. Bowerman, and G. E. Biehl, "Hysteresis in metal/hydrogen systems," *Scripta Metallurgica*, vol. 14, no. 4, pp. 443–447, 1980.

[107] J. Matsuda and E. Akiba, "Lattice defects in V–Ti BCC alloys before and after hydrogenation," *Journal of Alloys and Compounds*, vol. 581, pp. 369–372, Dec. 2013.

[108] J. Matsuda, Y. Nakamura, and E. Akiba, "Microstructure of Ti–V–Mn BCC alloys before and after hydrogen absorption–desorption," *Journal of Alloys and Compounds*, vol. 509, no. 11, pp. 4352–4356, Mar. 2011.

[109] J. R. Lacher, "A Theoretical Formula for the Solubility of Hydrogen in Palladium," *Proceedings of the Royal Society A: Mathematical, Physical and Engineering Sciences*, vol. 161, no. 907, pp. 525–545, Aug. 1937.

[110] F. Feng, M. Geng, and D. O. Northwood, "Mathematical model for the plateau region of P–C-isotherms of hydrogen-absorbing alloys using hydrogen reaction kinetics," *Computational Materials Science*, vol. 23, no. 1–4, pp. 291–299, Apr. 2002.

[111] S. Qian and D. O. Northwood, "Hysteresis in metal-hydrogen systems: a critical review of the experimental observations and theoretical models," *International Journal of Hydrogen Energy*, vol. 13, no. 1, pp. 25–35, 1988.

[112] T. B. Flanagan, C.-N. Park, and W. A. Oates, "Hysteresis in solid state reactions," *Progress in Solid State Chemistry*, vol. 23, no. 4, pp. 291–363, Jan. 1995.

[113] C.-N. Park, S. Luo, and T. B. Flanagan, "Analysis of sloping plateaux in alloys and intermetallic hydrides," *Journal of Alloys and Compounds*, vol. 384, no. 1–2, pp. 203–207, Dec. 2004.

[114] S. Luo, C.-N. Park, and T. B. Flanagan, "Analysis of sloping plateaux in alloys and intermetallic hydrides," *Journal of Alloys and Compounds*, vol. 384, no. 1–2, pp. 208–216, Dec. 2004.

[115] E. R. Pinatel, M. Palumbo, F. Massimino, P. Rizzi, and M. Baricco, "Hydrogen sorption in the LaNi5-xAlx-H system (0 ≤ x ≤ 1)," *Intermetallics*, vol. 62, pp. 7–16, Jul. 2015.

[116] W. A. Oates and T. B. Flanagan, “On the origin of increasing hydrogen pressures in the two solid phase regions of intermetallic compound-hydrogen systems,” *Scripta Metallurgica*, vol. 17, no. 8, pp. 983–986, 1983.

[117] M. Martin, C. Gommel, C. Borkhart, and E. Fromm, “Absorption and desorption kinetics of hydrogen storage alloys,” *Journal of Alloys and Compounds*, vol. 238, no. 1–2, pp. 193–201, May 1996.

[118] A. Léon, Ed., *Hydrogen Technology*. Berlin, Heidelberg: Springer Berlin Heidelberg, 2008.

[119] F. Eisenberg and P. Goodell, “cyclic response of reversible hydriding alloys in hydrogen containing carbon monoxide,” *Journal of the Less Common Metals*, vol. 89, pp. 55–62, 1983.

[120] B. P. Somerday and C. S. Marchi, “3 - Hydrogen containment materials,” in *Solid-State Hydrogen Storage*, G. Walker, Ed. Woodhead Publishing, 2008, pp. 51–81.

[121] B. Bogdanović and M. Schwickardi, “Ti-doped alkali metal aluminium hydrides as potential novel reversible hydrogen storage materials,” *Journal of Alloys and Compounds*, vol. 253–254, pp. 1–9, May 1997.

[122] W. Lohstroh, A. Roth, H. Hahn, and M. Fichtner, “Thermodynamic effects in nanoscale NaAlH4.,” *Chemphyschem : a European journal of chemical physics and physical chemistry*, vol. 11, no. 4, pp. 789–92, Mar. 2010.

[123] M. Fichtner, O. Fuhr, O. Kircher, and J. rg Rothe, “Small Ti clusters for catalysis of hydrogen exchange in NaAlH 4,” *Nanotechnology*, vol. 14, no. 7, pp. 778–785, Jul. 2003.

[124] A. Züttel, P. Wenger, S. Rentsch, P. Sudan, P. Mauron, and C. Emmenegger, “LiBH4 a new hydrogen storage material,” *Journal of Power Sources*, vol. 118, no. 1–2, pp. 1–7, 2003.

[125] A. F. Gross, J. J. Vajo, S. L. Van Atta, and G. L. Olson, “Enhanced Hydrogen Storage Kinetics of LiBH 4 in Nanoporous Carbon Scaffolds,” *The Journal of Physical Chemistry C*, vol. 112, no. 14, pp. 5651–5657, Apr. 2008.

[126] J. Yang, A. Sudik, and C. Wolverton, “Destabilizing LiBH4 with a Metal (M = Mg, Al, Ti, V, Cr, or Sc) or Metal Hydride (MH2 = MgH2, TiH2, or CaH2),” *Journal of Physical Chemistry C*, vol. 111, no. 51, pp. 19134–19140, Dec. 2007.

[127] P. Chen, Z. Xiong, J. Luo, J. Lin, and K. L. Tan, “Interaction of hydrogen with metal nitrides and imides.,” *Nature*, vol. 420, no. 6913, pp. 302–4, Nov. 2002.

[128] J. J. Hu, E. Röhm, and M. Fichtner, “Feasibility and performance of the mixture of MgH2 and LiNH2 (1:1) as a hydrogen-storage material,” *Acta Materialia*, vol. 59, no. 14, pp. 5821–5831, Aug. 2011.

[129] U. Ulmer, J. Hu, M. Franzreb, and M. Fichtner, “Preparation, scale-up and testing of nanoscale, doped amide systems for hydrogen storage,” *International Journal of Hydrogen Energy*, vol. 38, no. 3, pp. 1439–1449, Feb. 2013.

[130] Z. Zhao-Karger, J. Hu, A. Roth, D. Wang, C. Kübel, W. Lohstroh, and M. Fichtner, “Altered thermodynamic and kinetic properties of MgH(2) infiltrated in microporous scaffold.,” *Chemical communications (Cambridge, England)*, vol. 46, no. 44, pp. 8353–5, Nov. 2010.

[131] M. Dornheim, S. Doppiu, G. Barkhordarian, U. Boesenberg, T. Klassen, O. Gutfleisch, and R. Bormann, “Hydrogen storage in magnesium-based hydrides and hydride composites,” *Scripta Materialia*, vol. 56, no. 10, pp. 841–846, May 2007.

[132] U. Bösenberg, S. Doppiu, L. Mosegaard, G. Barkhordarian, N. Eigen, A. Borgschulte, T. R. Jensen, Y. Cerenius, O. Gutfleisch, T. Klassen, M. Dornheim, and R. Bormann, “Hydrogen sorption properties of MgH2–LiBH4 composites,” *Acta Materialia*, vol. 55, no. 11, pp. 3951–3958, Jun. 2007.

[133] G. Sandrock, K. Gross, and G. Thomas, “Engineering considerations in the use of catalyzed sodium alanates for hydrogen storage,” *Journal of Alloys and Compounds*, vol. 330, pp. 696–701, 2002.

[134] J. Van Vucht, F. Kuijpers, and H. Bruning, “REVERSIBLE ROOM-TEMPERATURE ABSORPTION OF LARGE QUANTITIES OF HYDROGEN BY INTERMETALLIC COMPOUNDS,” *Philips Res. Rep.*, vol. 25, pp. 133–140, 1970.

[135] E. M. Gray, C. J. Webb, J. Andrews, B. Shabani, P. J. Tsai, and S. L. I. Chan, “Hydrogen storage for off-grid power supply,” *International Journal of Hydrogen Energy*, vol. 36, no. 1, pp. 654–663, Jan. 2011.

[136] D. M. Gruen, M. H. Mendelsohn, and I. Sheft, “Metal hydrides as chemical heat pumps,” *Solar Energy*, vol. 21, no. 2, pp. 153–156, 1978.

[137] J. Kim, “A hydrogen-compression system using porous metal hydride pellets of LaNi5-xAlxLaNi5-xAlx,” *International Journal of Hydrogen Energy*, vol. 33, no. 2, pp. 870–877, Jan. 2008.

[138] H. Diaz, A. Percheron-Guégan, J. C. Achard, C. Chatillon, and J. C. Mathieu, “Thermodynamic and structural properties of LaNi5−yAly compounds and their related hydrides,” *International Journal of Hydrogen Energy*, vol. 4, no. 5, pp. 445–454, 1979.

[139] J.-M. Joubert, M. Latroche, R. Černý, A. Percheron-Guégan, and K. Yvon, “Hydrogen cycling induced degradation in LaNi5-type materials,” *Journal of Alloys and Compounds*, vol. 330–332, pp. 208–214, Jan. 2002.

[140] P. Thompson and J. Reilly, “The crystal structure of LaNi5D7,” *Journal of Physics F*, vol. 16, pp. 675–685, 1986.

[141] Y. Nakamura and E. Akiba, “In-situ X-ray diffraction study on LaNi5 and LaNi4.75Al0.25 in the initial activation process,” *Journal of Alloys and Compounds*, vol. 308, no. 1–2, pp. 309–318, Aug. 2000.

[142] Y. Chung, T. Takeshita, O. D. McMasters, and K. A. G. Jr., “Influence of the lattice and electronic factors on the hydrogenation properties of the RNi5-base (R is a rare earth) haucke compounds: Results of low temperature heat capacity measurements,” *Journal of the Less Common Metals*, vol. 74, no. 1, pp. 217–223, 1980.

[143] T. Takeshita, S. K. Malik, and W. E. Wallace, “Hydrogen absorption in {RNi4Al} (R = Rare Earth) ternary compounds,” *Journal of Solid State Chemistry*, vol. 23, no. 3–4, pp. 271–274, 1978.

[144] J. Shinar, D. Shaltiel, D. Davidov, and A. Grayevsky, “Hydrogen sorption properties of the La1−xCaxNi5 and La(Ni1−xCux)5 systems,” *Journal of the Less Common Metals*, vol. 60, no. 2, pp. 209–219, 1978.

[145] M. H. Mendelsohn, D. M. Gruen, and A. E. Dwight, “The effect on hydrogen decomposition pressures of group {IIIA} and {IVA} element substitutions for Ni In LaNi5 alloys,” *Materials Research Bulletin*, vol. 13, no. 11, pp. 1221–1224, 1978.

[146] A. Percheron-Guégan, C. Lartigue, and J. C. Achard, “Correlations between the structural properties, the stability and the hydrogen content of substituted LaNi5 compounds,” *Journal of the Less Common Metals*, vol. 109, no. 2, pp. 287–309, Jul. 1985.

[147] G. Sandrock and P. Goodell, “Surface poisoning of LaNi5, FeTi and (Fe,Mn)Ti by o2, co and h2o,” *Journal of the Less Common Metals*, vol. 73, pp. 161–168, 1980.

[148] R. Beck and W. M. Mueller, “Summary Report, AEC Contract AT (33-3)-3, Denver Research Institute.” pp. 1–59, 1962.

[149] J. Reilly and R. Wiswall, “Report BNL 21322, Brookhaven National Lab,” 1976.

[150] B. Sakintuna, F. Lamaridarkrim, and M. Hirscher, “Metal hydride materials for solid hydrogen storage: A review☆,” *International Journal of Hydrogen Energy*, vol. 32, no. 9, pp. 1121–1140, Jun. 2007.

[151] T. B. Zhang, X. W. Yang, J. S. Li, R. Hu, X. Y. Xue, and H. Z. Fu, “On the poisoning effect of O2 and N2 for the Zr0.9Ti0.1V2 hydrogen storage alloy,” *Journal of Power Sources*, vol. 202, pp. 217–224, Mar. 2012.

[152] F. R. Block and H.-J. Bahs, “Selective absorption of hydrogen by Ti-Mn-based alloys from gas mixtures containing CO or CH4,” *Journal of the Less Common Metals*, vol. 104, no. 2, pp. 223–230, 1984.

[153] O. Bernauer, J. Töpler, D. Noréus, R. Hempelmann, and D. Richter, “Fundamentals and properties of some Ti/Mn based Laves phase hydrides,” *International Journal of Hydrogen Energy*, vol. 14, no. 3, pp. 187–200, Jan. 1989.

[154] B. S. Chao, R. C. YOUNG, S. R. Ovshinsky, D. A. Pawlik, B. Huang, J. S. Im, and B. C. CHAKOUMAKOS, “Effect of Alloy Composition on the Structure of Zr Based Metal Alloys,” in *Symposium CC – New Materials for Batteries & Fuel Cells*, 1999, vol. 575.

[155] J. J. Reilly and R. H. Wiswall, “Formation and properties of iron titanium hydride,” *Inorganic Chemistry*, vol. 13, no. 1, pp. 218–222, Jan. 1974.

[156] F. Reidinger, J. F. Lynch, and J. J. Reilly, “An X-ray diffraction examination of the FeTi-H 2 system,” *Journal of Physics F: Metal Physics*, vol. 12, no. 3, pp. L49–L55, Mar. 1982.

[157] P. Thompson, J. J. Reilly, and J. M. Hastings, “The application of the Rietveld method to a highly strained material with microtwins: TiFeD 1.9,” *Journal of Applied Crystallography*, vol. 22, no. 3, pp. 256–260, Jun. 1989.

[158] P. Thompson, M. A. Pick, F. Reidinger, L. M. Corliss, J. M. Hastings, and J. J. Reilly, “Neutron diffraction study of β iron titanium deuteride,” *Journal of Physics F: Metal Physics*, vol. 8, no. 4, pp. L75–L80, Apr. 1978.

[159] D. G. Johnson and J. B. Pangborn, “The effect of activation process parameters on initial formation rates of FeTiHx,” *Journal of the Less Common Metals*, vol. 73, no. 1, pp. 127–134, 1980.

[160] T. Sasai, K. Oku, and H. Konno, “HYDROGEN STORAGE CHARACTERISTICS OF Fe-Ti-Zr-Nb ALLOYS,” *Journal of the Less Common Metals*, vol. 89, pp. 281–285, 1983.

[161] N. Nishimiya and T. Wada, “Hydriding characteristics of zirconium-substituted FeTi,” *Journal of alloys and Compounds*, vol. 313, pp. 53–58, 2000.

[162] V. Bronca, P. Bergman, V. Ghaemmaghami, D. Khatamian, and F. D. Manchester, “Hydrogen absorption characteristics of an FeTi + misch metal alloy,” *Journal of the Less Common Metals*, vol. 108, no. 2, pp. 313–325, 1985.

[163] S. Lee, T. Perng, and H. Juang, “Microstructures and hydrogenation properties of TiFe l− x M χ alloys,” *Journal of alloys and Compounds*, vol. 187, pp. 49–57, 1992.

[164] H. S. Chung and J.-Y. Lee, “Effect of partial substitution of Mn and Ni for Fe in FeTi on hydriding kinetics,” *International Journal of Hydrogen Energy*, vol. 11, no. 5, pp. 335–339, 1986.

[165] M. Williams, M. V. Lototsky, M. W. Davids, V. Linkov, V. a. Yartys, and J. K. Solberg, “Chemical surface modification for the improvement of the hydrogenation kinetics and poisoning resistance of TiFe,” *Journal of Alloys and Compounds*, vol. 509, pp. S770–S774, Sep. 2011.

[166] H. Nagai, M. Nakatsu, K. Shoji, and H. Tamura, “Effect of simultaneous addition of oxygen with copper or niobium on the hydriding characteristics of FeTi for hydrogen storage,” *Journal of the Less Common Metals*, vol. 119, no. 1, pp. 131–142, 1986.

[167] K. Edalati, J. Matsuda, H. Iwaoka, S. Toh, E. Akiba, and Z. Horita, “High-pressure torsion of TiFe intermetallics for activation of hydrogen storage at room temperature with heterogeneous nanostructure,” *International Journal of Hydrogen Energy*, vol. 38, no. 11, pp. 4622–4627, Apr. 2013.

[168] K. Edalati, J. Matsuda, A. Yanagida, E. Akiba, and Z. Horita, “Activation of TiFe for hydrogen storage by plastic deformation using groove rolling and high-pressure torsion: Similarities and differences,” *International Journal of Hydrogen Energy*, vol. 39, no. 28, pp. 15589–15594, Sep. 2014.

[169] J. J. Reilly and R. H. Wiswall, “Higher hydrides of vanadium and niobium,” *Inorganic Chemistry*, vol. 9, no. 7, pp. 1678–1682, Jul. 1970.

[170] A. Maeland, “Investigation of the Vanadium—Hydrogen System by X-Ray Diffraction Techniques1, 2,” *The Journal of Physical Chemistry*, vol. 68, no. 8, pp. 2197–2200, 1964.

[171] D. Chandra, A. Sharma, R. Chellappa, W. N. Cathey, F. E. Lynch, R. C. Bowman, J. R. Wermer, and S. N. Paglieri, “Hydriding and structural characteristics of thermally cycled and cold-

worked V–0.5at.%C alloy,” *Journal of Alloys and Compounds*, vol. 452, no. 2, pp. 312–324, Mar. 2008.

[172] “University Kiel.” [Online]. Available: http://www.tf.uni-kiel.de/matwis/amat/def_en/kap_1/illustr/h_okta.gif, August 2015.

[173] W. Borchardt-Ott and H. Sowa, *Kristallographie*. Berlin, Heidelberg: Springer Berlin Heidelberg, 2013.

[174] K. Asano, S. Hayashi, Y. Nakamura, and E. Akiba, “Effect of substitutional Cr on hydrogen diffusion and thermal stability for the BCT monohydride phase of the V–H system studied by 1H NMR,” *Journal of Alloys and Compounds*, vol. 524, pp. 63–68, May 2012.

[175] K. Asano, S. Hayashi, and Y. Nakamura, “Enhancement of hydrogen diffusion in the BCT monohydride phase of the V-H system by substitutional Al studied by 1H NMR;,” *Acta Materialia*, 2014.

[176] K. Asano, S. Hayashi, and Y. Nakamura, “Enhancement of hydrogen diffusion in the body-centered tetragonal monohydride phase of the V–H system by substitutional Al studied by proton nuclear magnetic resonance,” *Acta Materialia*, vol. 83, pp. 479–487, Jan. 2015.

[177] S. M. Ko and L. D. Schmidt, “Adsorption and solution of H2 and N2 by Ta and Nb,” *Surface Science*, vol. 42, no. 2, pp. 508–524, Apr. 1974.

[178] J. A. Pryde and C. G. Titcomb, “Solution of hydrogen in niobium,” *Transactions of the Faraday Society*, vol. 65, p. 2758, 1969.

[179] E. Fromm and H. Uchida, “effect of oxygen sorption layers on the kinetics of hydrogen absorption by tantalum at 77-700 k,” *Journal of the Less Common Metals*, vol. 66, pp. 77–88, 1979.

[180] M. A. Pick, “Kinetics of hydrogen absorption-desorption by niobium,” *Physical Review B*, vol. 24, no. 8, pp. 4287–4294, Oct. 1981.

[181] M. A. Pick, J. W. Davenport, M. Strongin, and G. J. Dienes, “Enhancement of Hydrogen Uptake Rates for Nb and Ta by Thin Surface Overlayers,” *Physical Review Letters*, vol. 43, no. 4, pp. 286–289, Jul. 1979.

[182] G. G. Libowitz and a. J. Maeland, “Hydride Formation by B.C.C. Solid Solution Alloys,” *Materials Science Forum*, vol. 31, pp. 177–196, 1988.

[183] Y. Yan, Y. Chen, H. Liang, C. Wu, and M. Tao, “Hydrogen storage properties of V30–Ti–Cr–Fe alloys,” *Journal of Alloys and Compounds*, vol. 427, no. 1–2, pp. 110–114, Jan. 2007.

[184] R. Guo, L. Chen, Y. Lei, and B. Liao, “The effect of Ni content on the phase structures and electrochemical properties of V2:1TiNix (x =0:1–0.9) hydrogen storage alloys,” *International journal of Hydrogen Energy*, vol. 28, pp. 803–808, 2003.

[185] C.-C. Shen and H.-C. Li, “Passivation and reactivation of Ti25V35Cr40 hydrides by cycling with impure hydrogen gas,” *International Journal of Hydrogen Energy*, vol. 40, no. 8, pp. 3277–3282, Mar. 2015.

[186] S. Suwarno, Y. Gosselin, J. K. Solberg, J. P. Maehlen, M. Williams, B. Krogh, B. T. Børresen, E. Rytter, E. Ochoa-Fernández, and V. a. Yartys, “Selective hydrogen absorption from gaseous mixtures by BCC Ti-V alloys,” *International Journal of Hydrogen Energy*, vol. 37, no. 5, pp. 4127–4138, Mar. 2012.

[187] S.-W. Cho, C.-S. Han, C.-N. Park, and E. Akiba, “The hydrogen storage characteristics of Ti–Cr–V alloys,” *Journal of Alloys and Compounds*, vol. 288, no. 1–2, pp. 294–298, Jun. 1999.

[188] S.-W. Cho, G. Shim, G.-S. Choi, C.-N. Park, J.-H. Yoo, and J. Choi, “Hydrogen absorption–desorption properties of Ti0.32Cr0.43V0.25 alloy,” *Journal of Alloys and Compounds*, vol. 430, no. 1–2, pp. 136–141, Mar. 2007.

[189] C. Wu, X. Zheng, Y. Chen, M. Tao, G. Tong, and J. Zhou, “Hydrogen storage and cyclic properties of V60Ti(21.4+x)Cr(6.6−x)Fe12 (0 ≤ x ≤ 3) alloys,” *International Journal of Hydrogen Energy*, vol. 35, no. 15, pp. 8130–8135, Aug. 2010.

[190] C. Wu, A. Borgschulte, U. Frischknecht, Y. Yan, F. Yang, L. Luo, Y. Chen, and A. Züttel, “Surface properties of V40(TiCr)51Fe8Mn alloy during hydrogenation/dehydrogenation cycles,” *Journal of Alloys and Compounds*, vol. 40, pp. 30–32, Feb. 2013.

[191] T. Huang, Z. Wu, B. Xia, J. Chen, X. Yu, N. Xu, C. Lu, and H. Yu, “TiCr 1.2 (V–Fe) 0.6 —a novel hydrogen storage alloy with high capacity,” *Science and Technology of Advanced Materials*, vol. 4, no. 6, pp. 491–494, Nov. 2003.

[192] S. F. Santos and J. Huot, “Hydrogen storage in TiCr1.2(FeV)x BCC solid solutions,” *Journal of Alloys and Compounds*, vol. 472, no. 1–2, pp. 247–251, Mar. 2009.

[193] Y. Yan, Y. Chen, C. Wu, M. Tao, and H. Liang, “A low-cost BCC alloy prepared from a FeV80 alloy with a high hydrogen storage capacity,” *Journal of Power Sources*, vol. 164, no. 2, pp. 799–802, Feb. 2007.

[194] K. Nomura and E. Akiba, “H2 Absorbing-desorbing characterization of the Ti瑕V瑕Fe alloy system,” *Journal of Alloys and Compounds*, vol. 231, no. 1–2, pp. 513–517, Dec. 1995.

[195] H. Taizhong, W. Zhu, C. Jinzhou, Y. Xuebin, X. Baojia, and X. Naixin, “Dependence of hydrogen storage capacity of TiCr1.8−X(VFe)X on V–Fe content,” *Materials Science and Engineering: A*, vol. 385, no. 1–2, pp. 17–21, Nov. 2004.

[196] M. Tousignant and J. Huot, “Replacement of Vanadium by Ferrovanadium in Ti-Based BCC Alloys for Hydrogen Storage,” *Solid State Phenomena*, vol. 170, pp. 144–149, Apr. 2011.

[197] T. Dou, Z. Wu, J. Mao, and N. Xu, “Application of commercial ferrovanadium to reduce cost of Ti–V-based BCC phase hydrogen storage alloys,” *Materials Science and Engineering: A*, vol. 476, no. 1–2, pp. 34–38, Mar. 2008.

[198] Y. Yan, Y. Chen, H. Liang, C. Wu, and M. Tao, “The effect of Si on V30Ti35Cr25Fe10 BCC hydrogen storage alloy,” *Journal of Alloys and Compounds*, vol. 441, no. 1–2, pp. 297–300, Aug. 2007.

[199] Y. Yan, Y. Chen, H. Liang, C. Wu, M. Tao, and T. Mingjing, “Effect of Al on hydrogen storage properties of V30Ti35Cr25Fe10 alloy,” *Journal of Alloys and Compounds*, vol. 426, no. 1–2, pp. 253–255, Dec. 2006.

[200] M. Tsukahara, K. Takahashi, T. Mishima, A. Isomura, and T. Sakai, "Influence of various additives in vanadium-based alloys V3TiNi0.56 on secondary phase formation, hydrogen storage properties and electrode properties," *Journal of Alloys and Compounds*, vol. 245, no. 1–2, pp. 59–65, Nov. 1996.

[201] J. Shi, T. Sakai, H. T. Takeshita, N. Kuriyama, and M. Tsukahara, "Influence of carbon impurity on microstructures and electrode properties for V-based battery alloys," *Journal of Alloys and Compounds*, vol. 290, no. 1–2, pp. 267–272, Aug. 1999.

[202] C.-C. Shen, J. C.-P. Chou, H.-C. Li, Y.-P. Wu, and T.-P. Perng, "Effect of interstitial boron and carbon on the hydrogenation properties of Ti25V35Cr40 alloy," *International Journal of Hydrogen Energy*, vol. 35, no. 21, pp. 11975–11980, Nov. 2010.

[203] G. Sandrock, S. Suda, and L. Schlapbach, "Hydrogen in intermetallic compounds II," *Topics in Applied Physics*, vol. 67, 1992.

[204] "Ergenics Corp., Ringwood, NJ, USA." [Online]. Available: http://www.ergenics.com/ha.html, September 2015.

[205] "H Bank Technology Inc., Taiwan." [Online]. Available: http://www.hbank.com.tw/fc/3300.html, September 2015.

[206] X. Wang and S. Suda, "Stability and tolerance to impurities of the fluorinated surface of hydrogen-absorbing alloys," *Journal of alloys and compounds*, vol. 227, pp. 58–62, 1995.

[207] X. Wang and S. Suda, "Surface characteristics of fluorinated hydriding alloys," *Journal of alloys and compounds*, vol. 231, pp. 380–386, 1995.

[208] F. Liu and S. Suda, "Properties and characteristics of fluorinated hydriding alloys," *Journal of alloys and compounds*, vol. 231, pp. 742–750, 1995.

[209] J. Ren, M. Williams, M. Lototskyy, W. Davids, and Ø. Ulleberg, "Improved tolerance of Pd/Cu-treated metal hydride alloys towards air impurities," *International Journal of Hydrogen Energy*, vol. 35, no. 16, pp. 8626–8630, Aug. 2010.

[210] M. V. Lototsky, M. Williams, V. a. Yartys, Y. V. Klochko, and V. M. Linkov, "Surface-modified advanced hydrogen storage alloys for hydrogen separation and purification," *Journal of Alloys and Compounds*, vol. 509, pp. S555–S561, Sep. 2011.

[211] "PlasmaLab." [Online]. Available: http://www.plasmalab.ru/metallurgy.htm, September 2015.

[212] G. Brückmann and H. Scholz, "7 - Vacuum Arc Metal Processing," in *Handbook of Vacuum Arc Science and Technology*, R. L. B. M. S. J. Martin, Ed. Park Ridge, NJ: William Andrew Publishing, 1996, pp. 552–589.

[213] J. Lee, S. Kim, D. Kim, and K. Kim, "Effect of H2SO4 concentration in washing solution on regeneration of commercial selective catalytic reduction," *Korean Journal of …*, vol. 29, no. 2, pp. 270–276, 2012.

[214] W. M. Gitari, O. O. Fatoba, L. F. Petrik, and V. R. K. Vadapalli, "Leaching characteristics of selected South African fly ashes: Effect of pH on the release of major and trace species," *Journal of Environmental Science and Health, Part A*, vol. 44, no. 2, pp. 206–220, 2009.

[215] A. Ognyanova, A. T. Ozturk, I. De Michelis, F. Ferella, G. Taglieri, A. Akcil, and F. Vegliò, "Metal extraction from spent sulfuric acid catalyst through alkaline and acidic leaching," *Hydrometallurgy*, vol. 100, no. 1–2, pp. 20–28, 2009.

[216] L. Zeng and C. Y. Cheng, "A literature review of the recovery of molybdenum and vanadium from spent hydrodesulphurisation catalysts: Part I: Metallurgical processes," *Hydrometallurgy*, vol. 98, no. 1–2, pp. 1–9, 2009.

[217] Q. Li, Z. Liu, and Q. Liu, "Kinetics of Vanadium Leaching from a Spent Industrial V 2 O 5 / TiO 2 Catalyst by Sulfuric Acid," *Industrial Chemistry,* 2014.

[218] S.-L. Tsai and M.-S. Tsai, "A study of the extraction of vanadium and nickel in oil-fired fly ash," *Resources, Conservation and Recycling*, vol. 22, no. 3–4, pp. 163–176, 1998.

[219] R. Navarro, J. Guzman, I. Saucedo, J. Revilla, and E. Guibal, "Vanadium recovery from oil fly ash by leaching, precipitation and solvent extraction processes.," *Waste management (New York, N.Y.)*, vol. 27, no. 3, pp. 425–38, Jan. 2007.

[220] C. Suryanarayana and M. G. Norton, *X-Ray Diffraction*. Boston, MA: Springer US, 1998.

[221] C. Wall, "Mangan-Nickel-und Cobaltverbindungen als Konversionselektrodenmaterialien für Lithium-Ionen-Batterien," Dissertation, TU Darmstadt, 2013.

[222] W. Massa, *Crystal Structure Determination*. Berlin, Heidelberg: Springer Berlin Heidelberg, 2004.

[223] L. Spieß, G. Teichert, R. Schwarzer, H. Behnken, and C. Genzel, *Moderne Röntgenbeugung*. Wiesbaden: Vieweg+Teubner, 2009.

[224] B. H. Toby, "R factors in Rietveld analysis: How good is good enough?," *Powder Diffraction*, vol. 21, no. 01, pp. 67–70, Mar. 2012.

[225] A. Gavezzotti, "Computational studies of crystal structure and bonding.," *Topics in current chemistry*, vol. 315, pp. 1–32, Jan. 2012.

[226] J. I. Goldstein, D. E. Newbury, P. Echlin, D. C. Joy, C. E. Lyman, E. Lifshin, L. Sawyer, and J. R. Michael, *Scanning Electron Microscopy and X-ray Microanalysis*. Boston, MA: Springer US, 2003.

[227] B. Fultz and J. Howe, *Transmission Electron Microscopy and Diffractometry of Materials*. Berlin, Heidelberg: Springer Berlin Heidelberg, 2013.

[228] S. Hofmann, *Auger- and X-Ray Photoelectron Spectroscopy in Materials Science*, vol. 49. Berlin, Heidelberg: Springer Berlin Heidelberg, 2013.

[229] "Product website of PCT Pro, Setaram," 2015. [Online]. Available: http://www.setaram.com/wp-content/uploads/2015/07/PCTPro-pages-JUILLET2015.pdf, September 2015.

[230] G. W. H. Höhne, W. F. Hemminger, and H.-J. Flammersheim, *Differential Scanning Calorimetry*. Berlin, Heidelberg: Springer Berlin Heidelberg, 2003.

[231] K. Dettmer-Wilde and W. Engewald, Eds., *Practical Gas Chromatography*. Berlin, Heidelberg: Springer Berlin Heidelberg, 2014.

[232] P. Muthukumar, M. Linder, R. Mertz, and E. Laurien, “Measurement of thermodynamic properties of some hydrogen absorbing alloys,” *International Journal of Hydrogen Energy*, vol. 34, no. 4, pp. 1873–1879, Feb. 2009.

[233] H. Itoh, H. Arashima, K. Kubo, T. Kabutomori, and K. Ohnishi, “Improvement of cyclic durability of BCC structured Ti–Cr–V alloys,” *Journal of Alloys and Compounds*, vol. 404–406, no. December 2004, pp. 417–420, Dec. 2005.

[234] H. Lin, K. Lin, K. Wu, H. Hsiung, and H. Tsai, “Cyclic hydrogen absorption–desorption characteristics of TiCrV and Ti0.8Cr1.2VTi0.8Cr1.2V alloys,” *International Journal of Hydrogen Energy*, vol. 32, no. 18, pp. 4966–4972, Dec. 2007.

[235] I. I. Kornilov and N. M. Matveeva, “THE METAL CHEMISTRY OF VANADIUM,” *Russian Chemical Reviews*, vol. 31, no. 9, pp. 512–528, Sep. 1962.

[236] R. M. Wood, “The Lattice Constants of High Purity Alpha Titanium,” *Proceedings of the Physical Society*, vol. 80, no. 3, pp. 783–786, Sep. 1962.

[237] S. Yamaguchi, K. Hiraga, and M. Hirabayashi, “Interstitial Order-Disorder Transformation in the Ti-O Solid Solution. IV. A Neutron Diffraction Study,” *Journal of the Physical Society of Japan*, vol. 28, no. 4, pp. 1014–1023, Apr. 1970.

[238] S. Yamaguchi, “Interstitial Order-Disorder Transformation in the Ti-O Solid Solution. I. Ordered Arrangement of Oxygen,” *Journal of the Physical Society of Japan*, vol. 27, no. 1, pp. 155–163, Jan. 1969.

[239] J. L. Murray and H. a. Wriedt, “The O−Ti (Oxygen-Titanium) system,” *Journal of Phase Equilibria*, vol. 8, no. 2, pp. 148–165, Apr. 1987.

[240] P. Karen and A. Kjekshus, *High-Temperature Superconductors - I*, vol. 30. Elsevier, 2000, pp. 229–373.

[241] J. L. Murray, “The Ti−V (Titanium-Vanadium) system,” *Bulletin of Alloy Phase Diagrams*, vol. 2, no. 1, pp. 48–55, Jun. 1981.

[242] H. E. and Y. N. K. Asano, S. Havashi, K. Mimura, “Hydrogen diffusion in V studied by 1H-NMR.pdf,” in *Collected book of abstracts, Metal Hydrides conference*, 2012, p. 375.

[243] D. Elanski, J.-W. Lim, K. Mimura, and M. Isshiki, “Impurity removal from Fe, Cr, Ti, and V metals by hydrogen plasma arc melting and thermodynamic estimation of hydride and sulfide formation,” *Journal of Alloys and Compounds*, vol. 421, no. 1–2, pp. 209–216, Sep. 2006.

[244] J. C. S. Pires, J. Otubo, a. F. B. Braga, and P. R. Mei, “The purification of metallurgical grade silicon by electron beam melting,” *Journal of Materials Processing Technology*, vol. 169, no. 1, pp. 16–20, Oct. 2005.

[245] J. Lim, K. Mimura, and M. Isshiki, “emoval of metallic impurities from zirconium by hydrogen plasma arc melting,” *Journal of materials science*, vol. 40, pp. 4109–4111, 2005.

[246] C. Lartigue, A. Le Bail, and A. Percheron-Guegan, “A new study of the structure of LaNi5D6.7 using a modified Rietveld method for the refinement of neutron powder diffraction data,” *Journal of the Less Common Metals*, vol. 129, pp. 65–76, Feb. 1987.

[247] U. Ulmer, K. Asano, T. Bergfeldt, V. S. K. Chakravadhanula, R. Dittmeyer, H. Enoki, C. Kübel, Y. Nakamura, A. Pohl, and M. Fichtner, “Effect of oxygen on the microstructure and hydrogen storage properties of V–Ti–Cr–Fe quaternary solid solutions,” *International Journal of Hydrogen Energy*, vol. 39, no. 35, pp. 20000–20008, Dec. 2014.

[248] S. Fabík, V. Cháb, V. Dudr, K. Mašek, K. C. Prince, F. Šutara, K. Veltruská, N. Tsud, M. Vondráček, and V. Matolín, “Activation of binary Zr–V non-evaporable getters: a soft X-ray photoemission study of carbide formation,” *Surface Science*, vol. 566–568, pp. 1246–1249, Sep. 2004.

[249] X. Yang, J. Li, T. Zhang, R. Hu, X. Xue, X. Wang, and H. Fu, “In situ investigation on transformation of valence on the surface of the alloy during thermal activation,” *Solid State Communications*, vol. 151, no. 11, pp. 842–845, Jun. 2011.

[250] F. Šutara, I. Matolínová, T. Skála, K. Mašek, and V. Matolín, “Residual surface oxide on ZrV getter—XPS, LEIS and SIMS study,” *Vacuum*, vol. 74, no. 2, pp. 305–309, May 2004.

[251] V. Matolín, K. Mašek, I. Matolínová, T. Skála, and K. Veltruská, “XPS and SIMS study of the ageing mechanism of Zr–V non-evaporable getter films,” *Applied Surface Science*, vol. 235, no. 1–2, pp. 202–206, Jul. 2004.

[252] J. L. Armstrong, “Thermal decomposition reactions of acetaldehyde and acetone on Si(100),” *Journal of Vacuum Science & Technology A: Vacuum, Surfaces, and Films*, vol. 15, no. 3, p. 1146, May 1997.

[253] K. Soga, H. Imamura, and S. Ikeda, “Hydrogenation of ethylene over lanthanum-nickel (LaNi5) alloy,” *The Journal of Physical Chemistry*, vol. 81, no. 18, pp. 1762–1766, Sep. 1977.

[254] S. Kato, A. Borgschulte, D. Ferri, M. Bielmann, J.-C. Crivello, D. Wiedenmann, M. Parlinska-Wojtan, P. Rossbach, Y. Lu, A. Remhof, and A. Züttel, “CO2 hydrogenation on a metal hydride surface.,” *Physical chemistry chemical physics : PCCP*, vol. 14, no. 16, pp. 5518–26, Apr. 2012.

[255] E. Fromm, “effect of oxide layers on the absorption kinetics of hydrogen by metals at room temperature,” *Zeitschrift für Physikalische Chemie*, vol. 147, pp. 61–75, 1986.

[256] J. Chupin, N. Gnep, S. Lacombe, and M. Guisnet, “Influence of the metal and of the support on the activity and stability of bifunctional catalysts for toluene hydrogenation,” *Applied Catalysis A: General*, vol. 206, pp. 43–56, 2001.

[257] B. Pawelec and R. Mariscal, “Hydrogenation of aromatics over supported Pt-Pd catalysts,” *Applied Catalysis A: General*, vol. 225, no. 2002, pp. 223–237, 2002.

[258] A. Masalska, “Ni-loaded catalyst containing ZSM-5 zeolite for toluene hydrogenation,” *Applied Catalysis A: General*, vol. 294, no. 2, pp. 260–272, Oct. 2005.

[259] M.-L. Frauwallner, F. López-Linares, J. Lara-Romero, C. E. Scott, V. Ali, E. Hernández, and P. Pereira-Almao, “Toluene hydrogenation at low temperature using a molybdenum carbide catalyst,” *Applied Catalysis A: General*, vol. 394, no. 1–2, pp. 62–70, Feb. 2011.

[260] S. Miraglia, P. de Rango, S. Rivoirard, D. Fruchart, J. Charbonnier, and N. Skryabina, “Hydrogen sorption properties of compounds based on BCC Ti1−xV1−yCr1+x+y alloys,” *Journal of Alloys and Compounds*, vol. 536, pp. 1–6, Sep. 2012.

[261] T. Hirata, “Decomposition of the FeTi1.13 hydride after hydrogen absorption-desorption cycles in oxygen-contaminated hydrogen,” *Journal of the Less Common Metals*, vol. 113, no. 2, pp. 189–196, 1985.

[262] L. Schlapbach and T. Riesterer, “The activation of FeTi for hydrogen absorption,” *Applied Physics A*, vol. 182, 1983.

[263] F. Šutara, N. Tsud, K. Veltruská, and V. Matolín, “XPS and ESD study of carbon and oxygen chemistry on TiZrV NEG,” *Vacuum*, vol. 61, pp. 135–139, 2001.

[264] F. Schweppe, M. Martin, and E. Fromm, “Hydrogen absorption of LaNi5 powders precovered with O2, CO, H2S, CO2 or N2,” *Journal of Alloys and Compounds*, vol. 253–254, pp. 511–514, May 1997.

[265] H. Pan, R. Li, M. Gao, Y. Liu, Y. Lei, and Q. Wang, “Effects of Ni on the structural and electrochemical properties of Ti–V-based hydrogen storage alloys,” *International Journal of Hydrogen Energy*, vol. 31, no. 9, pp. 1188–1195, Aug. 2006.

[266] M. Taxak, S. Kumar, B. B. Kalekar, and N. Krishnamurthy, “Effect of nickel addition on the solubility of hydrogen in tantalum,” *International Journal of Hydrogen Energy*, vol. 38, no. 18, pp. 7561–7568, Jun. 2013.

[267] M. V. Lototsky, V. a. Yartys, and I. Y. Zavaliy, “Vanadium-based BCC alloys: phase-structural characteristics and hydrogen sorption properties,” *Journal of Alloys and Compounds*, vol. 404–406, pp. 421–426, Dec. 2005.

[268] P. Marcus, “Surface science approach of corrosion phenomena,” *Electrochimica Acta*, vol. 43, no. 1–2, pp. 109–118, 1998.

[269] P. Marcus, “On some fundamental factors in the effect of alloying elements on passivation of alloys,” *Corrosion Science*, vol. 36, no. 12, pp. 2155–2158, 1994.

[270] H. H. Uchida, H.-G. Wulz, and E. Fromm, “Catalytic effect of nickel, iron and palladium on hydriding titanium and storage materials,” *Journal of the Less Common Metals*, vol. 172–174, pp. 1076–1083, Jan. 1991.

[271] L. Schlapbach, A. Seiler, F. Stucki, and H. C. Siegmann, “Surface effects and the formation of metal hydrides,” *Journal of the Less Common Metals*, vol. 73, no. 1, pp. 145–160, 1980.

[272] J. Greeley and M. Mavrikakis, “Alloy catalysts designed from first principles.,” *Nature materials*, vol. 3, no. 11, pp. 810–5, Nov. 2004.

[273] M. Pozzo and D. Alfè, “Hydrogen dissociation and diffusion on transition metal (=Ti, Zr, V, Fe, Ru, Co, Rh, Ni, Pd, Cu, Ag)-doped Mg(0001) surfaces,” *International Journal of Hydrogen Energy*, vol. 34, no. 4, pp. 1922–1930, Feb. 2009.

[274] A. Groß, “Hydrogen dissociation on metal surfaces–a model system for reactions on surfaces,” *Applied Physics A: Materials Science & Processing*, vol. 635, pp. 627–635, 1998.

[275] C. Seo, J. Kim, P. S. Lee, and J. Lee, “Hydrogen storage properties of vanadium-based b.c.c. solid solution metal hydrides,” *Journal of Alloys and Compounds*, vol. 348, no. 1–2, pp. 252–257, Jan. 2003.

Appendix

A Inductively coupled plasma optical emission spectrometry (ICP-OES)

Induced coupled plasma optical emission spectrometry (ICP-OES) is an analytical tool for the determination of metals. Liquid or solubilized samples are injected into a radiofrequency induced argon plasma, where they are quickly vaporized and energized through collisional excitation at high temperature up to 10,000 K, promoting them to exited states. Both the atomic and ionic excited state species may then relax by the emission of a photon. These photons have characteristic energies that are determined by the quantized energy level structure for the atoms or ions. Thus the wavelength of the photons can be used to identify the element from which they originated. The total number of photons is directly proportional to the concentration of the originating element in the sample.

For the measurements, the samples with the solvent extraction were diluted by 2. The internal standard Sc was added to the solution and acidulated with nitric acid (sub boiled grade). The analysis of the components was accomplished with four different calibration solutions with the internal standard (Sc). The range of the calibration solutions did not exceed a decade. The two or three major wavelengths of the elemental emission spectra were used for calculation.

B Oxygen/nitrogen analysis

The oxygen/nitrogen was analyzed by carrier gas hot extraction (CGHE). A commercial oxygen/nitrogen analyzer TC600 (LECO) was used which was calibrated with dried Fe powder (JK47) and verified with a standard from LECO (502-201) and a standard from Alpha Resources (AR 640-ZR702B). The calibration range was close to the concentration of the samples. The standard oxides and the samples weighed with a mass in the range from 50 to 300 mg (weighing accuracy ± 0.002 mg) in Sn crucibles (9-10 mm). Together with a Ni capsule (about 500 mg), which served as fusion aid, the package was put into an outgassed high temperature graphite crucible (outgassing power: 6300 W). The measurements were performed at 5800 W heating power. The evolving gases CO_2 and CO were swept out by He as inert carrier gas and measured by infrared detectors. The oxygen concentration of each material was measured three times, and an average value was calculated. After removing the CO and CO_2 gas the N_2 gas was measured with a thermal conductivity detector.

C Carbon analysis

The carbon content was analyzed with a CS analyzer from LECO (CS 600). The carbon concentration was calibrated with two different Fe standards (Euro AKP 077-1-3472, AKP 230-1-1872) and verified with another Fe standard (BCS-CRM 406). The calibration range was close to the concentration of the samples. The standards and the samples were weighed with a mass in the range from 50 to 200 mg (weighing accuracy ±0,005 mg) in ceramic crucibles. The measurements were performed at 100 % power. The evolving gases CO_2 and CO were swept out by oxygen gas and measured by infrared detectors.

D Sample preparation for gas chromatography

Samples for gaschromatoraphy (GC) and gas chromatography combined with mass spectrometry (GC-MS) measurements were prepared by hydrogenating $V_{40}Fe_8Ti_{26}Cr_{26}$ in a reactor construced specifically for this purpose, which is shown schematically in Figure D-1.

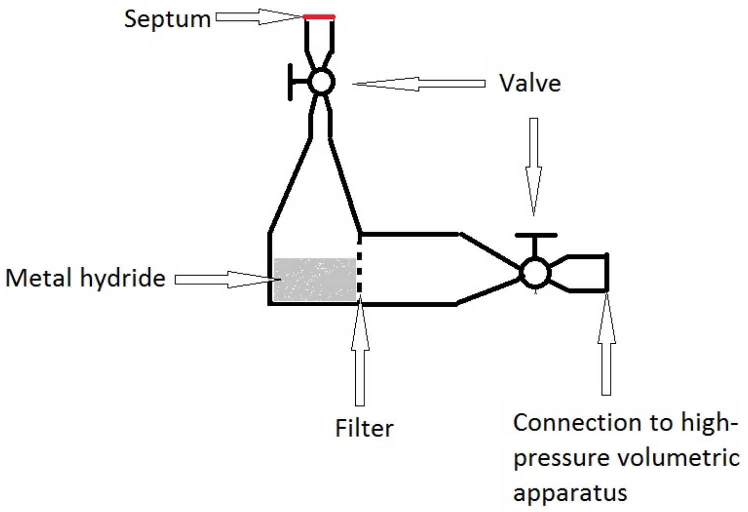

Figure D-1: Schematic representation of the self-designed reactor to prepare the GC samples.

The reactor consisted of a sample holder, which was surrounded by filters to prevent the powdery sample to escape, and two connections. The connections could be closed by valves. One connection was used to connect the reactor with a high-pressure volumetric apparatus. Another valve with a septum enabled the addition of acetone/toluene and later the removal of gaseous GC or GC/MS samples with minimal intrusion of air. The reactor was filled with 2 g of sample and then connected to the high-pressure volumetric apparatus. The samples were activated following the method described above. After hydrogenation at 5 MPa at room temperature for at least 30 min, the reactor was cooled down by immersing it into liquid nitrogen (77 K). After 30 min cooling, the reactor valve was closed, and the reactor was removed from the liquid nitrogen bath and left to warm up until the temperature at the outside of the sample holder reached the melting temperature of acetone or toluene, respectively (178 K for both liquids). Then 5 mL of the respective organic liquid was injected with a syringe. After 15 min, a gaseous sample was removed with a gas-tight syringe and introduced into the GC (in the case of toluene) or GC-MS (in the case of acetone) system. Another gaseous sample was measured after after the reactor had warmed up and had reached room temperature for at least 10 min. Blank tests of pure acetone/toluene were also measured.

E Scanning Electron Microscopy-Energy Dispersive X-ray Analysis (SEM-EDX)

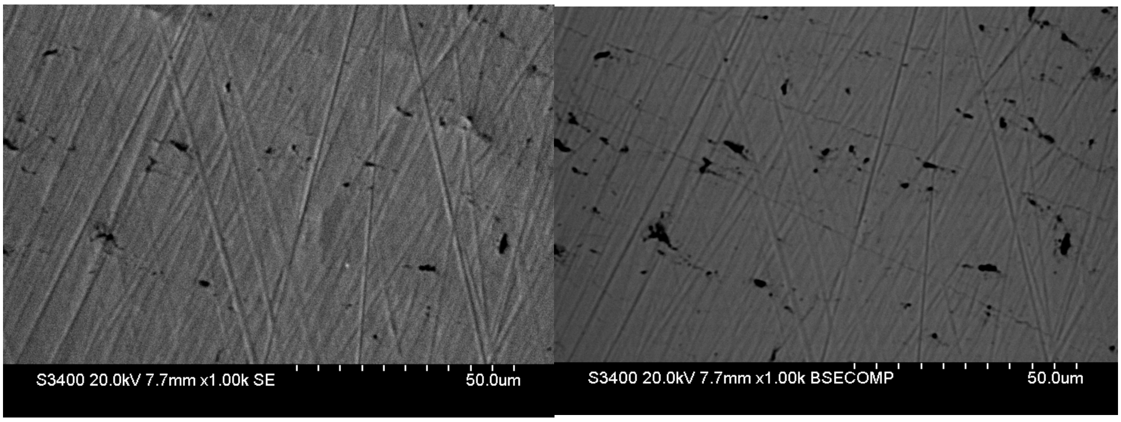

Fig. E-1: SEM images of $V_{40}Fe_8Ti_{26}Cr_{26}$ in the annealed state. SE: secondary electron image (left), and BSE: back-scattered electron image (right).

Sample	Phase	V [at%]	Fe [at%]	Ti [at%]	Cr [at%]
	Target composition	40	8	26	26
Low-oxygen	Main phase	41.4 – 43.8	6.4 – 7.1	22.5 – 24.1	26.8 – 27.3
	Ti-rich phase	28.4 – 32.7	11.2 – 13.6	34.0 – 38.2	19.8 – 22.1
High-oxygen	Main phase	41.2 – 42.9	8.1 – 8.9	21.9 – 24.1	26.2 – 27.4
	Ti-rich phase	2.8 – 13.4	0.1 – 2.9	78.3 – 95.9	0.7 – 6.5
Deoxidized	Main phase	38.1 – 44.0	7.1 – 8.5	22.9 – 24.3	23.9 – 27.9
	Ti-rich phase	27.6 – 34.1	6.9 – 11.9	35.5 – 46.1	15.3 – 21.5

Table E-1: Relative concentrations of constituent phases in low-oxygen, high-oxygen and deoxidized $V_{40}Fe_8Ti_{26}Cr_{26}$ determined by SEM-EDX. Oxygen is not included.

x	Phase	V [at%]	Fe [at%]	Ti [at%]	Cr [at%]	Al [at%]	Si [at%]
0	Main phase	41.4 – 43.8	6.4 – 7.1	22.5 – 24.1	26.8 – 27.3	0 – 0.5	0.1 – 0.3
	Sec. phase	28.4 – 32.7	11.2 – 13.6	34.0 – 38.2	19.8 – 22.1	0 – 0.1	0 – 0.2
	Average	40.7	8.1	26.9	24.5	0.1	0.1
0.15	Main phase	36.4 – 46.0	4.9 – 8.7	20.7 – 29.6	23.2 - 27.1	0.9 - 1.5	0.6 - 0.9
	Sec. phase	9.7 – 31.1	7.9 – 11.1	35.1 - 73.5	7.1 – 20.8	1.0 – 1.2	0.7 - 0.8
	Average	40.4	7.8	26.5	24.3	1.1	0.7
0.3	Main phase	36.4 – 43.8	5.7 - 8.0	21.5 – 28.3	24.0 - 26.4	0.7 – 2.4	0.4 – 1.0
	Sec. phase	16.7 - 26.6	4.6 – 12.9	39.7 – 69.2	15.2 - 18.2	1.8 - 2.0	0.7 - 2.0
	Average	40.2	7.3	26.9	23.8	2.0	0.9
0.45	Main phase	36.7 – 41.0	5.2 – 6.6	23.9 – 26.2	26.5 – 30.4	2.0 – 2.7	0.4 – 1.9
	Sec. phase	2.6 – 30.5	0.2 – 1.9	62.2 – 94.2	1.4 – 12.3	0.9 – 1.3	0.4 – 0.7
	Average	40.6	6.2	25.4	24.7	2.2	0.9
0.6	Main phase	38.6 – 46.7	5.2 – 6.6	21.4 – 26.3	21.5 – 30.4	1.9 – 2.8	0.6 – 1.9
	Sec. phase	28.7 – 32.5	0.3 – 6.9	38.1 – 72.9	15.6 – 17.3	1.6 – 2.4	0.3 – 0.8
	Average	40.5	6.6	26.7	22.5	2.7	1.3
0.75	Main phase	33.0 - 43.8	4.9 – 8.5	21.4 – 32.3	23.2 - 25.8	2.8 – 3.5	0.5 – 1.3
	Sec. phase	15.6 - 29.4	2.0 - 4.7	45.7 - 71.4	9.1 - 17.3	1.2 - 2.1	0.3 - 0.5
	Average	39.8	5.9	26.3	23.6	3.2	1.2
0.9	Main phase	37.9 – 42.8	5.1 – 5.5	23.4 – 27.8	23.6 – 25.9	3.6 – 4.3	0.5 – 1.6
	Sec. phase	21.2 – 26.0	4.1 – 4.9	48.7 – 87.0	13.8 – 17.0	2.7 – 2.9	0.3 – 0.8
	Average	39.2	5.6	25.6	24.1	4.1	1.3

Table E-2: Concentrations of constituent phases in $V_{(40-40\bullet x)}Fe_{(8-8\bullet x)}Ti_{26}Cr_{26}(FeV)_{(48\bullet x)}$ with x = 0, 0.3, 0.6 and 0.9. FeV 1 was used.

Substitution	Phase	V [at%]	Fe [at%]	Ti [at%]	Cr [at%]	Al [at%]	Si [at%]
FeV 2	Main phase	36.4 – 43.6	6.1 – 8.1	21.6 – 25.9	21.1 – 27.8	0.6 – 0.8	0.3 – 0.8
	Sec. phase	30.7 – 33.2	11.8 – 12.5	34.0 – 64.1	19.7 – 22.3	0.6 – 0-7	0.9 – 1.1
	Average	40.3	7.5	26.9	24.5	0.7	0.3 – 1.0

Table E-3: Concentrations of the constituent phases in $V_{40}Fe_8Ti_{26}Cr_{26}$ after substitution of (V + Fe) with FeV 2.

Substitution	Phase	V [at%]	Fe [at%]	Ti [at%]	Cr [at%]	Mg [at%]
Ti sponge	Main phase	37.8 – 42.9	6.8 – 7.9	22.0 – 26.9	23.0 – 25.3	< 0.1
	Sec. phase	27.9 – 32.2	9.3 – 12.1	27.0 – 34.0	16.4 – 23.0	< 0.1
	Average	39.7	7.8	25.5	25.1	< 0.1

Table E-4: Concentrations of the constituent phases in $V_{40}Fe_8Ti_{26}Cr_{26}$ after substitution of Ti with Ti sponge.

Current [A]	Phase	V [at%]	Fe [at%]	Ti [at%]	Cr [at%]	Al [at%]	Si [at%]
400	Main phase	33.1 – 43.6	6.1 – 6.7	21.5 – 26.8	21.8 –27.3	0.7 – 0.8	0.3 – 0.6
	Sec. Phase	30.7 – 32.7	8.7 – 11.7	28.0 – 40.1	19.3 – 23.2	0.7 – 0.9	1.0
	Average	38.4	7.4	25.6	26.3	0.8	0.5
500	Main phase	32.5 – 42.7	6.3 – 6.6	22.3 – 26.6	22.0 –26.9	0.6 – 0.8	0.4 – 0.7
	Sec. Phase	28.9 – 31.6	8.3 – 12.7	31.1 – 38.9	12.9 – 21.0	0.7 – 0.9	0.8 – 1.2
	Average	38.6	7.4	24.9	25.9	0.8	0.4

Table E-5: Concentrations of the constituent phases in $V_{40}Fe_8Ti_{26}Cr_{26}$ after substition with Ti sponge and FeV 2 at melting currents of 400 A and 500 A as determined by SEM-EDX.

Current [A]	V [at%]	Fe [at%]	Ti [at%]	Cr [at%]
400	39.7	8.0	25.8	26.5
450	40.1	7.9	25.6	26.5
500	40.0	7.9	25.8	26.4

Table E-6: Concentrations of the main components in $V_{40}Fe_8Ti_{26}Cr_{26}$ after substition with Ti sponge and FeV 2 at melting currents of 400 A, 450 A and 500 A as determined by ICP-OES.

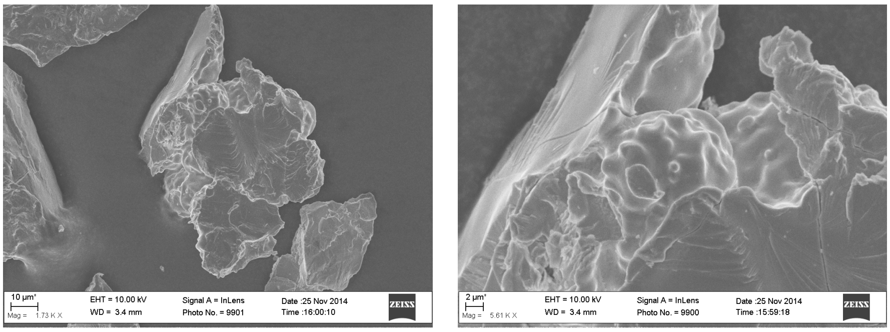

Figure E-2: SEM micrographs of the NaOH-leached material.

The morphology of the NaOH-leached particles was similar to the morphology of the cycled sample.

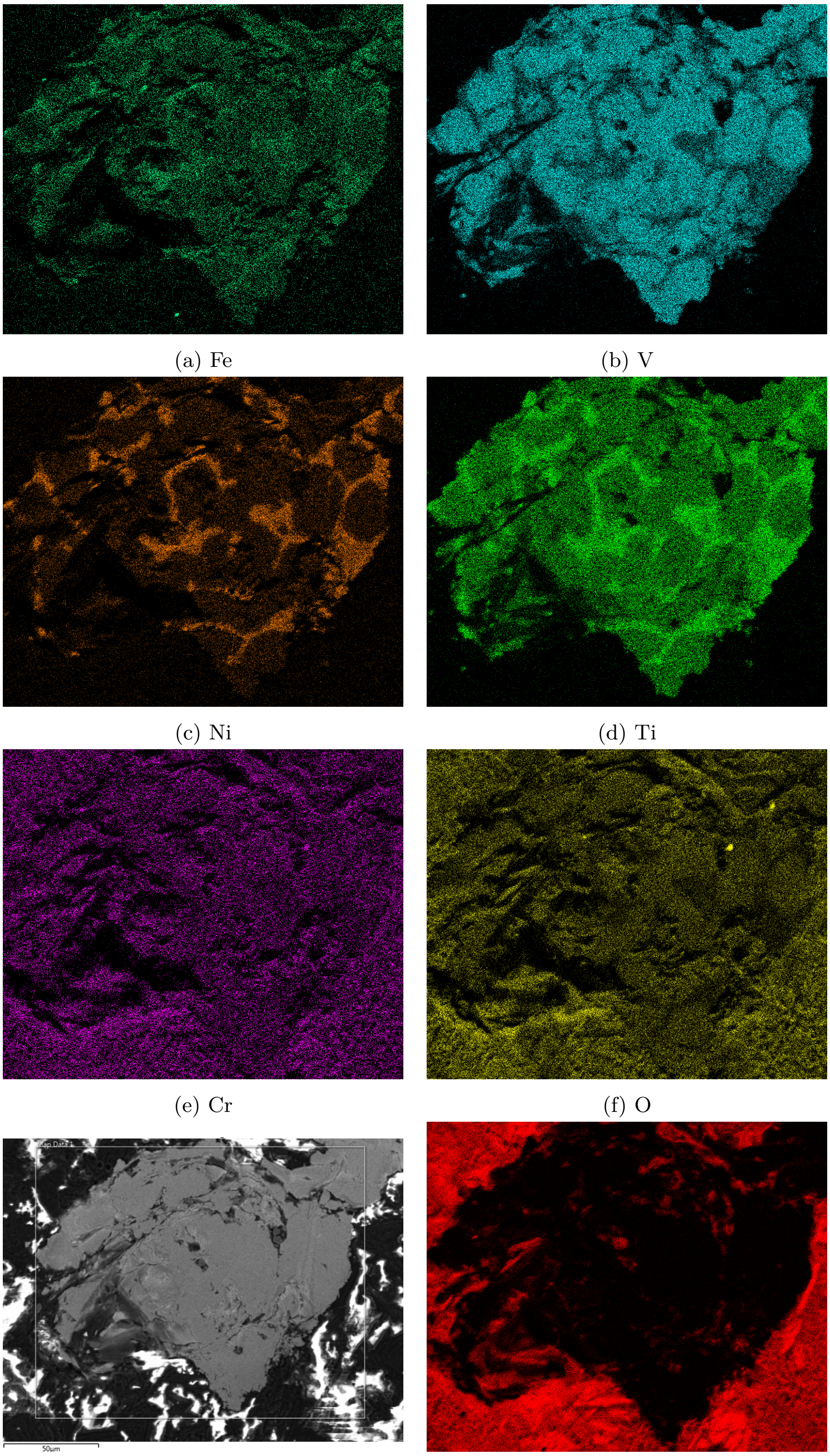

(a) Fe (b) V

(c) Ni (d) Ti

(e) Cr (f) O

(g) REM (h) C

Figure E-3: EDX elemental distributions of the cross-section of an NaOH-leached particle.

The elemental distribution of the leached sample was similar to that of the cycled sample. Ti- and Ni-rich areas were observed in the bulk. No compositional inhomogeneity was observed in the near-surface regions of the leached particles.

F Volumetric measurements

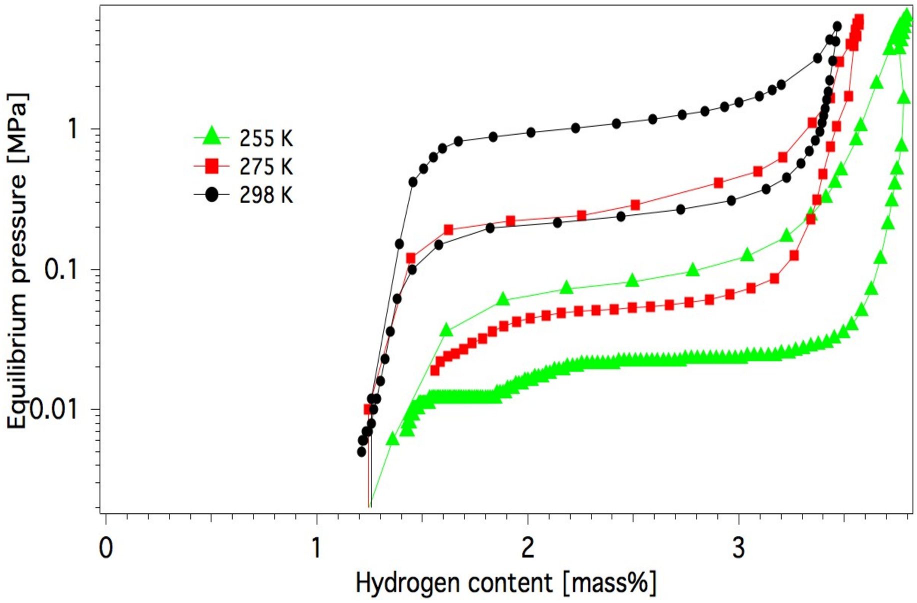

Fig. F-1: Pressure-composition isotherms of $V_{40}Fe_8Ti_{26}Cr_{26}$ at 255 K, 275 K and 298 K during the first cycle.

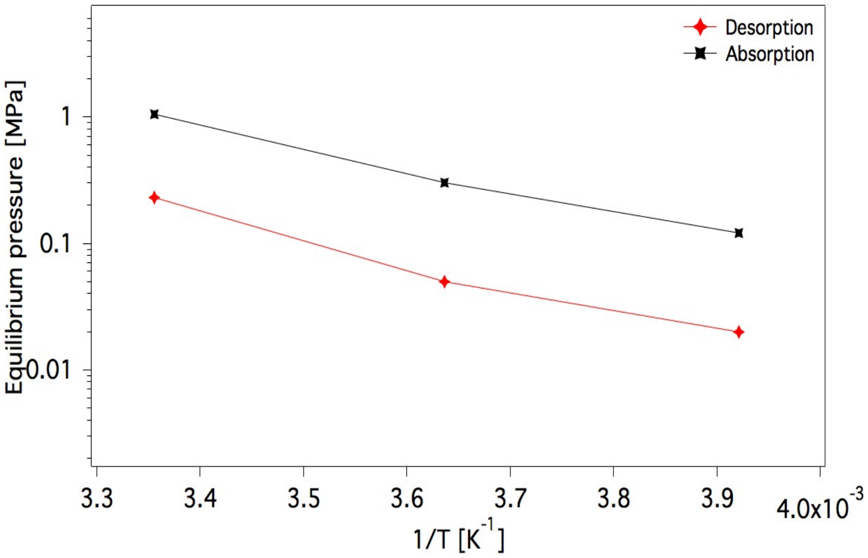

Fig. F-2: Van't Hoff plots for the PCI curves depicted in Fig. F-1.

x-value	Total capacity at 6 MPa [mass%]	Formation/ Dissociation plateau pressure at 298 K [MPa]	Pressure hysteresis H = p_f/p_d	Plateau slope S = $d(p_f)/d(mass\%)$
0	3.5	1.2 / 0.2	6	0.6
0.15	3.1	1.2 / 0.2	6	0.8
0.3	3.3	1.5 / 0.3	5	1.3
0.45	3.0	2.0 / 0.4	5	2.3
0.6	2.5	3.0 / 0.5	6	4.3
0.75	2.6	4.0 / 0.8	5	3.4
0.9	1.9	5.0 / 1.0	5	4.4

Table F-1: Thermodynamic properties of the FeV 1-substituted materials.

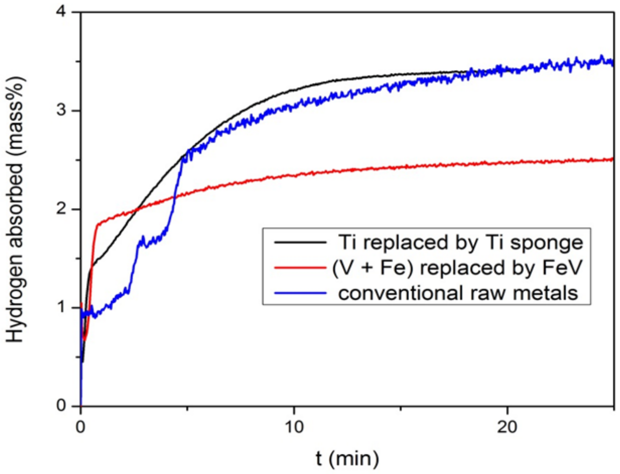

Fig. F-3: Initial absorption of $V_{40}Fe_8Ti_{26}Cr_{26}$ prepared with conventional raw metals, Ti sponge or FeV 2.

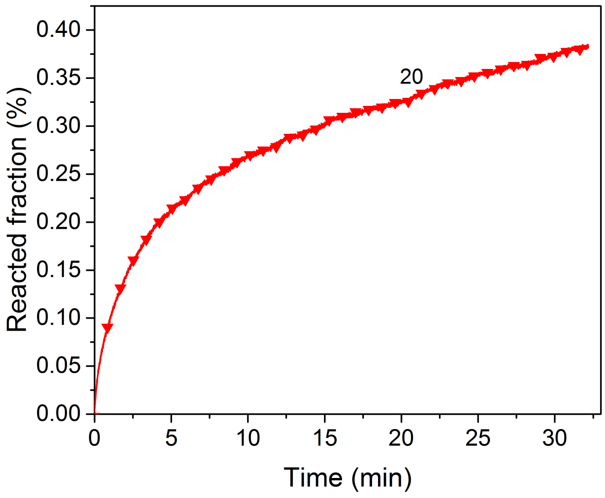

Figure F-4: Hydrogen absorption of $V_{40}Fe_8Ti_{26}Cr_{26}$ with 6 mass% Mm during the 20th cycle.

G X-ray Diffraction (XRD)

x-value	0	0.15	0.3	0.45	0.6	0.75	0.9
Lattice parameter [Å]	a_v = 3.0308(3)	a_v = 3.0284(2) a_{Fe} = 3.0278(2)	a_v = 3.0270(2) a_{Fe} = 3.0278(2)	a_v = 3.0214(2)	a_v = 3.0297(3)	a_v = 3.0300(2)	a_v = 3.0305(2)
R_{wp} [%]	11.598	14.944	12.607	15.691	17.416	11.862	11.267

Table G-1: Crystallographic parameters of $V_{(40-40\bullet x)}Fe_{(8-8\bullet x)}Ti_{26}Cr_{26}(FeV)_{(48\bullet x)}$ with x = 0, 0.15, 0.3, 0.45, 0.6, 0.75 and 0.9.

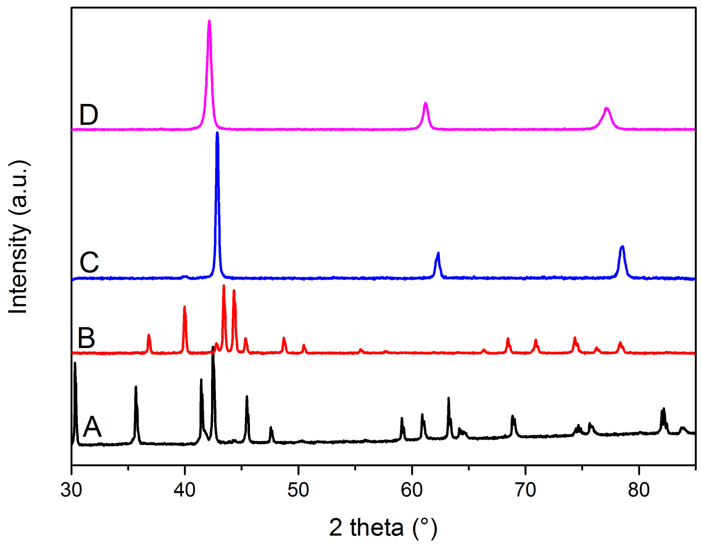

Fig. G-1: XRD patterns of $LaNi_5$ (A), Hydralloy C (B), TiFe (C) and $V_{40}Fe_8Ti_{26}Cr_{26}$ (D) in as-cast state.

Material	Lattice parameter as-cast [Å]	Lattice parameter desorbed at room temperature [Å]	Phase composition after acetone treatment	Lattice parameters after acetone treatment	Phase composition after toluene treatment	Lattice parameters after toluene treatment
$LaNi_5$	a = 5.023 Å, c = 3.99 Å	a = 5.01 Å, c = 4.00 Å	100 % $LaNi_5$ (P6/mmm)	a = 5.00 Å, c = 3.99 Å	100 % $LaNi_5$ (P6/mmm)	a = 5.01 Å, c = 3.985 Å
Hydralloy C	a = 4.878 Å, c = 7.995 Å	a = 4.881 Å, c = 8.002 Å	77 ± 2 % hydride (hexagonal, $P6_3/mmc$); 23 ± 2 % in desorbed state (hexagonal, $P6_3/mmc$)	Hydride: a = 5.188 Å, c = 8.4786 (6) Å; desorb: a = 4.935 Å, c = 8.002 Å	2 ± 1 % hydride; 88 ± 1 % in desorbed state (hexagonal)	Desorbed: a = 4.886 Å, c = 8.010 Å
TiFe		a = 2.98 Å	69 wt.% TiFeH (orthorhombic; P2221); 31 wt.% $TiFeH_{0.019}$ (cubic, Pm-3m)	Orthorhombic: a = 2.98 Å, b = 4.53 Å, c = 4.39 Å; Cubic: a = 2.98 Å	20 wt.% TiFeH (orthorhombic, P2221); 80 wt.% $TiFeH_{0.019}$ (cubic, Pm-3m)	Orthorhombic: a = 2.966 Å, b = 4.54 Å, c = 4.39 Å; Cubic: a = 2.98 Å
$V_{40}Fe_8Ti_{26}Cr_{26}$	a = 3.025 Å	a = 3.098 Å	100 wt.% face-centered cubic (Fm-3m)	a = 4.275 Å	82 wt.% face-centered cubic (Fm-3m); 18 wt.% body-centered cubic (Im-3m)	FCC: a = 4.272 Å; BCC: a = 3.099 Å

Table G-2: Crystallographic parameters of $LaNi_5$, Hydralloy C, TiFe and $V_{40}Fe_8Ti_{26}Cr_{26}$ in as-cast, desorbed state and after acetone/toluene treatment.

For $LaNi_5$ and TiFe, all parameters of the as-cast and de-/hydrided samples were in the expected range as compared to previous reports.[140], [141], [157], [158], [246]

For $V_{40}Fe_8Ti_{26}Cr_{26}$ the lattice parameter in the as-casted state is slightly reduced as compared to Ref. [247], which is likely due to the omission of an annealing procedure [275]. Lattice parameters of this material in the fully hydrogenated or monohydride state have not been reported before. Wu *et al.* reported lattice parameters of the as-cast BCC phase and fully hydrogenated FCC phase of a $V_{60}Ti_{22.4}Cr_{5.6}Fe_{12}$ alloy to amount to 3.042 Å and 4.256 Å, respectively [189]. Nakamura *et al*. studied a $Ti_{33.3}V_{36.7}Mn_{30.0}$ alloy and reported lattice parameters of 3.038 Å and 4.35 Å for the as-cast BCC phase and fully hydrogenated FCC phase, respectively.[16] Our results were in a similar range as compared to these reports. Nakamura *et al.* and Wu *et al.* observed a body-centered tetragonal structure of the monohydrides.[16], [189] The pattern of our monohydrided (desorbed at atmospheric temperature and pressure) sample exhibited a body-centered cubic structure. The structure of the monohydride is known to depend strongly on the composition of the alloy.[176] V-based solid solutions exhibit two distinct pressure plateaus, but only the upper plateau was dehydrogenated at ambient conditions.[247] The peak shift towards lower angles as compared to the as-cast sample is due to the remaining hydrogen content of the monohydride, which caused an expansion of the unit cell. It should be further noted that the XRD peaks of the monohydride were broadened significantly as compared to the dihydride and as-cast peaks. This indicates that the unit cells were distorted significantly.

Hydralloy C5 showed an orthorhombic structure (space group $P6_3/mmc$). The considerable peak shift observed after hydrogenation was in agreement with a previous report by Chao *et al.*, who observed a 3 ° (Cu-kα radiation) shift of a hydrogenated Zr-based multiphase AB_2-type alloy towards lower angles.[154] XRD of the hydride of this particular material has, to the best of our knowledge, not been reported yet. Isotropic lattice expansion by 6 % in both a- and c-direction was observed.

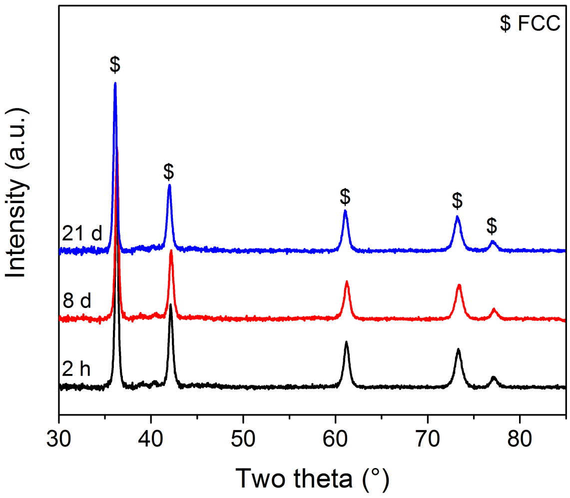

Fig. G-2: XRD patterns of acetone-treated $V_{40}Fe_8Ti_{26}Cr_{26}$ after storing in the glove box for 2 hours (2 h), 8 days (8 d) and 21 days (21 d).

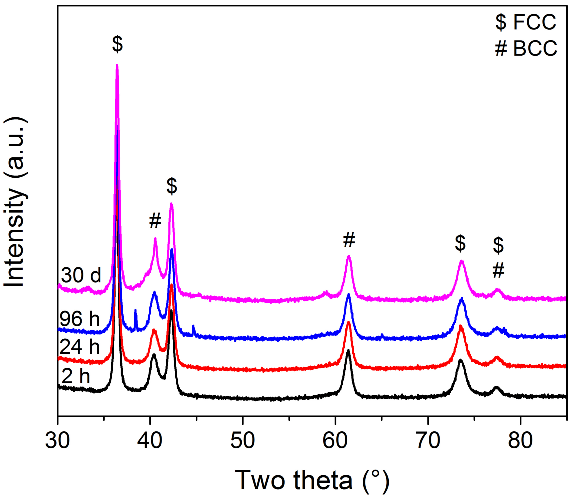

Fig. G-3: XRD patterns of toluene-treated $V_{40}Fe_8Ti_{26}Cr_{26}$ after storing in the glove box for 2 hours (2 h), 24 hours (24 h), 96 hours (96 h) and 30 days (30 d).

H Leaching experiments

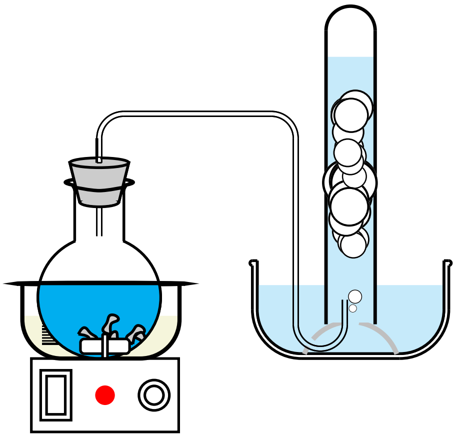

Figure H-1 Experimental setup for the leaching experiments.

The leaching experiments were performed in an experimental setup composed of a two-neck flask with a Schlenk connection, which was tempered in an oil bath. A tube led from the neck of the flask to a upside-down measuring cylinder, which was filled with water and was immersed in a water bath. The cylinder was used to measure the volume of escaped gas, which was formed during the leaching process. The oxidation of the metal is in equilibrium with the reduction of the electrolyte. Gaseous hydrogen may form during leaching in acidic solutions according to reaction equation (20):

$$2H_3O^+ + 2e^- \Leftrightarrow 2H_2O + H_2. \tag{20}$$

Gas evolution may also be observed in alkaline solutions. Corrosion occurs in the case of neutral/alkaline solution only in the presence of oxygen and without any H_2 evolution:

$$2H_2O + O_2 + 4e^- \Leftrightarrow 4OH^-, \tag{21}$$

But hydrogen evolution in absence of oxygen is also possible:

$$2H_2O + 2e^- \Leftrightarrow 2OH^- + H_2. \tag{22}$$

In order to gain insights into the leaching behavior of the various metals, different acidic and alkaline electrolytes were tested. The different acids and bases are summarized in Table H-1. The varied leaching parameters were the ratio between the electrolyte concentration, leaching time, leaching temperature and the ratio between solid and electrolyte (S/L).

Investigated parameter	**NaOH**	**Na_2CO_3**	**H_2SO_4**	**HCl**	**HNO_3**	**HNO_3 + HCl**
Concentration [mg/L]	0.5 – 9		0.5 - 9	1.5 - 8	1.5 - 5	3 - 6
Time [min]	10 – 50		-	-	-	-
Temperature [°C]	20 – 90		-	-	-	-
S/L [mg/3mL]	0.05 – 0.25		-	-	-	-

Table H-1: Acids and bases tested for leaching and the experimental parameters that were varied.

For variation of the leaching parameters, 0.15 g of the material were weighed using a high-precision balance and 3 mL of electrolyte were added. The flask was closed and connected to the experimental setup. The sample was leached at the given conditions. The standard leaching parameters were c = 2 mol/L, t = 30 min, T = 60 °C, and S/L = 0.15 g/3 mL. If any of the parameters was varied, the remaining parameters were kept constant. The flask was then removed from the oil bath and filled up with 47 mL of distilled water. Subsequently, the liquid was removed in a Büchner funnel using a water-jet vacuum pump and filter paper (pore diameter < 2 um). The filtrate was analysed using ICP-OES. Blind samples were measured with the highest acid or base concentrations. The same procedure was applied as described above, except without the sample. The leached samples were washed with distilled water until the pH value was 7 and then dried in air over night.

I X-ray Photoelectron Spectroscopy (XPS)

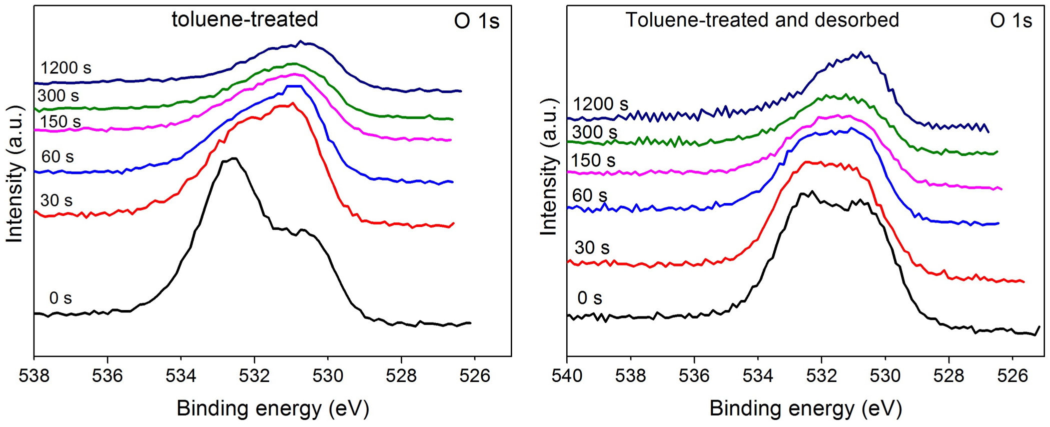

Fig. I-1: O 1s XP spectra of toluene-treated $V_{40}Fe_8Ti_{26}Cr_{26}$ (left) and toluene-treated and subsequently desorbed $V_{40}Fe_8Ti_{26}Cr_{26}$ (right).

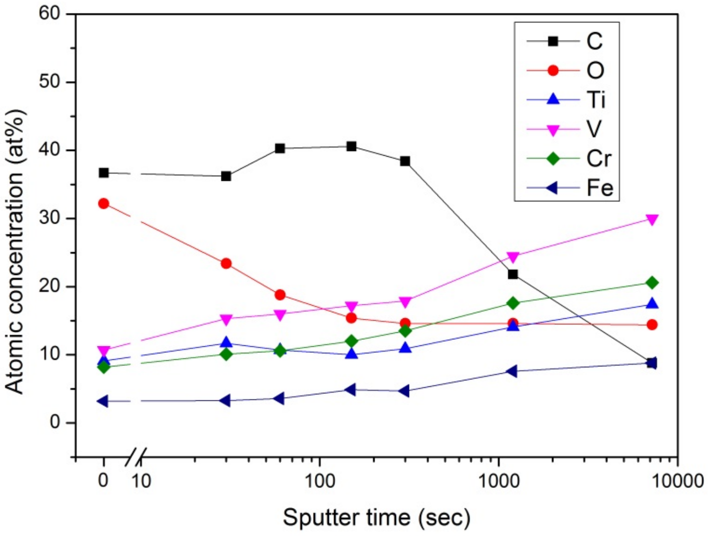

Fig. I-2: Depth profiles of the atomic concentrations of the surface and subsurface of the cycled sample.

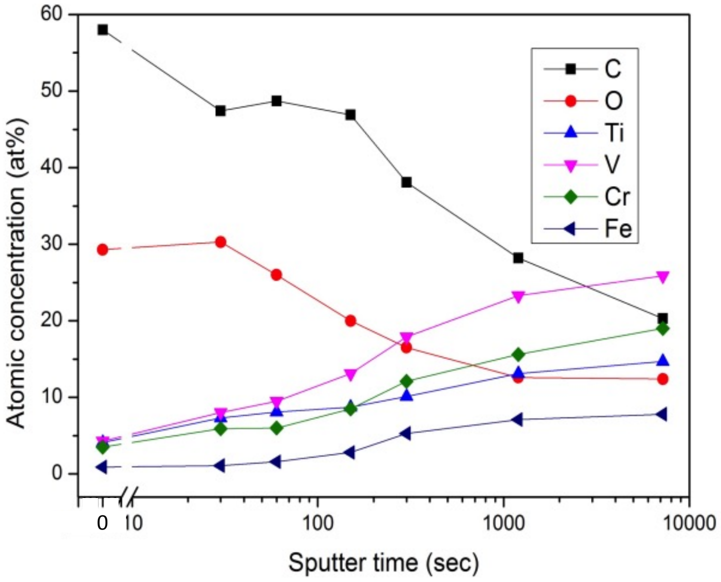

Fig. I-3: Depth profiles of the atomic concentrations of the surface and subsurface of the acetone-treated sample.

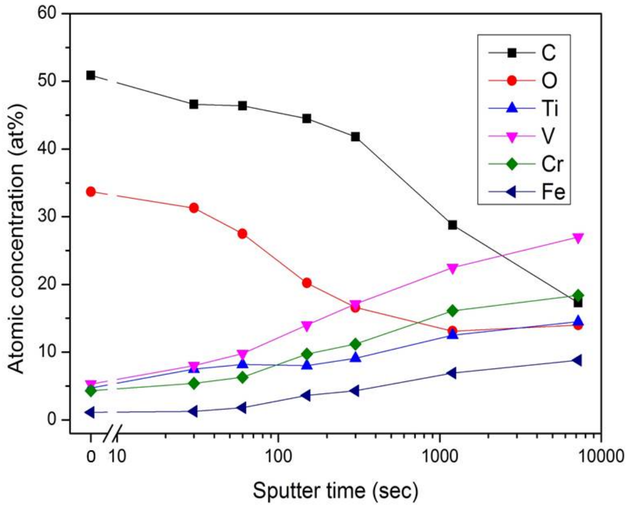

Fig. I-4: Depth profiles of the atomic concentrations at the surface and subsurface of the acetone-treated and desorbed sample.

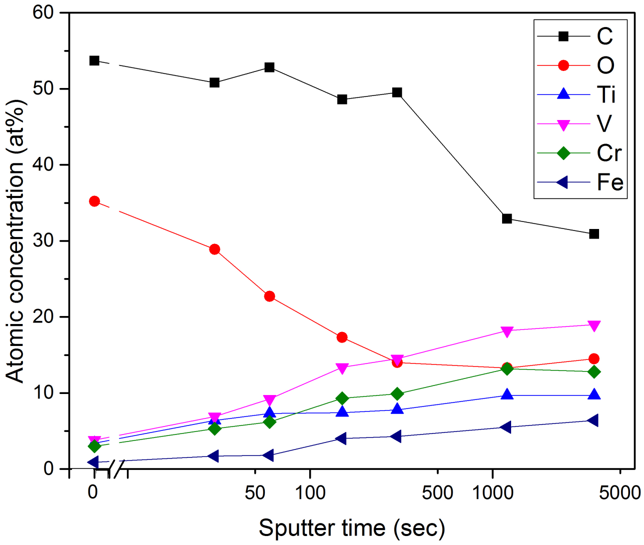

Fig. I-5: Depth profiles of the atomic concentrations at the surface and subsurface of the toluene-treated sample.

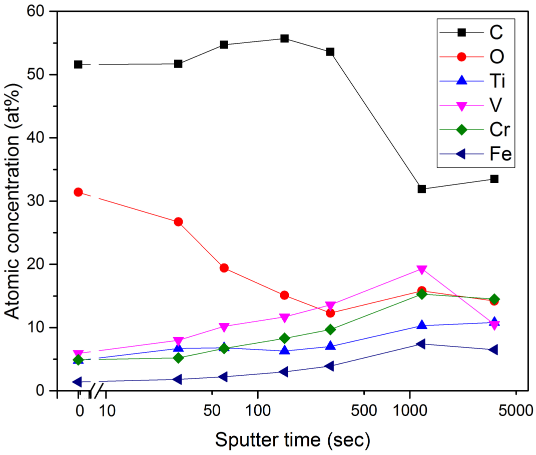

Fig. I-6: Depth profiles of the atomic concentrations at the surface and subsurface of the toluene-treated and desorbed sample.

Publication list

As first author:

Ulrich Ulmer, Daria Oertel, Marek Bielewski, Thomas Diemant, Pietro Moretto, Roland Dittmeyer and Maximilian Fichtner: “Improvement of the cyclic stability of V-Fe-Ti-Cr-based solid solution alloys in impure hydrogen gas”, in preparation

Ulrich Ulmer, Mila Dieterich, Alexander Pohl, Marc Linder, Roland Dittmeyer and Maximilian Fichtner: “Development of low-cost BCC hydrogen storage alloys – effects of V and Ti substitution with their low-cost alternatives”, in preparation

Ulrich Ulmer, Mila Dieterich, Alexander Pohl, Marc Linder, Roland Dittmeyer and Maximilian Fichtner: “Cost reduction possibilities in AB_2-type hydrogen storage alloys – Microstructural and cyclic effects of V and Ti substitution”, in preparation

Ulrich Ulmer, Christian Bonatto Minella, Martin Cholewa, Thomas Diemant, Roland Dittmeyer and Maximilian Fichtner: “Reactions of organic liquids on metal hydride surfaces”, submitted

Ulrich Ulmer, Kohta Asano, Andreas Patyk, Hirotoshi Enoki, Yumiko Nakamura, Alexander Pohl, Roland Dittmeyer and Maximilian Fichtner: “Cost reduction possibilities of vanadium-based solid solutions - microstructural, thermodynamic, cyclic and environmental effects of ferrovanadium substitution”, *J. of Alloys and Compounds*, 648, (2015), 1024 - 1030

Ulrich Ulmer, Kohta Asano, Thomas Bergfeldt, Venkata Sai Kiran Chakravadhanula, Roland Dittmeyer, Hirotoshi Enoki, Christian Kübel, Yumiko Nakamura, Alexander Pohl and Maximilian Fichtner: „Effect of oxygen on the microstructure and hydrogen storage properties of V–Ti–Cr–Fe quaternary solid solutions”, *Int. J. of Hydrogen Energy*, 39, (2014), 20000-20008

Ulrich Ulmer, Jianjiang Hu, Matthias Franzreb and Maximilian Fichtner: „Preparation, scale-up and testing of nanoscale, doped amide systems for hydrogen storage”, *Int. J. of Hydrogen Energy*, 38, (2013), 1439-1449

As co-author:

Alexey Volodin, Chubin Wan, R.V. Denys, G.A.Tsirlina, B.P.Tarasov, M. Fichtner, **Ulrich Ulmer**, D Scheptyakov, Yingda Yu, C.C. Nwakwuo, and V.A.Yartys: “Phase-structural transformations in a metal hydride battery anode $La_{1.5}Nd_{0.5}MgNi_9$ alloy and its electrochemical performance.”, submitted

Pietro Moretto, **Ulrich Ulmer,** Maximilian Fichtner, Marek Bielweski, Christoph Frommen, Vasile Iosub, Andreas Borgschulte, Petra De Jongh, Marcelo Barricio, Kohta Asano, Etsuo Akiba, Benjamin Villeroy, David Grant: “A Round Robin Test excercise of MgH_2 using Differntial Scanning Calorimerty”, in preparation

Christin Wagner, Martin Cholewa, **Ulrich Ulmer**, Dominik Poncette, Andreas Patyk, Maximilian Fichtner, Roland Dittmeyer, Peter Pfeifer: “Konzept zur Chemischen Wärmespeicherung mithilfe flüssiger organischer Hydride (LOHC)“, in preparation

Henrik Mauroy, Magnus Sorby, **Ulrich Ulmer**, Ralf Witte, Maximilian Fichtner, Björn Hauback: “Total scattering investigation of the local structure of Fe-containing BCC alloys“, in preparation

Noboru Taniguchi, Beatriz Caramés, Lorenza Ronfani, **Ulrich Ulmer**, Setsuro Komiya, Marco E. Bianchi and Martin Lotz: “Aging-related loss of the chromatin protein HMGB2 in articular cartilage is linked to reduced cellularity and osteoarthritis“, *Proc. Nat. Acad. Sci.*, 106, (2009), 1181 – 1186